De productie en moleculaire verschijningsvorm van radiotoxisch Po-210
in kernfusie- en splijtingsreactoren

The Production and Molecular Occurrence of Radiotoxic Po-210
in Nuclear Fusion and Fission Reactors

Die Produktion und die molekularen Erscheinungsformen von radiotoxischem
Po-210 in Kernfusions- und Kernspaltungsreaktoren

Merlijn Mertens

Promotors: Prof S. Cottenier, PhD, Prof R. Stieglitz, PhD, Prof J.-M. Noterdaeme, PhD
Doctoral thesis submitted in order to obtain the academic degrees of
Doctor of Engineering Physics (Ghent University) and
Dr.-Ing. (Karlsruhe Institute of Technology)

GHENT
UNIVERSITY

Department of Electrical Energy, Metals, Mechanical Constructions and Systems
Head of Department: Prof L. Dupré , PhD
Faculty of Engineering and Architecture

Karlsruhe Institute of Technology

Department of Mechanical Engineering
Head of Department: Prof C. Proppe, PhD

Academic year 2019 - 2020

ISBN 978-94-6355-302-5
NUR 928, 961
Wettelijk depot: D/2019/10.500/110

Members of the Examination Committee

Chair

Prof. Luc Taerwe, PhD (Ghent University)

Co-chair

Prof. Anton Möslang, PhD (Karlsruhe Institute of Technology)

Other voting members

Prof. Louis Vanduyfhuys, PhD (Ghent University)
Ulrich Fischer, PhD (Karlsruhe Institute of Technology)
Jörg Neuhausen, PhD (Paul Scherrer Institute)
Ivan Infante, PhD (Italian Institute of Technology)

Supervisors

Prof. Stefaan Cottenier, PhD (Ghent University)
Prof. Jean-Marie Noterdaeme, PhD (Ghent University)
Prof. Robert Stieglitz, PhD (Karlsruhe Institute of Technology)

Preface

If in doubt, paddle out.
Robert Harold 'Nat' Young

Wijze woorden van de Australische surflegende en auteur Nat Young. De onderliggende boodschap leunt dicht aan bij de hedendaagse slogan van Nike: *'Just do it'*. En zo is het volgens mij ook in het leven. Een mens heeft dikwijls meer spijt van een kans die hij liet schieten, dan één die slecht afloopt. Dus greep ik de kans om te doctoreren met beide handen. Het was zeker niet altijd gemakkelijk en soms voelde die slechte afloop veel te dichtbij, maar bij het indienen van dit boekje vervagen de dieptepunten in een oogwenk en blijven enkel de goede herinneringen plakken.

Allereerst was het een waar genoegen om te mogen samenwerken met mijn collega's van het Center for Molecular Modeling van de universiteit Gent en deze van het Institute for Neutron Physics and Reactor Technology van het Karlsruhe Institute for Technology. De verhelderende discussies en de aangename lunchpauzes hebben ervoor gezorgd dat ik telkens weer met veel zin richting het werk kon vertrekken. In het bijzonder had ik graag mijn (ex-)kantoorgenoten Sam De Waele, Michiel Larmuseau, Michael Sluydts en Senne Caroes willen bedankten voor zowel hun kennis als het jolijt die we samen deelden. Daarnaast ook Sven Rogge en Kurt Lejaeghere voor hun diepgaande kennis van het bestuur en de administratie van de UGent en Elena Nunnenmann voor haar hulp bij het vertalen van mijn samenvatting naar het Duits.

Ook mijn promotoren Stefaan Cottenier, Robert Stieglitz en Jean-Marie Noterdaeme verdienen een expliciete bedanking. Hun expertise en gegronde feedback, maar ook persoonlijke steun hielden me op het rechte pad en hielpen me de kwaliteit van zowel de gepubliceerde artikels als dit werk

te verbeteren. Ulrich Fischer zorgde ook voor een uitstekende begeleiding tijdens mijn verblijf aan KIT.

Maar met enkel mijn promotoren en mijn collega's had ik de voorbije vier jaar niet even goed doorstaan als dat nu het geval is. Mijn ouders steunen me nu reeds 27 jaar lang ten volle in alles wat ik doe, en dit heeft een enorme impact gehad op waar ik nu sta. Daar ben ik hen enorm dankbaar voor. Betere zussen en broers (Marie, Lieze, Lukas en Melchior) had ik niet kunnen wensen. We blijven steeds beter overeenkomen en dat is een echte deugd. Mijn nieuwe nichtje Laure en petekindje Juul hebben onze band zelfs nog verder versterkt. Ook mijn vrienden, en in het bijzonder deze van de KSA, hielpen me telkens mijn hoofd boven water te houden via onvergetelijke nachtjes stappen, allerlei weekendjes, een bezoekje aan Karlsruhe en leuke KSA kampen.

Stephanie, de steun en liefde die jij me bood is van een nog heel ander niveau. Het is steeds leuk thuiskomen bij jou, de eeuwige optimist. Zeker tijdens de eindsprint verzorgde je me als nooit te voren en nam je naast je zware werk nog eens bijna het volledige huishouden op jou. *Achter elke sterke man, staat een sterkere vrouw*, zegt men. Of ik tot die eerste groep behoor, dat laat ik in het midden, maar van jou weet ik 100 procent zeker dat je tot de tweede groep behoort. Bedankt voor alles, liefje!

Merlijn A.J. Mertens
Gent, 30 oktober 2019

Contents

List of Symbols

Alphanumeric symbols	
A	mass number
A	slope in linear dependence of $N_{^{210}\mathrm{Po}}$ on $N_{^{209}\mathrm{Bi,i}}$
A	ampere
${}^{A}_{Z}\mathrm{X}$	element X with atom number Z and mass number A
$a0, a1, a2$	Dunham coefficients (Eq. 4.7)
$\mathrm{A1}$	atom 1
$\mathrm{A2}$	atom 2
a_{A}	coefficient of asymmetry term in SEMF
a_{C}	coefficient of coulomb term in SEMF
a_{P}	coefficient of pairing term in SEMF
Ar	argon
As	Arsenic
a_{S}	coefficient of surface term in SEMF
at%	atomic percentage
a_{V}	coefficient of volume term in SEMF
B_{e}	rotational constant
Be	beryllium
Bi	bismuth
Bq	bequerel
C	carbon
c	speed of light in vacuum
c	concentration
C_{N-N}	Coulomb attraction energy between nuclei (const)
c_V	molar heat capacity at constant volume
c_1, c_2	parameters in the Hulbert potential energy function (Eq. 4.6)
°C	degrees celsius

Cu	copper
Cr	chromium
D	deuterium
d	days
D	depth of the dissociation profile
D_0	dissociation energy at 0 kelvin
D_e	centrifugal distortion constant
E	energy
e	elemental charge
E_α	alpha-particle kinetic energy
E_ZPE	zero-point energy
E_a	Activation energy
E_b	binding energy
E_c	Coulomb energy
E_d	dissociation energy
E_el	electronic thermal energy correction
E_rovibel	rotational-vibrational-electrionic correction
E_tr	translational thermal energy correction
eV	electronvolt
Fe	iron
G	giga
G	Gibbs free energy
g	gram
g	photon
g	degeneracy
$\overrightarrow{g}$	gravity vector
Ge	Germanium
H	hydrogen
h	hour
h	Planck's constant
He	helium
$\widehat{H}$	Hamiltonian
i	electronic state
J	rotational quantum number
K	kelvin
K_P	equilibrium constant from the partial pressures
k	kilo
k_B	Boltzmann constant
Li	lithium
m	mass
m	meter

M	Mega
M	molecule
m_{e}	electron mass
M_{X}	mass of nucleus X
m_{n}	neutron mass
m_{p}	proton mass
N	nitrogen
n	neutron
N	atomic density
n	number of moles
$N_{^{209}\mathrm{Bi,i}}$	initial 209Bi impurtity level
$N_{^{210}\mathrm{Po}}$	final 210Po inventory
$\mathrm{N}_{^{210}\mathrm{Po}}^{\mathrm{noBi}}$	final 210Po inventory for 209Bi-free Pb-Li
Ni	nikkel
O	oxygen
P	phosphorus
P	total vapor pressure
P'	partial vapor pressure
Pa	pascal
Pb	lead
Po	polonium
Pu	plutonium
Q	partition function
r	radial axis
R	internuclear distance
R	gas constant
R_{e}	equilibrium bond length
Ra	radon
$\boldsymbol{R}$	nuclear postion vector
$\boldsymbol{r}$	electronic position vector
S	sulfur
Sb	Antimony
Se	Selenium
S_{el}	electronic entropy contribution
Si	silicon
Sn	Tin
S_{rovibel}	rotational-vibrational-electrionic entropy contribution
S_{tr}	translational entropy contribution
Sv	sievert
T	tritium
t	tonne
T	tera

T	temperature
$t_{1/2}$	half-life
Te	Tellurium
Ti	titanium
U	uranium
V	potential energy
vol%	volumetric percentage
W	tungsten
W	watt
W_e	watt electric
wt%	weight percentage
W_{th}	watt thermal
$\boldsymbol{x}$	space-spin coordinates
y	year
z	vertical axis
Z	atom number
Zr	zirconium

Greek symbols	
α_{e}	vibration-rotation coupling constant
β	share of delayed neutrons
β^{-}	beta minus decay
Δ	difference
ϵ_0	vacuum permittivity
γ	photon
μ	reduced mass
ν	vibrational quantum number
ω_{e}	fundamental vibration frequency
$\omega_{\mathrm{e}} x_{\mathrm{e}}$	first anharmonic vibration constant
$\omega_{\mathrm{e}} y_{\mathrm{e}}$	second anharmonic vibration constant
ϕ_{n}	neutron flux
φ	toroidal axis
π	pi
Ψ	(molecular) wave function
ψ	single-particle spin-orbital
Ψ_0^{HF}	Hartree-Fock electronic ground state wave function
$\psi_{\mathrm{electronic}}$	electronic wave function
ψ_{nuclear}	nulcear wave function
σ	cross section
σ_{eff}	effective one-group cross section
θ	poloidal axis

Mathematical symbols	
$\ln$	natural logarithm
∇	Gradient
Σ	summation

In general, vectors and matrices are printed in bold face throughout this work.

List of Abbreviations

2D	2-dimensional
3D	3-dimensional
ABWR	Advanced Boiling Water Reactor
ADS	Accelerator Driven System
AGCR	Advanced Gas-Cooled Reactor
ANO	Atomic Natural Orbital
AP	Advanced Passive
appm	atomic parts per million
appb	atomic parts per billion
appt	atomic parts per trillion
ARIES-AT	Advanced Reactor Innovation and Evaluation Study - Advanced Tokamak
AS	Active Space
ASD	Atomic Spectra Database
BB	Breeding Blanket
BM	Breeding Module
BP	Backplate
BSS	Back Supporting Structure
BSS	Barysz-Sadley-Snijders method
BU	Breeding Unit
BWR	Boiling Water Reactor
CAD	Computer Aided Design
CANDU	CANada Deuterium Uranium
CASPT2	Complete Active Space Perturbation Theory 2^{th} order
CASSCF	Complete Active Space Self-Consistent Field
CASSI	Complete Active Space State Interaction
CCSD	Coupled Cluster Single-Double
CCSD(T)	Coupled Cluster Single-Double and perturbative Triple
CENDL	Chinese Evaluated Nuclear Data Library
CI	Configuration Interaction

CP	Cooling Plate
CPS	Current Policies Scenario
CS	Central Solenoid
DC	Dirac-Coulomb
DCLL	Dual Coolant Lithium Lead
DEMO	DEMOnstration power plant
DFT	Density Functional Theory
DIV	divertor
DKH	Douglas-Kroll-Hess
dpa	displacements per atom
EAF	European Activation File
ECP	Effective Core Potential
ENDF	U.S. Evaluated Nuclear Data File
EPR	European Pressurized Reactor
ESPLT	Energy splitting variance reduction technique
EU	European Union
FBR	Fast Breeder Reactor
FPP	Fusion Power Plant
FPY	Full-Power Year
FW	First Wall
FWO	Fonds Wetenschappelijk Onderzoek
GCR	Gas-Cooled Reactor
GDP	Gross Domestic Product
Gen.	Generation
GFR	Gas-cooled Fast Reactor
GIF	Gen. IV International Forum
HCLL	Helium Cooled Lithium Lead
HCPB	Helium Cooled Pebble Bed
HEX	Heat exchanger
hetero	heterogeneous
HF	Hartree-Fock
homo	homogeneous
hSP	horizontal Stiffening Plate
HVAC	Heating-Ventilation-Air Conditioning
IAEA	International Atomic Energy Agency
IB	inboard
IEA	International Energy Agency
IG	Iter-Grade
INEEL	Idaho National Engineering and Environment Laboratory
irrep	irreducible representation
ITER	International Thermonuclear Experimental Reactor
JAEA	Japan Atomic Energy Agency

JEFF	Joint Evaluated Fission and Fusion File
JENDL	Japanese Evaluated Nuclear Data Library
JET	Joint European Torus
L	layer
LBE	Lead-Bismuth Eutectic
LFR	Lead (alloy) cooled Fast Reactor
LSODES	Livermore Solver for Ordinary Differential Equations with general Sparse Jacobian matrices
LWGR	Light Water Graphite Reactor
LWR	Light Water Reactor
MCAM	Monte Carlo particle transport Automatic Modeling system
MCK	MCKINLEY module (Molcas)
MCNP	Monte Carlo N-Particle
MF	manifold
MIT	Massachusetts Institute of Techology
MOX	Mixed OXide
MS	Multi State
MSR	Molten Salt Reactor
MYRRHA	Multi-purpose hYbrid Research Reactor for High-tech Applications
NEA	Nuclear Energy Agency
NIST	National Institute of Standards and Technology
NPS	New Policies Scenario
OB	outboard
Out	Outside
PAV	Permeator Against Vacuum
PES	Potential Energy Surface
PF	Poloidal Field
Ph.D.	Philisophiae Doctor
PHWR	Pressurized Heavy Water Reactor
ppb	parts per billion
ppm	parts per million
PPPT	Power Plant Physics and Technology
ppt	parts per trillion
PWR	Pressurized Water Reactor
R&D	Research & Development
rovibel	rotational-vibrational-electronic
SCF	Self-Consistent Field
SCK · CEN	StudieCentrum voor Kernenergie · Centre d'étude de l'Énergie Nucléaire
SCWR	Super Critical Water Reactor
SDS	Sustainable Development Scenario

SEMF	Semi-Empirical Mass Fromula
sf	spin-free
SFR	Sodium-cooled Fast Reactor
SMR	Small Modular Reactor
SO	Spin-Orbit
SS	Stainless Steel
TBR	Tritium Breeding Ratio
TENDL	TALYS-based Evaluated Nuclear Data Library
TER	Tritium Extraction and Removal
TERS	Tritium Extration and Removal System
TES	Tritium Extraction System
TF	Toroidal Field
TP	Tritium Plant
U.K.	United Kingdom
U.S.	United States
UNGG	Uranium Naturel Graphite Gaz (Fr.)
VDT	Vacuum Droplets' Tower
VFA	Valence Field Analysis
VHTR	Very High Temperature Reactor
VQZP	Valance Quadruple Zeta Polarized
vSP	vertical Stiffening Plate
VST	Vacuum Sieve Tray
VV	Vacuum Vessel
VVER	Vodo-Vodyanoi Energetichesky Reactor
WCLL	Water Cooled Lithium Lead
WGT	weight
ZORA	Zero-Order Regular Approximation

Summary

Over the past decades, people have become fully aware of the impact of energy production on the climate, the environment and our health. The vast majority of the scientific society has agreed on the direct correlation between burning fossil fuels and the climate change. Weather anomalies such as devastating hurricanes, extreme droughts and enormous wildfires as well as the rising sea level have been widely ascribed to the recorded global warming and have resulted in millions of climate refugees. The International Energy Agency has published recommendations on how these new trends can be sustainably countered by profoundly transforming the present energy supply scheme. Their most optimistic scenario is realized by a drastic boost of the renewables' share in the energy mix. However, as most scalable renewable energy sources are intermittent, they argue that this can only be achieved within a realistic time and cost frame if it is combined with a serious expansion of the installed nuclear power capacity.

As the installed fission reactors are not inherently safe, produce considerable amounts of nuclear waste and require high capital investments, there is need for a new generation of fission reactors. An interesting concept is the lead (alloy) cooled fast reactor, offering advantages such as long refueling times, possibly natural cooling after shutdown, no explosion hazard, solidification of leaking coolant and no overpressurization by overheating. The Belgian Multi-purpose hYbrid Research Reactor for High-tech Applications (MYRRHA) will serve as European Pilot Plant for their development. It is a lead-bismuth eutectic (LBE) cooled pool-type fast fission reactor, to be fully operational by 2033. LBE is used rather than lead because of its lower melting point (125°C vs. 327°C). A drawback of this is that the implemented ^{209}Bi can capture fission neutrons, producing radiotoxic polonium (^{210}Po). The ingestion and inhalation radiotoxicity of ^{210}Po is among the highest of all known radionuclides. A considerable build-up of this isotope within the coolant can therefore jeopardize the safe

operation of the reactor.

A similar problem is expected to occur in nuclear fusion reactors. In these reactors, deuterium (D) and tritium (T) will be fused to produce energy. As tritium is extremely scarce, at least as much T will have to be produced within the reactor, as there is consumed. This is achieved by making neutrons originating from the fusion reactions interact with lithium, resulting in the production of tritium. As some neutrons will be absorbed in the structural materials or simply escape the reactor, a neutron multiplier (emitting additional neutrons when interacting with high-energy neutrons) has to be implemented. Both Pb and Be are being considered for this purpose. The European DEMOnstration (DEMO) Power Station will be the first (European) reactor aiming to demonstrate tritium self-sufficiency, as well as the ability to generate a net electrical output from fusion energy. This reactor is currently at the end of its pre-conceptual phase, while its construction is due to start in 2040. A possible breeding concept consists in using liquid lead-lithium eutectic (Pb-Li) as breeder/multiplier material, implemented within a breeding blanket surrounding the fusion plasma. An open problem with this concept is that beside multiplying neutrons, lead can also capture them, resulting in the production of ^{209}Bi. Similarly as in MYRRHA, the produced ^{209}Bi can interact with the numerous neutrons, resulting again in the production of the problematic ^{210}Po. An extensive discussion on the energy problem, the prominent role that nuclear energy could have in a sustainable solution, the history and future of nuclear energy and how polonium is undesirably produced in some fission and fusion reactor concepts is presented in **Chapter 1**.

The aim of this work is to provide essential information required to asses the actual risk associated with the appearance of ^{210}Po in a nuclear fission or fusion reactor. One important factor is the magnitude of the overall ^{210}Po inventory, which has been previously estimated for MYRRHA but is unknown for the current design of DEMO. Other essential knowledge is the chemical behavior of ^{210}Po within the reactor environment, which can guide the development of dedicated Po extraction systems and can provide information on the expected radiological release in case of an accident. This part of the work focuses on the chemistry of gaseous Po-containing molecules as these can escape the reactor most easily and form a severe threat when inhaled.

The ^{210}Po inventory in DEMO was determined by combining neutron transport calculations with dedicated inventory calculations. The

Monte-Carlo N-Particle (MCNP) neutron transport code was used to probabilistically track fusion neutrons, as well as the secondary particles they produce, from birth to death. Doing so for a large number of fusion neutrons, the energy- and space-dependent neutron flux can be obtained. Multiplying this flux with the energy-dependent cross section (probability) of a given neutron interaction and with the space-dependent atomic density of the involved target nucleus, the occurrence rate of that reaction can be obtained. This methodology was previously used in MYRRHA to determine the neutron capture rate by ^{209}Bi resulting in ^{210g}Bi, which relatively quickly β^-–decays to ^{210}Po ($t_{1/2}$ = 5 d).

For the DEMO fusion reactor, the exact same procedure can not be followed as the ^{210}Po production process is now a two-step neutron interaction process ($^{208}\text{Pb} \xrightarrow{n,\gamma} {}^{209}\text{Pb} \xrightarrow{\beta^-} {}^{209}\text{Bi} \xrightarrow{n,\gamma} {}^{210g}\text{Bi} \xrightarrow{\beta^-} {}^{210}\text{Po}$). Instead, the obtained neutron flux spectra are used as input for the FISPACT-II inventory code. Using (i) these flux spectra, (ii) the local atomic density of ^{208}Pb and ^{209}Bi, (iii) the energy-dependent neutron capture cross sections of ^{208}Pb and ^{209}Bi, (iv) the half-life of all unstable nuclides, and (v) an irradiation schedule of interest, the program allows to determine the ^{210}Po inventory at any desired time. In this work, two blanket concepts were considered: the Helium Cooled Lithium Lead and the Water Cooled Lithium Lead concept. A homogeneous and heterogeneous model for both concepts was considered, resulting in comparable neutron flux spectra and inventories. In all calculations, the continuous circulation of the Pb-Li within the blanket was accounted for and two irradiation schedules of interest were studied. Different nuclear data libraries (containing the neutron cross sections) were compared and were found to have a considerable impact on the final Po inventory. In fact, larger differences were found for the same model with different data libraries than between the models themselves. The negative impact of the initial ^{209}Bi impurity level in the Pb-Li on the ^{210}Po inventory was also studied and quantified. A detailed discussion on the methodology used and the obtained results can be found in respectively **Chapter 2** and **Chapter 3**.

The high radiotoxicity of ^{210}Po makes experiments risky and expensive, resulting in very few reports on the chemical behavior of ^{210}Po. In this work, an alternative approach was chosen: high level-of-theory ab initio (quantum chemistry) calculations were performed. As polonium is a heavy element with many electrons, effects such as electron correlation and spin-orbit are very prominent and have to be accurately accounted for, increasing the complexity of the calculations. As a first step, gaseous

diatomic molecules were considered containing Po and another element expected to be presents in the reactors of interest i.e. Pb or Li (relevant for fusion reactor Pb-Li breeding blankets), Pb or Bi (relevant for fission reactor Pb-(Bi) coolants), H or O (relevant for water contamination) or another Po atom. The used ab initio method was validated by applying it to analogue molecules for which experimental data is available. In addition, detailed test calculations were performed for Pb_2, PbO and Po_2. To obtain the temperature-dependent stability of the Po-molecules of interest, their dissociation profiles were determined to be used in a statistical thermodynamics analysis. The obtained stabilities were then combined with the initial atomic concentrations of the different elements in the plenum gas of the MYRRHA and DEMO reactor (for Po depending on the final inventory obtained in the first part of this work), to obtain the relative occurrence of the different Po species. In addition a risk analysis was performed for a leak-of-PbLi accident in DEMO. It was found that Po will probably not present a threat in this case, instead possibly when it makes contact with water and volatile (oxy)hydroxides form. The methodology and obtained results are discussed in detail in respectively **Chapter 4** and **Chapter 5**.

Finally, **Chapter 6** presents some final conclusions and perspectives for future work.

Samenvatting

De afgelopen decennia is de mensheid zich steeds meer bewust geworden van de grote impact die energieproductie heeft op het klimaat, het milieu en onze gezondheid. De overgrote meerderheid van de wetenschappelijke gemeenschap is het eens dat er een directe correlatie bestaat tussen het intensief verbranden van fossiele brandstoffen en de klimaatsverandering. Afwijkende weersverschijnselen zoals verwoestende orkanen, extreme droogtes en enorme bosbranden, maar ook de stijging van de zeespiegel worden algemeen toegeschreven aan de opgemeten opwarming van de aarde en hebben reeds geleid tot miljoenen klimaatvluchtelingen. Het International Energy Agency (IEA) heeft enkele aanbevelingen gepubliceerd over hoe deze trends op een duurzame manier kunnen worden tegengegaan door de huidige energiebevoorading grondig te hervormen. Hun meest optimistische scenario kan worden gerealiseerd door het aandeel van hernieuwbare energie in de energiebevoorading drastisch te verhogen. Aangezien de op te schalen hernieuwbare energiebronnen echter intermitterend zijn, stelt het IEA dat dit enkel te verwezenlijken is in combinatie met een serieuze uitbreiding van de geïnstalleerde kernenergiecapaciteit.

Omdat de huidige splijtingsreactoren niet inherent veilig zijn, aanzienlijke hoeveelheden kernafval produceren en hoge kapitaalinvesteringen vereisen, is er nood aan een nieuwe generatie splijtingsreactoren. Een interessant concept is de lood(legering) gekoelde snelle reactor die voordelen biedt als: langere tijdsintervallen tussen splijtstofaanvullingen, eventueel natuurlijke koeling na stillegging, geen explosiegevaar, het stollen van lekkend koelmiddel en geen opbouw van overdruk bij oververhitting. De Belgische *Multi-purpose hYbrid Research Reactor for High-tech Applications* (MYRRHA) zal dienst doen als Europese testreactor voor de ontwikkeling van dit type reactor. Het is een snelle splijtingsreactor gekoeld door een poel van eutectisch lood-bismut (LBE) die tegen 2033 volledig operationeel zal zijn. LBE wordt gebruikt in plaats van lood omwille van het lager smeltpunt

(125°C i.p.v. 327°C). Een nadeel hiermee onlosmakelijk verbonden is dat het gebruikte bismut (^{209}Bi) neutronen kan absorberen, wat leidt tot de productie van radiotoxisch ^{210}Po . De radiotoxiciteit gelinkt aan het innemen of inademen van ^{210}Po behoort tot de hoogste van alle gekende radionucliden. Een te hoge opstapeling van deze isotoop in het koelmiddel kan daarom de veilige werking van de reactor in het gedrang brengen.

Een gelijkaardig probleem wordt verwacht voor toekomstige kernfusiereactoren. In deze reactoren wordt deuterium (D) en tritium (T) gefuseerd om energie te produceren. Omdat tritium in de natuur slechts sporadisch voorkomt, zal de fusiereactor minstens evenveel tritium moeten produceren als ze verbruikt. Dit kan gerealiseerd worden door de neutronen afkomstig uit fusiereacties te laten interageren met met lithium, was leidt tot de productie van tritium. Aangezien sommige neutronen echter geabsorbeerd zullen worden in de contructiematerialen of gewoonweg uit de reactor zullen ontsnappen, is er nood aan een neutronenvermenigvuldiger (die extra neutronen uitstuurt bij interactie met hoogenergetische neutronen). Zowel lood (Pb) als beryllium (Be) zijn kandidaat-materialen hiervoor. De Europese *DEMOnstration Power Station* (DEMO) zal de eerste (Europese) reactor zijn die zal trachten de zelfvoorziening van tritium en de mogelijkheid voor het genereren van een netto elektrisch vermogen uit kernfusie, aan te tonen. De DEMO reactor is momenteel aan het eind van zijn pre-conceptuele ontwerpfase, terwijl de bouw ervan pas in 2040 zou worden aangevat. Een mogelijke strategie voor het kweken (produceren) van tritium is het gebruik van eutectisch lood-lithium als kweek-en vermenigvuldigingsmateriaal. Een open probleem bij dit concept is dat, naast het vermenigvuldigen van neutronen, ^{208}Pb ook neutronen kan absorberen, wat leidt tot de productie van ^{209}Bi. Net als in de MYRRHA reactor kan dit bismuth interageren met de vele neutronen, resulterend in de vormig van de problematische ^{210}Po -isotoop. Een diepere discussie omtrent het energievraagstuk, de prominente rol die kernenergie kan spelen in de oplossing, de geschiedenis/toekomst van kernenergie en hoe polonium ongewenst wordt geproduceerd in sommige reactorconcepten wordt voorgesteld in **Hoofdstuk 1**.

Het doel van dit werk is het verstrekken van informatie die noodzakelijk is voor het beoordelen van het werkelijke risico verbonden aan de aanwezigheid van ^{210}Po in nucleaire splijtings- of fusiereactoren. Een belangrijke factor hierin is de verwachte totale hoeveelheid ^{210}Po in de reactor. Deze werd reeds eerder geschat voor MYRRRHA, maar is onbekend voor het huidige ontwerp van DEMO. Een andere essentiële factor is het chemisch gedrag van

^{210}Po in de reactoromgeving. Deze informatie kan helpen bij het ontwikkelen van Po-extractiesystemen en kan inzicht verschaffen in over de hoeveelheid ^{210}Po die zou vrijkomen bij bepaalde ongevallen. Hierbij wordt in dit werk gefocust op de chemie van gasvormige Po-bevattende molecules, aangezien deze het gemakkelijkst kunnen vrijkomen en een ernstige bedreiging vormen bij inademing.

De total hoeveelheid ^{210}Po in DEMO werd bepaald door neutronentransportberekeningen te combineren met specifieke activatieberekeningen. De *Monte-Carlo N-Particle* (MCNP) neutronentransportcode werd gebruikt om de fusieneutronen en de secundaire deeltjes die ze produceren, op een probabilistische manier van ontstaan tot vergaan te volgen. Door dit te doen voor een groot aantal fusieneutronen kan de energie- en ruimte-afhankelijke neutronenflux worden bepaald. De verkregen flux kan dan vermenigvuldigd worden met de energieafhankelijke werkzame doorsnede (waarschijnlijkheid) voor een van belang zijnde neutroneninteractie en met de ruimte-afhankelijke atoomdichtheid van de betrokken nuclide, om zo het tempo waarmee deze reactie optreedt te bepalen. Deze methodologie werd eerder gebruikt in MYRRRHA om het tempo van de neutronenvangst door ^{209}Bi te bepalen, een interactie die aanleiding geeft tot het vormen van^{210g}Bi, dewelke relatief snel β^--vervalt in ^{210}Po ($t_{1/2}$ = 5 d).

In geval van de DEMO fusiereactor is het niet mogelijk exact dezelfde procedure te volgen, omdat de productie van ^{210}Po nu een neutroneninteractieproces van twee stappen is ($^{208}\text{Pb} \xrightarrow{n,\gamma} {}^{209}\text{Pb} \xrightarrow{\beta^-} {}^{209}\text{Bi} \xrightarrow{n,\gamma} {}^{210g}\text{Bi} \xrightarrow{\beta^-} {}^{210}\text{Po}$). In plaats daarvan worden de verkregen neutronenflux spectra ingevoerd in de FISPACT-II activatiecode. Gebruik makend van (i) deze flux spectra, (ii) de lokale atoomdichtheid van ^{208}Pb en ^{209}Bi, (iii) de energieafhankelijke werkzame doorsnedes voor neutronenvangst door ^{208}Pb en ^{209}Bi, (iv) de halveringstijd van alle onstabiele nucliden, en (v) het beoogd bestralingsschema, kan het programma de totale hoeveelheid ^{210}Po op elk ogenblik bepalen. In dit werk werden twee concepten voor het produceren van tritium onderzocht: het Helium Cooled Lithium Lead en het Water Cooled Lithium Lead concept. Voor beide concepten werd zowel een homogeen als heterogeen model beschouwd, die aanleiding gaven tot vergelijkbare neutronenflux spectra en ^{210}Po hoeveelheden. In alle berekeningen werd rekening gehouden met de continue circulatie van het Pb-Li doorheen de plasma-omgevende constructie en twee realistische bestralingsschema's werden bestudeerd. Verschillende nucleaire gegevensbibliotheken (die de werkzame doorsnedes bevatten) werden vergeleken en bleken een aanzienlijke impact te hebben op de uiteindelijke

hoeveelheid ^{210}Po in de reactor: grotere verschillen werden gevonden voor hetzelfde model met verschillende databibliotheken dan tussen de modellen onderling. Ook de negatieve impact van de initiële concentratie aan ^{209}Bi-onzuiverheden in het Pb-Li op de ^{210}Po productie werd bestudeerd en gekwantificeerd. Een gedetailleerde bespreking van de aangewende methodologie en de verkregen resultaten is te vinden in respectievelijk **Hoofdstuk 2** en **Hoofdstuk 3**.

De hoge radiotoxiciteit van Po maakt experimenten ermee duur en riskant, waardoor er weinig rapportering bestaat over het chemische gedrag van ^{210}Po. In dit werk werd gekozen voor een alternatieve aanpak: ab initio (kwantumchemie) berekeningen van een hoog theoretisch niveau. Aangezien polonium een zwaar element met veel elektronen is, zijn effecten zoals elektronencorrelatie en spin-baan interactie van enorm belang en moeten deze nauwkeurig in rekening gebracht worden. Als eerste stap werden gasvormige diatomische molecules bestudeerd bestaande uit Po en een ander element aanwezig in de betrokken reactoren, namelijk Pb of Li (relevant voor het Pb-Li in fusiereactoren), Pb of Bi (relevant voor de Pb-(Bi)-koelvloeistof in splijtingsreactoren), H of O (relevant voor watercontaminatie) of een ander Po atoom. De gebruikte ab initio methode werd gevalideerd door deze eerst toe te passen op analoge molecules waarvoor wel experimentele gegevens beschikbaar zijn. Daarnaast werden gedetailleerde testberekeningen uitgevoerd op Pb_2, PbO en Po_2. Om de temperatuurafhankelijke stabiliteit van de relevante Po-molecules te verkrijgen, werden hun dissociatieprofielen bepaald en gebruikt in een statistische thermodynamische analyse. De verkregen stabiliteit werd vervolgens gecombineerd met de initiële atomaire concentraties van de verschillende elementen in de holle ruimte boven het LBE van MYRRRHA en het Pb-Li van DEMO, om het relatieve voorkomen van de verschillende Po-species te bekomen (voor Po hangt de initiële concentratie af van de hoeveelheden bekomen in het eerste deel van dit werk). Daarnaast werd een risicoanalyse uitgevoerd voor het geval van een Pb-Li lek in DEMO. Er werd vastgesteld dat Po in dit geval waarschijnlijk geen bedreiging zal vormen, tenzij mogelijk indien er contact met water optreedt, iets wat aanleiding kan geven tot vluchtige Po-bevattende (oxy)hydroxiden. De methodologie en de verkregen resultaten worden in detail besproken in respectievelijk **Hoofdstuk 4** en **Hoofdstuk 5**.

Tot slot worden in **Hoofdstuk 6** enkele eindconclusies gepresenteerd, alsook perspectieven voor toekomstig werk.

Zusammenfassung

In den letzten Jahrzehnten wurde den Menschen der Einfluss der Energieerzeugung auf das Klima, die Umwelt und unsere Gesundheit bewusst. Die überwiegende Mehrheit der wissenschaftlichen Gemeinschaft hat sich auf den direkten Zusammenhang zwischen der Verbrennung fossiler Brennstoffe und dem Klimawandel geeinigt. Wetteranomalien wie verheerende Hurrikane, extreme Dürren und enorme Waldbrände sowie der steigende Meeresspiegel wurden weitgehend der gemessenen globalen Erwärmung zugeordnet und haben zu Millionen von Klimaflüchtlingen geführt. Die Internationale Energieagentur hat Empfehlungen veröffentlicht, wie diesen neuen Trends durch eine tiefgreifende Transformation des derzeitigen Energieversorgungssystems nachhaltig begegnet werden kann. Ihr optimistischstes Szenario wird durch eine drastische Erhöhung des Anteils der erneuerbaren Energien am Energiemix realisiert. Da die meisten skalierbaren erneuerbaren Energiequellen jedoch intermittierend sind, argumentieren sie, dass dies nur in einem realistischen Zeit- und Kostenrahmen erreicht werden kann, wenn es mit einem ernsthaften Ausbau der installierten Kernenergiekapazität kombiniert wird.

Da die installierten Kernspaltungsreaktoren von Natur aus nicht sicher sind, erhebliche Mengen an Atommüll produzieren und hohe Investitionen erfordern, besteht Bedarf an einer neuen Generation von Kernspaltungsreaktoren. Ein interessantes Konzept ist der blei-(legierungs-)gekühlte schnelle Reaktor, der Vorteile wie lange Treibstoffwechselzeiten, möglicherweise natürliche Kühlung nach dem Abschalten, keine Explosionsgefahr, Verfestigung von auslaufendem Kühlmittel und keinen Überdruck durch Überhitzung bietet. Der belgische Mehrzweck-HYbrid-ForschungsReaktor für Hightech-Anwendungen (MYRRHA) wird als europäische Pilotanlage für deren Entwicklung dienen. Es handelt sich um einen mit einem Blei-Bismut-Eutektikum (LBE) gekühlten schnellen Reaktor in Poolbauweise, der bis 2033 vollständig

betriebsbereit sein soll. LBE wird wegen seines niedrigeren Schmelzpunktes (125°C vs. 327°C) eher als Blei verwendet. Ein Nachteil davon ist, dass das ^{209}Bi Spaltneutronen einfangen kann, wodurch radiotoxisches Polonium (^{210}Po) erzeugt wird. Die Ingestions- und Inhalationsradiotoxizität von ^{210}Po gehört zu den höchsten aller bekannten Radionuklide. Eine erhebliche Anreicherung dieses Isotops im Kühlmittel kann daher den sicheren Betrieb des Reaktors gefährden.

Ein ähnliches Problem wird voraussichtlich bei Kernfusionsreaktoren auftreten. In diesen Reaktoren werden Deuterium (D) und Tritium (T) zur Energiegewinnung fusioniert. Da Tritium extrem knapp ist, muss im Reaktor mindestens so viel T produziert werden, wie verbraucht wird. Dies wird erreicht, indem Neutronen, die aus den Fusionsreaktionen stammen, mit Lithium interagieren, was zur Bildung von Tritium führt. Da einige Neutronen in den Strukturmaterialien absorbiert werden oder einfach aus dem Reaktor entweichen, muss ein Neutronenmultiplikator (der bei der Interaktion mit hochenergetischen Neutronen zusätzliche Neutronen emittiert) verwendet werden. Sowohl Pb als auch Be werden für diesen Zweck in Betracht gezogen. Der europäische DEMOnstrations (DEMO)-Fusionsreaktor wird der erste (europäische) Reaktor sein, der die Selbstversorgung mit Tritium sowie die Fähigkeit zur Erzeugung einer elektrischen Nettoleistung aus Fusionsenergie demonstrieren soll. Dieser Reaktor befindet sich derzeit am Ende seiner vorkonzeptionellen Phase, während der Bau im Jahr 2040 beginnen soll. Ein mögliches Brutkonzept besteht darin, flüssiges Blei-Lithium-Eutektikum (Pb-Li) als Brut-/Multiplikatormaterial zu verwenden, das in einem das Fusionsplasma umgebenden *breeding blanket* eingebaut ist. Ein offenes Problem bei diesem Konzept ist, dass Blei neben der Multiplikation von Neutronen auch diese einfangen kann, was zur Produktion von ^{209}Bi führt. Ähnlich wie in MYRRHA kann das produzierte ^{209}Bi mit den zahlreichen Neutronen interagieren, was wiederum zur Produktion des problematischen ^{210}Po führt. Eine ausführliche Diskussion über das Energieproblem, die herausragende Rolle, die die Kernenergie für eine nachhaltige Lösung spielen könnte, die Geschichte und Zukunft der Kernenergie und wie Polonium in einigen Spalt- und Fusionsreaktorkonzepten unerwünschterweise erzeugt wird, wird in **Kapitel 1** präsentiert.

Ziel dieser Arbeit ist es, wesentliche Informationen bereitzustellen, die erforderlich sind, um das tatsächliche Risiko zu bewerten, das mit dem Auftreten von ^{210}Po in einem Kernspaltungs- oder Fusionsreaktor verbunden ist. Ein wichtiger Faktor ist die Größe des gesamten ^{210}Po -Bestands, der

für MYRRHA bereits geschätzt wurde, aber für das aktuelle Design von DEMO unbekannt ist. Eine weitere wesentliche Erkenntnis ist das chemische Verhalten von ^{210}Po innerhalb der Reaktorumgebung, das die Entwicklung spezieller Po-Extraktionssysteme anleiten und Informationen über die zu erwartende radiologische Freisetzung im Falle eines Unfalls liefern kann. Dieser Teil der Arbeit konzentriert sich auf die Chemie der gasförmigen Po-haltigen Moleküle, da diese am leichtesten aus dem Reaktor entweichen können und beim Einatmen eine schwere Bedrohung darstellen.

Der ^{210}Po -Bestand in DEMO wurde durch die Kombination von Neutronentransportrechnungen mit speziellen Bestandsberechnungen bestimmt. Der Monte-Carlo N-Particle (MCNP) Neutronentransportcode wurde verwendet, um Fusionsneutronen sowie die von ihnen produzierten Sekundärteilchen von Geburt bis Tod probabilistisch zu verfolgen. Durch die Verfolgung einer großen Anzahl von Fusionsneutronen kann der energie- und ortsabhängige Neutronenfluss erhalten werden. Multipliziert man diesen Fluss mit dem energieabhängigen Wirkungsquerschnitt (Wahrscheinlichkeit) einer gegebenen Neutroneninteraktion und mit der ortsabhängigen Atomdichte des beteiligten Nukleus, erhält man die Vorkommensrate dieser Reaktion. Diese Methodik wurde zuvor in MYRRHA verwendet, um die Neutroneneinfangrate durch ^{209}Bi zu bestimmen, was zu ^{210g}Bi reagiert, welches relativ schnell zu ^{210}Po ($t_{1/2}$ = 5 d) β^--zerfällt.

Für den DEMO-Fusionsreaktor kann nicht genau das gleiche Verfahren angewendet werden, da der ^{210}Po -Produktionsprozess nun ein zweistufiger Neutroneninteraktionsprozess ist ($^{208}\mathrm{Pb} \xrightarrow{n,\gamma} {}^{209}\mathrm{Pb} \xrightarrow{\beta^-} {}^{209}\mathrm{Bi} \xrightarrow{n,\gamma} {}^{210g}\mathrm{Bi} \xrightarrow{\beta^-} {}^{210}\mathrm{Po}$). Stattdessen werden die erhaltenen Neutronenflussspektren als Input für den FISPACT-II Inventarcode verwendet. Verwenden von (i) diesen Flussspektren, (ii) der lokalen Atomdichte von ^{208}Pb und ^{209}Bi, (iii) den energieabhängigen Neutroneneinfangquerschnitten von ^{208}Pb und ^{209}Bi, (iv) der Halbwertszeit aller instabilen Nuklide und (v) einem Bestrahlungsplan von Interesse, erlaubt dem Programm, das ^{210}Po -Inventar zu jedem gewünschten Zeitpunkt zu bestimmen. In dieser Arbeit wurden zwei *breeding blanket*-Konzepte betrachtet: das heliumgekühlte Lithium-Blei und das wassergekühlte Lithium-Blei-Konzept. Es wurde ein homogenes und ein heterogenes Modell für beide Konzepte betrachtet, das zu vergleichbaren Neutronenflussspektren und Inventaren führt. In allen Berechnungen wurde die kontinuierliche Zirkulation des Pb-Li innerhalb des Brutbereichs berücksichtigt und zwei Bestrahlungspläne untersucht. Verschiedene Kerndatenbanken (welche die Neutronenwirkungsquerschnitte enthalten)

wurden verglichen und es wurde festgestellt, dass sie einen erheblichen Einfluss auf das endgültige Po-Inventar haben. Tatsächlich wurden für das gleiche Modell mit unterschiedlichen Kerndatenbanken größere Unterschiede festgestellt als zwischen den Modellen selbst. Die negativen Auswirkungen des anfänglichen ^{209}Bi-Verunreinigungsniveaus im Pb-Li auf das ^{210}Po -Inventar wurden ebenfalls untersucht und quantifiziert. Eine detaillierte Beschreibung der verwendeten Methodik und der erzielten Ergebnisse befinden sich in **Kapitel 2** und **Kapitel 3**.

Die hohe Radiotoxizität von ^{210}Po macht Experimente riskant und teuer, was zu wenigen Berichten über das chemische Verhalten von ^{210}Po führt. In dieser Arbeit wurde ein alternativer Ansatz gewählt: Es wurden Berechnungen auf hohem theoretischen Niveau ab initio (Quantenchemie) durchgeführt. Da Polonium ein schweres Element mit vielen Elektronen ist, sind Effekte wie Elektronenkorrelation und Spin-Orbit sehr ausgeprägt und müssen genau berücksichtigt werden, was die Komplexität der Berechnungen erhöht. In einem ersten Schritt wurden gasförmige zweiatomige Moleküle betrachtet, die Po und ein weiteres Element enthalten, von dem erwartet wird, dass es in den Reaktoren von Interesse vorhanden ist, d.h. Pb oder Li (relevant für die Brutbereiche des Fusionsreaktors Pb-Li), Pb oder Bi (relevant für die Kühlmittel des Spaltungsreaktors Pb-(Bi)), H oder O (relevant für die Wasserverschmutzung) oder ein anderes Po-Atom. Die verwendete ab initio-Methode wurde validiert, indem sie auf analoge Moleküle angewendet wurde, für die experimentelle Daten vorliegen. Darüber hinaus wurden detaillierte Testberechnungen für Pb_2, PbO und Po_2 durchgeführt. Um die temperaturabhängige Stabilität der relevanten Moleküle zu erhalten, wurden deren Dissoziationsprofile für die Verwendung in einer statistischen thermodynamischen Analyse bestimmt. Die erhaltenen Stabilitäten wurden dann mit den anfänglichen atomaren Konzentrationen der verschiedenen Elemente im Luftraum des MYRRHA- und DEMO-Reaktors kombiniert (für Po abhängig von der im ersten Teil dieser Arbeit erhaltenen Endinventur), um das relative Auftreten der verschiedenen Po-Arten zu erhalten. Zusätzlich wurde eine Risikoanalyse für einen Leckage-des-PbLi-Unfalls in DEMO durchgeführt. Es wurde festgestellt, dass Po in diesem Fall wahrscheinlich keine Gefahr darstellt, sondern möglicherweise wenn es mit Wasser in Berührung kommt und sich flüchtige (Oxy)hydroxide bilden. Die Methodik und die erzielten Ergebnisse werden in **Kapitel 4** und **Kapitel 5** behandelt.

Schließlich präsentiert **Kapitel 6** einige endgültige Schlussfolgerungen und Perspektiven für die zukünftige Arbeit.

1

Introduction

No energy is more expensive than no energy.

Homi J. Bhabha (1909–1966)

1.1 The energy problem

1.1.1 The growing energy demand

Over the past three centuries, the supply and use of energy has known a vibrant evolution. Until the 1750's, the primary sources of energy were muscular and biomass. The land was worked by manual labor and animals, while firewood was used to heat the houses and to cook food. It wasn't until the First Industrial Revolution (1760-1840) that coal was introduced as new energy source. Initially, it was used to drive steam engines being used in the textile industry, which was the leading industry at that time and the first to adapt the new production methods. At the start of the 19th century, coal-fired steam locomotives were introduced to allow for a faster long-distance transportation. These transformations triggered an unprecedented consistent growth in population and standard of living, resulting in a steady increase of the energy demand. At the end of the 19th century, coal-fired power plants were installed to meet this demand. A few decades later, natural gas power stations started to become more prevalent

while crude oil was extracted and processed to be used for transportation and heating purposes. A new fossil fuel-based economy had been established.

The global energy demand is a function of the world's population, the standard of living (which is closely related to the gross domestic product GDP per capita) and the energy intensity of the population and economy (which varies widely across the globe) [Sii14]. The global energy demand is clearly directly proportional to the world's population. This also used to be true for its relation to the GDP of a country. Recent trends, however, show that this is no longer always the case as countries with a high GDP per capita tend to shift their economy to a less energy-intensive knowledge-based economy rather than holding on to a more energy-intensive economy based on manufacturing and transportation. Another factor curbing the growing energy demand are the continuous improvements in energy efficiency.

The global population

The United Nations Department of Economic and Social Affairs has kept track of the world and regional populations over the last century and has published well-founded projections onward up to 2100 [noa17b]. Their projections are based on the historical data as well as the plausible assumptions of a decreasing fertility rate, an increasing life expectancy and expected migration flows. The result is presented in Figure 1.1.

The global population has increased from 2.5 billion to 7.4 billion between 1950 and 2015, which is an increase of 196 % in 65 years. Within the next 65 years, by 2080, the global population is expected to reach 10.8 billion (47 % increase). The growth rate of the global population is thus predicted to decrease and in fact the global population appears to be evolving to a stable value of about 11.3 billion by 2120. It should be noted that in a projection performed in 2004, it was estimated to stabilize already at slightly over 9 billion by 2080 [noa04]. This latter projection also predicted a global population of 8.9 billion in 2050, compared to 9.8 billion in the current projection. It is therefore self-evident that great uncertainties are associated with the presented projections. This is also demonstrated in Figure 1.1, showing the lowest and highest possible variant of the in 2017 obtained projections, resulting in the quite distinct predicted global populations in 2100 of respectively 7.2 billion and 16.5 billion. In short, although the global population will further increase within the next century, it is expected to stabilize at a value around 11.3 billion, an overall increase of 47 %.

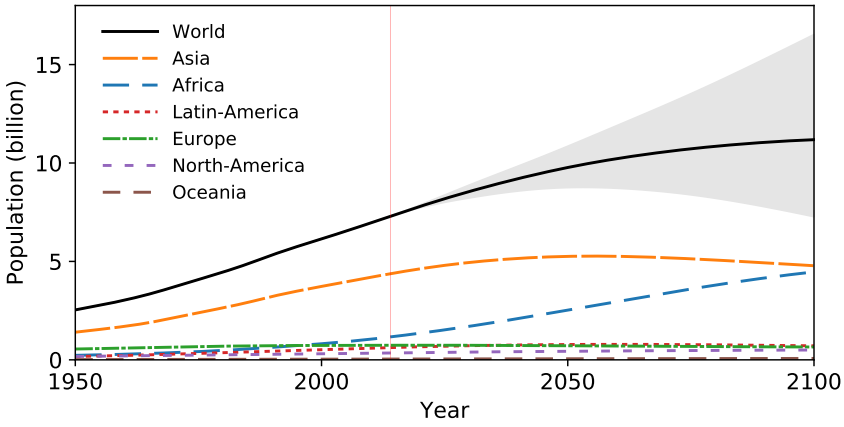

Figure 1.1: The global and continental populations from 1950 till 2014 and their median projections up to 2100 as estimated by the United Nations Department of Economic and Social Affairs [noa17b]. The highest and lowest variant of the projections are also visualized.

Standard of living and energy intensity of the economy

So far, no consensus has been reached about the directionality of the relation between a country's GDP and energy consumption. It is not clear whether the access to energy drives an increase of the GDP or whether an increased GDP triggers a higher energy consumption [Cho08]. Anyhow, in general a high GDP per capita is associated with a high energy consumption per capita [noa17b]. However, as nations become more prosperous, their economies tend to evolve into a less energy intensive one. Moreover, as the energy efficiency is steadily improving for low-income as well as high-income countries, the overall global economy is becoming less energy-intensive [noa19, Rit19] (see Figure 1.2).

Projections of the global energy demand

Summarizing, the global energy demand depends on the world's population which is expected to increase by half and then stabilize, the standard of living which is predicted to further increase in the near future, and the energy intensity of the population and economy which is decreasing over time due to both advances in energy efficiency and a shift towards less energy-intensive economic sectors. The complex nature of the factors influencing the global energy demand, makes it hard to produce reliable long-term

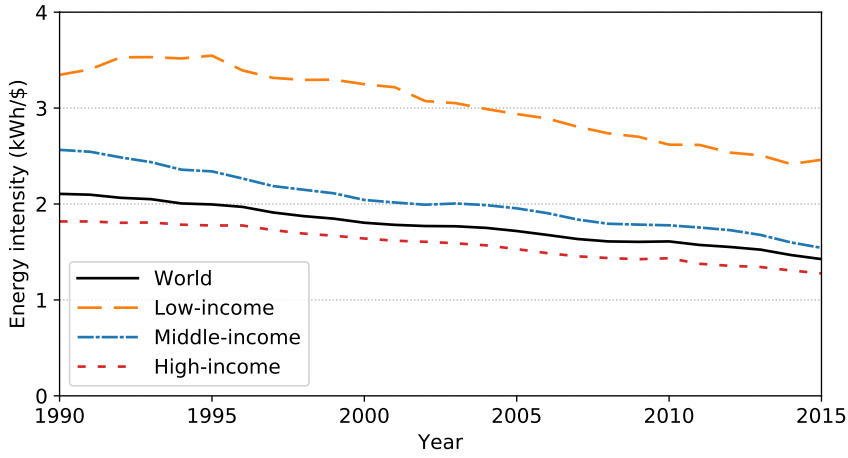

Figure 1.2: The energy intensity of the economies for countries with low, middle and high income as well as the global average expressed in kWh/2011 international-$. It is a measure of how much energy is used to produce one unit of economic output [noa19, Rit19].

projections. In addition, there are two energy-intensive processes that could significantly increase the future energy demand i.e. carbon management (capture) and water pretreatment (desalination) [Sii14]. Nevertheless, the International Energy Agency (IEA) has published projections for the global energy demand up to 2040 considering 3 possible scenarios [Int18b] which are based on the fact that the growing energy demand cannot be met using a fossil fuel-dominant energy production scheme in a way that is sustainable for the earth's climate. The huge amounts of carbon dioxide being exhausted into the atmosphere for energy production purposes (currently about 33 Gt/y [noa17b]) are bringing the earth's carbon cycle out of balance, increasing the atmospheric CO_2 concentrations annually by 2.5 ppm, currently having reached a level of 410 ppm [Nat] (cfr. the pre-industrial level of 260-270 ppm [Wig83]). The present CO_2 concentration corresponds to a contribution to the radiative forcing (i.e. the difference between sunlight absorbed by the Earth and the energy radiated back to space) of 2.16 W/m^2K [Ram01], making up about 66 % of the overall value (while CH_4 is responsible for about 16.5 %) [But19]. This makes atmospheric carbon dioxide the primary cause for global warming and at the present level, CO_2 alone is expected to account for a global temperature increase of about 1.27°C [Gre16]).

The 3 scenarios defined by the IEA are: (i) the **Current Policies Scenario**

(CPS) in which coal and oil do not tend to make much room for other energy sources, keeping the fossil fuel share of the world primary energy demand at a steady value around 79 % and assuming a 38 % increase in global energy demand by 2040, (ii) the **New Policies Scenario (NPS)** in which the fossil fuel share is reduced to 74 % by 2040 and assuming a smaller 27 % increase in global energy demand and, (iii) the **Sustainable Development Scenario (SDS)** in which the fossil fuel share is reduced to 60 % by 2040 (primarily by increasingly avoiding coal) and assuming a global energy demand in 2040 similar to the present one, together expected to limit the global temperature increase to 1.7 - 1.8 °C.

In 2017, 32.6 Gt of CO_2 was emitted globally (41 % more than in 2000). In 2040, the emission is estimated at 42.5 Gt (30 % increase), 35.9 Gt (10 % increase) and 17.6 Gt (46 % decrease) for the CPS, NPS and SDS respectively. Figure 1.3 summarizes the main characteristics of the 3 scenarios. To achieve the sustainable development goals, a complete reversal of the historic relationship between economic growth, energy demand and CO_2 emissions is required.

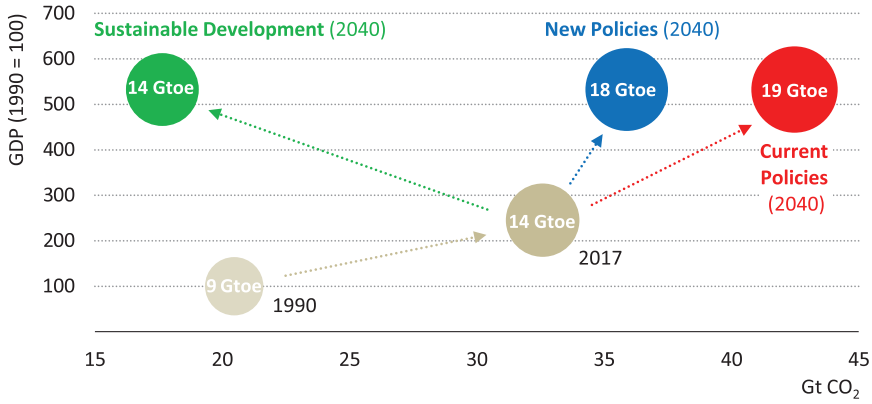

Figure 1.3: World primary energy demand, related CO_2 emissions and target GDP for the three energy production scenarios defined by the International Energy Agency [Int18b].

1.1.2 The energy mix for the future

In order to meet the growing energy demand in a sustainable way, a profound transformation of the present energy supply scheme is required. The IEA has examined what the energy mix of 2040 should look like in order to meet the targets specific to each of the predefined scenarios [Int18b]. Their findings

for the world electricity generation are summarized in Table 1.1. In order to realize the Sustainable Development Scenario, the fossil fuel share in the electricity supply needs to be reduced from the present 64.9 % to 20.3 %. This enormous cut in supply would be compensated by an expansion of the electricity generation capacity of renewable and nuclear sources.

Table 1.1: World electricity generation by fuel, technology and scenario as recommended by the IEA, expressed in TWh. The envisioned fossil fuel, nuclear and renewables share is also presented.

Scenario	**Present**	**CPS**	**NPS**	**SDS**
Year	2017	2040	2040	2040
Coal	9858	13910	10335	1982
Oil	940	610	527	197
Gas	5855	10295	9071	5358
Nuclear	2637	3648	3726	4960
Hydro	4109	5973	6179	6990
Wind and solar PV	1519	6635	8529	14139
Other renewables	722	1653	2044	3456
Total generation	**25679**	**42755**	**40443**	**37114**
Electricity demand	22209	37258	35526	33176
Fossil fuel share	64.9 %	58.0 %	49.3 %	20.3 %
Nuclear share	10.3 %	8.5 %	9.2 %	13.4 %
Renewables share	24.7 %	33.4 %	41.4 %	66.2 %

Hydropower has been around for more than two centuries and by now most suitable sites have been exploited, which limits its potential for further expansion. As the other major renewable energy sources, i.e. photovoltaic solar and wind, have an intermittent nature, an expansion of their share in the future energy mix will also require substantial investments in energy storage, grid flexibility and demand-side response. In absence of these systems, the energy supply can only be secured using flexible thermal power plants, for which gas-fired power plants are currently primarily used (resulting in a higher CO_2 emission).

Nuclear fission reactors can provide large amounts of zero-emission baseload energy. This allows for a somewhat slower and more manageable transition to an energy mix in which renewable energy is dominant, while simultaneously keeping the CO_2 emissions at an acceptable level. Furthermore, a report published by the International Atomic Energy Agency

(IAEA) in April 2018 [Int18a] states that both existing and future nuclear fission reactors could also be operated in a flexible mode, therefore capable of supplementing the intermittent renewable energy sources instead of gas-fired power plants, thus avoiding detrimental CO_2 emissions. Therefore, while expanding the renewables share from 24.7 % to 66.2 %, also the nuclear share is increased from 10.3 % to 13.4 % (in the SDS), virtually doubling the total electricity generation of today's nuclear fleet (from 2637 TWh to 4960 TWh).

It is clear that nuclear energy will have a vital role in achieving a sustainable future in which the current climate change trends are countered (for a detailed discussion the reader is referred to the IAEA report *Climate Change and Nuclear Power 2018* [noa18]). Therefore, additional efforts should be invested in making future nuclear reactors as safe as possible and in finding ways to reduce and sustainably store radioactive waste.

1.2 Nuclear fission

1.2.1 Principle

Mass defect

The exploitation of nuclear energy is made feasible by the mass defect found in atomic nuclei. This comes down to the observation that the mass of a nucleus is smaller than the sum of the masses of the constituent nucleons (protons and neutrons). The missing mass is said to be converted into binding energy E_b according to the famous mass-energy equivalence postulated by Einstein in 1905 ($E = mc^2$) [Ein05]. For a nucleus ${}^A_Z\mathrm{X}$ with mass $m\left({}^A_Z\mathrm{X}\right)$, where Z denotes the atomic number (number of protons) and A the mass number (the number of protons and neutrons combined), we have:

$$Z\,m_\mathrm{p} + (A-Z)\,m_\mathrm{n} - m\left({}^A_Z\mathrm{X}\right) = \Delta m = E_\mathrm{b}/c^2,$$

with m_p and m_n being the proton and neutron mass respectively. Starting from the liquid drop model proposed by George Gamow, Carl Friedrich von Weizsäcker derived the semi-empirical mass formula (SEMF) approximating the mass of an atomic nucleus based on the atomic number Z and the mass number A [Wei35]:

$$E_\mathrm{b}(\mathrm{MeV}) = a_\mathrm{V}A - a_\mathrm{S}A^{2/3} - a_\mathrm{C}\frac{Z(Z-1)}{A^{1/3}} - a_\mathrm{A}\frac{(A-2Z)^2}{A} \pm a_\mathrm{P}A^{k_\mathrm{P}}, \quad (1.1)$$

in which the terms are consecutively called the volume term, the surface term, the Coulomb term, the asymmetry term and the pairing term. The latter term is positive if both A and Z are even, negative if both are odd and zero in the other cases. The coefficients a_{V} ,a_{S}, a_{C}, a_{A}, a_{P} and exponent k_{P} are calculated by fitting experimentally measured nuclei masses to this formula and their exact values depend on how the fit is performed. As this formula neglects the internal shell structure of the nucleus, it especially provides good values for the heavier nuclei and yield poorer results for the light nuclei (especially for ^{4}He).

The experimental binding energy per nucleon versus the number of nucleons is visualized in Figure 1.4. The three nuclides with the highest binding energy per nucleon are ^{62}Ni, ^{58}Fe and ^{56}Fe, making them the most stable nuclides. Nuclear fusion is based on the principle of fusing lighter less stable nuclides together to increase the overall binding energy and thus stabilizing the system, releasing energy in the process. Nuclear fission, on the other hand, splits heavier less stable nuclides into more stable fission products, again increasing the overall binding energy and releasing a large amount of energy.

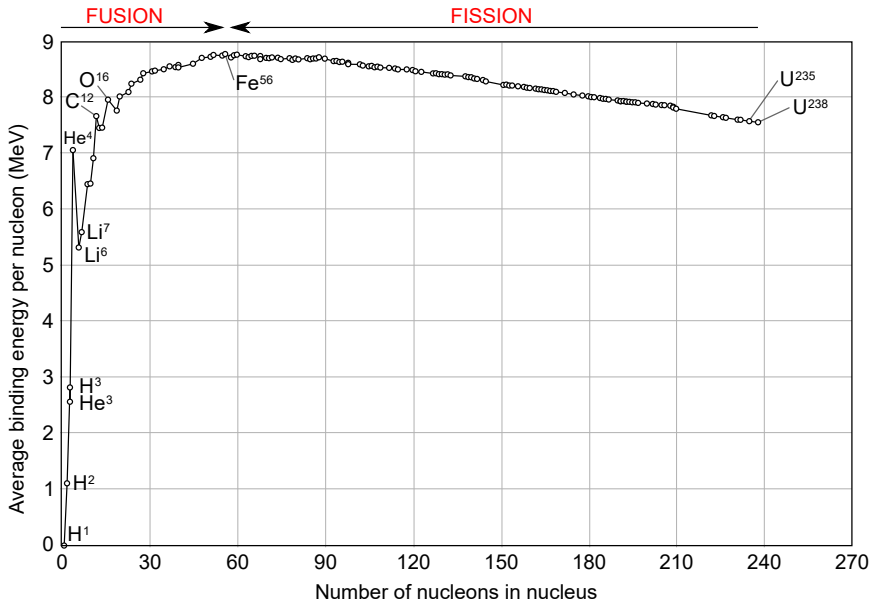

Figure 1.4: Average binding energy per nucleon versus the number of nucleons in the nucleus.

Fissionable and fissile nuclides

In a nuclear fission reactor, one wishes to control the fission process. Therefore, fission events should not take place spontaneously at random, but should rather be triggered. Figure 1.5 shows the qualitative reaction path of a fission process. Here, the dissociation energy E_{d} is the difference in binding energy of the fission products with respect to the ground state compound nucleus. E_{c} is the Coulomb repulsion energy between the two fission products. The activation energy E_{a} is the difference between the Coulomb repulsion energy and dissociation energy. For a very heavy nuclide, the activation energy can be negative or extremely small, resulting in a spontaneous fission process and these nuclides are therefore very short lived. For nuclei with a mass number A below 230, the activation energy is extremely large, making a fission process virtually inaccessible.

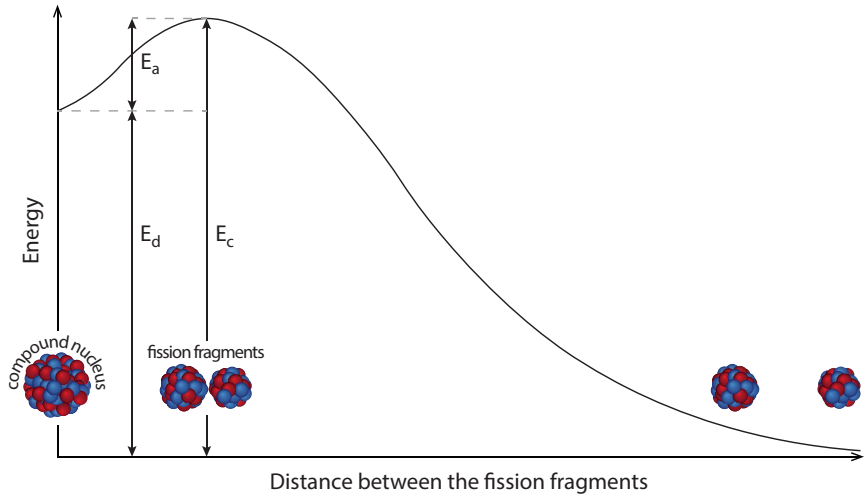

Figure 1.5: Energy path of a typical fission process. At the left you can see the compound nucleus in its ground state. E_{a} is the activation energy required to trigger the fission process. This energy is the difference between the coulomb repulsion energy of the fission fragments E_{c} and the difference in binding energy of the fission products with respect to the ground state compound nucleus E_{d}

.

A few nuclides exist for which the activation energy is high enough to prevent extensive spontaneous fission, but low enough to be triggered by external influences. The necessary activation energy can be supplied either by photons or by particles (neutrons, protons, etc.). When supplied

by a particle, both kinetic and binding energy is transferred. If a nuclide is capable of undergoing fission after capturing a neutron, it is called a fissionable nuclide.

In some cases, simply adding a low-energy (thermal) neutron to a target nucleus creates a compound nucleus in which the additional binding energy is large enough to initiate the fission process. Here, the pairing term of the SEMF (Eq. 1.1), plays an important role. If the target nucleus has an even number of protons and an odd number of neutrons, the additional binding energy supplied by the incoming neutron will be relatively large as also pairing energy is added. As a result, these nuclides can often be fissioned by slow thermal neutrons. These are called fissile nuclides. Examples are ^{233}U, ^{235}U, ^{239}Pu and ^{241}Pu.

Fission products and neutron emission

A fission reaction results in 2 major fission fragments and zero, one or multiple fission neutrons. The primary fission products resulting from a given target molecule are not fixed but rather follow an asymmetric mass distribution yielding one lighter and one heavier fission fragment. Figure 1.6 shows these distributions for the thermal fission of the most commonly used targets in nuclear fission reactors i.e. ^{235}U, ^{239}Pu and ^{233}U. Their upper peak was found to be quite similar while their lower peak is shifted relatively to each other. For all three, a fission process resulting in two fragments of similar mass is highly unlikely. It should be noted that the stable neutron-to-proton ratio of nuclides goes up with increasing atom number. Therefore, the primary fission products will often have an excess of neutrons and be highly unstable. They can get rid of this excess by either converting a neutron into a proton through a β^- decay or by simply emitting a so-called delayed neutron. The delay time of these neutrons depends on the half-life of the emitting fission product and is on average of the order of a few seconds for the products generated in a fission reactor. These delayed neutrons only represent a very small share β of all emitted neutrons (for ^{235}U β=0.0064 or, for ^{239}Pu β=0.0021 and for ^{233}U β=0.0026), but are extremely important as they allow to control a fission reactor.

Fission chain reaction

In a nuclear fission reactor, the emitted fission neutrons are used to trigger new fission reactions, thus aiming to maintain a chain reaction at constant

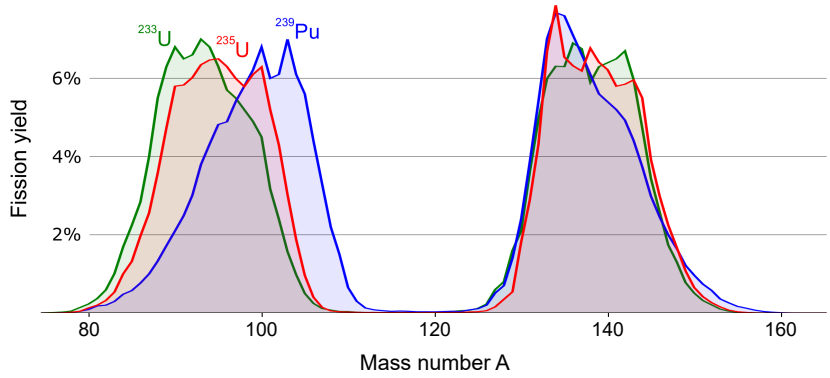

Figure 1.6: Primary fission product yield of most exploited fission reactions (obtained from [Lov17] and simplified).

fission rate. However, the neutron absorption cross-section (probability) of the fissile target nuclides is very low for the energy at which fission neutrons are emitted (order of 1 MeV), while it is a factor of 100 to 1000 times larger for thermal (0.025 eV) neutrons. Therefore, to avoid excessive leaking of neutrons from the reactors and to maintain the fission reaction chain, neutrons need to be slowed down (moderated) after being produced and before they can reach the walls of the reactor vessel.

The criteria for a good moderator are: a low mass (for effectively slowing down the neutron in as few interactions as possible), a large collision cross section and a small absorption cross section. The most appropriate elements have been found to be hydrogen (in the form of water), deuterium (in the form of heavy water), carbon (in the form of solid graphite) and beryllium (although used in a lesser degree due to its high toxicity and cost).

As the mean generation time (time between a prompt neutron emission to a capture that results in a new fission event) is extremely short (ranging between less than a microsecond up to 1 millisecond depending on the reactor type), it seems impossible to safely control a fission chain reaction. However, under normal operation conditions, it is the small fraction of delayed neutrons (being generated by decaying fission products on the timescale of seconds to minutes) that will finally result in a decreasing or increasing fission reaction rate. Therefore, the control and safety systems can be operated at these more manageable time scales, allowing to control the chain reaction at a desired output power. It should be noted however that accidents could still occur when the reactor is promptly taken out of normal operation conditions, uncontrollably increasing the fission reaction

rate. In modern reactors, many safety measures are taken to make this scenario virtually impossible.

Energy generation and transfer

In the process of a nuclear fission reaction, a large amount of energy is released. For ^{235}U the overall amount of emitted energy per fission event is 207 MeV. Most of this energy (168 MeV) is transformed into kinetic energy of the fission fragments and is absorbed in the immediately surrounding material (within 0.1 mm from birth). The other energy contributions is accounted for by the fission neutrons (5 MeV), the prompt γ-rays (7 MeV) and the fission product decay process (8 MeV as β^--particles, 7 MeV as γ-rays and 12 MeV as neutrinos). The energy carried by the neutrinos is lost due to their extremely low interaction cross sections, allowing them to escape the reactor. All other energy contributions are completely absorbed within the reactor as thermal heat. Besides this, neutron captures by other elements besides the fission target nuclei can result in additional γ-rays being emitted accounting for a total of 3-12 MeV per fission event depending on the reactor design. Adding up, the total energy that can be recovered from fissioning a ^{235}U nucleus amounts to 198 - 207 MeV [Sah18]. To put this into perspective, in order to operate a nuclear fission plant having a 3.5 GW thermal power output, 3.7 kg of ^{235}U per day is required, while a similar coal power plant would burn about 14000 tonnes of coal daily [Coo84]. The energy density of pure ^{235}U is thus 4 million times higher than the one of coal.

The major share of the generated fission energy is thus converted into thermal energy within the reactor and carried away by a reactor coolant after which it is finally transformed into electric power by driving a turbine. The next section gives an overview of the most common reactor designs as well as how these designs evolved over time.

1.2.2 Fission reactor designs

In the previous section, the concept of how nuclear fission can be used to generate energy was discussed. There are many possible ways to implement this concept in an actual reactor design. This basically boils down to making decisions on the fuel (composition, fissionable material, geometry), moderator (material and state of aggregation), coolant (material and state of aggregation), heat transfer cycle (direct versus indirect) and safety systems.

The world's first nuclear reactor was completed in secrecy in 1942 in the framework of the U.S. Manhattan Project. In order to reach criticality in this reactor, about 45 tons of natural uranium fuel were combined with 360 tonnes of ultra-pure graphite serving as moderator. As its output power was only 1.5 watt, it did not require a cooling system or radiation shield. In the following years, additional reactors were build with the purpose of producing plutonium to build the first atomic bombs. A few years later, nuclear reactors were introduced into submarines for propulsion having the advantage of being a zero-emission process with no need for air. These reactor designs laid the groundwork for the development of the first generation of fission reactors for the production of electricity for civil purposes, starting in the 1950s.

Generation I

The first generation of fission reactors was mainly developed (independently) in the U.S., the Sovjet Union, France and the U.K. As enrichment of uranium was not yet available for civilian purpose, all of these these reactors are characterized by the use of natural uranium as fuel. Natural uranium only contains 0.7 % of fissionable ^{235}U, while the remaining 99.3 % is accounted for by ^{238}U, which doesn't directly contribute to the fission process (although it does indirectly by the generation of fissionable ^{239}Pu, making ^{238}U a so-called fertile nuclide). In order to reach criticality and thus to maintain a fission chain reaction, heavy water (D_2O) or graphite had to be used as moderator as the hydrogen in light water (H_2O) was found to absorb too many neutrons. These were the only fixed design parameters and an incredible amount of reactor designs has been proposed and constructed in a short time, also partly because of the very light regulatory framework. Most of these reactors ran at a relatively low (proof-of-concept) power. Unlike today, nuclear fission energy had the benefit of a good public acceptance and good government support, making a fast development possible in which safety issues were progressively raised and solved. The most important reactor designs descending from this time period are:

- The Pressurized Heavy Water Reactor (PHWR), finally giving rise to the Gen. II CANada Deuterium Uranium (CANDU) reactor design,

- The Light Water Graphite-moderated Reactor (LWGR) or also called RBMK in Russia, developed in the Sovjet Union and later in Russia. The catastrophic Chernobyl reactor was of this type.

- The Gas-Cooled Reactor (GCR). The most common designs are the Magnox design from the U.K. and the UNGG from France, both moderated by graphite and cooled by CO_2 gas.

- The Fast Breeder Reactor (FBR) firstly developed at the United States. These reactors breed more fissile material than it consumes, making optimal use of the natural uranium fuel (but interest decreased as more uranium reserves were discovered).

Generation II

The introduction of uranium enrichment at large-scale in the late 1960s made the design of a critical fission reactor using light water as moderator possible. As a result, two new Light-Water Reactor (LWR) concepts were introduced: the Pressured Water Reactor (PWR) and the Boiling Water Reactor (BWR). Up to date, these are still the two main reactors concepts in operation with the PWR accounting for 71.2 % of the nuclear energy capacity and the BWR representing 18.0 % [Int19]. The main difference is that in a boiling water reactor, the reactor core heats the surrounding water which itself starts to boil and drives a steam turbine to produce electricity. In a pressurized water reactor however, the water surrounding the reactor core is pressurized, preventing it to boil. Instead the hot water exchanges heat with a lower pressure water system, which eventually turns into steam and drives the turbine. Therefore, as the steam generator is installed within the containment vessel, the radioactive water in the primary loop never leaves this vessel, reducing the overall contamination area and incorporating an additional safety barrier for the leak of radioactive water. In addition, PWR have the advantage that they produce less energy when the temperature of the pressurized water increases. This provides a negative feedback loop, making the reactor more stable. Disadvantages of the PWR are the fact that the water needs to be pressurized and that additives need to be used to control the fission process, resulting in higher corrosion rates. Other Gen. II reactor design include the CANada Deuterium Uranium (CANDU) reactor (a Canadian fast-spectrum PHWR), the Advanced Gas-Cooled Reactor AGCR (using graphite as moderator and CO_2 gas as coolant) and the Vodo-Vodyanoi Energetichesky Reactor VVER (a Russian PWR design).

Generation II reactors were primarily designed to be economical and reliable. Furthermore, more attention was devoted to safety: both active (requiring an electrical or mechanical operation by the operators) and passive (requiring no or little outside power or human control) safety systems were

implemented. The Gen. II reactors produce relatively high amounts of spent fuel demanding disposition in a high-level waste repository or reprocessing (meaning reusing the remaining ^{235}U and ^{238}U and the generated ^{239}Pu e.g. in mixed oxide fuel) as part of a partially or fully closed fuel cycle. Most of the Gen. II reactors have proven to allow for a longer operation time than the anticipated lifetime, resulting in many lifetime extension licenses being granted to existing reactors (extending the lifetime from 30-40 years to 50-60 years). Today, the existing fleet is still being continuously improved in the field of safety, spent fuel management, energy efficiency, availability and flexibility.

Generation III/III+

The deficiencies of Gen. II reactors are that they are still relatively expensive, produce considerable amounts of radioactive waste, suffer from incidental downtime, are not very fuel efficient and, probably most importantly, they are not inherently safe by design. Therefore, it was clear that a new generation of fission reactors was desirable. The main objectives of the generation III fission reactors can be summarized as:

- Using standardized designs to minimize the capital costs and to reduce the time required for licensing and construction.
- Making the structural design more simple and robust, allowing for an easier operation and making the reactor less sensitive to operation parameter changes, which enables a flexible operation scheme.
- Implementing additional passive safety systems relying on natural phenomena such as gravity, natural convection or negative feedback to elevated temperatures to automatically mitigate the effect of abnormal operation without the need for human interference. This makes the reactor inherently safe and simplifies the licensing procedure.
- Significantly reducing the probability of a catastrophic accident involving a core melt as well as including new mitigation measures to reduce their impact on the environment and population.
- Increasing the resistance against serious damage by external sources e.g. an airplane crash, aiming to avoid a radiological release.
- Achieving a higher burnup, reducing the required nuclear fuel as well as the produced amount of radioactive waste.

- Designing the reactors to last for a longer lifetime ($\pm$ 60 years).
- Increasing the time between refueling, increasing the utilization rate of the reactor (e.g. by the use of burnable neutron absorbers).

All of these objectives combined aim for an improved safety, competitive economics and a reliable and flexible operation. A whole range of Gen. III(+) reactor designs have been introduced which aim to satisfy most of these conditions (a concise review was published by J.G. Marques [Mar10]). Gen. III+ refers to evolutionary Gen. III reactor designs introduced after 2010 and offering improved economics. The first Gen. III to enter commercial operation was an Advanced Boiling Water Reactor (ABWR) in 1996 in Japan. Since then, several new Gen. III(+) reactor designs have obtained a safety license and were successfully constructed (primarily in Asia). However, also severe construction issues occurred, especially in Europe where construction of a 1.12 GWe Advanced Passive (AP1000) reactor in France and of a 1.66 GWe European Pressurized Reactor (EPR) in Sweden resulted in major construction delays and a multiplication of the estimated costs. This raises the question whether these designs will in fact be able to generate electricity in Europe at a competitive cost.

These issues increase the interest in moving to smaller reactors designs taking advantage of modular construction techniques i.e. Small Modular Reactors (SMR) [Gol11]. These reactors could be constructed in dedicated factories rather than on-site (reducing the costs and speeding up the construction time). Tens of these reactors could then be installed on existing nuclear sites or could replace closing coal-fired plants, and more can be installed as the demand increases. Their characteristics are also attractive for smaller countries or remote communities with a limited electrical grid. These reactors could be the size of a rail car, making underground installment possible for safety improvements. It is however not clear yet how efficient and cost-effective these small reactors can be.

Generation IV

Two important issues that need to be considered when aiming for a long-term energy production by nuclear fission are:

(i) the availability of uranium, and
(ii) a sustainable waste management.

About every two years, the Nuclear Energy Agency (NEA) publishes a status report on the available uranium resources [age19]. At the start of 2017, the total amount of identified available uranium recoverable at a cost below \$130/kgU was reported to be 6.14 Mt, while the annual global demand of uranium amounted to 62.8 kt. Therefore, enough identified uranium is available for energy production at the current rate for another 98 years. However, the demand for uranium is expected to increase as the sector expands, which could result in up to 25 % of the known resources already depleted by 2035. Nevertheless, because of the limited maturity of uranium exploration and the fact that uranium is found worldwide, confidence exists that many new uranium reserves will be discovered in the next decades. Moreover, also a considerable amount of unconventional sources of uranium (e.g. phosphate deposits) are available. Therefore, it is expected that the uranium supply will be able to follow the demand well into the future. The deployment of advanced technology reactors and fuel recycling within the next decades could even prolong the availability of fission energy from hundreds to thousands of years.

On the contrary, the issue of sustainable radioactive waste management is extremely urgent. Until now, no worldwide consensus exists on an acceptable solution for the final disposal of high-level nuclear waste. The most realistic option remains to store it in repositories constructed deep underground in stable rock formations, but no study can fundamentally guarantee the unconditional safety of such a repository (e.g. acts of malevolence, unknown politics in 10000 years, unintentional accidents, etc.). Nevertheless, in the last years, Finland has build such a repository and is expected to start disposing waste in the early 2020s [Vir17]. Sweden is expected to start construction of a repository at that time. However, studies suggest that the amount of nuclear waste to be stored over time would be so high that finding enough suitable sites will be problematic [Mon03]. Therefore, in order to continue using nuclear energy for energy production, the amount and required storage time of the produced nuclear waste needs to be significantly reduced.

This can be realized by intensive fuel recycling and waste transmutation. Currently only about 5 % of the heavy metals (uranium, plutonium, etc) in the fuel is actually fissioned. Therefore, a lot of useful fissionable ^{235}U and ^{239}Pu and fertile ^{238}U can be recycled. This has two advantages:

(i) more energy can be produced with the same amount of natural uranium, and

(ii) the overall amount of produced high level radioactive waste is considerably reduced as the major portion (96.5 % [Her03]) consisting of uranium and plutonium is extracted (in the process reducing the required storage time by a factor ten to 20000 years).

About 3 % of the initial waste are short-lived or stable fission products which do not pose major disposal issues. Another 0.3 % are cesium and strontium which decay in a reasonable time of a few centuries. This leaves only 0.2 % of the original waste being problematic for storage. Half of amount is long-lived iodine and technetium, while the other half are long-lived minor actinides (primarily neptunium, americium and curium). A possible solution is using fast neutron reactors (having a more energetic neutron spectrum due to the absence of a moderator) to transmute iodine and technetium into shorter-living isotopes and fission the minor actinides. Doing so, only a small amount of cesium and strontium need to be stored for a few centuries, which is considered manageable.

This is one of the major objectives for future Gen. IV reactors [Mar10, Buc17, Gol11, Pio16] as well as further advancements in safety, economy and proliferation resistance. In 2001, the Gen IV International Forum (GIF) was founded to promote the research and development required to establish innovative nuclear reactor concepts (both for fission and fusion energy [Bog08]). By the end of 2002, this organization of 14 members representing more than one third of the global population has selected 6 reactor designs out of 130 proposals for further development. The selected reactor designs include: the Sodium-cooled Fast Reactor (SFR), the Lead (alloy) Cooled Fast Reactor (LFR), the Gas-cooled Fast Reactor (GFR), the Very High Temperature Reactor (VHTR), the Supercritical Water Cooled Reactor (SCWR) and the Molten Salt Reactor (MSR). The designs are varying in reactor core, energy conversion and fuel cycle technology, but all have certain characteristics leading to a new nuclear energy production using very limited resources and producing only small amounts of relative short-lived nuclear waste, while simultaneously also ensuring safety, resistance to proliferation and terrorism, reliability and economic performance.

It should be noted that four of the designs aim for a high-temperature operation improving the efficiency of heat to electricity conversion, but more importantly enabling the thermo-chemical production of hydrogen and other synthetic fuels to be used in the transport sector. The LFR is considered to be one of the more mature reactor concepts partly due to the 80 years of experience by Russia with lead-cooled reactors primarily installed

in nuclear submarines. However, the characteristics of these reactors were quite different with their lower capacity, epithermal neutron spectra and lower operation temperature. The LFR can offer advantages such as: a very long refueling time of over 10 years, possibly no electricity requirement for cooling after shutdown (depending on core size and layout), no explosion hazard, fast solidification of the coolant in case of a leak, a low operation pressure, no risk for overpressurization by overheating, and a low reactivity of the coolant with air and water. Because of these characteristics the LFR reactor promises to be safer than the current LWRs.

1.2.3 The MYRRHA Pb-Bi cooled fission reactor

One of the research reactors to assist in the development of the Lead alloy cooled Fast Reactor is the Belgian Multi-purpose hYbrid Research Reactor for High-tech Applications (MYRRHA) [AA12, Eng15, DB15], planned to be fully operational by 2033. A 3D and 2D model of the MYRRHA reactor vessel and its internals is shown in Figure 1.7 and Figure 1.8 [SCK16, wik19a].

The reactor core is essentially submerged in a pool of lead-bismuth eutectic (LBE) which serves as a coolant and heats up as it rises from the cold (lower) pool to the hot (upper) pool, which are separated by a diaphragm. Next, using 2 pumps the LBE is guided through one of the four primary heat exchangers, transferring the heat to the pressurized water in the secondary cooling system, after which the LBE returns to the cold pool. The 7600 tonnes of LBE does not reach all the way to the top of the reactor vessel, instead there is a 270 m^3 inert (Ar) gas plenum at the top, tightly sealed off by the reactor's cover (lid). This cover gas will contain trace levels of oxygen to control the amount of dissolved oxygen in the LBE (enough to avoid major corrosion of structural steel and not too much to avoid formation and precipitation of PbO and other oxides).

MYRRHA can be operated both in sub-critical and critical mode. In the sub-critical mode (k_{eff}=0.95), a proton beam of energies up to 600 MeV (4 mA) is coupled to a spallation target assembly consisting of the same LBE as the primary coolant. The resulting spallation reactions generate enough neutrons to initiate and maintain a fission reaction chain in the surrounding sub-critical core. Whenever the proton accelerator is shut down, the fission chain reaction is also immediately terminated. This inherently safe operation concept is called an Accelerator Driven System (ADS) and MYRRHA will aim to demonstrate this operation mode at a reasonable

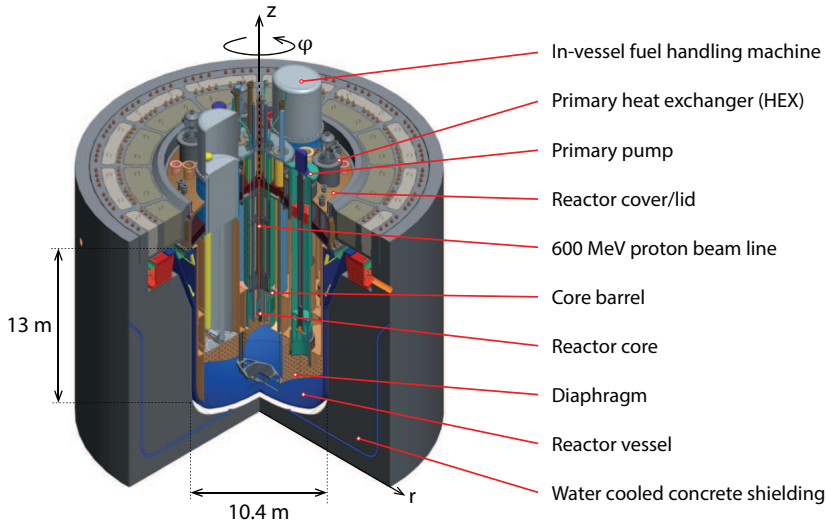

Figure 1.7: 3D model of the MYRRHA reactor vessel and its internals components as presented in the MYRRHA technical brochure published by SCK · CEN in 2016 [SCK16]. The dimensions were obtained from a Japan Atomic Energy Agengy (JAEA) review [JAE17].

power level (100 MW_{th}) providing the necessary information to scale-up the concept to an industrial demonstrator.

Because of the heavy atomic species used as a coolant (Pb and Bi), the neutrons are not effectively moderated resulting in a fast neutron spectrum. This allows for efficient transmutation of minor actinides as well as testing adapted fuel assemblies (e.g. Mixed Oxide (MOX) fuel with an increased ^{239}Pu content up to 35 wt%) to be used in innovative fission reactor designs. Also, several so called In-Pile test Sections are foreseen within the core to allow for material developments for Gen. IV reactor by investigating how candidate materials cope with the high intensity fast neutron flux.

Directly below the spallation target (and only there), the problematic He production, material damage (dpa) and thus also their ratio is calculated to be of the same order of what can be expected in fusion reactors ($\sim$30 dpa/y and 11 appm He/dpa for Fe), presenting the rare opportunity to test candidate fusion reactor materials [Zin13, Abd14]. Furthermore, MYRRHA

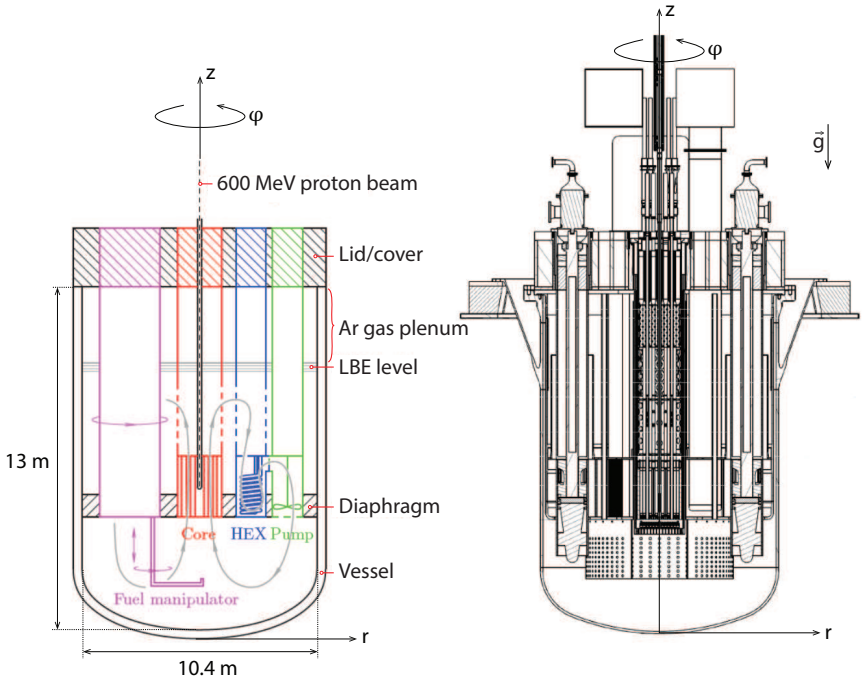

Figure 1.8: 2D cut of the MYRRHA reactor vessel and its internals components as presented in the MYRRHA technical brochure published by SCK · CEN in 2016 [SCK16].

will also be used for radioisotope production for medical and industrial applications as well as for Si-doping. In critical mode, the spallation target assembly is removed from the core and control and shutdown rods are inserted, as well as additional fuel assemblies.

As MYRRHA is based on heavy liquid metal technology, it will serve as the European Pilot Plant for the development of Lead (alloy) cooled Fast Reactors (LFRs) in this operation mode. However, as noted before, MYRRHA will use lead-bismuth eutectic (44.5 wt% Pb, 55.5 wt% Bi) rather than a pure lead melt. Both coolants offer an excellent chemical stability and they both have a high boiling point (1749°C for Pb, 1670°C for LBE) allowing a higher thermal efficiency, possibly enabling hydrogen production and requiring no coolant pressurization (which considerably reduces the probability of a loss of coolant accident and enables the option of a passive safe design). Furthermore, they are both almost transparent for neutrons while offering excellent shielding characteristics against gamma rays and their reactivity with water and air is very low.

The big advantage of LBE over lead is the reduced melting point of 125°C with respect to 327°C. This simplifies the coolant handling as well as the reactor's design and lowers the risk of major solidification of the coolant when operating at lower temperatures. There are however some drawbacks in the use of LBE. As Bi is relatively rare, LBE is (currently about 7 times) more expensive than pure Pb. Also, the solubility of Cr and Ni (representing a considerable portion of the used steel) is higher in bismuth than in lead. But most importantly, bismuth tends to become activated in presence of neutrons. In fact, a neutron capture by bismuth results in the production of highly radiotoxic polonium-210 (^{210}Po), which represent a major safety concern to be addressed in the reactor's licensing.

1.2.3.1 Radiotoxic ^{210}Po production in MYRRHA

In MYRRHA, three isotopes of polonium will be generated as undesired byproduct [Fio18], all three being α-emitters: ^{208}Po ($t_{\frac{1}{2}}$ = 2.9 y, E_α = 5.215 MeV), ^{209}Po ($t_{\frac{1}{2}}$ = 125.2 y, E_α = 4.979 MeV), ^{210}Po ($t_{\frac{1}{2}}$=138 d, E_α = 5.407 MeV). When ingested or inhaled in the human body, Po is primarily absorbed in the kidney, spleen and liver [OA09] where it is can be retained for several months (half-time $>$ 100 days [Tho01]). Upon decay of the polonium isotopes, these organs completely absorb the high energy of the α-particle resulting in irreversible damage. The ^{210}Po isotope is calculated to be the most abundant one [Fio18, FG96]. Moreover, due to its relative short half-life of 138 days, this isotope is also the most radiotoxic one. In fact, its ingestion and inhalation radiotoxicity is among the highest of all known radionuclides [Eck13]. ^{210}Po has a specific activity of 166 TBq/g [Hea10] (4500 times higher than ^{226}Ra) and an effective dose varying between $6.1 \cdot 10^{-7}$ and $2.6 \cdot 10^{-5}$ Sv/Bq depending on the age and exact way of inhalation/ingestion, resulting in 0.1 – 4.3 GSv/g of ^{210}Po (note that a few Sieverts is often fatal). Based on this extremely high radiotoxicity, the maximum permissible body burden was set at 1.11 kBq, corresponding to only $6.8 \cdot 10^{-12}$ g. The maximal permissible concentration in the air and in water is respectively 0.2 Bq/m^3 ($1.2 \cdot 10^{-15}$ g/m^3) and 0.83 Bq/l ($5 \cdot 10^{-15}$ g/l) [OA09].

The dominant production channel of ^{210}Po in MYRRHA is the following:

$$^{209}\mathrm{Bi} \xrightarrow{n,\gamma} {}^{210g}\mathrm{Bi} \xrightarrow[t_{1/2}=5\,\mathrm{d}]{\beta^-} {}^{210}\mathrm{Po}. \tag{1.2}$$

After one irradiation cycle (90 days [Eyn15]) at nominal power, about 350 g of ^{210}Po (equivalent to $5.8 \cdot 10^4$ TBq) is estimated to be present [Fio18]. This corresponds to 7.6 GBq/kg LBE, while in a typical neutron environment of fast reactors (neutron fluxes of order 10^{15} n/(cm^{2}s)), the concentration could even reach 100 GBq/kg LBE [Hei11, Cet10]. In MYRRHA, most ^{210}Po will be retained in the LBE and thus sealed within the primary system , posing no problems except in case of a coolant leakage or if access to the submerged structures is required during maintenance. However, some ^{210}Po will migrate to the cover gas until an equilibrium concentration is reached, which depends on the volatility of the ^{210}Po species in which it primarily evaporates from the LBE. More volatile species, will increase the ^{210}Po concentration in the cover gas. The gaseous ^{210}Po could diffuse outside the primary system if the reactor cover is not perfectly tight or when the reactor cover needs to be opened for refueling or maintenance. ^{210}Po may also limit access to surfaces on which it deposits, thus increasing maintenance costs and/or collective doses. The ^{210}Po hazard could be significantly reduced by continuously extracting Po from the LBE melt, as the ^{210}Po evaporation rate is always proportional to the ^{210}Po concentration in the LBE. Moreover, ^{210}Po also contributes to most of the decay heat of the activated LBE thus determining the strategy for its handling after definitive shutdown, providing additional motivation for ^{210}Po removal during operation.

An extraction system for ^{210}Po is therefore foreseen and five candidate Po extraction techniques have been selected by a research collaboration of the Idaho National Engineering and Environmental Laboratory (INEEL) and the Massachusetts Institute of Technology (MIT): H_2Po stripping, electrodeposition, distillation, alkaline extraction and rare-earth filtration. These techniques were evaluated in the context of an ADS reactor and none have been tested at large scale. Unfortunately, it was concluded that none of the techniques can be currently considered as ideal [OA09]. The H_2Po stripping technique could remove most of the Po but involves working with high pressure H_2, which is to be avoided because of the explosion hazard. No convincing results were published so far on electrodeposition, therefore this technique was also ruled out. The distillation technique is rather simple, but an extremely large transfer area is necessary and the LBE needs to be heated to high temperatures (900°C-1100°C) to be effective, requiring other structural materials than stainless steel. Moreover, Po is extracted in the gas phase, presenting an inherent danger. Although the technique is very effective at small scale, it would be rather impractical and costly at reactor scale. The alkaline extraction technique has been studied most extensively because it can readily be tested using Te as a Po surrogate and this technique

is recommended by most users of LBE as coolant. However, to operate this system at reactor scale, the challenge remains of finding a material that can cope with the higher operation temperature and the corrosivity of the molten alkali. The fifth technique, rare-earth filtration, is the most elegant one and is based on the fact that Po can form very stable polonides with rare-earth elements that have a very low vapor pressure. It could be applied to both the Po in the cover gas or the Po in the LBE. This technique looks promising, but a lot of future R&D is still required e.g. to develop rare-earth coating techniques and investigating the unfavorable effect of rare-earths on the protective oxide layers in the reactor.

Much research on these and alternative extraction techniques is still ongoing. However, as experiments involving ^{210}Po are often cumbersome and costly due to the high safety risk, Te is often used as ^{210}Po surrogate and the exact chemical characteristics of ^{210}Po often remain unknown.

One of the aims of this work is therefore to **provide accurate information on the temperature-dependent chemical stability of possibly occurring Po-containing molecules** by performing high level-of-theory ab initio (quantum chemistry) calculations (thus avoiding experiments involving ^{210}Po). This information can then be used both in a detailed risk analysis of possibly occurring accidents (e.g. to determine the evaporation rate and molecular species of volatile Po escaping from the LBE), as well as in the development of (alternative) extraction techniques to efficiently remove Po from the LBE melt.

1.3 Nuclear fusion

Although planned to be much more fuel efficient, Gen. IV fission reactors will still require certain amounts of heavy fissile or fertile elements such as uranium and plutonium, but also thorium [Gyo16]. As the readily available supply of these elements is not unlimited and alternative extraction methods are expected to be cost intensive, using nuclear fission for energy production can not last forever. More immanently, the requirement of inherently safe nuclear reactors and the necessary processing and transmutation of high level radioactive waste, as well as proliferation issues that comes along, is quite complex and will increase the overall costs of the energy production, reducing the economical competitiveness of nuclear fission compared to alternative energy sources.

Another opion of nuclear energy is directed towards exploiting nuclear fusion rather than fission.

1.3.1 Principle

Nuclear fusion aims to merge light (abundant) elements to produce energy. Figure 1.4 on page 8 shows that the binding energy per nucleon is much lower for lighter nuclei as compared to ^{56}Fe. Therefore, when fusing lighter nuclei into a heavier nucleus with a larger overall binding energy, a large amount of energy is set free. It can be seen that the hydrogen isotopes and ^{3}He have a particular low binding energy per nucleon and are therefore excellent candidates to be used in fusion reaction. On the other hand, some nuclei are particularly stable (as compared to neighboring nuclei) such as ^{4}He, ^{12}C and ^{16}O and, therefore, represent superior fusion products.

Stars are powered by nuclear fusion. Depending on the stage in their lifetime and the distance to the core, they can fuse hydrogen to helium, helium to carbon and oxygen, carbon to neon and magnesium, oxygen to silicon and sulfur and finally silicon to extremely stable ^{56}Fe nuclei. The further along this reaction, the more energy is required to overcome the coulomb barrier between the nuclei and the less energy per mass of reactants is produced. Therefore, the most feasible as well as most profitable fusion reaction to attempt would be those of the very lightest elements. The criteria for a suitable fusion reaction to use for energy production can be summarized as:

- being as exothermic as possible (focusing on the steepest part of the curve in Figure 1.4 and thus the lightest elements),
- involving low atomic number nuclei to minimize the Coulomb barrier to be overcome,
- involving only two reactants, as simultaneously fusing three nuclei is too improbable,
- involving two or more products so that energy and momentum can be conserved without the need for the emission of photons (gamma rays) or neutrinos,
- both protons and neutrons should be conserved as otherwise weak interactions have to be involved which have a very low probability.

Only a few reactions meet these criteria and have a large enough cross section [Kik12]. The three reactions that satisfy these requirements with the largest cross section are:

$$ {}^{2}_{1}\mathrm{D} \; + \; {}^{3}_{1}\mathrm{T} \; \rightarrow \; {}^{4}_{2}\mathrm{He} \; (3.5\,\mathrm{MeV}) \; + \; {}^{1}_{0}\mathrm{n} \; (14.1\,\mathrm{MeV}) \tag{1.3a} $$

$$ \begin{aligned} {}^{2}_{1}\mathrm{D} \; + \; {}^{2}_{1}\mathrm{D} \; &\rightarrow \; {}^{3}_{1}\mathrm{T} \quad (1.01\,\mathrm{MeV}) \; + \; {}^{1}_{1}\mathrm{H} \; (3.02\,\mathrm{MeV}) \quad (50\%) \\ &\rightarrow \; {}^{3}_{2}\mathrm{He} \; (0.82\,\mathrm{MeV}) \; + \; {}^{1}_{0}\mathrm{n} \; \; (2.45\,\mathrm{MeV}) \quad (50\%) \end{aligned} \tag{1.3b} $$

$$ {}^{2}_{1}\mathrm{D} \; + \; {}^{3}_{2}\mathrm{He} \; \rightarrow \; {}^{4}_{2}\mathrm{He} \; (3.6\,\mathrm{MeV}) \; + \; {}^{1}_{1}\mathrm{H} \; (14.7\,\mathrm{MeV}) \tag{1.3c} $$

Two important aspects needs to be considered when selecting a suitable fusion reaction to exploit for energy production:

(i) the abundance of the reactants on earth, and
(ii) the reactivity (probability of a fusion reaction at a given temperature) and the corresponding fusion power density.

Deuterium (${}^{2}_{1}\mathrm{D}$) is available in virtually inexhaustible quantities as 0.0156 % of the hydrogen isotopes in the earth's ocean water is deuterium (according to the Vienna Standard Mean Ocean Water [Gat81]), resulting in a estimated supply of about 24 trillion tonnes. Tritium (${}^{3}_{1}\mathrm{T}$), having a half-life of 12.32 years, only appears in trace amounts in nature. The very limited global inventory of tritium available today has been almost exclusively generated in CANDU-type fission reactors. The at present available global inventory is of the order of only 40 kg [Kov17]. Also helium-3 (${}^{3}_{2}\mathrm{He}$) is very rare on earth, representing only 0.0002 % of all helium on earth. Although being the second most abundant element in the universe, helium in general is quite scarce on earth being a very light gas easily escaping the earth's gravitational field. Most helium found on earth today, is the result of the natural decay of uranium and thorium, a process generating ^{4}He. The ^{3}He still found on earth is believed to date back to the earth's formation at which it was entrapped. Limited supplies of ^{3}He could be extracted while exploiting natural gas reserves (order of tens of kilograms per year). Nevertheless, the ^{3}He inventory available for use today is almost entirely the product of the radioactive decay of tritium ($t_{\frac{1}{2}}$=12.32 y). As the focused production of tritium is rather limited, so is the current supply of ^{3}He. Higher concentrations of ^{3}He were found to exist on the moon [Fa10] and commercial lunar mining of ^{3}He as fusion fuel is sometimes being considered as a possibility for the future, but currently not yet profitable.

The reactivity $\langle \sigma v \rangle$, is the product of the energy-dependent reaction cross section and the relative velocity of the fusing nuclei, averaged over the velocity distribution of the participating nuclei. When multiplying the reactivity with the particle densities, the reaction rate is obtained. In thermonuclear fusion, high temperatures are used to achieve the particle energies necessary to overcome the Coulomb barrier. As the energies required to overcome the Coulomb barrier are very high (e.g. 0.1 – 1 MeV equivalent to $1.2 \cdot 10^9$ – $1.2 \cdot 10^{10}$ K for D-T fusion), in general only the nuclei in the high-energy tail of the temperature-dependent velocity distribution manage to undergo fusion reactions. It should be noted though that in fact even these high-energy nuclei do not have enough energy to classically overcome the barrier, but rather quantum tunnel through the remaining part of the barrier This can be achieved by particles with an energy of 10 keV (∼120 million K) or higher. The temperature-dependent reactivity for the 3 proposed fusion reactions is shown in Figure 1.9.

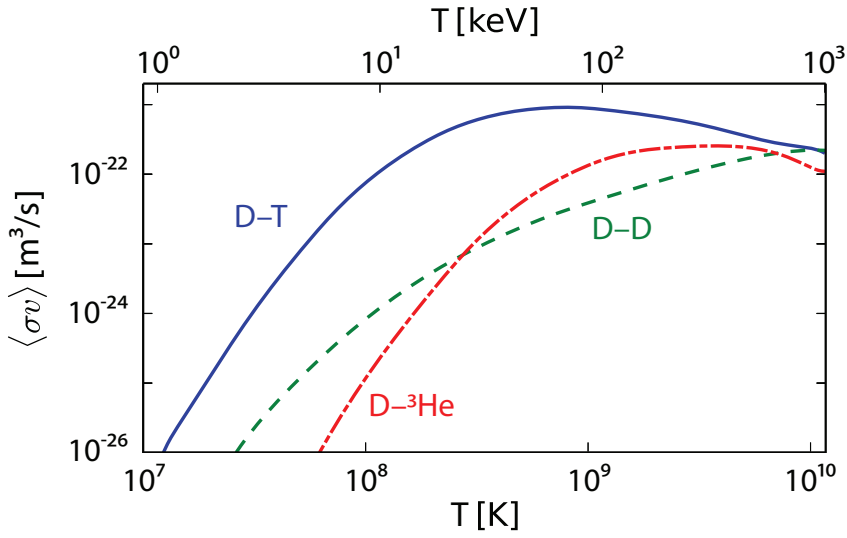

Figure 1.9: Temperature-dependent reactivity $\langle \sigma v \rangle$ of the D-T, D-D and D-^{3}He fusion reaction. The plot is based on data from the NRL: Plasma Formula, 2006 revision [Hub06], obtained from wikipedia [wik19b] and slightly adapted.

The D-T fusion reaction has the highest reactivity peak of all fusion reactions and reaches this peak at the lowest temperature. For most confinement concepts being considered for fusion reactors (see below in section 1.3.3) the density and the temperature can be varied over a wide

range, while the maximum achievable pressure is a constant defined by the design of the reactor. Given this pressure, the largest fusion power density is obtained for a maximum value of $\langle \sigma v \rangle / T^2$, defining the most efficient operational temperature of a thermonuclear reactor. For the D-T, D-D and D-$^3\mathrm{He}$ reaction, this maximum value is reached at respectively 157 million K, 174 million K and 673 million K (equivalt to 13.5, 15.0 and 58.0 keV). Comparing these temperatures to the one found at the core of the sun (15 million K or 1.29 keV), it is clear that achieving these conditions on earth represent a huge technological challenge.

The maximum value of the fusion power density obtained for D-T can be estimated to be 68 times larger than the one for D-D and 80 times larger than the one for D-$^3_2\mathrm{He}$. At this point, it should be noted that the temperatures under consideration are far above the ionization temperatures of the hydrogen and helium. Therefore, these elements will be completely ionized and form a plasma existing of ions and electrons. The notably higher fusion power density achievable at a given temperature for D-T fusion reaction is essential when aiming to achieve a self-sustaining/self-heating fusion plasma which produces enough power so that the power fraction absorbed within the fuel itself is enough to cover its own heat losses (by radiation and particle loss), achieving so-called ignition. At this point, external heating of the plasma is no longer necessary and a large portion of the excess power produced by the plasma can be fed to the electricity grid (apart from the energy consumed by the other auxiliary systems of the power plant). Even for the high fusion power density D-T fusion reaction, achieving this state is a huge technological as well as engineering challenge. Therefore, for now, the only candidate fusion reaction imaginable to be used for commercial energy production is the D-T fusion reaction.

Considering the discussion above, the D-T fusion reaction is the only reaction capable of providing a high enough fusion power density at reasonable temperatures possibly allowing to ignite the plasma. This reaction also has sufficiently high energy yield of 17.6 MeV (18.3 MeV D-$^3\mathrm{He}$ and 3.65 MeV for D-D). A major problem with this reaction path, however, is the scarcity of tritium. In order to be able to exploit the D-T fusion reaction for energy production, a supply for tritium has to be established. One solution might be tritium breeding.

1.3.2 Tritium breeding

The concept of tritium breeding refers to the production of tritium within a fusion reactor itself during operation. It was found that tritium can be efficiently produced by making neutrons interacts with lithium:

$$^{1}_{0}\mathrm{n} + {}^{6}_{3}\mathrm{Li} \rightarrow {}^{3}_{1}\mathrm{T} + {}^{4}_{2}\mathrm{He} + 4.784\,\mathrm{MeV}, \tag{1.4a}$$

$$^{1}_{0}\mathrm{n} + {}^{7}_{3}\mathrm{Li} \rightarrow {}^{3}_{1}\mathrm{T} + {}^{4}_{2}\mathrm{He} + {}^{1}_{0}\mathrm{n} - 2.467\,\mathrm{MeV}. \tag{1.4b}$$

The latter reaction (Eq. 1.4b) is endothermic and can only occur for neutron energies exceeding the 3.65 MeV threshold. Therefore, this reaction can only occur for fusion neutrons that have not been slowed down significantly. The former reaction with ^{6}Li (Eq. 1.4a) is exothermic and can therefore contribute to the overall energy production in the reactor. Moreover, it has a much larger cross section (probability of occurring), except for neutron energies exceeding 5 MeV. This probability gradually increases for decreasing neutron energy and reaches about 950 barns (1 barn = 10^{-24}cm^2) for thermal neutrons. Being a light element, lithium also moderates neutrons relatively well, guiding them to the low energy region of high tritium production by ^{6}Li. The natural abundance of lithium on earth is 92.41 % of ^{7}Li and only 7.59 % of ^{6}Li. Therefore, to achieve a high tritium production yield, the used lithium will have to be enriched.

One can imagine that not all fusion neutrons will interact with lithium to produce tritium. Some will be captured by the structural materials, others will simply escape the reactor. Moreover, not all produced tritium can be extracted and be refueled to the plasma (tritium, being a hydrogen isotope, easily diffuses in the structural material). Also, tritium is unstable and beta decays with a half-life of 12.32 years, therefore part of the produced tritium will decay before it can be refueled. Finally, in order to scale-up nuclear fusion, ideally more tritium should be produced in a fusion reactor than there is being consumed.

All these arguments call for the implementation of a so-called neutron multiplier. This is an element that, when interacting with a high-energy neutron, emits one or more additional neutrons and has a relatively low neutron absorption cross section. The two major candidates for this purpose are Be and Pb. Table 1.2 summarizes some important characteristics of the neutron multiplication potential of Pb (in its natural abundance) and Be. The major advantage for using Be is the considerably lower threshold for neutron doubling (n,2n) of 1.75 MeV w.r.t. the 7.46 MeV for Pb (averaged).

Table 1.2: Neutron multiplication performance parameters for Be and Pb

multiplier X	X(n,2n)		X(n,3n)	
	$E_{\text{threshold}}$ (MeV)	$\sigma_{\max}$ (b)	$E_{\text{threshold}}$ (MeV)	$\sigma_{\max}$ (b)
^{9}Be	1.75	0.55	25	0.009
^{208}Pb (52.4 %)	7.41	2.2	14.18	1.8
^{206}Pb (24.1 %)	8.13	2.3	14.9	1.8
^{207}Pb (22.1 %)	6.80	2.2	14.9	1.8
^{204}Pb (1.4 %)	8.44	2.3	15.4	1.8

The maximum cross section is however 4 times larger for Pb than for Be. The energies of the neutrons generated in thermal fusion reactions folllow a narrow gaussian-like distribution around 14.1 MeV with a width depending on the plasma temperature (e.g. ranging between 12.5 MeV and 15.5MeV for a 50%D/50%T plasma at 150 million K)[Eri19]. The highest energy neutrons can therefore even trigger a neutron tripling reaction in Pb, however this effect has only a limitted contribution considering the small fraction of high energy neutrons and the low probability of reaching Pb without being down-scattered first. Anyhow, this neutron tripling is not possible for Be because of the high threshold (25 MeV). Pb was found to have a considerably larger absorption cross section than Be (about 100 times larger for thermal neutrons and even more in the epithermal and fast region), however this cross section is still very small compared to the tritium production cross section of ^{6}Li (except in the resonance region of Pb between 0.5 and 1 MeV).

A disadvantage for the use of Be is the fact the resources are rather limited, making it quite expensive. Also, Be dust is poisonous and can cause berylliosis, a chronic disabling and sometimes even fatal respiratory disease, requiring a careful and therefore more costly manufacturing and handling process. Finally, Be chemically interacts with Li, therefore these two substance cannot be directly mixed. Pb is cheaper, less reactive and compatible with Li but has, as previously discussed, a higher energy threshold. Until now, no final decision has been made on which of both has the better characteristics to be used in a fusion reactor and both are being developed in parallel. An extensive review of possible breeder/multiplication materials can be found in [Her18].

Lithium has its melting point at 180.6°C and boiling point at 1347°C. The major problem with lithium however is that it is highly flammable and

possibly explosive when exposed to air and especially to water, its molten form even more so than as a solid. Therefore, is was decided to avoid the implementation of pure Li in a tritium breeding concept. Instead, Li is implemented in either the form of liquid PbLi eutectic (15.7-16.98 at.% Li) or in the form of a solid ceramic (e.g. Li_4SiO_4, Li_2TiO_3 or Li_2ZrO_3). The actual designs of the tritium breeding structures under consideration in the European program will be briefly discussed in section 1.3.5.1.

1.3.3 Confinement concepts

The produced fusion power generates a thermal pressure in the plasma. In order to sustain a dense enough fusion plasma, it needs to be confined. Another reason for confinement is to prevent the fusion plasma of touching any structural material.

Gravitational confinement

As previously mentioned, stars are powered by nuclear fusion. Due to the huge mass contained within a star (ranging between about $1.6 \cdot 10^{29}$ and $3 \cdot 10^{32}$ kg), it generates a significant gravitational field. The radius of a star is determined by the balance between the outward thermal pressure and the inward force of gravity, residing in a hydrostatic equilibrium. It is obvious that this method of confinement cannot be used when aiming to build a compact fusion reactor on earth. Therefore, alternative confinement concepts had to be devised.

Magnetic confinement

As a plasma consists of ion and electrons, both charged particles, confinement by magnetic fields seems a viable option. Since the late 1940s research has been performed on the most suitable magnetic configuration to create and contain a fusion plasma. This narrowed down the field into two design concepts still being studied in parallel today: the **tokamak** design introduced by the Soviet scientists Igor Tamm and Andre Sacharov in 1950 and the **stellarator** design introduced a year later by the American Lyman Spitzer.

Both concept are based on a fusion plasma having a torus (donut/ring) shape. The direction along this torus is referred to as toroidal and the direction perpendicular to the toroidal one and wrapped around the torus is

called poloidal. As charged particles tend to follow the magnetic field lines and not easily cross between these lines, the plasma could be confined by generating a magnetic field with ring shaped field lines (along the torus) connected on themselves and equally spaced (i.e. a homogeneous field strength). It is however very challenging to create a magnetic field with these characteristics. The ring shaped field lines can be achieved by the use of superconducting toroidal field (TF) coils, which are poloidally wrapped around the torus (see Figure 1.11 on p. 36). The problem is, however, that the TF coils are spaced close together at the inside of the torus (inboard) and further away at the outside of the torus (outboard). Therefore, the magnetic field is stronger inboard than outboard. The resulting magnetic field gradient leads to charge separation and an outward drift of the plasma, making confinement impossible. This can be solved by introducing a poloidal field component. Doing so, the field lines are not longer simply ring-shaped but are now helically wrapped around the torus axis. As the charged particles follow these field lines, they are alternately at the high field side (being pushed towards the torus axis and thus the center of the plasma) and at the low field side (being pulled away from the plasma center). The net result is a more stable plasma no longer being strongly driven outward.

The difference between a tokamak and stellarator primarily boils down to the way in which the required poloidal field component is realized. In a tokamak, this is achieved by driving a current in the plasma along the torus, resulting in a poloidal field generated by the moving charged particles. This plasma current is driven by a central solenoid (CS) at the center of the torus, making use of Farady's law (the transformer principle). While doing so, the plasma is simultaneously heated by friction. As the generated poloidal field is not perfect, small drift forces may still occur. Therefore poloidal field (PF) coils having a ring shape and running along the torus are installed with the purpose of pushing the plasma back to its central position whenever it starts to drift away. They can also be use to shape the plasma cross section to a desired form. The tokamak concept is currently the most advanced design concept in the race to achieve a practical fusion power plant. A drawback is however that it is destined to operate in a pulsed mode as it relies on a transformer principle (requiring an increasing current in the CS, a trend which cannot be continued indefinitely) to maintain magnetic confinement.

The stellarator concept has been studied in a somewhat lesser degree, partly because it is considerably harder to build. Since the 1990s, the required construction techniques have become available, renewing the interest in stellarators. Instead of making use of a plasma current to generate the

necessary poloidal field, a stellarator aims to achieve this by shaping the toroidal field coils in complex forms, resulting in both a toroidal and poloidal field component. Using the increased computing power, it became possible to optimize the desired magnetic field configuration and the corresponding coil shapes. Advanced manufacturing techniques nowadays allow to build the complex-shaped superconducting coils at high precision. By getting rid of the a central solenoid, a stellarator can in principle operate in a continuous mode.

Both concepts are still being developed in parallel and no final decision exists on which technology is more suitable to be used in commercial fusion reactors. Future results of the most advanced stellarator i.e. Wendelstein 7-X (operation started in 2015) and tokamak i.e. the International Thermonuclear Experimental Reactor (ITER) planned to start operation in 2025, might trigger a final decision.

Inertial confinement

This confinement comprises two major approaches. In the direct drive approach, a spherical array of powerful lasers are used to symmetrically heat a fuel pellet containing small amounts of deuterium and tritium. As a result, the outer layer of the pellet is heated extremely fast, making it explode. As a result, the inner portion of the fuel pellet implodes as it is driven inwards. This process initiates a shockwave that further heats and compresses the fuel at the center until fusion conditions are reached. The triggered fusion burn propagates to the cooler outer parts of the pellet faster than it manages to expand (hence the *inertial* confinement), resulting in a virtually complete consumption of the fuel.

In the indirect drive approach, rather than using the lasers to heat the pellet itself, they are used to heat the inside of a gold cavity which contains the pellet at the center. This generates a uniform distribution of soft X-rays (shorter wavelength than the lasers) within the capsule, quickly heating up the fuel pellet and finally resulting in the same result as with the direct drive approach. The advantage here is that the final pellet heating is more uniform (allowing a larger error margin on the laser orientations). As a trade-off some of the laser's energy is sacrificed.

The major research facility investigating this confinement regime is the National Ignition Facility in the USA, who has reached a fusion energy gain

factor exceeding unity in 2014 using the indirect drive approach [Hur14]. Nevertheless, there is no final decision on which of the two approaches is most suitable for future implementation in a commercial fusion reactor. A review on the state-of the art of both concepts as well as for some advanced ignition schemes was published by Betti and Hurricane [Bet16].

1.3.4 International Thermonuclear Experimental Reactor

The International Thermonuclear Experimental Reactor (ITER) is a tokamak fusion reactor currently under construction in the south of France. It is build within the framework of an unprecedented international research collaboration with the fully participating entities being Europe, the USA, China, India, Japan, South-Korea and Russia. It is planned to start operation in 2025 and, with a plasma volume of 840 m^3, will be by far larger than the largest tokamak currently in operation, the Joint European Torus (JET) with a plasma volume of 100 m^3. ITER has been designed to deliver 500 MW_{th} of fusion power for about 400 seconds using 50 MW of heating power and thus aims to achieve a fusion energy gain factor Q equal to 10. The current record of this factor Q in a tokamak is 0.67 held by JET for generating 16 MW_{th} of fusion power using 24 MW input power. The main goal of ITER is thus to demonstrate the principle of producing more thermal power from fusion than is consumed to heat the plasma. It should be noted that the latter is not equal to the total electrical power consumed by the reactor, which will be multiple times larger. ITER will aim to provide the last essential knowledge to be incorporated in the final design of the next-step European DEMOnstration (DEMO) fusion reactor.

1.3.5 European demonstration (DEMO) fusion reactor

DEMO is the next step in the *European Research Roadmap to the Realisation of Fusion Energy* (see Figure 1.10). DEMO is currently in its pre-conceptual design phase. Its conceptual design phase is planned to last from 2020 till 2027, its engineering design phase from 2029 till 2038 and the construction would be initiated in 2040 (when the foreseen operational schedule of ITER comes to an end, providing no new input). With its plasma volume around 2200-2500 m^3, DEMO will be about three times bigger than ITER [Fed17]. A CAD model of the 2014 DEMO design obtained from [Rap15] and slightly adpated is shown in Figure 1.11.

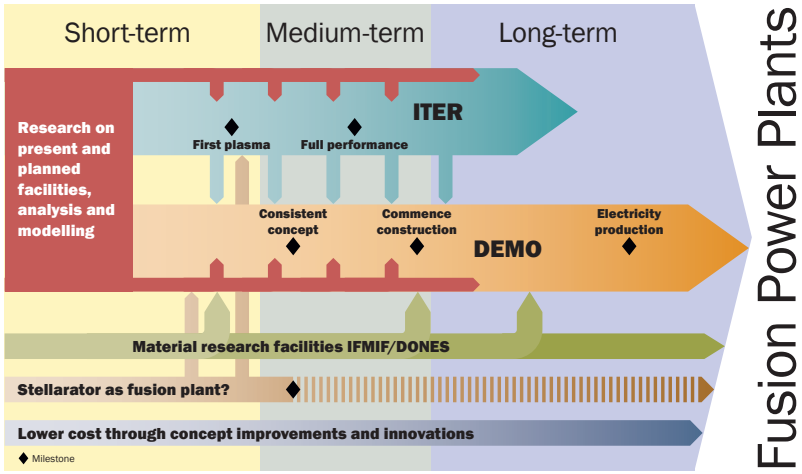

Figure 1.10: Illustration of the *European Research Roadmap to the Realisation of Fusion Energy*. This image and the associated written report is freely available on the EUROfusion website [EUR18].

The DEMO reactor has three major goals that will have never been achieved before:

(i) demonstrating a net electrical output from fusion power,
(ii) demonstrating tritium self-sufficiency, and
(iii) proving the material and reactor relevant technologies to enable the design and construction of a Fusion Power Plant (FPP) after DEMO.

DEMO plans to generate 2.0 GW_{th} of fusion power [Fed17, Fra17] aiming to export 300-500 MW electrical power to the grid [Ell17]. Tritium self-sufficiency is an absolute requirement for D-T fusion reactors considering the very limited supply. With an envisioned tritium breeding ratio over unity, DEMO aims to produce more tritium than it consumes. Moreover, the produced tritium will be extracted using a Tritium Extraction System (TES) and will be refueled to the plasma to prove the entire concept of tritium self-sufficiency. DEMO will also be able to field-test the resistance against the extremely high neutron and heat fluxes of the materials selected from experiments in the IFMIF/DONES neutron irradiation facility, which initiates its construction phase in the early 2020s [Arb18, Ber19, Fis19]. Finally, remote handling and maintenance schemes, that will be required in

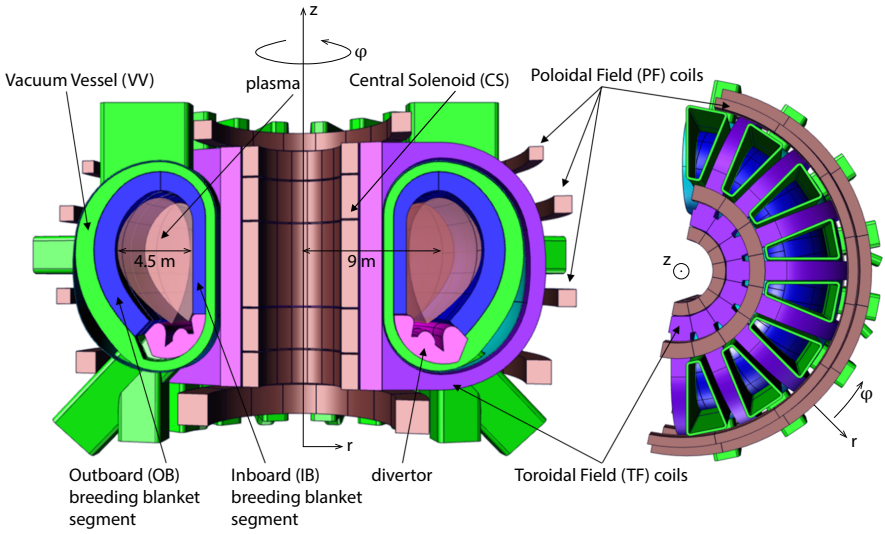

Figure 1.11: The 2014 DEMO CAD model. In total there are 16 similar sectors forming a complete torus. The space dedicated to the tritium breeding blankets is colored in dark blue. The fusion plasma will be contained at the center of this structure. Image was obtained from [Rap15].

a Fusion Power Plant, will be tested.

In the next sections, a short qualitative description of the tritium breeding concepts as well as the tritium extraction and removal systems being developed in Europe and considered for implementation in DEMO is given.

1.3.5.1 Tritium breeding blanket concepts

The tritium breeding will be realized by implementing a dedicated tritium breeding blanket completely surrounding the fusion plasma (see blue structure in Figure 1.11). Currently, 4 breeding blanket concepts are being developed in Europe and are considered for implementation in the European DEMO [Boc16, Cis18]: Helium Cooled Lithium Lead (HCLL), Water Cooled Lithium Lead (WCLL), Dual Coolant Lithium Lead (DCLL) and Helium Cooled Pebble Bed (HCPB). Their main characteristics are listed in Table 1.3. The HCLL, WCLL and DCLL blankets all use liquid eutectic Pb-Li (15.7-16.98 at.% Li, melting point = 235°C) [Val08] as a combined breeder/multiplier material, but differ by the fact that they are cooled by respectively helium, water or a combination of Pb-Li (breeder zone) and He (first wall). The

tritium produced in these blankets is carried away from the reactor's internals within the liquid PbLi towards a dedicated Tritium Extraction and Removal (TER) system. These blankets are referred to as liquid breeder blankets. The HCPB on the other hand is the only solid breeder blanket being developed in the EU. It uses a layered structure of alternately ceramic Li_4SiO_4 or Li_2TiO_3 (60 % ^{6}Li) breeder pebbles and Be or beryllide (e.g. $Be_{12}Ti$, $Be_{12}Cr$, $Be_{12}V$) multiplier pebbles, separated by EUROFER structural plates. The tritium produced in the Li pebble bed is removed using He purge gas (1% H, 0.15 MPa) and later separated again from this gas.

Table 1.3: Main characteristics of the tritium breeding concepts being developed at Europe. Data was obtained from references [Fra17, Her19, Rap15].

	HCLL	WCLL	DCLL	HCPB
Breeder	Pb-Li	Pb-Li	Pb-Li	Li_4SiO_4/Li_2TiO_3
Multiplier				$Be_{12}Ti/Be_{12}Cr/Be_{12}V$
^{6}Li enrichment	90 %	90 %	90 %	60 %
Coolant (BZ)	He	H_2O	Pb-Li	He
Coolant (FW)	He	H_2O	He	He
Tritium carrier	Pb-Li	Pb-Li	Pb-Li	He purge gas
$Q_{\mathrm{Pb-Li}}$ (kg/s)	810	560	21192	N/A
Q_{coolant} (kg/s)	2400	4800	1177(He)	2400

BZ = breeder zone, FW = first wall, Q = overall mass flow rate

It should be noted that tritium production is not the only task of a breeding blanket. A second task is an efficient heat extraction from the fusion plasma. Finally, it also has a shielding purpose against excessive neutron flux intensities, atom displacement damage, He production and nuclear heating in components such as the Nb_3Sn superconducting coils, the vacuum vessel, the epoxy insulator, the winding pack, the Cu/CuNi stabilizer used in the superconducting coils and components with re-weldability requirements [Fis15].

1.3.5.2 Tritium Extraction and Removal Systems (TERS)

The purpose of the Tritium Extraction and Removal System (TERS) in DEMO is to extract T from the breeder and to route it to the Tritium Plant (TP). As this work focuses on liquid breeding blankets, only the techniques considered for the extraction of tritium from Pb-Li will be

discussed. The requirements for the extraction system to be implemented in DEMO are: a continuous operation mode, a concept involving as few steps as possible, a compact system to facilitate integration in the reactor design and a high extraction efficiency ($>90\,\%$). Three techniques being investigated in Europe are [Uti19b]: Permeator Against Vacuum (PAV) [D'A17, Gar17], Regenerable Getters [Feu91, Feu95] and the Vacuum Sieve Tray (VST) [Oki12, Oki15, Mer16].

In the PAV concept, the Pb-Li flows in a vacuum through a tube made of a material highly permeable to tritium. The low solubility of tritium in Pb-Li promotes its permeation through the membrane into the vacuum, after which it is collected. The advantage of this system are its simplicity, its continuous one-step operation and the efficiencies up to $90\,\%$. Drawbacks are the relative high capital cost, the required research on optimal permeator materials and the lower efficiency at low temperature.

In the Regenerable Getters concept, the Pb-Li flows through getter beds manufactured of a material having a higher solubility for tritium than Pb-Li. As a result, tritium is transferred from the Pb-Li to the getter beds. This concept offers a high extraction efficiency, but has the major drawback that it is operated in batch mode. In addition, much more research is required on optimizing the regeneration process after loading, as well as on the impact of impurities on the performance. This makes them less attractive for near-term deployment.

In the VST concept, also called Vacuum Droplets' Tower (VDT), the Pb-Li is pumped through a sieve tray installed at the top of a vacuum chamber, resulting in Pb-Li droplets falling through a vacuum. The tritium is transported from within the droplet to its outer surface where it recombines and evaporates as T_2. Initially, this transport was thought to be diffusion-based and therefore too slow for the system to be efficient, however the droplets were found to oscillate, greatly enhancing the tritium transport. The major advantage of this method is its simplicity and expected high efficiency. However, this technique is still in its conceptual phase requiring more R&D. M. A. J. Mertens, the author of this Ph.D. dissertation, performed his Master's thesis on the *Engineering Design of the Test Section for Tritium Extraction from PbLi using a Vacuum Sieve Tray* and, at the start of this Ph.D. project, a paper was published on the results obtained during that project [Mer16].

1.3.5.3 Radiotoxic ^{210}Po production in DEMO

As the goal of the breeding blankets is to produce as much tritium as possible by interacting with the fusion neutrons, they are implemented close to and surrounding the entire plasma. This is a very harsh environment with extreme heat and neutron loads. A tungsten coating of 2 mm at the plasma side protects the blankets against major damage. Due to the very high neutron fluxes, material transmutation is intrinsic and some problematic radioisotopes are produced. Similarly as in lead-(bismuth) cooled fission reactors, highly radiotoxic ^{210}Po is produced in the Pb-Li used in the liquid breeder blanket concepts. The problematic reaction chain is visualized in Figure 1.12. Instead of multiplying a neutron, ^{208}Pb can also capture a

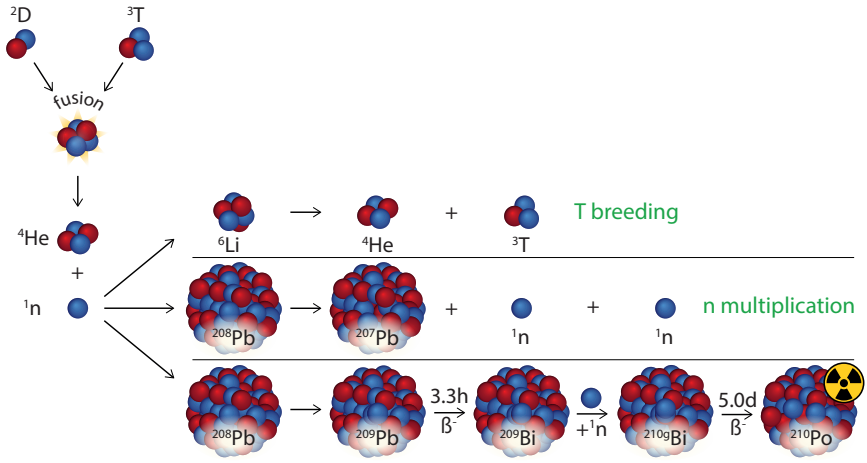

Figure 1.12: A visual summary of the ^{210}Po production reaction chain. The problematic chain is initiated when a (fusion) neutron is captured by ^{208}Pb instead of being multiplied (lower reaction path).

neutron, resulting in ^{209}Pb which quickly β^- decays into ^{209}Bi ($t_{\frac{1}{2}}$=3.3 h). If this nuclide captures another neutron, it can either form ground-state ^{210g}Bi or metastable ^{210m}Bi. The former β^- decays with a half-life $t_{\frac{1}{2}}$=5.0 d, generating highly radiotoxic ^{210}Po. If ^{209}Bi impurities are present in the used Pb-Li from the start, these provide a shortcut in the problematic reaction chain, resulting in an increased ^{210}Po production. Being highly radiotoxic, ^{210}Po can compromise the safe operation of the reactor if not properly confined. This work aims to provide accurate estimates of the production rate and total inventory of ^{210}Po during operation in DEMO (source term). Furthermore, high level-of-theory ab initio calculations are performed to obtain insight on the chemical form in which ^{210}Po will occur in the cover gas of the Pb-Li or in the air in case of an accident (migration form). The

combination of these results can facilitate the development of intelligent strategies for the filtration of ^{210}Po from Pb-Li and can assist in performing realistic risk analyses.

In contrast to the Pb-Bi coolant used in MYRRHA, a Pb-Li breeding blanket does not use bismuth as functional material. Therefore, if the ^{210}Po inventories are calculated to be too high, it would be beneficial to focus on the extraction of the intermediate ^{209}Bi in the problematic reaction chain (impeding ^{210}Po production), rather than trying to extract ^{210}Po after its formation. Note that, for obvious reasons, this strategy cannot be applied for LBE cooled fast fission reactors as MYRRHA. However, if necessary, it could be applied for future fast fission reactors using pure lead as coolant.

1.4 Goal and outline

The work aims to shed light on the hazard associated with undesired radiotoxic ^{210}Po generation in lead (alloy) cooled fast fission reactors as well as in future fusion reactors using eutectic Pb-Li to achieve tritium self-sufficiency. For each of both reactor types, a prototype reactor was selected to perform focused calculations: the lead-bismuth eutectic cooled pool-type fast fission reactor MYRRHA (currently at the start of its implementation/construction phase) and the European DEMOnstration Power Plant fusion reactor EU-DEMO (currently at the end of its pre-conceptual design phase).

The estimated ^{210}Po inventory in MYRRHA after one irradiation cycle of 90 days can be found in the literature [Fio18] and amounts to 350 g. Similar calculations were not yet performed for the current design of the DEMO fusion reactor. Therefore, one of the goals of this work is to predict the ^{210}Po inventory in a DEMO fusion reactor using an HCLL or WCLL breeding blanket. These results are obtained by combining Monte-Carlo neutron transport calculations in the MCNP code and inventory calculations in the FISPACT-II code. MCNP is the mainstream code for neutron transport calculations and its validity has been extensively proven by comparison of calculations with experiments or other transport codes. The MCNP DEMO models used are provided by EUROfusion and have been used in previous calculations. The obtained neutron flux spectra and tritium breeding ratios were in agreement with those reported in literature, which suggests that the code was correctly used. The methodology and obtained results are

discussed in **chapters 2 and 3**, respectively.

Once the ^{210}Po inventories expected to be present in the MYRRHA and DEMO reactor have been estimated, this information can be used in a risk analysis of possible accident scenarios, as well as in the design of ^{210}Po removal systems. However, to do so, complementary information is required on the chemical behavior of ^{210}Po. Due to the high radiotoxicity of ^{210}Po, few experiments have been performed and the data available in literature is very limited. A second goal of this work is therefore to provide some essential lacking chemical data on small ^{210}Po -containing molecules in the gas phase (as these can escape from the reactor most easily and pose a large threat in case of inhalation), using high level-of-theory ab initio calculations and thus avoiding risky and cumbersome experiments.

The used level-of-theory, which had to be capable of properly accounting for the large spin-orbit effects associated with heavy elements, was verified and validated by performing a literature review of the results obtained for heavy molecules using this method and by performing extensive test calculations on PbO, Pb_2 and Po_2, as well as on all chemical analogues of the studied Po-containing molecules. By combining the obtained T-dependent stability of the 9 studied Po-containing molecules (PoH, LiPo, PoO, PbPo ,BiPo, Po_2, PoH_2, PoO_2 and H_2PoO_2) with the calculated ^{210}Po inventories, it is possible to make statements on the molecular composition of a gas in contact with the Po-containing eutectic (LBE or Pb-Li). Also it allows to determine the appearance of Po in an inert or pure gas containing H_2 or O_2 gas, as well as under typical atmospheric conditions. The data obtained can also prove useful for performing realistic risk analyses and in the development of efficient ^{210}Po extraction systems. The ab initio methodology, the obtained results and their application to determine the relative occurrence of the different Po species in a gas mixture are discussed in **chapters 4 and 5** respectively.

Finally, **chapter 6** summarizes the major conclusions from this work and highlights some ideas for future work.

Part I

^{210}Po production in the European DEMO fusion reactor

2

Methods – ^{210}Po production in DEMO

The problematic reaction chain resulting in the undesired production of ^{210}Po in a fusion reactor using Pb-Li as breeder/multiplication material is given by:

$$\mathbf{^{208}Pb} \xrightarrow[\sigma_c]{n,\gamma} \mathbf{^{209}Pb} \xrightarrow[t_{1/2}]{\beta^-} \mathbf{^{209}Bi} \xrightarrow[\sigma_c]{n,\gamma} \mathbf{^{210g}Bi} \xrightarrow[t_{1/2}]{\beta^-} \mathbf{^{210}Po}. \tag{2.1}$$

To calculate the amount of ^{210}Po being generated at DEMO, one needs:

1.) **The location and amount of ^{208}Pb**: a geometric model of the European DEMO reactor defining the shape and material composition of all components.

2.) **The neutron flux spectrum at the ^{208}Pb-containing regions**: a probabilistic neutron transport code is used to mimic neutron tracks throughout the geometrical model to obtain the 3-dimensional energy-dependent neutron flux in the regions of interest.

3.) **A Nuclear data library**: the energy-dependent neutron capture cross-section σ_c of ^{208}Pb (resulting in ^{209}Pb) and ^{209}Bi (resulting in ^{210g}Bi), as well as the half-life of the unstable products.

4.) **The recirculation of the generated ^{209}Bi**: the neutron capture rate by ^{209}Bi depends on whether these generated isotopes will gradually accumulate in the high neutron flux regions or rather will be continuously redistributed due to the Pb-Li circulation.

The next sections discuss how or where the required input data are acquired.

2.1 Neutron transport calculations

2.1.1 Monte-Carlo N-Particle (MCNP) code

To calculate the 3-dimensional energy-dependent neutron flux in the different components of the DEMO fusion reactor, neutron transport calculations are performed using the MCNP (Monte Carlo N-Particle) transport code [Wer17], which is currently the reference code for neutron transport calculations. It uses the Monte Carlo principle to probabilistically track the neutrons on a microscopic level from birth to death throughout a 3D geometry in which the material composition is defined. Along this track, all possible physical interactions between the neutron and the material are modeled based on their energy-dependent probability of occurrence (quantified by the corresponding cross section). Events of interest can be tallied (counted). Figure 2.1 illustrate the interaction between the 3D geometry, the relevant physics and the specified tallies.

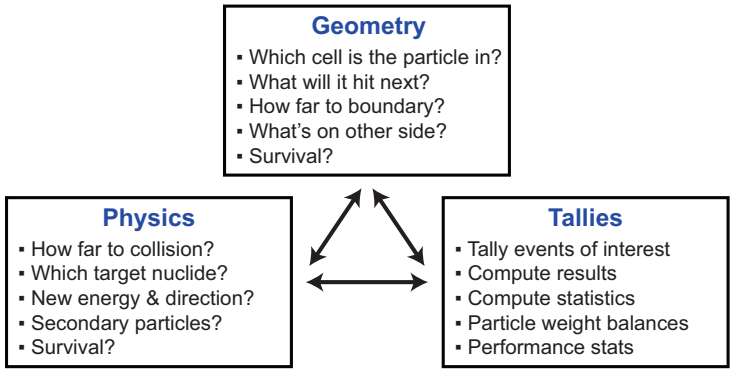

Figure 2.1: A schematic representation of the interaction occurring between the 3D geometry, the physics and the recorded tallies in an MCNP particle transport calculation.

The 3D geometry is divided in cells having a specific material composition and density. The code always monitors the cell in which the particle is moving as well as the distance to all surrounding cells. When a particle enters a cell of a defined zero importance (i.e. not of interest), it is killed and no longer tracked. This is done to avoid wasting computing time to non-relevant particle paths. While the particle is moving through a given

cell, all possible interactions are given a realistic probability based on the current energy of the particle, the interaction cross section corresponding to its energy, the material composition and the density of the cell.

Based on the Monte Carlo principle, these probabilities are then used as weight in the random selection of the next event. A similar principle is used in the selection of possible secondary particles and for the energy and direction of these particles (note that the secondary particles are banked i.e. put on hold until the primary particle has died).

The occurrence rate of events of interest can be determined as well as the corresponding statistical error. Improved statistical performance can be achieved by applying so-called variance reduction techniques. This boils down to artificially forcing an event or particles of interest to occur more within the simulation. One of these techniques called *energy splitting* duplicates a neutron every time it falls below a certain energy threshold. Doing so, the statistics for the low-energy side of the neutron spectrum are improved by artificially increasing the neutron population at these lower energies. Note that the weight (importance) of a neutron is reduced accordingly upon splitting in order to preserve the initial neutron weight and to make sure that only the statistics change and not the actual physical result. Section 3.1.1 discusses how this technique was applied in the performed calculations.

By tracking a large sample fusion neutron tracks (histories), the overall 3-dimensional energy-dependent neutron distribution can be determined with an accuracy depending on the number of histories, the applied variance reduction techniques and the desired spatial and energy resolution. Besides the flux, MCNP also allows to determine reaction rates e.g. the production rate of ^{209}Pb resulting from neutron captures by ^{208}Pb. The neutron flux spectrum obtained for a DEMO fusion reactor in its original material composition can be used for the whole lifetime of the reactor, as the Li burn-up and inventory build-up in DEMO is quite limited, making the neutron flux spectrum approximately constant over time.

2.1.2 MCNP model of the European DEMO fusion reactor

Over the years, different generic models of the European DEMO reactor have been proposed by the Power Plant Physics and Technology (PPPT)

programme of the EUROfusion Consortium. These reference designs define the most important design parameters and contain the foreseen implementation of the major components of the reactor (vacuum vessel, magnetic field coils, divertor, etc.) as well as the residual space available for the breeding blanket. In this work, the DEMO baseline configuration 'DEMO1 2014' has been used, for which the most important characteristics are listed in Table 2.1 [Fed14]. In order to keep the computational cost reasonably low, neutron transport calculations are performed only in an 11.25° toroidal section of this model (making optimal use of the toroidal symmetry of the model) and using reflecting boundary conditions at the lateral sides of this wedge-shaped model. In the neutron transport calculations, a realistic fusion neutron source model has been used, based on the characteristics of the 'DEMO1 2014' baseline and a mathematical description of a typical tokamak fusion neutron source [Fis14, Fis12].

Number of TF coils	16
Major radius	9.0 m
Minor radius	2.25 m
Aspect ratio	3.6
Plasma elongation	1.56
Plasma triangularity	0.33
Fusion power	1572 MW
Average neutron wall loading	1.07 MW/m^2
Net electric power	500 MW
Fusion neutron source intensity	$5.581 \cdot 10^{20}$ n/s

Table 2.1: Characteristics of the 'DEMO1 2014' baseline [Fed14].

Four breeding blanket concepts are currently being developed in the EU and are considered for implementation in the European DEMO [Cis18]: Helium Cooled Pebble Bed (HCPB), Helium Cooled Lithium Lead (HCLL), Water Cooled Lithium Lead (WCLL) and Dual Coolant Lithium Lead (DCLL) (see section 1.3.5.1). As the name suggest, the latter three use liquid Pb-Li as breeder/multiplier combination. In this work, only calculations on the HCLL and WCLL blanket designs are performed. For both concepts, two implementations in the generic model were considered:

(i) a homogeneous implementation in which the blanket models are filled by a concept-specific homogeneous material mixture [Ead17, Gil15], and
(ii) a heterogeneous implementation of the concept-specific blanket module including e.g. cooling pipes and stiffening plates [Vil15, Pal15].

The idea behind this approach is to examine whether a homogeneous model of the design yields results comparable to the ones obtained for a detailed heterogeneous model. If this is the case, there is no need to create a heterogeneous model for all future intermediate blanket designs (which can be time-intensive), but instead the material mixture in the homogeneous model can be adapted accordingly to acquire a good (first) estimation of the ^{210}Po inventory.

In MCNP, the entire space has to be divided into cells which are defined by one or more boundary surfaces and have a specified material composition and density. These surfaces can be planes, spheres, cylinders, cones, ellipsoids, hyperboloids, paraboloids, circular tori or elliptical tori. By properly defining the DEMO model of interest, realistic neutron transport calculations can be performed throughout the full model and the neutron flux in the components where Pb-Li is present can be determined. Figure 2.2 shows a poloidal section of the MCNP-compatible models used in the calculations. The most important regions are explicitly indicated. The material compositions used for these regions are specified in Table 2.2. In

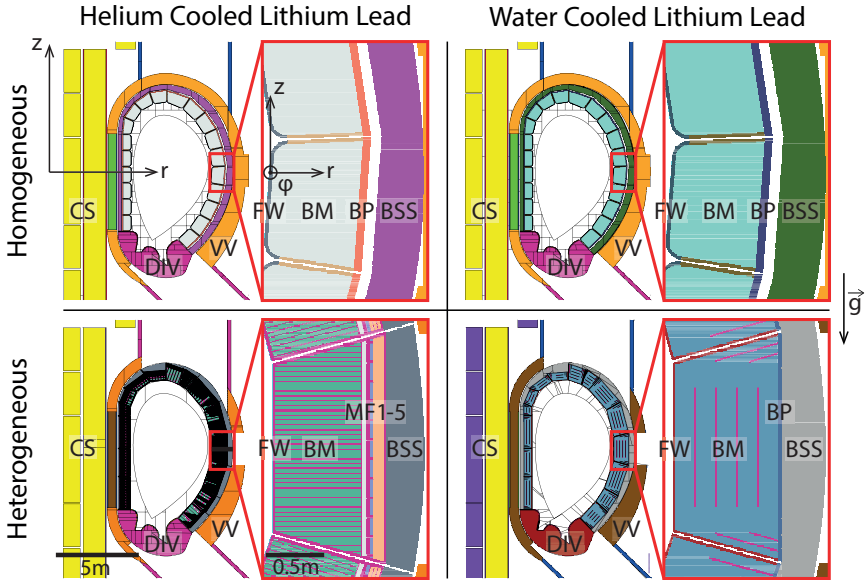

Figure 2.2: A poloidal section of the 4 DEMO models used in the neutron transport calculations. For each model, the equatorial (at the vertical mid-plane) outboard module is also shown in detail. The most important regions are explicitly indicated. The used abbreviations are explained in the text on page 51.

Region	Material	homogeneous		heterogeneous	
		HCLL	WCLL	HCLL	WCLL
FW coating	W	100%	100%	100%	none
FW	EUROFER-97	62.5%	67.1%	100.0%	73.0%
	H_2O	-	7.9%	-	9.0%
	He	26.8%	-	-	-
Caps	EUROFER-97	90.0%	95.2%	100.0%	73.0%
	H_2O	-	4.8%	-	9.0%
	He	10.0%	-	-	-
Breeder	Pb-15.8Li	78.0%	80.1%	100.0%	94.0%
mix in BM	EUROFER-97	13.0%	18.0%	-	3.9%
	H_2O	-	1.9%	-	2.1%
	He	8.0%	-	-	-
CP	EUROFER-97			100.0%	
SP	EUROFER-97			100.0%	100.0%
BP/MF1	Pb-15.8Li	8.0%	0.0%	90.0%	1.0%
	EUROFER-97	24.0%	100.0%	6.0%	98.0%
	H_2O	-	-	-	1.0%
	He	68.0%	-	-	-
MF2	Pb-15.8Li			4.0%	
	EUROFER-97			3.0%	
MF3-5	Pb-15.8Li			1.0%	
	EUROFER-97			1.0%	
BSS	Pb-15.8Li	11.0%	9.2%	7.0%	9.0%
	EUROFER-97	29.0%	74.4%	35.0%	26.0%
	H_2O	-	-	-	8.0%
	He	60.0%	-	-	-
	CuCrZr	4.8%	-	-	-
VV (IB,out)	SS316	-	-	100.0%	100.0%
	SS316-LN(IG)	100.0%	100.0%	-	-
VV (IB,in)	SS316	-	-	80.0%	80.0%
	SS316-LN(IG)	80.0%	80.0%	-	-
	H_2O	20.0%	20.0%	20.0%	20.0%
VV(OB)	SS316	-	-	83.6%	80.0%
	SS316-LN(IG)	83.6%	83.6%	-	-
	H_2O	-	-	16.4%	20.0%
DIV L1	W	100.0%	100.0%	100.0%	100.0%
DIV L2	EUROFER-97	-	-	30.0%	-
	W	55.0%	55.0%	12.0%	-
	CuCrZr	13.0%	13.0%	-	100.0%
	Cu	10.0%	10.0%	1.0%	-
	H_2O	22.0%	22.0%	-	-
DIV L3	EUROFER-97	100.0%	100.0%	100.0%	-
	SS-316LN(IG)	-	-	-	80.0%
	H_2O	-	-	-	20.0%

Table 2.2: (Caption on the next page.)

Table 2.2: (Previous page.) The material composition of the most important regions in the considered MCNP DEMO models. These regions are explicitly indicated in Figure 2.2. The given values represent the volume fraction accounted for by a specific material. The remaining volume fraction not accounted for, corresponds to void (vacuum). For all models, the lithitum within the Pb-Li eutectic is enriched to a 90% ^{6}Li content to enhance the breeding performance. The CuCrZr alloy has a composition of 99.3 % Cu, 0.6 % Cr and 0.1 % Zr. The used abbreviations are explained in the text on page 51.

this figure and table, the following abbreviations have been used: FW = First Wall, CP = Cooling Plate, SP = Stiffening Plate, BP = Backplate, MF = manifold, BSS = Back Supporting Structure, VV = Vacuum Vessel, IB = inboard, OB= outboard, out = outside, in = inside, DIV = divertor, L = layer, SS = stainless steel, and IG = ITER Grade. In the heterogeneous HCLL model, the Pb-Li manifold (MF1) and He manifolds (MF2-4) have been explicitly implemented, while this is not the case for the other models. These 5 manifolds are each separated from each other by EUROFER-97 backplates. Note that both for the HCLL and WCLL breeding blanket concept, the lithium within the Pb-Li eutectic is enriched to a 90% ^{6}Li content to enhance the tritium breeding capability. The conversion of the CAD design to an MCNP-compatible geometry for the heterogeneous blanket modules was previously completed using the MCAM CAD converter tool (version 4.8.4.4.9) [Wu15].

A concise discussion on the detailed breeding blanket designs considered in the MCNP calculations is presented in sections 2.1.2.1 and 2.1.2.2.

2.1.2.1 MCNP model of the HCLL breeding blanket

Figure 2.3 shows the 2014 design of the HCLL breeding blanket. The layout is a multi-module segment design, meaning that the entire blanket surrounding the fusion plasma is divided (both horizontally as vertically) in similar parts called Breeding Modules (BM). Vertically, 7 or 8 of these BM are attached to a single stiff poloidal back plate, forming banana-shaped inboard or outboard segments respectively which can be removed through the upper ports by remote handling for maintenance or replacement.

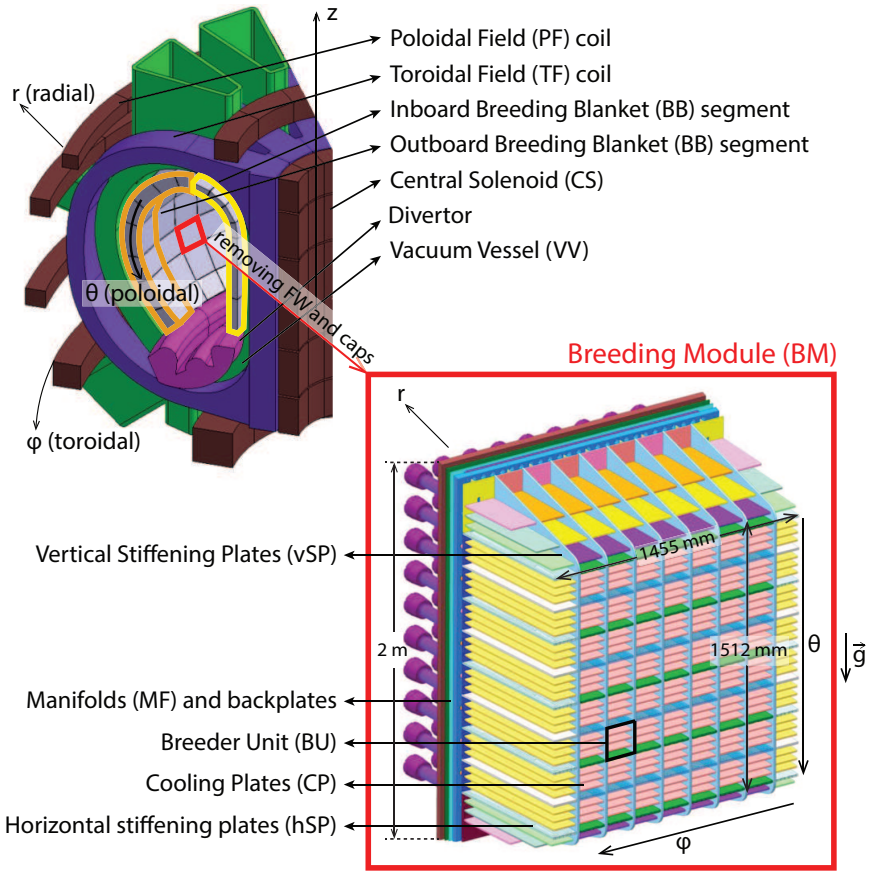

Figure 2.3: A 3D CAD model of the 2014 design of the equatorial (i.e. at the vertical center) outboard HCLL breeding module. Some components of this image were obtained from an internal EUROfusion report [Aie15].

The Breeding Modules are EUROFER steel boxes enclosed at the plasma-facing side by the so-called first wall, at the top and bottom by the upper and bottom walls, at the sides by Side Cover plates and at the back by a number of Back Plates and tie rods to be attached to the Back Supporting Structure (which contains the Pb-Li manifold). The breeding modules are reinforced by horizontal (radial-toroidal) and vertical (radial-poloidal) stiffening plates. All plates (except for the back plates) are actively cooled by high-pressure He (8 Mpa) flowing in narrow rectangular channels incorporated within these plates. The stiffening grid is required to withstand the high pressures occurring in case of a leak of high-pressure He inside the breeding module. This grid also defines an array of cells for the Breeding Units (BU). Each

BU contains three additional actively-cooled horizontal Cooling Plates (CP) attached to the back. After entering the BU, the Pb-Li flows around these horizontal CPs before it is collected at the back to be processed by the Pb-Li loop (see section 2.2.2). The helium operates at an inlet/outlet temperatures of 300°C and 500°C respectively, while the operational temperature for Pb-Li is set at 300°C. More information on the considered design can be found in references [Jab16, Aub16, Aie15].

2.1.2.2 MCNP model of the WCLL breeding blanket

Similar to the HCLL blanket design, the WCLL blanket design also has a multi-module segment layout. The major differences are found in the internal design of the breeding models. A CAD model of a WCLL breeding model is shown in Figure 2.4.

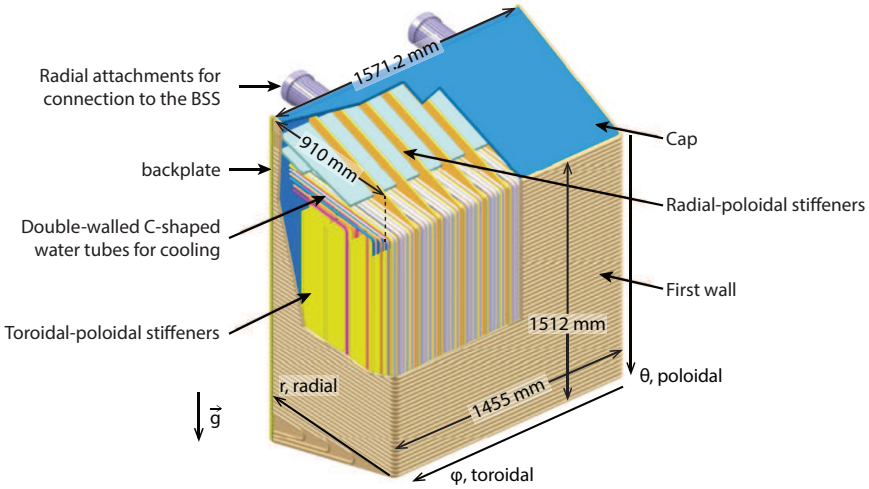

Figure 2.4: A 3D CAD model of the 2014 design of the equatorial (i.e. at the vertical center) outboard WCLL breeding module. This image was obtained from an internal EUROfusion report [DN14] and adapted appropriately.

In the WCLL design, toroidal-poloidal stiffening plates are used instead of the radial-toroidal ones found in the HCLL design. The generated heat is now extracted by pressurized water (15.5 MPa, 285°C – 315°C, i.e. typical PWR conditions) flowing through double-walled C-shaped tubes (to reduce probability of water/Pb-Li interaction) which are implemented inside the blanket module, as well as in the caps and first wall. The Pb-Li flows from the bottom to the top (at flow rates comparable to HCLL) and is fed and extracted through Pb-Li connectors installed at the bottom and the top of

the back plate. It should be noted that in the used heterogeneous WCLL MCNP model, the cooling pipes within the beeding zones are not separately implemented, but their presence is taken into account by using a material mixture of 94 vol% Pb-Li and 6 vol% cooling channels (which itself exists of 64.88 vol% steel, 35.12 vol% water) instead of pure Pb-Li in the breeding zones. More information on the considered design can be found in references [DN17, Fro17, DN14].

2.1.3 Nuclear data libraries for neutron transport

The probability of a nuclear interaction is given by the corresponding energy-dependent cross section, which is predicted using theoretical models, which are based on covariance modeling and complemented by experiments. Relying on different theoretical models, large distinctions sometimes exist between the same cross section found in different nuclear data libraries. Therefore, the choice of nuclear data library can have a significant impact on the obtained neutron flux spectrum. To allow for an unambiguous comparison of results, a common set of evaluated nuclear data for fission and fusion applications has been developed by the Nuclear Energy Agency (NEA) participating countries: the Joint Evaluated Fission and Fusion (JEFF) nuclear library [Nuc17]. The EUROfusion project demands that all neutron transport calculations on the European DEMO are performed using this library. In this work, the JEFF-3.2 version is used.

2.2 Inventory calculations

2.2.1 The FISPACT-II inventory code

As MCNP can not calculate the time-dependent material composition in the model, a dedicated inventory code is used. FISPACT-II is a Fortran code developed by the United Kingdom Atomic Energy Authority allowing to perform inventory calculations [Sub17]. The required input consists of:

(i) the initial density of the material,
(ii) the initial chemical composition, and
(iii) the time-dependent neutron flux spectrum in the material.

The program allows to determine the material composition at any requested time, as well as as the corresponding activities of the generated radionuclides.

In addition, the primary reaction paths responsible for the production of a given isotope can be obtained, as well as material damage (displacements per atom, dpa), gas production and the overall heat generation.

Solving the Bateman equation

Performing neutron activation (inventory) calculations in essence corresponds to solving the following set of stiff ordinary differential equations (Bateman equations) [Rut04, Bat10, Cet06]:

$$\frac{\mathrm{d}N_i}{\mathrm{d}t} = -N_i\left(\lambda_i + \sigma_i\phi\right) + \sum_{j\neq i} N_j\left(\lambda_{ij} + \sigma_{ij}\phi\right) \tag{2.2}$$

In this equation, N_i and N_j are the number of nuclides of type i and j, λ_i is the total decay constant of nuclide i, σ_i is the total cross-section for neutron-induced nuclide-transforming reactions on nuclide i, ϕ is the neutron flux, σ_{ij} is the cross-section for reactions on nuclide j producing nuclides i and λ_{ij} is the constant for decay of nuclide j in nuclide i.

The first term in the equation thus accounts for the reduction of nuclide i over time, while the other terms account for all possible production paths. One equation of this type is linked to each nuclide that could possibly occur within the system. They form a set of coupled equations which is numerically solved in FISPACT-II using the LSODES 2003 (Livermore Solver for Ordinary Differential Equations with general Sparse Jacobian matrices) algorithm. It should be noted that besides neutrons, FISPACT-II is also capable of considering photons, protons, deuterium and alpha particles.

Nuclear data use in FISPACT-II

Also, FISPACT-II makes use of nuclear data libraries. For this type of calculations EUROfusion has not imposed a standard nuclear data library to be used. Therefore, in this work, ten nuclear data libraries have been compared of which finally four are selected for further detailed calculations (see section 3.6). To speed up the calculations, FISPACT-II collapses each energy-dependent cross section to a single value (effective one-group cross section) by weighing it over the neutron flux spectrum in the region under consideration. This way, the reaction rate only depends on the total flux intensity. Given the relatively small burn-up of Li and the limitted activation of the material, the energy-dependence of the neutron flux is assumed to be constant over time (up to a factor connected to the operation power).

Therefore, the cross sections are collapsed only once, at the start of the calculation.

2.2.2 Circulation of the Pb-Li breeder

The liquid Pb-Li is not static within the breeding blanket but continuously circulates through a dedicated Pb-Li loop of which some parts are located close to and others far away from the fusion plasma. The loop is essentially composed of the breeding blanket modules (high neutron flux), the Pb-Li manifold (lower but non-negligible neutron flux) and a storage tank, (possibly) a heat exchanger, an expansion tank, a Tritium Extraction and Removal System (section 1.3.5.2), a purification system (continuously controlling the chemistry of the Pb-Li) and the (permanent magnetic) pumps (negligible neutron flux). Electric heaters will be used to ensure that the Pb-Li remains in the liquid state at all times in all components. In the HCLL blanket concept the Pb-Li is foreseen to complete a total of 11 recirculations per day, while in the WCLL about 10 recirculations per day are expected [Uti19b]. This has two important consequences on the ^{210}Po inventory:

(i) all activation products are continuously being redistributed over the whole Pb-Li circuit rather than remaining in the area where they were produced, and
(ii) not all Pb-Li is constantly being exposed to a high neutron flux, therefore regions of different neutron flux have to be distinguished.

The total amount of Pb-Li present in each model, both within and outside the actual breeding blanket is listed in Table 2.3.

Table 2.3: The Pb-Li volumes implemented inside and outside the breeding blanket (BB) for the different models.

$V_{Pb\text{-}Li}$ (m^3)	HCLL		WCLL	
	homo.	het.	homo.	het.
Inside BB	575	563	575	668
Outside BB	150	150	150	150
Total	725	713	725	818

2.2.3 Initial ^{209}Bi impurity level

Commercial eutectic Pb-Li available today typically contains between 10 – 33 appm ^{209}Bi impurities [Con14]. These impurities have an effect on the final ^{210}Po inventory as they provide a shortcut in the problematic reaction chain presented in Equation 2.1 on page 45. The neutrons can now be captured directly by these ^{209}Bi impurities, resulting in a higher overall ^{210}Po production. This effect has to be considered to decide whether it is necessary to use a higher quality "nuclear grade" Pb-Li or even to install an on-site Pb-Li purification system to continuously extracting ^{209}Bi (interrupting the problematic reaction chain) and/or ^{210}Po.

2.2.4 Irradiation schedule

DEMO is foreseen to have two breeding blanket phases. In the first phase, a so-called starter blanket will be installed limited to a maximum displacement damage to the structural material of 20 dpa (displacements per atom). For the second phase, a new blanket generation allowing for 50 dpa structural material damage is expected, based on the progress achieved by material irradiation studies [Cis18].

In this work, the focus is on the starter blanket as this is the one currently under design. This blanket will be used during the first 5.2 years of DEMO operation and the approximate irradiation schedule presented in Figure 2.5 is assumed for the inventory calculations. In this schedule, DEMO is operated at 30% of its full power capacity for 5.173 years, followed by 48 4-hour pulses at full power with 1-hour intervals at zero power. The total lifetime of DEMO is set at 6 full-power years (FPY). A conservative irradiation schedule would therefore be a continuous operation for 6 years at full power, which can also be considered as more representative for a first generation commercial fusion reactor. Both of the discussed irradiation schedules have been simulated and compared.

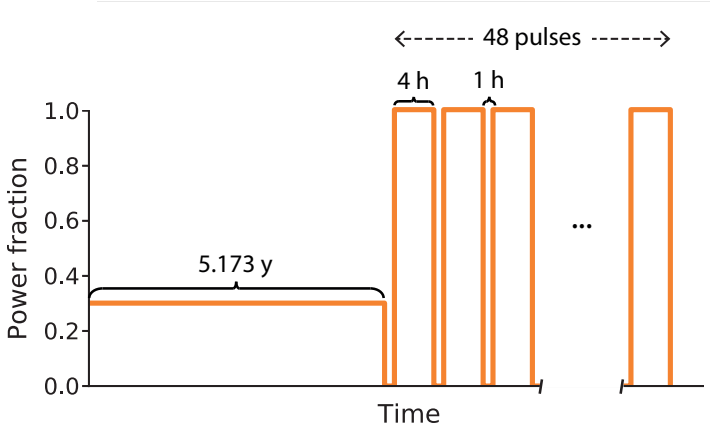

Figure 2.5: Approximate irradiation schedule used to model the DEMO first blanket phase in the activation calculations.

3

Results – ^{210}Po production in DEMO

The most significant results have been condensed in a paper entitled *'^{210}Po production in the European DEMO fusion reactor'* published in the peer reviewed international scientific journal *Nuclear Fusion* jointly issued by IAEA and IOP Publishing [Mer19b]. The author of this Ph.D. dissertation has performed all calculations required to obtain the results presented in this paperand has fully written the text, which is reprinted with permission of IAEA in Appendix A on pages 143–159.

This chapter not only discusses the results published in this paper in considerably more detail, but also presents several results that have not been previously published.

3.1 Neutron flux spectra

The MCNP calculations are run using the following settings:

- A total of 10^7 fusion source neutrons (histories) are simulated for each model.
- The generation of both secondary neutrons and photons is considered and tracked.
- Neutrons with energies below 10^{-11} MeV are automatically killed because of their insignificance for the results (to save computing time).

- Neutrons with an energy above 10^{-10} MeV are never explicitly captured, but instead implicity reduced in weight/significance (intially being unity).
- Whenever a neutron's weight WGT drops below 0.02, it survives with a probabilty of only WGT/0.1 and if so, its weight is increased back to 0.1.
- 616 equidistant logarithmic energy bins between 10^{-11} and 20 MeV are used to tally the energy-dependent neutron flux.

3.1.1 Variance reduction: Energy Splitting

The orange plot in Figure 3.1 shows the energy-dependent neutron flux in the blanket filler of a single equatorial outboard blanket module for the homogeneous HCLL blanket, obtained using the settings above and no (other) variance reduction techniques. The upper plot represents the neutron flux per unit lethargy i.e. the neutron flux measured for an energy bin divided by $\ln(E_{i+1}/E_i)$ with E_i and E_{i+1} the boundaries of considered energy bin (with $\ln(E_{i+1}/E_i)$=0.04605 for the used equidistant logarithmic energy bins). It is found that a satisfactory precision (relative statistical error $<5\%$) is achieved for the higher neutron energies ($>10^{-4}$ MeV), while the result becomes too unreliable for energies below this value (see orange plot in lower graph in Figure 3.1). This is because of the smaller amount of neutrons being tallied in the finer bins used at low energy (as the bin boundaries are logarithmically equidistant).
4

In order to reduce the relative error at these lower energies, a variance reduction technique called *'energy splitting'* which is available in MCNP through keyword *ESPLT* is used. This technique artificially increases the neutron population at lower energies by splitting every neutron falling below a certain energy threshold in multiple neutrons with a lower weight. This increases the total number of low-energy neuron being tracked (but leaves their total weight unchanged), thus improving the statistics at these energies. In practice, the energy splitting technique is used to duplicate every neutron falling below the following energies expressed in MeV: 10^{-2}, $3 \cdot 10^{-3}$, 10^{-3}, $3 \cdot 10^{-4}$, 10^{-4}, $3 \cdot 10^{-5}$, 10^{-5}, $3 \cdot 10^{-6}$, 10^{-6}, $3 \cdot 10^{-7}$, 10^{-7} and $3 \cdot 10^{-8}$.

3.1.2 Spectra in the different regions

A distinction can be made between Pb-Li containing regions with different neutrons flux intensities and spectra. Figure 3.2 shows the neutron flux

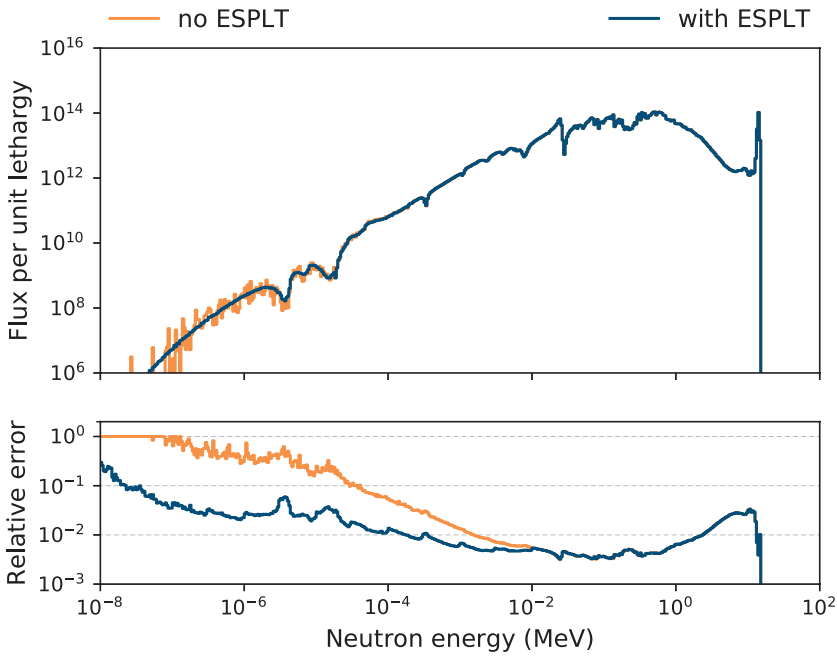

Figure 3.1: The average neutron flux averaged over all blanket filler material for the HCLL homogeneous model, obtained using 10^7 histories (source neutrons) both with and without the use of the ESPLT variance reduction technique.

spectra in all Pb-Li containing regions for each considered model (for DEMO at full power). For every subplot, the regions in the legend are ordered according to their increasing distance from the fusion plasma. The Pb-Li containing regions are: the Breeding Module (BM), the Backplate (BP) or Pb-Li/He manifolds (MF1-5) for the heterogeneous HCLL model, the Back Supporting Structure (BSS) containing the Pb-Li manifold and the region outside of the breeding blanket (out) with negligible neutron flux. These different regions are indicated in Figures 2.2–2.4. It should be noted that the presented BM flux corresponds to respectively the flux in the blanket filler material mixture for the homogeneous HCLL and WCLL, the flux in the pure Pb-Li within the BM for the heterogeneous HCLL and the flux in the 'Pb-Li + 6 vol% cooling channels'-mix for the heterogeneous WCLL (the material composition of the important regions is presented in Table 2.2 on p. 50, which should be considered in combination with Figure 2.2). The percentages denoted in the legend corresponds to the volume fraction of the total Pb-Li contained within that region for the considered model.

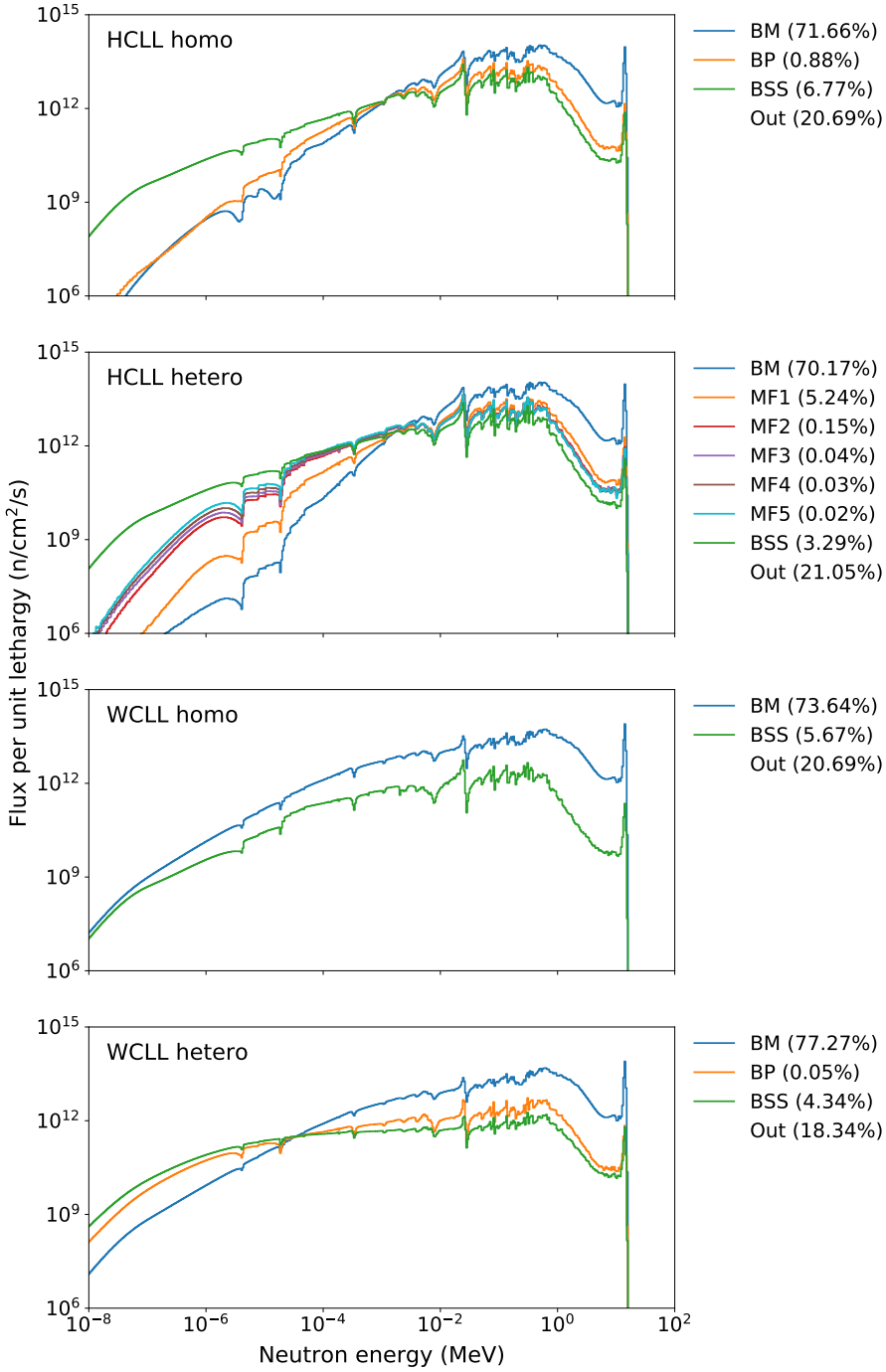

Figure 3.2: The calculated energy dependent neutron flux in the different Pb-Li containing regions for each of the considered models. The percentages denote the volumetric fraction of Pb-Li within that specific component. The abbreviations are explained in sections 2.1.2 and 3.1.2.

As expected, the high energy part of the spectrum drops when moving further away from the fusion plasma, due to absorption and elastic down-scattering. Also due to this down-scattering and the generation of secondary low-energy neutrons, the low-energy portion of the spectrum is often higher for regions further away from the fusion plasma (however, when traveling even further from the plasma these neutrons will be efficiently captured and the neutron flux will drop). It can be seen that for the WCLL blanket models, a softer (less-energetic) spectrum is found due to the moderation of the neutrons by water molecules.

3.2 ^{209}Pb production

MCNP allows to calculate the occurrence rate of a given interaction. By multiplying the obtained energy-dependent neutron fluxes $\phi_{\mathrm{n}}(E)$, the energy-dependent radiative neutron capture cross section of ^{208}Pb denoted as $\sigma^{\mathrm{n},\gamma}_{^{208}\mathrm{Pb}}(E)$ (Figure 3.3) and the atomic density of ^{208}Pb in a given region $N_{^{208}\mathrm{Pb}}$ and integrating this product over the whole energy range, the ^{209}Pb production rate (through neutron capture by ^{208}Pb) in that specific region can be obtained:

$$\int_E \phi_{\mathrm{n}}(E) \times \sigma^{\mathrm{n},\gamma}_{^{208}\mathrm{Pb}}(E) \times N_{^{208}\mathrm{Pb}} \mathrm{d}E = {}^{209}\mathrm{Pb\ production\ rate}. \qquad (3.1)$$

Since the produced ^{209}Pb is quickly converted in ^{209}Bi through β^- decay ($t_{1/2}$ = 3.3 h), the obtained value is also a good appproximation for the ^{209}Bi production rate. This represents the first step of the ^{210}Po production reaction chain (Eq. 2.1 on page 45). The total ^{209}Pb production rate (atoms/s) in the four considered models, as well as the fractional contribution of each region, is given in Table 3.1.

It can be seen that a higher ^{209}Pb production is obtained for the HCLL blanket concept. This difference was found to originate from the higher neutron flux found in the 0.1 - 1 MeV region for the HCLL blanket (Figure 3.2). As shown in Figure 3.3, this energy region is characterized by strong resonance absorption peaks, making a neutron capture highly probable. Due to the higher neutron flux for the HCLL blanket at these energies, twice as much neutrons are capture by ^{209}Pb in this resonance region as compared to the

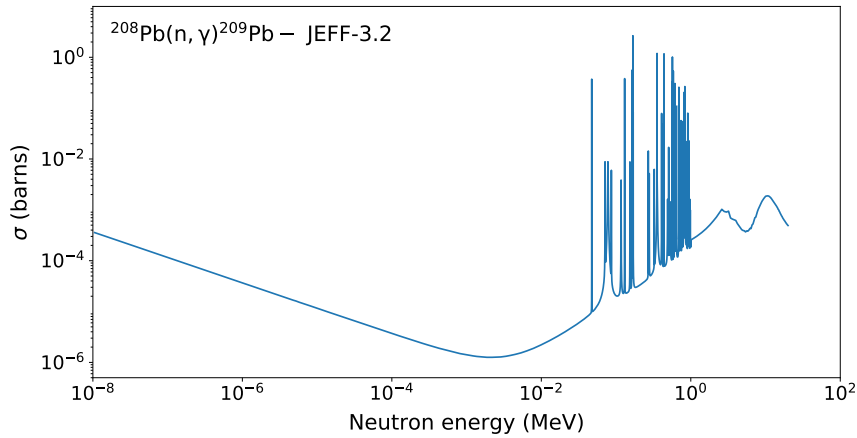

Figure 3.3: The energy-dependent radiative neutron capture cross section of ^{208}Pb as obtained from the Joint Evaluated Fission and Fusion Nuclear Data Library (JEFF 3.2).

Table 3.1: Calculated total ^{209}Pb production (atoms/s) in the 'DEMO1 2014' baseline at full power for the four considered breeding blanket models. The fractional contribution of each region is also presented. The abbreviations are explained in section 3.1.2.

^{209}Pb	**HCLL homo.**	**HCLL het.**	**WCLL homo.**	**WCLL het.**
Total	$1.29 \cdot 10^{18}$/s	$1.29 \cdot 10^{18}$/s	$7.34 \cdot 10^{17}$/s	$8.22 \cdot 10^{17}$/s
BM	98.50 %	97.58 %	99.55 %	99.79 %
BSS	1.21 %	0.53 %	0.45 %	0.21 %
BP	0.29 %			0.01 %
MF1		1.80 %		
MF2		0.05 %		
MF3		0.01 %		
MF4		0.01 %		
MF5		0.01 %		

WCLL blanket. In fact, for the HCLL blanket concept about 36.5 % of the all neutron captures by ^{209}Pb occur within this 0.1 - 1 MeV energy region, while for the WCLL concept this is 25.5 %. Another major contribution to the ^{209}Pb production rate stems directly from the high energy (14.1 MeV) fusion neutrons, accounting for respectively 43 % and 52.7 % of the overall value for HCLL and WCLL. All of the remaining neutron captures by ^{209}Pb occur in between these energy regions (1 MeV - 14.1 MeV). No significant amount of neutron captures is observed below 0.1 MeV. The higher ^{209}Pb production

rate for the HCLL blanket concept will again be highlighted in the results of the FISPACT-II inventory calculations. Table 3.1 also shows that almost all neutron captures by ^{209}Pb occur in the breeding module (BM), which is as expected given the considerably higher neutron flux (as it is closer to the fusion plasma than the other considered region).

As MCNP is not capable of simulating the resulting ^{209}Bi build-up in the Pb-Li during the neutron transport calculations, a dedicated neutron activation code such as FISPACT-II has to be used to obtain the ^{210}Po inventory.

3.3 Tritium breeding ratio

Using MCNP, it is also possible to determine the tritium breeding ratio (TBR) i.e. the amount of tritium nuclei produced with respect to the number that are consumed. In the following estimation of the TBR, it is initially assumed that only D-T fusion reactions occur in the DEMO 50% D/50% T fusion plasma, each producing exactly one high energy neutron (14.1 MeV). The average number of tritium atoms generated during the interaction of such a fusion neutron with the breeding blanket (which corresponds to the TBR under the given assumption) is then estimated using MCNP, similarly as the ^{209}Pb production rate in the previous section. Table 3.2 shows the overall TBR obtained for each of the considered models. The TBR of the homogeneous and heterogeneous model show an excellent agreement. It is found that the expected TBR for the WCLL models is considerably higher than for the HCLL models.
In fact the obtained TBR for these HCLL models does not satisfy the intended objective of achieving a TBR of at least 1.1 without taking into account the ports, diagnostics and some other systems. The TBR obtained for the HCLL 2014 model is in agreement with the value found in literature i.e. 1.08 [Jab17], which gives confidence that the calculated neutron flux spectra are reliable.

Table 3.2: The tritium breeding ratio (TBR) achieved by each of the considered models.

TBR	HCLL	WCLL
Homogeneous	1.075	1.146
Heterogeneous	1.075	1.150

In the meantime, the HCLL design has been drastically updated and achieves a TBR as high as 1.21 for the 'DEMO 2015' baseline [Jab17]. The TBR

of the new WCLL designs for this baseline, on the other hand, has remained around 1.14 [Mor18, Noc19] and its characteristics seem to leave less room for improvement [Per16]. In the new 'DEMO 2017' baseline, the radial space foreseen for the breeding blanket has been severely reduced (at the outboard side from 130 cm to 100 cm). This was done to optimize the radial build of the entire reactor [Bac18], while still providing sufficient neutron shielding. An optimized HCLL and WCLL design for the new baseline still has to be developed, but the reduction in radial extent is expected to have a somewhat larger negative impact on the HCLL concept as compared to the WCLL concept [Per16]. In conclusion, recent results suggest that the HCLL concept offers a better tritium breeding performance than WCLL, however the WCLL concept was found to have a superior shielding capability [Fed19].

It should be noted that besides D-T fusion reactions, also D-D fusion reactions will occur, but at a considerably lower rate. At 150 million kelvin, the reactivity of the D-D fusion reaction is about 100 times smaller than for the D-T fusion reaction (see Figure 1.9 on p. 27). The reaction rate is directly proportional to this reactivity and to the density of the reactants. As in a D-D fusion reaction, deuterium interacts with nuclei of its own kind, the associated reaction rate is further reduced by a factor 2. Therefore, about 200 times less D-D fusion reactions will occur as compared to D-T fusion reactions. Half of these D-D fusion reactions result in T and a proton, while the other half results in ^{3}He and a 2.45 MeV neutron (see Eq. 1.3b on p. 26). For the first reaction path (RP 1), the generated T either (i) fuses with D, generating a 14.1 MeV neutron which behaves as a regular fusion neutron and thus produces 1×TBR tritium atoms, or (ii) does not burn up and is collected at the plasma exhaust, thus resulting in exactly one tritium atom. A burn-up fraction of at least 5 % is envisioned, but preferably it would be much higher (>20 %) as this could considerably reduce the required TBR as well as the tritium refueling rate and associated T inventory [Saw06, EG09]. For the second reaction path (RP 2), the fusion neutron's energy is too low to trigger a neutron multiplication interaction in Pb (see Table 1.2 on p. 30), it can however still be absorbed by ^{6}Li, thus producing at most 1 tritium atom. From the discussion above, a maximal contribution of D-D fusion reactions to the overall TBR can be estimated:

$$\max\left(\Delta TBR\right) = \underbrace{\frac{1}{200}}_{\text{rate}} \left(\underbrace{0.5 \cdot TBR}_{\text{RP 1}} + \underbrace{0.5 \cdot 1}_{\text{RP 2}} \right) = 0.0025\left(1 + TBR\right) \tag{3.2}$$

For HCLL and WCLL, we thus get a maximum contribution of respectively 0.0052 and 0.0054 (both below 0.5 % of the overall value). These contributions are clearly minor and much smaller than the expected TBR reduction

due to the implementation of the heating systems, diagnostics and ports. Nevertheless, it should be noted that these usually left out contributions could be of great importance as a recent study proposes to use a pure deuterium start-up plasma to generate tritium and gradually transition towards a 50% D/50% T plasma [Zhe16]. Their results suggest that a D-D campaign with continuous feedback of the produced T into the plasma might enable a D-T fusion reactor start-up in a short enough time (order of months) and without the need for a tritium start-up inventory (which would be very beneficial given the scarcity and cost of T).

3.4 Continuous mixing of activation products

The neutron flux spectra obtained with MCNP in the different Pb-Li containing regions are now used in FISPACT-II to calculate the ^{210}Po inventory build-up. In a preliminary calculation, only internal circulation of Pb-Li is allowed, meaning that activation products generated within a given region (breeding module, backplate, back supporting structure) always stay within that same region. This results in an accumulation of activation products in the breeding zones where the neutron flux is higher than in the other regions. The increased ^{209}Bi concentration in the breeding zones promotes the ^{210}Po production, resulting in a higher overall ^{210}Po inventory.

In reality however, the Pb-Li circulates through the entire Pb-Li loop at a rate specific to the breeding blanket concept. For the HCLL concept one cycle takes 2.2 hours (11 recirculations/day), while for the WCLL concept one cycle takes 2.4 hours (10 recirculations/day) [Uti19b]. For a 6 FPY irradiation schedule, this amounts to respectively 24107 and 21915 recirculations for the HCLL and WCLL blanket. It is now assumed that all activation products are homogeneously redistributed over the whole Pb-Li after each recirculation and this will be called a redistribution step. As simulating the actual amount of redistribution steps showed to be quite demanding, fewer redistribution steps (and so longer redistribution intervals) are initially assumed. The number of redistribution steps is then gradually increased towards the target value to study the evolution of the result. The final ^{210}Po inventory within the whole Pb-Li as a function of the number of redistribution steps is shown in Figure 3.4 (for both the EAF-2010 [Sub10] and TENDL-2014 nuclear data library [Kon14]). It can be seen that the ^{210}Po inventory has converged to a stable value long before the actual number of redistribution steps is reached. The crosses in Figure 3.4 are obtained assuming instantaneous

mixing (using a single volume-averaged flux). It can be seen that the obtained results coincides with the converged result. Therefore, instantaneous mixing is justified, meaning that the flux spectra can be volume-averaged over the different regions to obtain a single effective neutron flux spectrum for the whole Pb-Li. This allows to consider more complex irradiation schedules using limited computational resources. Note that the final ^{210}Po inventory obtained using the EAF-2010 and TENDL-2014 nuclear data library show a rather large discrepancy (18 % difference). This considerable impact of the choice of the nuclear data library on the results is discussed in detail in section 3.6.

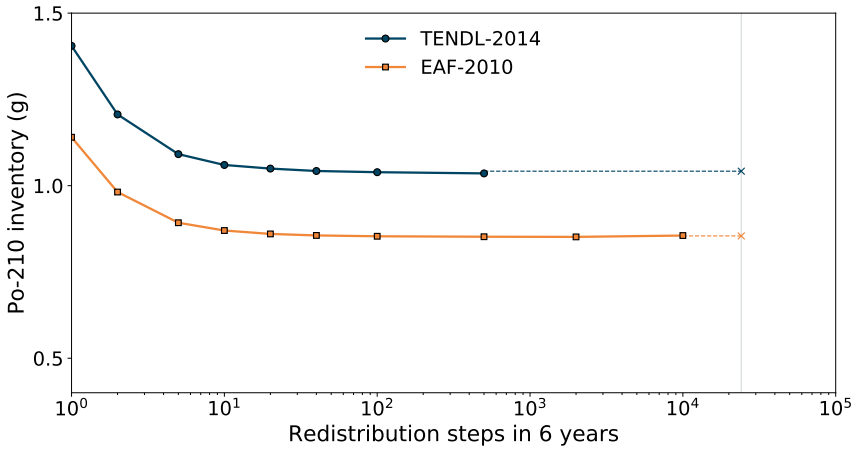

Figure 3.4: Calculated total ^{210}Po inventory in the whole Pb-Li versus the number of redistribution steps imposed during a 6 FPY irradiation schedule for the homogeneous HCLL model for both the EAF-2010 and TENDL-2014 libraries. The gray vertical line marks the anticipated number of Pb-Li cycles in 6 years. The crosses and dashed lines show the obtained value assuming instantaneous mixing.

3.5 Effective neutron flux

Figure 3.5 shows the obtained effective volume-averaged neutron flux spectra for the whole Pb-Li in each of the considered models. A good correspondence is found between the flux spectra obtained for the homogeneous and heterogeneous model of the same breeding blanket concept. The softer (less-energetic) character of the neutron flux spectrum in the WCLL blanket (due to the moderation by the water molecules) again

emerges, however this time somewhat less-pronounced, as the flux spectra in the BM are averaged together with other regions where a softer spectrum exists for both blanket concepts (due to down-scattering by the coolant, structural material or Pb-Li). The total neutron flux intensity was found to be almost a factor two higher for the HCLL blanket as compared to the WCLL blanket (Table 3.3). This is probably the result of the considerable capture rate by hydrogen (found in water molecules for WCLL) of down-scattered low-energy neutrons. H is known to have a relatively large neutron capture cross section and this is actually also the primary reason why critical natural-uranium fission reactors cannot be constructed using light water with coolant/moderator (something which is feasible with heavy water, given the considerably lower neutron absorption cross section of deuterium).

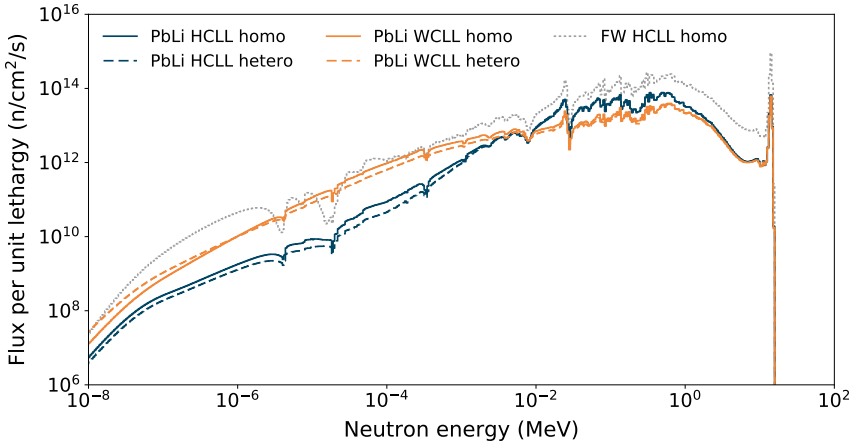

Figure 3.5: Calculated energy dependent volume-averaged neutron flux over the whole Pb-Li for each of the considered DEMO models. The neutron flux spectrum at the first wall in the homogeneous HCLL blanket is also included as a reference.

Table 3.3: The total neutron flux for the considered breeding blanket models for DEMO at full-power.

Total flux (n/cm^2/s)	HCLL	WCLL
Homogeneous	$2.091 \cdot 10^{14}$	$1.229 \cdot 10^{14}$
Heterogeneous	$2.153 \cdot 10^{14}$	$1.114 \cdot 10^{14}$

The flux at the first wall of the homogeneous HCLL blanket concept was also included as a reference. As we move radially into the breeding module,

the overall neutron flux decreases as more and more neutrons are being absorbed. As the presented PbLi-averaged neutron fluxes are an integration of neutron fluxes ranging to the very back of the BM (and further), the lower averaged flux intensity found for the PbLi over the entire energy spectrum as compared to the spectrum of first wall is no surprise (given the fact that it is very close to the fusion plasma and not many neutron captures have occurred yet). The neutrons found in the low energy region at the fist wall are to large extent the result of back-scattered neutron from the BM. The two minima found in the first wall flux spectrum found at $5 \cdot 10^{-6}$ and $2 \cdot 10^{-5}$ MeV result from two strong resonance absorption peaks of the tungsten found in the EUROFER making up the first wall and in the W coating of the first wall.

3.6 Comparison of nuclear data for FISPACT-II

FISPACT-II collapses the energy-dependent cross sections to a single value by multiplying it with the energy-dependent neutron flux spectra and integrating this product over the whole energy range. The result is the so-called effective one-group cross section. As long as the energy-dependence of the neutron flux remains the same, this value can be used to consider every desired power-fraction the reactor is operating at. Instead of comparing the actual energy-dependent radiative capture cross sections of ^{208}Pb and ^{209}Bi between different nuclear data libraries, it is more useful to compare them for the envisioned application by calculating the (energy-averaged) effective one-group cross sections and multiplying the result with the total neutron flux intensity of the model under consideration. The resulting value is an indication for the occurrence rate of the interaction under consideration, which is a useful property to compare between different models and nuclear data libraries. Note that the actual occurrence rate is obtained by multiplying the obtained value with the (time-dependent) atomic density of the target nuclei in the Pb-Li.

Another essential element to compare between different nuclear data libraries is the branching occurring at a neutron capture by ^{209}Bi. This capture can either result in ^{210g}Bi (which β^--decays to the problematic ^{210}Po with a half-life of 5 days) or in ^{210m}Bi (which α-days to ^{206}Tl with a half-life of 3 million years). As our interest is focused on the ^{210}Po production, it desirable to know how much of the neutron captures by ^{209}Bi will follow the former branch. The amount of neutron captures by ^{209}Bi resulting in ^{210m}Bi as compared to the total amount of neutron captures is referred to as the

branching ratio of ^{210g}Bi (yielding a value between 0 and 1).

Figure 3.6 shows the $\phi_n \cdot \sigma_{eff}$ product for the ^{208}Pb(n,γ)^{209}Pb (upper plot) and ^{209}Bi(n,γ)^{210g}Bi (center plot) interactions for all 4 considered models and 10 different nuclear data libraries. The lower plot shows the branching ratio of ^{210g}Bi. The error bars (representing 1 standard deviation) have been calculated by FISPACT-II and are based on the errors on the energy-dependent cross section that are included in some of the nuclear data libraries.

It can be seen that different versions of the same library tend to give similar results. The JENDL-4.0 library was found to give exactly the same result as the JEFF-3.3 library, which shows that these libraries share nuclear data. Comparing $\phi_n \cdot \sigma_{eff}$ products corresponding to the same model (same color), one can see that the calculated error on the values do not always cover the large discrepancies found between different nuclear data libraries. Due to these large discrepancies, calculations have been performed for multiple nuclear data libraries, enabling to define a range in which the final ^{210}Po inventory is expected to lie.

For the neutron capture by ^{208}Pb, the $\phi_n \cdot \sigma_{eff}$ products for the homogeneous and heterogeneous model of the same breeding blanket concepts (comparing blue with yellow and red with green for a single nuclear data library) are found to be in good agreement, as could be expected from the almost identical volume-averaged neutron flux spectra (Figure 3.5). For the neutron capture by ^{209}Bi, however, some small distinction is found between the homogeneous and hetergenoneous model of the WCLL blanket. This is probably because the resonance region (where high capture cross sections occur) of this interaction falls in a lower energy range (0.0008–0.1 MeV), where the discrepancies between the obtained flux spectra are higher (cfr. the resonance region of the ^{208}Pb(n,γ)^{209}Pb interaction lies between 0.05–1 MeV) (see Figures 3.7 and 3.8). The neutron capture rate by ^{208}Pb is found to be higher in the HCLL blanket (by about a factor two) than for the WCLL blanket. This effect has been discussed in section 3.2 and is because of the higher neutron flux found for the HCLL blanket in the 0.1 - 1 MeV energy region, where strong resonance absorption peaks occur for ^{208}Pb. The neutron capture rate by ^{209}Bi, on the other hand, is found to be similar for all models except the homogeneous WCLL blanket, for which the value is slightly (10 % - 30 %) higher resulting in a more-pronounced dependency on the initial ^{209}Bi-impurity level as will be

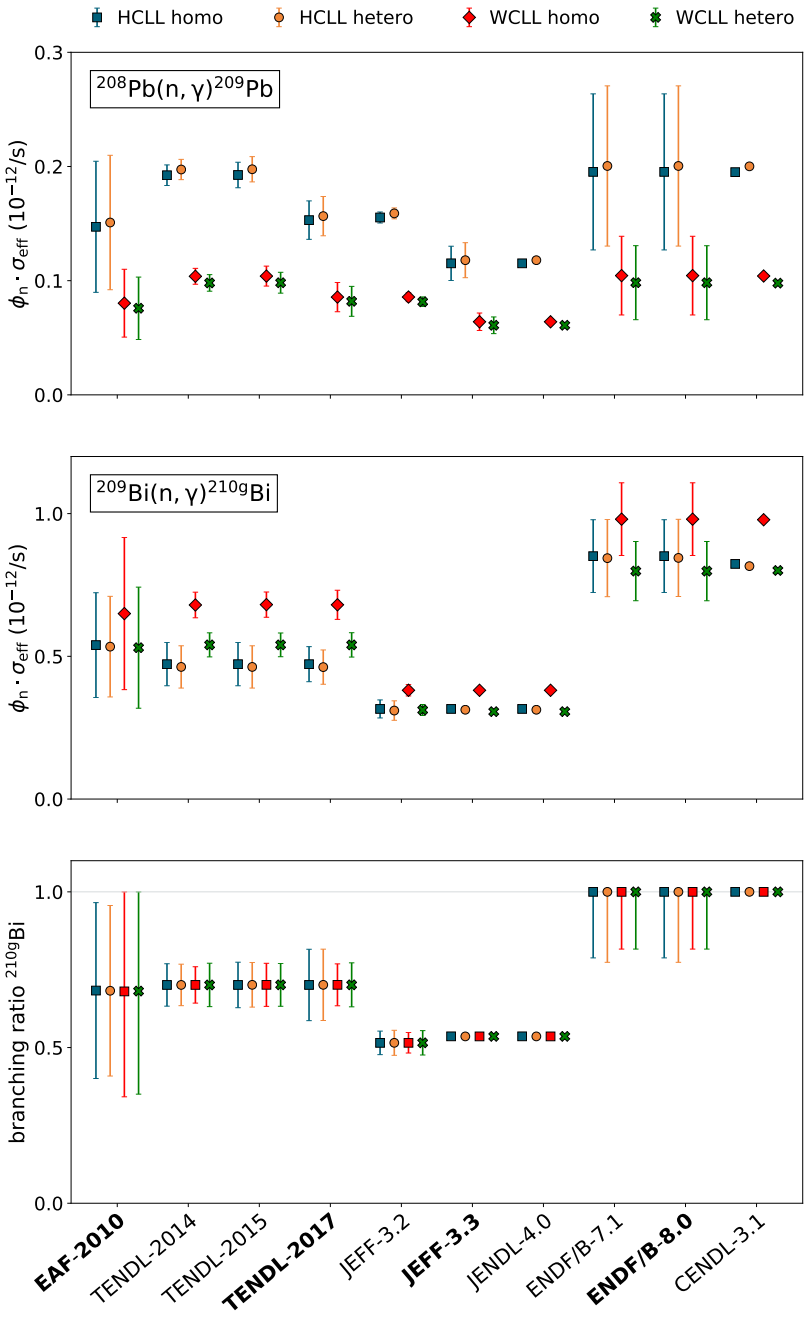

Figure 3.6: The product of the total neutron flux intensity with the effective one-group cross sections of the ^{208}Pb(n,γ)^{209}Pb (upper plot) and ^{209}Bi(n,γ)^{210g}Bi (center plot) reactions, as well as the braching ratio of ^{210g}Bi (lower plot), for all 4 considered models, 10 different nuclear data libraries and DEMO at full power.

discussed in the next section.

The largest discrepancies between libraries are found for the $\phi_{\mathrm{n}} \cdot \sigma_{\mathrm{eff}}$ product of ^{209}Bi(n,γ)$^{210\mathrm{g}}$Bi interaction (up to a factor 2.6 between the JEFF-3.3 and ENDF/B-8.0 library). It can be seen that the values are roughly directly proportional to the presented branching ratios, proving that an approximate consensus exists about the total neutron capture cross section of ^{209}Bi (shown in Figure 3.8), but not on the branching ratios. This issue has been addressed in detail by Fiorito et al. [Fio18] and in conclusion they urge the need for dedicated experiments in order to remove these discrepancies. This urge is again emphasized in this work. Anyhow, also considerable discrepancies are found for the ^{208}Pb(n,γ)^{209}Pb interaction (up to factor 1.7 between the JEFF-3.3 and ENDF/B-8.0 library).

Four last-versions of well-established nuclear data libraries have been selected for further detailed calculations: the European Activation File 2010 (EAF-2010) [Sub10], the TALYS-based Evaluated Nuclear Data Library 2017 (TENDL-2017) [noa17a], the Joint Evaluated Fission and Fusion File 3.3 (JEFF-3.3) [Nuc17] and the U.S. Evaluated Nuclear Data File 8.0 (ENDF/B-8.0) [Bro18]. As they enclose the whole spectrum of obtained values for the $\phi_{\mathrm{n}} \cdot \sigma_{\mathrm{eff}}$ products, they represent a good test set to demonstrate the considerable impact of the choice of library on the final ^{210}Po inventories. For completeness, the energy-dependent total neutron capture cross sections of ^{208}Pb and ^{209}Bi for these nuclear data libraries has been plotted in Figures 3.7 and 3.8.

3.7 Final ^{210}Po inventory in DEMO

3.7.1 ^{209}Bi impurity level effect

^{209}Bi impurities found in commercial Pb-Li can increase the final ^{210}Po inventory in a DEMO reactor. To study this effect, multiple ^{210}Po inventory calculations has been performed using different initial ^{209}Bi impurity levels in the Pb-Li. A linear relationship is found between the final ^{210}Po inventory and the initial ^{209}Bi impurity level:

$$N_{^{210}\mathrm{Po}} = \mathrm{N}^{\mathrm{noBi}}_{^{210}\mathrm{Po}} + \mathrm{A} N_{^{209}\mathrm{Bi,i}}. \tag{3.3}$$

In this equation, $N_{^{210}\mathrm{Po}}$ denotes the final ^{210}Po inventory for a given initial Bi impurity level $N_{^{209}\mathrm{Bi,i}}$, $\mathrm{N}^{\mathrm{noBi}}_{^{210}\mathrm{Po}}$ is the final ^{210}Po inventory for impurity-free Pb-Li and A is the determined slope. The obtained values of

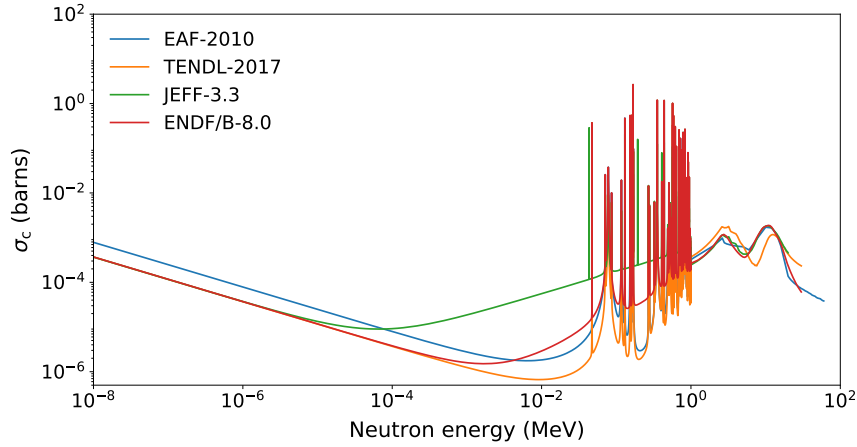

Figure 3.7: Extracted energy-dependent radiative neutron capture cross section of ^{208}Pb from the EAF-2010 [Sub10], TENDL-2017 [noa17a], JEFF-3.3 [Nuc17] and ENDF/B-8.0 [Bro18] nuclear data libraries.

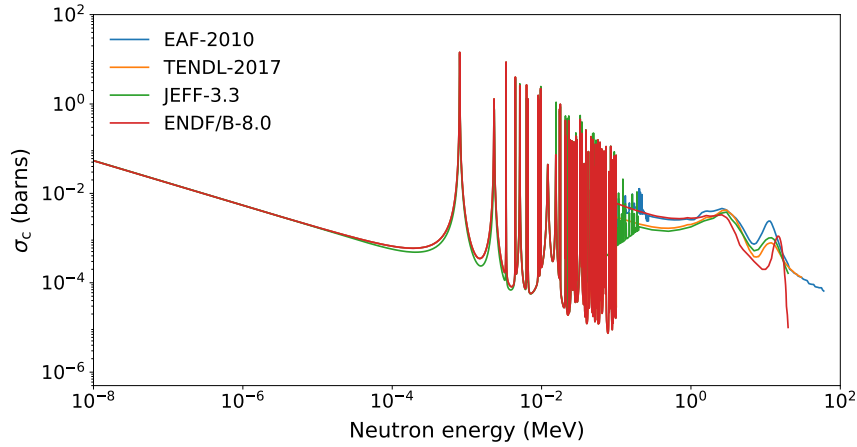

Figure 3.8: Extracted energy-dependent radiative neutron capture cross section of ^{209}Bi from the EAF-2010 [Sub10], TENDL-2017 [noa17a], JEFF-3.3 [Nuc17] and ENDF/B-8.0 [Bro18] nuclear data libraries.

N^{noBi}_{210Po} in units appt and A in units appt/appm for both irradiation schedules and all considered breeding blanket models and nuclear data libraries are presented in Table 3.4 and Table 3.5. They can also be converted to units of mg and mg/appm respectively by multiplying the reported values by 8.52 for the homogeneous HCLL, 8.38 for the heterogeneous HCLL, 8.52 for the homogeneous WCLL and 9.62 for the heterogeneous WCLL (these factors are obtained using the total Pb-Li volumes shown in Table 2.3 on page 56 and using an average Pb-Li density of 9800 kg/m^3 corresponding to a Pb-Li temperature of 330°C [Sch91]).

Table 3.4: The final ^{210}Po inventory obtained for a Pb-Li breeder free of ^{209}Bi impurities for all considered blanket models, nuclear data libraries and irradiation schedules (N^{noBi}_{210Po} in Eq. A.1).

N^{noBi}_{210Po} (appt)	1st blanket irradiation				6 FPY irradiation			
	HCLL		WCLL		HCLL		WCLL	
	homo	het	homo	het	homo	het	homo	het
EAF-2010	8.30	8.41	5.44	4.19	104	105	67.9	52.4
TENDL-2017	7.68	7.68	6.12	4.65	99.9	100	77.8	58.9
JEFF-3.3	3.78	3.85	2.54	1.95	47.2	48.0	31.8	24.3
ENDF/B-8.0	17.3	17.7	10.7	8.18	216	221	133	102

Table 3.5: The obtained coefficient A in Eq. A.1 for all considered blanket models, nuclear data libraries and irradiation schedules.

A (appt/appm)	1st blanket irradiation				6 FPY irradiation			
	HCLL		WCLL		HCLL		WCLL	
	homo	het	homo	het	homo	het	homo	het
EAF-2010	2.90	2.86	3.49	2.84	9.30	9.19	11.19	9.13
TENDL-2017	2.62	2.56	3.70	2.93	9.06	8.90	12.3	9.73
JEFF-3.3	1.69	1.68	2.04	1.64	5.42	5.38	6.56	5.27
ENDF/B-8.0	4.56	4.53	5.26	4.28	14.6	14.5	16.9	13.7

The obtained ^{210}Po inventories are higher for the 6 FPY irradiation schedule as this is a more intensive irradiation schedule than the one foreseen for DEMO's first breeding blankets. The higher slopes A (and thus higher dependency on the initial ^{209}Bi impurity level) obtained for the homogeneous WCLL model is the result of its higher $\phi \cdot \sigma_{\text{eff}}$ products for the ^{209}Bi(n,g)^{210g}Bi interaction (Figure 3.6). The higher ^{210}Po inventory for ^{209}Bi-free Pb-Li (N^{noBi}_{210Po}) obtained for the HCLL models, on the other hand,

results from their considerably higher $\phi \cdot \sigma_{\text{eff}}$ products for the ^{208}Pb(n,γ)^{209}Pb interaction. It can be seen that the choice of nuclear data library has a prevalent impact on the resulting ^{210}Po inventory e.g. the ENDF/B-8.0 library produces values up to 4.6 times (360%) higher than the ones obtained for the JEFF-3.3 library. The differences in the flux spectra obtained using the homogeneous and heterogeneous model (Figure 3.5) are found to have an almost negligible effect for the HCLL blanket (maximum discrepancy in the ^{210}Po concentration is only 2%), while for the WCLL blanket the effect is somewhat larger due to the larger flux discrepancies in the ^{209}Bi(n,g)^{210g}Bi resonance region, resulting in a ^{210}Po concentration up to 30% higher for the homogeneous model (corresponding to a total ^{210}Po inventory higher by at most 15% given the larger Pb-Li volume in the heterogeneous model, see Table 2.3 on p .56).

However, the uncertainties on the final ^{210}Po inventory introduced by the discrepancies found between the cross sections taken from different nuclear data libraries are found to be larger than those resulting from the spatial homogenization of the model. Therefore, it can be concluded that the homogeneous models can be used to obtain a good first indication of the expected ^{210}Po inventory for future intermediate blanket designs, certainly as long as there is no good consensus on the capture cross sections. Nevertheless, it is advisable to use a detailed heterogeneous model to estimate the ^{210}Po inventory in the final blanket design.

Using the obtained coefficients of equation A.1, it is now possible to calculate the ^{209}Bi impurity level corresponding to a 10 % increase in the final ^{210}Po inventory. The obtained values are presented in Table 3.6 and are a good indication for the Bi impurity level at which a noticeable impact on the final ^{210}Po inventory is expected. All Bi impurities levels lower than the reported ones could thus be considered as having negligible impact. In case of a 6 FPY irradiation schedule, a larger fraction of the generated ^{210}Po will originate from ^{208}Pb compared to the first DEMO blanket irradiation schedule. This reduces the relative significance of the initial ^{209}Bi impurities present in the Pb-Li, thus resulting in higher $N^{\mathbf{no\,Bi}}_{\mathbf{^{210}Po}}$ values.

Commercial eutectic Pb-Li available today typically contains between 10–33 appm ^{209}Bi impurities [Con14]. It can be seen that all values in Table 3.6 are lower than these values, which means that the Pb-Li requires purification before operation to at least these levels if one wants to nullify the impact of the initial Bi impurities. A similar approach can be used to

Table 3.6: Maximum initial ^{209}Bi impurity level resulting in a ^{210}Po inventory increase below 10 % w.r.t. pure Pb-Li for all considered blanket models, nuclear data libraries and irradiation schedules.

$N^{10\%}_{^{209}Bi,i}$ (appm)	1st blanket irradiation				6 FPY irradiation			
	HCLL		WCLL		HCLL		WCLL	
	homo	het	homo	het	homo	het	homo	het
EAF-2010	0.286	0.294	0.156	0.147	1.11	1.14	0.607	0.574
TENDL-2017	0.293	0.300	0.165	0.158	1.10	1.12	0.632	0.606
JEFF-3.3	0.224	0.229	0.124	0.118	0.872	0.892	0.484	0.461
ENDF/B-8.0	0.380	0.390	0.203	0.191	1.48	1.52	0.790	0.743

calculate the Bi impurity limits for e.g. a final ^{210}Po inventory of 1 appb or a total ^{210}Po inventory of 1 g in the total Pb-Li volume.

3.7.2 Risk analysis: leak-of-PbLi accident

In 2006, Petti et al. [Pet06] have performed a safety analysis on a conceptual 1000 MWe fusion power plant ARIES-AT. In this analysis, they estimated that in case of an ex-vessel leak-of-PbLi accident a ^{210}Po concentration of 100 appt in the eutectic Pb-Li would result in a total amount of 0.43 TBq ^{210}Po being released into the environment in the first hour after the accident before the heating-ventilation-air conditioning (HVAC) system of the lower functional area (where the Pb-Li pool forms) is shut down. This quantity showed to be about half the allowable no-evacuation release limit of 0.92 TBq for a release point close to the ground, a 1 km site boundary and average weather conditions. Note that, for a release point elevated by 100 m via a stack coupled to the HVAC, the allowable no-evacuation release limit is ten times higher. It was decided to focus on the more hazardous case of a release incident close to the ground.

Consider a DEMO reactor using 'dirty' commercial Pb-Li (33 appm ^{209}Bi) and no purification system. Under these conditions, ^{210}Po inventories between 56.1 and 184 appt (depending on the nuclear data library and breeding blanket model considered) are found for the DEMO first blanket irradiation schedule and between 198 and 700 appt for a 6 FPY irradiation schedule. For both cases the maximum predicted inventory is above the 100 appt limit determined for ARIES-AT. However, the ARIES-AT fusion power plant is designed to use Pb-Li both as breeder and coolant. As a result, the Pb-Li blanket outlet temperature is as high as 1125°C, which is far above the Pb-Li operation temperature foreseen for a DEMO

fusion reactor using an HCLL or WCLL blanket i.e. 300°C and 328°C respectively [Uti19b, Uti19a, Uti15]. Petti et al. [Pet06] demonstrated that in case of an ex-vessel leak-of-PbLi accident at ARIES-AT, 0.64 TBq of ^{210}Po is expected to evaporate in the form of PbPo from the leaked Pb-Li pool (initially at 980°C) within the first two hours. Using the same evaporation data as Petti et al., the amount of PbPo expected to evaporate within the first two hours from the Pb-Li pool below 300°C occurring in case of a leak-of-PbLi accident at DEMO was found to be at least 30000 times smaller. This is because the PbPo mobilization rate is governed by a diffusion-limited bulk process at high temperatures, whilst being limited by a slower surface evaporation process at low temperatures.

As the surface evaporation rate is directly proportional to the ^{210}Po concentration in the Pb-Li, it could be proposed to allow ^{210}Po inventories 30000 times higher than the 100 appt limit determined for ARIES-AT. However, although PbPo is indeed expected to be the primary evaporating species in an inert atmosphere (see chapter 5 and as published in Paper II [Mer19a] reprinted on pages 163–173), recent experiments suggest that in contact with air, Po-containing (oxy-)hydroxides will form, having a higher volatility than the formed polonium oxides (e.g. PoO_2), but lower than elementary Po [Mau14]. Using the known evaporation rate of elementary Po [Pet06, Bro55], a conservative upper limit of the ^{210}Po amount evaporating within 2 hours from a DEMO-conditioned Pb-Li pool in contact with air has been estimated and found to be still at least 15 times smaller than the evaporated PbPo amount at ARIES-AT. Based on these findings, a safe ^{210}Po concentration limit for DEMO might be as high as 1500 appt.

In the previous paragraph, it was shown that the predicted ^{210}Po inventories for DEMO using 'dirty' Pb-Li (33 appm ^{209}Bi) are at least a factor 2 below this new limit. Therefore, ^{210}Po is expected not to pose a threat in case of a leak-of-PbLi accident in which the Pb-Li is in contact with air, even if dirty commercial Pb-Li is used. It should be noted however, that in case the leaked Pb-Li makes contact with water (e.g. the coolant in the case of WCLL), Po species more volatile than elementary Po are expected to form [Mau14]. If these species increase the evaporation rate by more than a factor two, certain safety measures will be required. A dedicated study of the stability and volatility of these Po-containing (oxy-)hydroxides is required to make statements on the required ^{210}Po concentration threshold keeping the ^{210}Po release below the safe limit for this specific accident scenario.

If the evaporation rate increases by not more than a factor 15, the simple

risk analysis presented above suggests that a safe ^{210}Po concentration threshold would be of the order of 100 appt, which can be satisfied for the DEMO first blanket irradiation schedule by using relatively clean commercial Pb-Li ($<$ 17 appm ^{209}Bi) and for the 6 (or longer) FPY irradiation schedule by incorporating an on-site Pb-Li purification system keeping the ^{209}Bi level always below 5 appm.

3.7.3 Comparison to the ^{210}Po inventory in MYRRHA

The ^{210}Po concentration in the Pb-Li of DEMO after the first blanket irradiation schedule is found not to exceed 184 appt, even for the worst assumptions of Pb-Li purity, nuclear data library and DEMO model. This conservative value corresponds to a total inventory of 1.52 grams of ^{210}Po distributed over the whole Pb-Li breeder.

The ^{210}Po inventory in MYRRHA after one irradiation cycle of 90 days at nominal power is reported to be at least 231 times higher (350 grams) [Fio18] (details on the performed MCNP calculation are considered as being confidential and have not been publicly shared). Table 3.7 presents the ^{210}Po inventory and concentration in DEMO (after the first blanket irradiation schedule spanning 6 years) and MYRRHA (after one irradiation cycle spanning 90 days) in multiple units, as well as their ratio. To calculate the volumetric concentration, an average density of 9800 kg/m^3 is used for a 725 m^3 volume of Pb-Li in DEMO (correponding to a typical operational temperature of 330°C [Uti19a] using the temperature-dependent density recommended by Schulz [Sch91])) and of 10292 kg/m^3 for the 740 m^3 of LBE in MYRRHA (corresponding to a typical operational temperature of 325°C [Eng15] using the T-dependent density recommended by Fazio et al. [Faz15]).

The values for MYRRHA for both concentration and inventory, are found to be at least 200 times higher. It should be noted that in absence of LBE purification, the ^{210}Po inventory in MYRRHA after 6 years of operation (and thus many irradiation cycles) is expected to be even much higher than the presented values. The reason for the much higher ^{210}Po inventory in MYRRHA is because ^{209}Bi is implemented in large quantities as functional material, providing a short-cut in the problematic reaction chain presented in Figure 1.12 on p. 39 and thus resulting in a single neutron interaction ^{210}Po-production process. For the Pb-Li used in DEMO, this short-cut is also provided by the initially present ^{209}Bi impurities but in much lower

Table 3.7: A comparison of the expected ^{210}Po inventory in the European DEMO fusion reactor after the first blanket irradiation schedule (upper limit) and in the LBE-cooled MYRRHA fast fission reactor after one irradiation cycle of 90 days.

^{210}Po	**total inventory**		**concentration**		
	grams	PBq	ppb	GBq/kg	TBq/m^3
MYRRHA	350	58.1	45.1	7.64	78.6
DEMO	1.52	0.252	0.179	0.0354	0.347
Ratio	231	231	254	216	227

quantities. All other produced ^{210}Po originates from ^{208}Pb and is formed by two consecutive neutron interactions. Much larger ^{210}Po inventories will thus have to be handled in MYRRHA compared to DEMO, future fusion power plants and future pure lead cooled fission reactors. MYRRHA is expected be fully operation by 2033, while the DEMO engineering design phase is foreseen to last until 2038. Therefore, focused research and experience gained during MYRRHA's engineering design phase and first years of operation, is expected to provide useful information on how to safely handle and extract ^{210}Po in DEMO. This information can than still be incorporated during the design phase of DEMO, which represents a less-challenging system regarding ^{210}Po handling.

3.8 Conclusions

Combining MCNP neutron transport calculations and FISPACT-II inventory calculations, the expected ^{210}Po inventories in the HCLL and WCLL breeding blankets for the DEMO fusion reactor have been determined. The results show that the discrepancies resulting from using different nuclear data libraries (up to 360 %) are larger than those caused by the material homogenization of the models (up to 30 %). The varying branching ratio of the neutron capture by ^{209}Bi resulting in either ^{210g}Bi or ^{210m}Bi is found to be the primary inconsistency and dedicated experiments are required. As long as no consensus is reached on this branching ratio, the homogenized models, which are easier to implement, can be used for the ^{210}Po inventory estimation in future blanket designs. A comparable ^{210}Po inventory is expected for the HCLL and WCLL blankets, with the highest difference occurring for high-purity Pb-Li ($<$ 1 appm ^{209}Bi), in which case the HCLL concept results in up to 50 % more ^{210}Po.

The ^{209}Bi impurity level in the Pb-Li has been found to have a considerable impact on the final ^{210}Po inventory. Using clean commercial Pb-Li (10 appm ^{209}Bi) results in 3 times less ^{210}Po than when using more contamined Pb-Li containing 33 appm ^{209}Bi. If the Pb-Li is initially purified to 1 appm ^{209}Bi levels, even 16 times less ^{210}Po is produced.

A safety analysis based on inventory arguments and evaporation rates taken from literature shows that in case of an ex-vessel leak-of-PbLi accident in DEMO, a ^{210}Po concentration below 1500 appt limits the environmental ^{210}Po release to values below the no-evacuation limit. Even for the worst assumptions of Pb-Li purity, irradiation schedule, blanket model and nuclear data library, the ^{210}Po concentration stays below this limit by at least a factor 2, with no need for Bi or Po removal from the Pb-Li. However, if the Pb-Li makes contact with water, highly volatile Po-containing (oxy-)hydroxides are expected to form. If these species increase the evaporation rate by more than a factor 2, safety measures will be required (e.g. on-site Pb-Li purification).

In the MYRRHA fast fission reactor, large amounts of bismuth will be implemented to reduce the melting temperature of the coolant, and thus the minimal operation temperature of the reactor. This provides an undesired short-cut in the ^{210}Po production chain, resulting in a single irradiation cycle (90 days) ^{210}Po inventory expected to be at least 200 times larger than the one for DEMO after the whole reactor lifetime. MYRRHA is foreseen to start operation before the end of the design phase of DEMO, therefore experience gained during the design and operation of MYRRHA can proof extremely useful for the design of the less-challenging (regarding ^{210}Po handling) DEMO reactor.

Part II

Molecular occurrence of ^{210}Po in MYRRHA and DEMO

4

Methods – Molecular occurrence of ^{210}Po in MYRRHA and DEMO

In the previous chapter, the ^{210}Po inventory in the European DEMO fusion reactor has been estimated to be at least 200 times lower than the one previously estimated for the MYRRHA fast fission reactor. To ensure a safe operation, a ^{210}Po removal system will most probably have to be implemented in MYRRHA and possibly in DEMO. To devise efficient filtering techniques, accurate data is required on the chemical behavior of ^{210}Po. This data is also essential to perform reliable risk analyses for given accident scenarios, allowing to define a ^{210}Po concentration limit for safe operation. Due to the high radiotoxicity of ^{210}Po , few experiments have been performed and the empirical data reported in literature is very limited.

The second part of this work aims to provide some essential thermochemical data on Po-containing compounds through ab initio (quantum chemistry) calculations, thus avoiding risky and expensive experiments. The focus here is on gaseous compounds because these can escape from the reactor most easily and are also the most harmful species for the workers and environment as the inhalation of ^{210}Po results in severe health risks (maximum permissible air concentration of ^{210}Po is only 0.2 Bq or $1.2 \cdot 10^{-15}$ g per cubic meter [OA09]). The stability of possibly occurring Po-containing molecules (at zero Kelvin) can be obtained by comparing the total energy of the compound with the one of the dissociated state, both obtained by ab initio calculations. Temperature effects are included

by scanning the entire dissociation profile. As Po is a heavy element, both electron-correlation and relativistic effects have to be taken into account, requiring a high level-of-theory ab initio method capable of simultaneously treating both effects to the desired extent. The CASSCF/CASPT2/SO-CASSI approach [Roo04c, Roo04b] provided by the Molcas 8.0 code [al.16b] likely matches these requirements. In the next sections, the different steps in such a calculation are briefly explained.

4.1 Ab initio calculations in Molcas

4.1.1 Molecular Schrödinger equation

The Hamiltonian $\widehat{H}$ of a free molecule comprises potential energy terms corresponding to the nucleus-electron attraction (negative), the electron-electron repulsion (positive) and the nucleus-nucleus repulsion (positive), as well as the kinetic energy terms for both the nuclei and the electrons (positive). The molecular Schrödinger equation can thus be written as:

$$\widehat{H}\Psi = E\Psi, \tag{4.1a}$$

with

$$\widehat{H} = \frac{1}{4\pi\varepsilon_0}\left(\frac{1}{2}\sum_{A\neq B}\frac{e^2 Z_A Z_B}{|\boldsymbol{R}_A - \boldsymbol{R}_B|} + \frac{1}{2}\sum_{i\neq j}\frac{e^2}{|\boldsymbol{r}_i - \boldsymbol{r}_j|} - \sum_A\sum_i\frac{e^2 Z_A}{|\boldsymbol{R}_A - \boldsymbol{r}_i|}\right) + \sum_A\frac{\hbar^2\nabla^2_{\boldsymbol{R}_A}}{2M_A} + \sum_i\frac{\hbar^2\nabla^2_{\boldsymbol{r}_i}}{2m_e}, \tag{4.1b}$$

where Ψ is the wave function of the system and E its total energy. Upper case letters (A,B) refer to the nuclei and lower case letters (i,j) to the electrons. $\boldsymbol{R}_X$, Z_X, M_X are nuclear positions, charges and masses respectively, while $\boldsymbol{r}_x$, m_e, e and ε_0 are the electron positions, the electron mass, the elemental charge and the vacuum permittivity. Note that Equation 4.1 also applies to isolated atoms and solids (as well as liquids and gases). The ultimate goal is to obtain the wave function Ψ which contains all information about the system. Although Equation 4.1 is quite straightforward to write down, to date it cannot be solved exactly, even for very small systems.

Therefore, some approximations have to be applied to obtain a good estimation for the wave function. One such an approximation is the one proposed by Born and Openheimer in 1927 [Bor27], suggesting to initially freeze the much heavier nuclei in space while solving the Schrödinger equation for the electrons with the nuclei's positions considered to be fixed parameters. This proposal is based on the fact that (classically speaking) nuclei are moving much more slowly than the electrons due to their larger mass (mass of a nucleon is 1836 times larger than of an electron) and almost seem not to be moving at all from the electrons point-of-view in their faster timescale. In practice, this boils down to splitting the total wave function in an electronic and nuclear part ($\Psi = \psi_{\text{electronic}} \times \psi_{\text{nuclear}}$) and the electronic Schrödinger equation being a simplified version of Equation 4.1:

$$\widehat{H}_e \psi_e = E_e \psi_e, \tag{4.2a}$$

$$\widehat{H}_e = \frac{1}{4\pi\varepsilon_0}\left(\frac{1}{2}\sum_{i\neq j}\frac{e^2}{|\boldsymbol{r}_i - \boldsymbol{r}_j|} - \sum_A\sum_i \frac{e^2 Z_A}{|\boldsymbol{R}_A - \boldsymbol{r}_i|}\right) + \sum_i \frac{\hbar^2 \nabla^2_{\boldsymbol{r}_i}}{2m_e} + C_{N-N}, \tag{4.2b}$$

where the kinetic energy of the nuclei is assumed to be zero and the nucleus-nucleus Coulomb attraction energy is a constant C_{N-N}. It should be noted that the electronic wave function corresponding to this Hamiltonian has to be antisymmetric, meaning it changes sign upon exchange of two electrons, as required for fermions according to the axioms of quantum mechanics (Pauli exclusion principle [Pau25, Str04]).

Over the past century, different methodologies have been introduced to find approximate solutions for this simplified equation. These can be classified in two groups: (post-)Hartree-Fock methods and Density Functional Theory (DFT). DFT methods are in general computationally less demanding and therefore often applied to large molecules, intermolecular interactions, and macromodels. The downside of DFT is that it is not possible to gradually unambiguously improve the result by simply applying more sophisticated DFT methods. Post-Hartree-Fock methods, on the other hand, do have this property but quickly tend to become computationally too expensive for larger molecules. As the focus of this work is to obtain high-quality chemical data on small gaseous Po-containing molecules, the use of a high level-of-theory post-Hartree-Fock approach called 'CASSCF/CASPT2/SO-CASSI' is more suitable.

4.1.2 Hartree-Fock

The initial step of any post-Hartree-Fock method is a Hartree-Fock calculation. As previously noted, the final electronic wave function is an antisymmetric function. These functions represent an infinite set and can appear in many different forms. The major assumption in the Hartree-Fock (HF) method (sometimes called the self-consistent field (SCF) method) [Har35] is to use, in case of fermions, a single Slater determinant of single-particle spin-orbitals ψ as approximation to the exact many-particle electron wave function:

$$\Psi_0^{\mathrm{HF}} = \frac{1}{\sqrt{N!}} \begin{vmatrix} \psi_1(\boldsymbol{x}_1) & \psi_1(\boldsymbol{x}_2) & \cdots & \psi_1(\boldsymbol{x}_N) \\ \psi_2(\boldsymbol{x}_1) & \psi_2(\boldsymbol{x}_2) & \cdots & \psi_2(\boldsymbol{x}_N) \\ \vdots & \vdots & \ddots & \vdots \\ \psi_N(\boldsymbol{x}_1) & \psi_N(\boldsymbol{x}_2) & \cdots & \psi_N(\boldsymbol{x}_N) \end{vmatrix}, \tag{4.3}$$

where Ψ_0^{HF} is the Hartree-Fock ground state wave function, N is the number of electrons, $\boldsymbol{x}$ are the space and spin coordinates of the electrons. The Slater determinant [Sla29], has an elegant simplicity and is guaranteed to satisfy the required antisymmetry property. A Slater determinant in which two electrons with the same spin occupy the same orbital results in a wave function that is zero everywhere.

As the potential energy in the system is bounded from below (there is a minimum value), the eigenfunctions of the Schrödinger equation also have energies bounded from below. For a closed system, the equilibrium state is the one that minimizes the energy. The aim of the HF method is therefore to find the single-particle spin-orbitals yielding this minimal energy, which then results in the HF electronic ground state Ψ_0^{HF}. The variational principle allows to find the Slater determinant with the lowest energy, yielding the best approximation of the actual electronic wave function within the collection of single Slater determinants. In fact, the problem is then reduced to finding the eigenfunctions (i.e. the single-particle spin-orbitals) of the so-called Fock operator [Fin93], which can be determined using an iterative procedure repeated until the obtained electronic mean field is consistent with the assumed one (hence the name self-consistent field method).

In practice, the single-particle spin-orbitals are expressed using a basis set. Only by using an infinite basis set can the exact Hartree-Fock ground state wave function be determined. As this is not feasible in reality, the choice of basis set is another approximation imposed on the final wave function. Molcas [al.16b] allows to make use of generally contracted Atomic Natural

Orbital (ANO) basis sets which are centered on the atoms and have been designed to give a balanced description of the corresponding atom in the ground, excited and ionized state, making them also suitable for molecular calculations. In the performed calculations the relativistic ANO basis sets (ANO-RCC) [Roo04d, Roo04a, Roo04c] have been used, which have been optimized using the CASSCF/CASPT2 method (see next section). The basis sets have been contracted using the Douglas-Kroll-Hess (DKH) Hamiltonian [Dou74, AH86] which is therefore also used in the calculations to include scalar relativistic effects. The ANO-RCC basis set is recommended by the Molcas developers for all regular calculations. The Valence Quadruple Zeta Polarized (VQZP) contraction of this basis set has been used.

4.1.3 CASSCF

By definition, the Hartree-Fock method completely accounts for the electron exchange energy which is an energy contribution having no classical analogue resulting completely from the Pauli exclusion principle [Pau25, Str04]. The main approximation in the Hartree-Fock method can be physically interpreted as assuming that each electron moves in the mean field generated by all other electrons, with no detailed electron-electron interaction taken into account. This is also referred to as the independent particle model. In reality however, all electron are entangled and the energy contribution not accounted for by the H-F approximation is called electron correlation energy.

Post-Hartree-Fock methods aim to recover most of this electron correlation energy by expanding the configuration space in which the optimal wave function is searched for. In HF, single-particle spin-orbitals are used to describe the electronic wave function and one Slater determinant represents exactly one possible electron configuration. The Complete Active Space Self-Consistent Field (CASSCF) method [Roo80] expands the accessible configurational space (active space) by dividing the orbital space in three sets:

- the orbitals that are always fully occupied i.e. the inactive space,
- the set of orbitals that can be (partially) (un)occupied i.e. the active space,
- the orbitals that are always unoccupied i.e. the virtual space.

By defining this division of the orbital space, one also unambiguously defines the number of electrons to be distributed over the orbitals within

the active space (i.e. the active electrons). The trial wave function in the CASSCF method is then a linear combination of multiple electron configurations (Slater determinants) defined within this active space.This method mainly corrects for the static electronic configuration, originating from the fact that a Slater determinant may be a poor representation of the actual many-electron system.

The CASSCF method allows to perform the orbital optimization with the specific goal of minimizing the average energy of a desired number of states (Configuration Interaction (CI) roots), rather than for the ground state alone. This is a essential feature as a large number of states have to be included in the calculation of the spin-orbit interaction contributions. How to find the appropriate number of CI roots to be included in the CASSCF calculation is discussed in the Supporting Info of Paper II on page 179.

4.1.4 CASPT2

Using the Complete Active Space Perturbation Theory of 2nd order (CASPT2) method [And92, Fin98], a 2nd order correction for the difference between the obtained CASSCF energy and full Configuration Interaction (CI) energy can be obtained. This latter energy corresponds to the CASSCF energy for an active space spanning the entire orbital space (the inactive and virtual spaces are empty) and is therefore the exact solution within the space spanned by the orbital basis set. The configurational space used in the CASPT2 method is the one generated by applying all single and double electron substitution operators on the CASSCF reference wavefunction Ψ_0, thus spanning exactly the first-order interaction subspace. This means that at most two electrons can be moved from the inactive/active space to the active/virtual space, with the option to define a space of frozen orbitals that always remain fully occupied (see Figure 4.1).

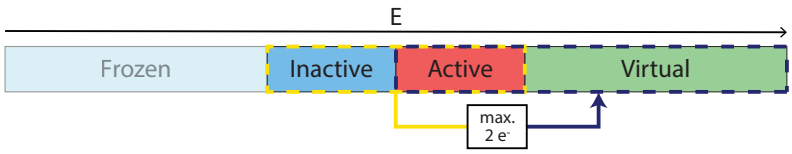

Figure 4.1: A schematic representation of the electron substitution operators used to generate the configuration space in the CASPT2 method.

A good CASSCF reference wavefunction is a must for this method to be successful (i.e. perturbations should be small). A common issue occurring when using this mehod is the appearance of so-called intruder states which can introduce singularities in the potential energy functions (the energy denominator becomes zero at some geometries), especially for excited states. This can be avoided by applying an imaginary shift to the energy levels, for which the final result is corrected afterwards [For97]. The discussion on how to select an appropriate imaginary level shift, capable of getting rid of the intruder states while having minimal impact on the final result, is discussed in the Supporting Info of Paper II on page 182.

The CASPT2 method primarily corrects for the dynamic electron correlation arising from the deficiency of HF to model the detailed electron-electron interaction and the fact that electrons tend to avoid each others instantaneous direct surroundings (classically speaking). In this work, the Multi-State CASPT2 method is used, which couples all CASPT2 states having the same symmetry (irreducible representation or irrep) and spin state.

4.1.5 SO-CASSI

The CASSCF and CASPT2 calculations are run for every symmetry (irrep) and spin state separately. The resulting CASSCF individually optimized states are still interacting and non-orthogonal. By performing a Complete Active Space State Interaction (CASSI) calculation [Mal02], they can be transformed into a set of unambiguous non-interacting and orthonormal eigenstates of the Hamiltonian which is dressed with the dynamic correlation obtained from the CASPT2 calculations.

Until now, the aim was to obtain the solution for Eq. 4.2, which does not include any relativistic effects. As previously mentioned, the scalar relativistic effects were included by using the DKH Hamiltonian, a scalar-relativistic variant of the one presented in Eq. 4.2b. It is possible to partially correct for spin-orbit (SO) interaction at the CASSI step, by instead determining the eigenstates of the sum of the spin-free Hamiltonian ánd the spin-orbit operator. In this calculation the optimized spin-free eigenstates are used as a basis in the optimization of the eigenstates for which spin-orbit interaction is included.

By running through the whole HF/CASSCF/CASPT2/(SO-)CASSI routine, the energy of the ground state and first excited states (either with or without

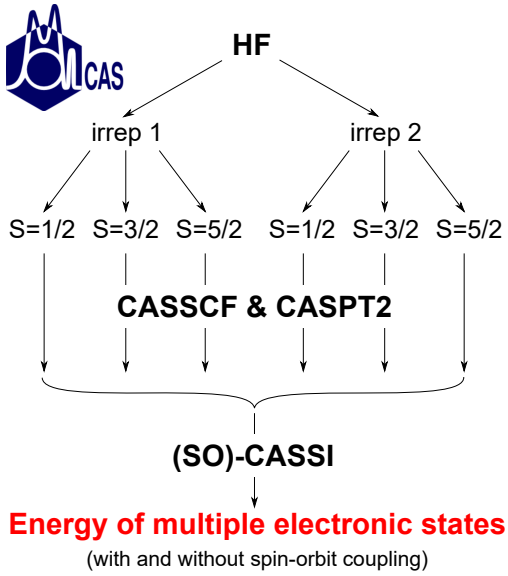

Figure 4.2: The entire workflow of the calculations performed for one single spatial configuration of the nuclei.

spin-orbit coupling) of a given system can be obtained. The entire workflow of the calculations performed for a single spatial configuration of the nuclei is schematically visualized in Figure 4.2. The implementation of this routine in Molcas is concisely discussed in the Supporting Info of Paper II on page 177.

Repeating this whole routine for a large number of spatial configurations of the nuclei, a potential energy surface (PES) can be constructed. In case of a diatomic molecule, the result is the dissociation profile of the ground and first excited states. The used methodology is based on the one used by Roos and Malmqvist [Roo04b] and the validity of this approach for heavy main group elements is discussed in the Supporting Info of Paper II on page 190. In order to accurately determine all electronic states of interest, the number of Configuration Interaction (CI) roots used for each symmetry type of the wave function (irrep) and each spin multiplicity in the CASSCF calculations as well as the imaginary shift used in the CASPT2 calculations had to be severely tested for convergence and correctness. This is discussed in the Supporting Info of Paper II (pp. 179–182).

4.2 Diatomic Po-containing molecules

4.2.1 Selection of candidate molecules

Performing accurate ab initio calculations on systems containing heavy main group elements such as Po, Pb and Bi is quite challenging. Therefore, at first, the focus is on diatomic molecules. Due to the high radiotoxicity of ^{210}Po , virtually no experimental chemical data is available on Po-containing molecules. The only diatomic Po-containing molecules for which an experimental dissociation energy has been reported is the Po_2 dimer (D_0 = 1.9 eV [Cha57, Hub79]) and even this was no direct measurement but rather deduced from an extrapolation of the lower state vibrational levels.

Hence, the ab initio calculations are focused on diatomic molecules containing Po combined with another element expected to be present in the reactors of interest i.e. Pb or Li (relevant for fusion reactor Pb-Li breeding blankets), Pb or Bi (relevant for fission reactor Pb-(Bi) coolants), H or O (relevant for water contamination) or another Po atom. This results in 6 diatomic molecules of interest: PoH, LiPo, PoO, PbPo, BiPo and Po_2. The selection of the studied molecules is thus based on the reasoning above rather than triggered by literature (however note that PbPo has been mentioned in literature as a prime candidate for the molecular form of Po evaporating from liquid Pb-Li eutectic [Feu92]).

4.2.2 Choice of active space

A critical setting for the CASSCF and CASPT2 calculations is the choice of the active space. It is not a straightforward choice to make and requires lots of experience and chemical intuition. Some general recommendations have been proposed by Veryazov et al. [Ver11]. However, rather than blindly following these guidelines, many candidate active spaces are extensively tested and quantitatively evaluated. As no experimental dissociation energies have been reported for the studied Po-containing molecules (except for Po_2), the evaluation is carried out using lighter analogue molecules. These analogue test molecules are defined by substituting the Po atom (single substitution) or both atoms (double substitution) by lighter analogue atoms of the same group in the periodic system (see Figure 4.3). The resulting dissociation energies of the test molecules for the different active spaces were compared to the experimental ones reported by Huber in 1979 [Hub79]. For each active space, all deviations for the molecules in a specific substitution series were

added. The active space resulting in the lowest total deviation for a specific substitution series was then considered to be most suitable for the associated Po-containing molecule of that series.

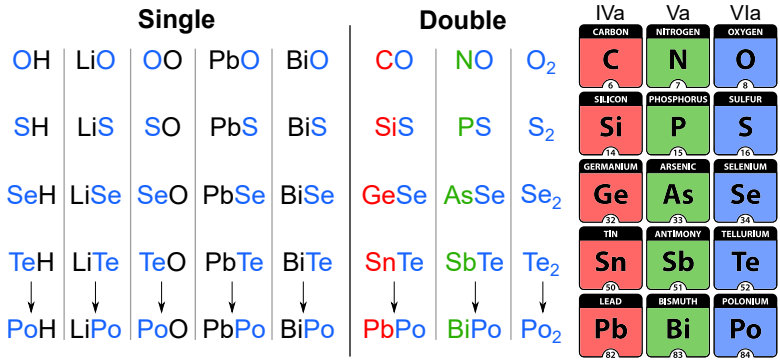

Figure 4.3: Substitution series used to quantitatively validate the active space selection.

4.2.3 Profile fitting and molecular constants

By performing 'CASSCF/CASPT2/SO-CASSI' calculations for a whole range of internuclear distances, a discrete ab initio dissociation profile for the ground and first excited states of the diatomic molecule can be obtained. These profiles can be characterized by useful molecular parameters which can be obtained by fitting a five-parameter potential energy function $f(D, R_\mathrm{e}, \omega_\mathrm{e}, \omega_\mathrm{e}x_\mathrm{e}, \alpha_\mathrm{e})$ proposed in 1941 by Hulbert and Hirschfelder [Hul41] to the ab initio computed data points. The function is given by:

$$V(R) = D[(1 - e^{-x})^2 + c_1 x^3 e^{-2x}(1 + c_2 x)], \tag{4.4}$$

with the dimensionless parameter x being:

$$x = \frac{\omega_\mathrm{e}}{2(B_\mathrm{e}D)^{1/2}} \left(\frac{R - R_\mathrm{e}}{R_\mathrm{e}} \right), \tag{4.5}$$

and the parameters c_1 and c_2 given by

$$c_1 = 1 + a_1 \left(\frac{D}{a_0} \right)^{1/2}, \tag{4.6a}$$

$$c_2 = 2 + \left[\frac{7}{12} - \frac{D a_2}{a_0} \right] \Big/ c_1, \tag{4.6b}$$

where a_0, a_1 and a_2 are the Dunham coefficients [Dun32]

$$a_0 = \frac{\omega_e^2}{4B_e}, \tag{4.7a}$$

$$a_1 = -1 - \frac{\alpha_e \omega_e}{6B_e^2}, \tag{4.7b}$$

$$a_2 = \frac{5}{4}a_1^2 - \frac{2}{3}\frac{\omega_e x_e}{B_e}, \tag{4.7c}$$

and the rotational constant B_e being

$$B_e = \frac{h}{8\pi^2 \mu R_e^2 c}. \tag{4.8}$$

The five parameters to be fitted are: the depth of the well D, the equilibrium bond length R_e, the fundamental vibration frequency ω_e, the first anharmonic constant $\omega_e x_e$ and the vibration-rotation interaction constant α_e. Other physical quantities appearing are Planck's constant h, the reduced mass of the molecule μ and the speed of light in vacuum c. This five-parameter function can be reduced to a four-parameter function by assuming that

$$\alpha_e = 6B_e x_e \left[\left(\frac{B_e}{\omega_e x_e} \right)^{1/2} - \frac{B_e}{\omega_e x_e} \right], \tag{4.9}$$

as Pekeris showed to good approximation by calculating the rotational energy using perturbation theory [Pek34]. A second free parameter can be excluded by assuming that all anharmonic constants except the first one ($\omega_e x_e$) are equal to zero. In that case we have

$$\omega_e x_e = \frac{\omega_e^2}{4D}. \tag{4.10}$$

With these 2 assumptions, the general five-parameter potential energy function is reduced to the three-parameter Morse potential [Mor29]:

$$V(R) = D[(1 - e^{-x})^2]. \tag{4.11}$$

By fitting any of the 3 discussed potential energy functions (having respectively 3, 4 or 5 free parameters) to the computed data points, values can be calculated for D, ω_e, $\omega_e x_e$, B_e and α_e. As a direct fit to the five-parameter function was found to be quite sensitive to the initial guesses for the parameters, it was decided to start by performing a fit to the three-parameter Morse potential. The resulting values for D, R_e, ω_e and $\omega_e x_e$ have been consecutively used as initial guesses for the four-parameter

function fit. This way, we obtain a good initial guess for the 5 parameters appearing in Eq. 4.4 so that the five-parameter fit procedure resulted in correct and meaningful values for D, R_e, ω_e, $\omega_\mathrm{e}x_\mathrm{e}$ and α_e. These values can now be used to calculate the rotational constant B_e (Eq. 4.8), the centrifugal distortion constant D_e (Eq. 4.12), the second anharmonic constants $\omega_e y_e$ (Eq. 4.13) and the zero-point energy E_ZPE (Eq. 4.14) as explained below.

Assuming a negligible coupling between the rotation of the molecule and the spins and motions of the electrons, Pekeris [Pek34] proved the centrifugal distortion constants $D_{\mathrm{e},i}$ are given by (for electronic state i):

$$D_{\mathrm{e},i} = \frac{4B_{\mathrm{e},i}^3}{\omega_{\mathrm{e},i}^2}. \tag{4.12}$$

The second anharmonic constants $\omega_{\mathrm{e},i}y_{\mathrm{e},i}$ were determined by imposing that the maximal reachable vibrational energy for the considered electronic state $\max(E_{\nu,i})$ is equal to the depth of its energy well D_i:

$$D_i = \max\left(\omega_{\mathrm{e},i}(\nu+\frac{1}{2}) - \omega_{\mathrm{e},i}x_{\mathrm{e},i}(\nu+\frac{1}{2})^2 + \omega_{\mathrm{e},i}y_{\mathrm{e},i}(\nu+\frac{1}{2})^3\right) \tag{4.13}$$

where the variable ν is the vibrational quantum number. This equation is then solved numerically for $\omega_{\mathrm{e},i}y_{\mathrm{e},i}$.

Finally, the zero-point energy E_ZPE is given by:

$$E_\mathrm{ZPE} = \frac{1}{2}\omega_{\mathrm{e},0} - \frac{1}{4}\omega_{\mathrm{e},0}x_{\mathrm{e},0} + \frac{1}{8}\omega_{\mathrm{e},0}y_{\mathrm{e},0}. \tag{4.14}$$

Applying this procedure to the electronic ground state as well as to the stable excited states, the energies of all rotational-vibrational-electronic (rovibel) levels with respect to the fundamental ground state can be calculated:

$$\begin{aligned} E_{i,\nu,J} = \Delta E_{\mathrm{e},i} &- E_\mathrm{ZPE} \\ &+ \omega_{\mathrm{e},i}(\nu+\frac{1}{2}) - \omega_{\mathrm{e},i}x_{\mathrm{e},i}(\nu+\frac{1}{2})^2 + \omega_{\mathrm{e},i}y_{\mathrm{e},i}(\nu+\frac{1}{2})^3 \\ &+ B_{\mathrm{e},i}J(J+1) - D_{\mathrm{e},i}J^2(J+1)^2 \\ &- \alpha_{\mathrm{e},i}(\nu+\frac{1}{2})J(J+1). \end{aligned} \tag{4.15}$$

with i, ν and J denoting the electronic, vibrational and rotational quantum number respectively.

4.2.4 T-dependent stability of the molecules

Assuming a constant pressure, the temperature-dependent stability of the molecules is described by the difference in Gibbs free energy of the molecular state w.r.t. the unbound state:

$$\begin{aligned}\Delta G(T) = -D &- (E_{\mathrm{tr}}^{\mathrm{A1}} + E_{\mathrm{el}}^{\mathrm{A1}} + E_{\mathrm{tr}}^{\mathrm{A2}} + E_{\mathrm{el}}^{\mathrm{A2}}) \\ &+ (E_{\mathrm{tr}}^{\mathrm{M}} + E_{\mathrm{ZPE}}^{\mathrm{M}} + E_{\mathrm{rovibel}}^{\mathrm{M}}) \\ &+ T(S_{\mathrm{tr}}^{\mathrm{A1}} + S_{\mathrm{el}}^{\mathrm{A1}} + S_{\mathrm{tr}}^{\mathrm{A2}} + S_{\mathrm{el}}^{\mathrm{A2}}) \\ &- T(S_{\mathrm{tr}}^{\mathrm{M}} + S_{\mathrm{rovibel}}^{\mathrm{M}}) - k_{\mathrm{B}}T,\end{aligned} \tag{4.16}$$

where D is the depth of the dissociation profile, E are thermal energy corrections and S are entropic contributions. The superscripts M and A denote molecular and atomic quantities respectively, while the subscripts tr, el and rovibel designate translational, electronic and rotational-vibrational-electronic contributions.

The thermal energy correction due to translation is given by (X= A,M):

$$E_{\mathrm{tr}}^{\mathrm{X}} = \frac{3}{2}RT, \tag{4.17}$$

while the translational contribution to the entropy is:

$$S_{\mathrm{tr}}^{\mathrm{X}} = R\ln\left(\frac{(2\pi m_{\mathrm{X}}k_{\mathrm{B}}T)^{3/2}}{h^3}k_{\mathrm{B}}\frac{T}{P}\right) + \frac{5}{2}R, \tag{4.18}$$

assuming that the particles behave as an ideal gas. Other thermal corrections to the energy are calculated using:

$$E_{(\mathrm{rovib})\mathrm{el}}^{\mathrm{X}} = \frac{\sum\limits_j g_j E_j \exp\left(\frac{-E_j}{k_{\mathrm{B}}T}\right)}{\sum\limits_j g_j \exp\left(\frac{-E_j}{k_{\mathrm{B}}T}\right)} = \frac{\sum\limits_j g_j E_j \exp\left(\frac{-E_j}{k_{\mathrm{B}}T}\right)}{Q(T)}, \tag{4.19}$$

where E_j is the energy of state j with degeneracy g_j and $Q(T)$ being the partition function. For the electronic contributions of the atoms $E_{\mathrm{el}}^{\mathrm{A}}$, the energies E_j are the excitation energies that can be found in the NIST database [Kra18]. For the coupled rotational-vibrational-electronic contributions of the molecules $E_{\mathrm{rovibel}}^{\mathrm{M}}$, they are calculated using Eq. 4.15. The thermal contributions to the entropy are similarly calculated:

$$S_{(\mathrm{rovib})\mathrm{el}}^{\mathrm{X}} = RT\frac{\mathrm{d}\ln Q}{\mathrm{d}T} + R\ln Q. \tag{4.20}$$

As can be seen in Eq. 4.19, a summation over the rotational-vibrational-electronic states is performed to calculate $E^{\mathrm{M}}_{\mathrm{rovibel}}$. All states contributing more than 10^{-6} to the partition function and having an energy lower than the dissociation energy D_0 were included in the sum which was performed as follows:

(i) First the electronic and vibrational ground state is considered and the rotational quantum number J is incremented until the state does not satisfy the criteria above.
(ii) Then the vibrational quantum number ν is incremented by 1 and J is scanned again.
(iii) Finally, when ν becomes high enough so that state ($i = 0, \nu, J = 0$) does not longer satisfy the criteria, the next electronic state is considered.

This procedure is continued until the final contributing electronic state is reached. The process of this summation is explained in detail is discussed in the Supporting Info of Paper II on page 209.

The whole methodology described above results in the central result of this work: the T-dependent stability of the 6 diatomic molecules of interest. The results are presented in paper II on pages 168–168 in this work and in more detail in the Supporting Info of paper II, specifically reprinted on pages 206–208 of this work.

4.2.5 The molar heat capacity

In addition to the temperature dependent Gibbs free energy difference between the molecular and dissociated state, the molar heat capacity c_V of the molecular gases is calculated as this quantity is determined more easily in experiments and is found to be more sensitive to the determined molecular constants than the Gibbs free energy differences. It is given by:

$$c_V = \frac{\mathrm{d}(E_{\mathrm{tr}} + E_{\mathrm{rovibel}})}{\mathrm{dT}}. \tag{4.21}$$

The results are presented in the Supporting Info of Paper II (p. 212).

4.3 Relative occurrence in a gas mixture

Using the T-dependent Gibbs free energy differences between the molecular and unbound states, the relative occurrences of the different Po species in a gas containing Po can be estimated. Given the initial atomic concentrations in the gas, the final molar fractions of the species x_i can be predicted by minimizing the total Gibbs free energy of the system $G_{\mathrm{tot}}(T)$:

$$G_{\mathrm{tot}}(T) = n \sum_{\mathrm{mol}} x_i \Delta G_i(T) + nRT \sum_{\mathrm{mol,at}} x_i \ln(x_i). \tag{4.22}$$

The first term accounts for the formation of molecular bonds and the second for the entropy of mixing. The final relative occurrences depend on the initial concentration of the different elements present in the system under consideration. The latter is controlled by the vapor pressure at the operational temperature and concentration in the liquid metal of the different elements. The estimated initial concentrations (based on Refs. [Sob11, Ohn05, al.16a, Fio18, GP14, Kon13, Feu92, Faz15]) are presented in detail in the Supporting Info of Paper II (pp. 213–215) as well as in Paper II (pp. 170–172) together with the final relative occurrence of the different Po species expected to occur in the plenum gas above the LBE pool in MYRRHA and the Pb-Li eutectic in DEMO both for within the operational temperature range [Eng15, Boc16] as far out of it.

4.4 Complex ^{210}Po -containing molecules

4.4.1 Selection of candidate molecules

Besides diatomic molecules, also more complex Po-containing molecules could appear in the gas mixture. In 2014, transpiration (also called transportation) experiments were performed to investigate the influence of temperature and the presence hydrogen and oxygen on the ^{210}Po evaporation rate from LBE [Riz14]. In these experiments, LBE samples containing ^{206}Po were heated and exposed to a flowing carrier gas. The evaporating ^{206}Po is carried away along a quartz glass tube (to prevent Po adsorption on metal surface) and finally condenses further downstream. By measuring the activity of the sample both before and after the experiment, as well as the activity of the condensed ^{206}Po, the amount of evaporated ^{206}Po can be determined. An increased evaporation rate (10-100 times higher) was observed when using H_2 as carrier gas instead of He. This effect

was even more apparent when a thin oxide layer was found to have formed on the LBE sample. This enhanced evaporation can only be the result of the formation of a Po-species with a volatility larger than the ones of elemental Po and the metal polonides.

An increased Po evaporation in the presence of moisture and/or hydrogen has been observed and reported before, but the volatile species causing the higher evaporation rate has never been properly characterized. The performed transpiration experiments seem to suggest a polonium hydride, probably H_2Po, as evaporating species. According to a previous report, however, H_2Po is only formed when hydrogen is present in an activated form. Also extrapolated data from analogue chalcogen compounds suggested that the formation of H_2Po is thermochemically unfavorable. However, a formation of H_2Po could possibly be explained by assuming that the observed thin oxide layer is serving as a catalyst in the H_2Po production process. In addition, a lower formation rate of the highly volatile Po species was observed at higher temperatures, an indication for a low thermal stability of the formed volatile species (a characteristic attributed to H_2Po).

Nevertheless, thermochromatography experiments performed in the same year [Mau14], found no evidence of an enhanced Po evaporation in presence of dry H_2, but only when using moist He or H_2. These experiments also indicated the formation of more than one highly volatile Po compound. The crucial role of moisture in the formation of the highly volatile Po species points into the direction of a volatile hydroxide rather than a hydride. The increased evaporation rate observed in the transpiration experiments could in that case be explained by oxygen impurities still present in the H_2 carrier gas or by an interaction of the H_2 carrier gas with the oxide layer on the sample, producing H_2O which can then interact with the polonium.

Based on this discussion and chemical intuition 4 complex Po-containing molecules of primary interest are identified: H_2Po, PoO_2, H_2PoO_2 and H_2PoO_3. The former three of these molecules have been studied using the high level-of-theory HF/CASSCF/CASPT2/(SO-)CASSI ab inito method. The latter was found to be computationally too demanding to be treated at this high level-of-theory and was therefore not considered in this work.

4.4.2 Dissociation well depth

For the treatment of these complex Po-containing molecules, a similar strategy is used as for the diatomic molecules i.e. chemical analogues in which Po is substituted by a lighter element of group VI (S, Se or Te) were used to determine the best choice for the active space (within computational reach). Also the check for convergence w.r.t. the number of CI roots included in the CASSCF/CASPT2 calculations is performed in the same way as has been done for the diatomic molecules.

A major difference exists in the fact that a diatomic is a linear molecule. Therefore the equilibrium geometry can be obtained simply by performing a scan on the internuclear distance. The considered complex molecules, however, have more than one degree of freedom. Molcas does not allow to obtain forces at the used level-of-theory. Therefore, the optimization had to be performed manually by scanning over all degrees of freedom. Similarly as in an automated optimization procedure, a certain initial compound structure is assumed for which the parameters are then optimized. While optimizing this structure based on a static energy minimization, the compound can not cross energy barriers towards potentially more stable isomers (molecular (meta)dynamics is required for this purpose). Therefore, the characteristics of the assumed structure for the compound are maintained (unless the structure under consideration is in fact unstable).

The initial guesses for the structure of the Po-containing compounds are based on the reported structures of their chemical analogues. Both H_2Po and PoO_2 are therefore assumed to be symmetric non-linear molecules. Regarding the H_2PoO_2 molecule, only on the structure of the H_2SO_2 analogue (ab initio) data was found in literature [Ste92, May83, Nap08]. These studies showed that the two most stable isomers were found to be very close in energy. Therefore, a manual geometry optimization of H_2PoO_2 was performed for both of these isomeric structures.

The depth of the potential energy well D is obtained by comparing the energy obtained for the optimized geometries with the one of the fully dissociated state. H_2Po was dissociated to two free hydrogen atoms and one polonium atom, while PoO_2 was dissociated to two oxygen atoms and one polonium atom. For the H_2PoO_2 molecule, advantage was taken of the result obtained for PoO_2 by instead considering a dissociation to PoO_2 and two free hydrogen atom. The total energy well depth is then obtained by

adding the contribution of the full dissociation of PoO_2.

4.4.3 T-dependent stability of the molecules

Zero-point vibrational energy

Molcas does not allow to calculate the forces at the used level-of-theory which includes the spin-orbit interaction. For the triatomic symmetric non-linear molecules H_2Po and PoO_2 the zero-point vibrational energy was therefore manually deduced from the obtained ab-initio energies by determining the frequencies of the vibrational normal modes. The latter were obtained by applying a vibrational analysis based on the assumption of pure valence forces. In this analysis, a strong restoring force is assumed in the line of every valence bond (the two Po–H bonds for H_2Po and the two Po–O bonds for PoO_2). In addition, a restoring force opposing a change of the angle between two valence bonds is assumed ($\widehat{\mathrm{HPoH}}$ and $\widehat{\mathrm{OPoO}}$ for H_2Po and PoO_2 respectively). Making these assumptions for a non-linear symmetric XY_2 molecule, the potential energy is given by (neglecting higher order terms) [Her56]:

$$V = \frac{k_1}{2}\left(Q_1^2 + Q_2^2\right) + \frac{k_\delta}{2}\delta^2, \tag{4.23}$$

where Q_1 and Q_2 are the absolute value of the changes in the X–Y distance with respect to the equilibrium bond distance l for the two equivalent bonds, and δ is the absolute value of the change in the $\widehat{\mathrm{YXY}}$ angle with respect to the equilibrium angle 2α (expressed in radians). k_1 and k_δ are the force constants corresponding to the stretching of a bond and the bending of the molecule's angle respectively.

The main assumption in this valence field approach (VFA) is that there are no cross terms in the potential energy function if it is expressed as a function of Q_i and δ (called the valence force coordinates). Making this assumption, the frequencies for the symmetric stretch (ν_1), the bending (ν_2) and the asymmetric stretch (ν_3) normal modes can be obtained from:

$$4\pi^2\nu_3^2 = \frac{k_1}{m_\mathrm{Y}}\left(1 + \frac{2m_\mathrm{Y}}{m_\mathrm{X}}\sin^2\alpha\right), \tag{4.24a}$$

$$4\pi^2\left(\nu_1^2 + \nu_2^2\right) = \frac{k_1}{m_\mathrm{Y}}\left(1 + \frac{2m_\mathrm{Y}}{m_\mathrm{X}}\cos^2\alpha\right) + \frac{2}{m_\mathrm{Y}}\frac{k_\delta}{l^2}\left(1 + \frac{2m_\mathrm{Y}}{m_\mathrm{X}}\sin^2\alpha\right), \tag{4.24b}$$

$$16\pi^4\nu_1^2\nu_2^2 = \frac{2k_1}{m_\mathrm{Y}^2}\frac{k_\delta}{l^2}\left(1 + \frac{2m_\mathrm{Y}}{m_\mathrm{X}}\right), \tag{4.24c}$$

where m_{X} and m_{Y} denote the masses of the central atom X and of of the adjacent atoms Y respectively. Note that k_δ/l^2 has the dimension of a force constant, as is the case for k_1.

From the obtained normal mode frequencies, the zero-point energy can be determined:

$$E_{\mathrm{ZPE}} = \frac{1}{2}h\left(\nu_1 + \nu_2 + \nu_3\right). \tag{4.25}$$

In practice, this approach boils down to determining the equilibrium bond distance l, the equilibrium bond angle 2α, the stretching force constant k_1 and the bending force constant k_δ. The former two were determined using the manual geometry optimization procedure described above (efficiently scanning the bond distance and angle until the geometry of minimal energy is found). The stretching force constant k_1 is determined by examining the variation in energy as the bond is stretched or compressed starting from the equilibrium geometry. The obtained energy describes a quadratic behavior against the bond length change with respect to the equilibrium geometry. As the bond angle remains the same, Eq. 4.23 is reduced to $V = k_1/2\left(Q_1^2 + Q_2^2\right)$. By performing a quadratic fit, k_1 can thus be determined. A similar procedure is followed to obtain k_δ, but this time keeping the bond length constant and bending the molecule. The obtained molecular constants (l,α,k_1,k_δ) and the masses of the constituting atoms is then filled out in Eq. 4.24 to obtain the three normal mode frequencies, which can be finally used to determine the zero-point energy E_{ZPE} using Eq. 4.25. To validate this procedure, it is also applied to the SO_2, SeO_2 and TeO_2 molecules for which the results can be compared available experimental data.

For the H_2PoO_2 molecule, this approach for determining the zero-point energy was found to be computationally to expensive due to the many more degrees of freedom (9 with respect to 3), and the more time-consuming calculations. Due to the lack of reported data for its lighter chemical analogues, extrapolation of the zero-point energies of these molecules was no option either. Instead, complementary lower level-of-theory CASPT2 calculations were performed on H_2PoO_2, as at these levels Molcas does in fact include a routine (MCKINLEY) which allows to determine the Hessian and E_{ZPE}. It should be noted that the largest contributions to E_{ZPE} for this molecule stem from the movement of the hydrogen atoms, which are bound to an oxygen atom. These O–H bond can be properly described at the lower level-of-theory as the spin-orbit coupling for this bond is negligible. Larger (relative) errors are expected to result from the Po–O bond stretch and and the $\widehat{\mathrm{OPoO}}$ bending, as in these bonds spin-orbit coupling, which is no longer

included, plays a major role. To obtain an estimate of the magnitude of the introduced errors, the same procedure was also applied to PoO_2 and the results are then compared with the ones obtained using the valence force approach described above.

Having estimated the zero-point energy for all three molecules, these contributions can be added to the depth of the energy potential well in order to obtain the dissociation energy at 0 kelvin:

$$\Delta G_{0\,\mathrm{K}} = \Delta H_{0\,\mathrm{K}} = D_0 = D + E_{\mathrm{ZPE}}. \tag{4.26}$$

Temperature dependence of the Gibbs free energy difference

Determining the temperature-dependent stability of the H_2Po, PoO_2 and H_2PoO_2 molecules at the SO-CASSI level-of-theory is computationally too demanding. Instead, the *FactSage* Thermochemical Database System [al.16a] was used to extract useful date on the lighter chemical analogues, which was then extrapolated to the Po-containing molecules. This data was used to extract the following two properties:

(i) Change in the Gibbs free energy difference (for the molecule w.r.t. the dissociated state) between 0 K and 298 K (i.e. the starting temperature of the FactSage database), and
(ii) The T-dependence of the Gibbs free energy difference from 298 K onward.

The final result is a temperature-dependent Gibbs free energy difference between the equilibrium molecular state and the dissociated state for the H_2Po, PoO_2 and H_2PoO_2 molecules. This new data can in the future be used in extensive thermodynamic models aiming to simulate the ^{210}Po evaporation behavior from liquid LBE or Pb-Li in presence of H_2, H_2O and O_2. These models could be used to assess the risk for a given accident scenario or to devise efficient Po extraction techniques. Moreover, the obtained results will also help to interpret the observations made during the transpiration and thermochromatography experiments discussed at the start of this section [Riz14, Mau14].

5

Results – Molecular occurrence of ^{210}Po in MYRRHA and DEMO

5.1 Verifcation of the CASSCF/CASPT2/SO-CASSI method

The suitablilty of the CASSCF/CASPT2/SO-CASSI approach to properly address the strong spin-obit effects in molecules containing elements as heavy as Po and the electron correlation effects crucial for all bond dissociation processes, has been examined by doing a literature review on the performance of this method on similar molecules. In addition, extensive test calculations have been performed on the PbO, Pb_2 and Po_2 molecules. A full discussion on this literature review and the performed tests can be found in the Supporting Info of paper II, specifically on pages 190–198 of this work.

5.2 Validation of the active space

The active space used in the calculations on the Po-containing molecules has not been simply chosen based on reported general guidelines, instead a whole series of possible active spaces have been quantitatively validated to select the one with the best performance. As no experimental data is

available for the Po-containing molecules (except for Po_2), this validation is achieved by performing calculations on the (lighter) chemical analogues of the studied molecules, i.e. the Po atom was successively substituted by other elements from the same group VI of the periodic table (O, S, Se and Te). For most of these diatomic molecules, experimental data is available and the dissociation energies obtained through ab initio calculations using different active spaces can be compared to their experimental counterpart. Doing so for each substituting atom in the considered series, an average performance in terms of overall accuracy can be obtained for each of the active spaces tested. The active space performing best for the chemical analogues of a given Po-containing molecule, is then assumed to be most suited for this molecule as well. A detailed discussion on how this validation method was performed and which active space definitions were tested, can be found in the Supporting Info of paper II and is reprinted specifically on page 182 of this work.

Figures 5.1 and 5.2 show the obtained dissociation energies at 0 K (D_0) for the single substitution and double substitution series respectively, obtained using the corresponding best performing active space. For all series, a quasi-linear decreasing trend in the dissociation energy is found with increasing period (row) of the constituting elements (the only exception is the SO molecule having a dissociation energy higher than the homoatomic O_2 molecule). This suggests that the dissociation energy of a Po-containing compound could be estimated by extrapolating the experimental values reported for the chemical analogues containing Se and Te. However, it was found that this quasi-linearity cannot be exploited to make reliable predictions, as for some series this extrapolation results in a value deviating by more than 0.5 eV from the one obtained by direct calculation.

In the Supplementary Info of paper II, the obtained dissociation energies for all studied molecules in the series are explicitly compared to their experimental counterparts (see Figures A.16–A.23 on pages 186–189 of this work). Figure 5.3 shows the overall comparison between the calculated dissociation energies and the corresponding experimental values reported by Huber and Herzberg [Hub79] for all considered chemical analogues and Po_2 (i.e. all studied molecules for which this experimental value exists). The diagonal solid line represents the exact match, while the dashed lines correspond to a deviation of respectively -0.25 eV and +0.25 eV. All molecules are found to lie well within this defined strip with the exception of four outliers: OH, NO, PbO and SbTe.

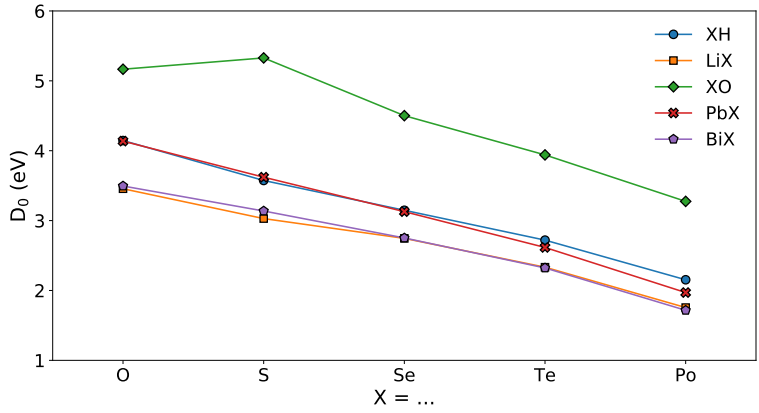

Figure 5.1: The obtained SO-CASSI dissociation energies at 0 K (D_0) for all single substitution series used in the validation procedure, obtained using the best performing active space for each of those series.

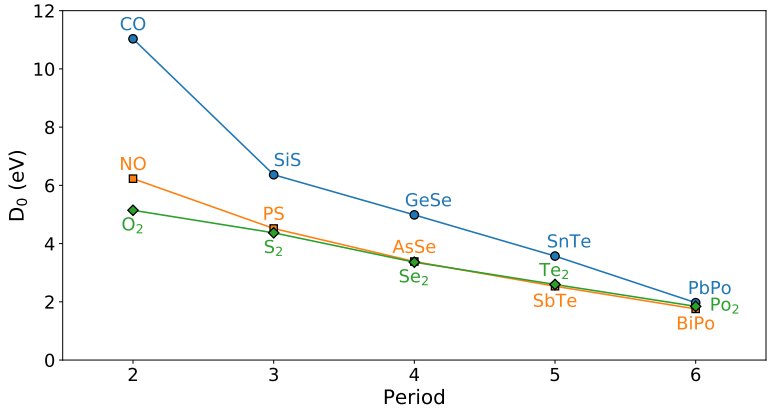

Figure 5.2: The obtained SO-CASSI dissociation energies at 0 K (D_0) for all double substitution series used in the validation procedure, obtained using the best performing active space for each of those series.

The former three of these outliers are all the lightest variant of a given chemical analogue series. It was found that for these particular molecules, the order of the orbital energies is shifted, making the definition used for the overall best performing active space not suitable for these particular molecules. Therefore, they do not represent reliable and optimized results

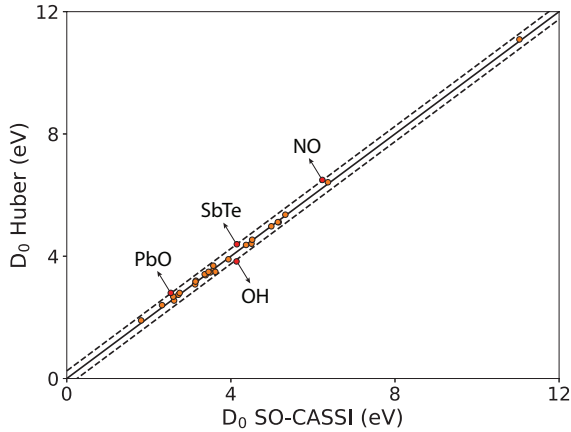

Figure 5.3: Comparison of the calculated dissociation energies with the experimental value reported by Huber and Herzberg [Hub79], for all considered chemical analogues and Po_2 (i.e. all molecules for which this experimental value exists). The diagonal solid line represent the exact match, while the dashed lines correspond to a deviation of respectively -0.25 eV and +0.25 eV. Four outliers are identified: OH, NO, PbO and SbTe.

and are thus not representative for the performance of the used method and active space. For the SbTe molecule, the obtained dissociation energy was 2.54 eV, which is found to considerably deviate from the reported value by Huber and Herzberg (2.8 eV). However, another experimental dissociation energy for this molecule has been reported by Darwent et al. [Dar70], being 2.6 eV and thus much closer to the calculated value, which cast some suspicion on the value reported by Huber. It should be noted that for many less often studied molecules, the range of reported dissociation energies easily spans over 0.2 eV. When leaving out the four identified outliers (which can be justified by the explanation above), the mean absolute deviation between the calculated values and the values reported by Huber is found to be only 0.05 eV, which is of the same magnitude as the average range in which experimental values are reported and thus showing an excellent agreement. Based on this value and the verified accuracy of the CASSCF/CASPT2/SO-CASSI approach for molecules containing period 6 main group elements, the calculated dissociation energies for the Po-containing molecules are expected to be correct within 0.1 eV.

5.3 Electron correlation and spin-orbit effects

In this section, the importance of properly accounting for electron correlation effects (for all molecules) and spin-orbit effects (for heavy molecules) is explicitly highlighted. To demonstrate this, the dissociation energies for Po_2 and its chemical analogues O_2, S_2, Se_2 and Te_2 obtained at different ab initio level-of-theory are presented in Figure 5.4. Also included in this figure are the experimental values for these dissociation energies as reported by Huber and Herzberg [Hub79].

The first thing that can be noticed is that Hartree-Fock predicts a completely wrong dissociation energy, which is considerably overestimated. This is due to the fact that Hartree-Fock does not include correlation energy. The correlation energy depends strongly on the internuclear distance in the system. Therefore, although being capable of producing useful results on conformational properties of a molecule e.g. predicting the rotational barrier in ethane, it is not suitable to predict bond dissociation energies.

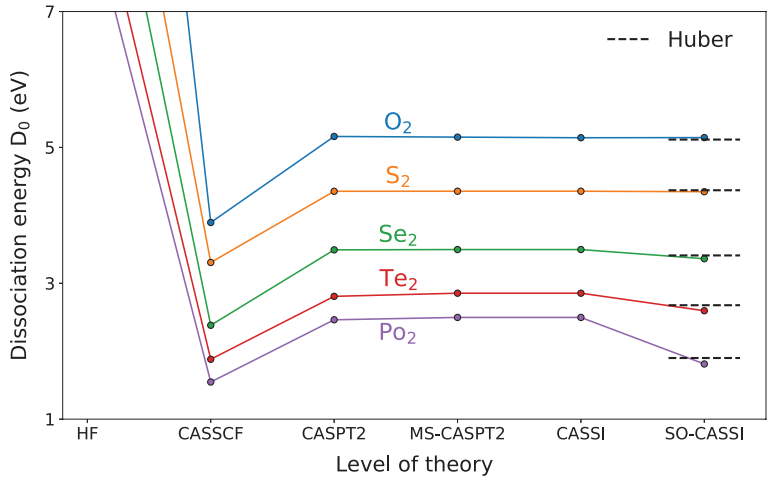

Figure 5.4: The dissociation energies for Po_2 and its chemical analogues O_2, S_2, Se_2 and Te_2, obtained different ab initio level-of-theory. The experimental dissociation energy reported by Huber and Herzberg [Hub79] is also included. This figure clearly visualizes the importance of including electron correlation for all of these molecules and of including spin-orbit coupling effects for the ones including heavy elements.

The inclusion of (primarily static) electron correlation through the CASSCF method is found to considerably destabilize the molecule. When accounting for (primarily dynamic) electron correlation, the molecule is found to recover part of its stability. These effects are found to be most prominent in the O_2 molecule, but are found to be crucial in the calculation of the dissociation energy for all molecules. Without properly including the electron correlation effects, no reliable dissociation energies can be obtained.

The resulting CASPT2 energy for O_2 is almost identical to the experimentally reported one, without the need for including spin-orbit effects. This is because spin-orbit effects are very small in row-2 elements. However, the magnitude of the spin-orbit coupling effect on the bond dissociation energy clearly grows as the period of the constituting elements increases. The spin-orbit coupling effect is larger for heavier elements due to the higher charge contained within the nucleus, resulting in faster moving electrons with the central ones approaching the speed of light (classically speaking). Therefore the electron's orbital angular momentum increases, which then couples more strongly to their spin angular momentum (through the magnetic fields these two momenta generate). Spin-orbit coupling is found to destabilize the bond dissociation energy. It should be noted though that in fact spin-orbit coupling both stabilizes the dissociated atoms and the molecule, but this effect is found to be larger for the dissociated atoms, thus decreasing the overall bond energy.

For the Po_2, this effect results in a reduction of the dissociation energy by 0.71 eV (for PbPo even as much as 1.68 eV). Therefore, it is impossible to obtain reliable values of the dissociation energy for molecules involving heavy elements without properly accounting for spin-orbit coupling. This can be seen in the figure, as only the spin-orbit corrected dissociation energies are in good agreement with the experimentally observed values. This result shows that the CASSCF/CASPT2/SO-CASSI approach provided by Molcas is capable of producing reliable dissociation energies, even for molecules including row-6 elements.

5.4 Diatomic Po-containing molecules

The most significant results on diatomic Po-containing molecules have been condensed in a letter entitled 'Po-containing molecules in fusion and fission reactors', which is accompanied by extensive Supporting Info and

has been published in the peer reviewed international scientific *Journal of Physical Chemistry Letters*, **2019**, *10* (11), 2879–2884 [Mer19a]. The author of this Ph.D. dissertation has performed all calculations required to obtain the results presented in this letter and has fully written the text, which is reprinted with permission from Merlijn A. J. Mertens, Alexander Aerts, Ivan Infante, Jörg Neuhausen, and Stefaan Cottenier, Po-containing molecules in fusion and fission reactors, *Journal of Physical Chemistry Letters* 2019, **10** (11), 2879–2884, June 2019 (copyright 2019 American Chemical Society) on pages 163–173 (letter) and pages 177–215 (Supplementary Info) of this work. This section discusses the most important results presented in this letter.

5.4.1 Hulburt-Hirschfelder fits and molecular constants

As discussed in section 4.2.3, for every studied diatomic molecule, analytical 5-parameter Hulburt-Hirschfelder functions $f(D, R_\mathrm{e}, \omega_\mathrm{e}, x_\mathrm{e}, \alpha_\mathrm{e})$ [Hul41] are fitted to the obtained ab initio SO-CASSI data points for a varying internuclear distance between the constituent atoms (for each electronic state i). The resulting fits and the corresponding molecular constants for all studied diatomic Po-containing molecules are presented in the Supporting Info of paper II, specifically on pages 201–205 of this work. For the electronic ground state, the molecular constants are given in Table 5.1.

Table 5.1: The obtained molecular constants for the ground state of the 6 studied Po-containing diatomic molecules.

Quantity	PoH	LiPo	PoO	PbPo	BiPo	Po_2
D(eV)	2.26	1.78	3.31	2.01	1.74	1.84
R_e(Å)	1.782	2.639	1.944	2.730	2.770	2.797
ω_e(cm^{-1})	1773	362.1	648.8	166.9	164.1	151.8
$\omega_\mathrm{e}x_\mathrm{e}$(cm^{-1})	34.7	2.49	2.66	0.316	0.336	0.312
$\omega_\mathrm{e}y_\mathrm{e}$(10^{-3}cm^{-1})	-425	2.6	-17	-0.62	-0.90	-0.40
B_e(10^{-2}cm^{-1})	533	35.7	30.0	2.16	2.10	2.05
D_e(10^{-6}cm^{-1})	193	1.39	0.256	0.00146	0.00137	0.00150
α_e(10^{-3}cm^{-1})	150	2.86	1.87	0.0486	0.0524	0.0524

As an illustration, Figure 5.5 shows the SO-CASSI data points and the obtained Hulburt fits for all stable electronic states of the PbPo molecule. The corresponding molecular constants obtained from this fitting procedure for all electronic states are presented in Table 5.2.

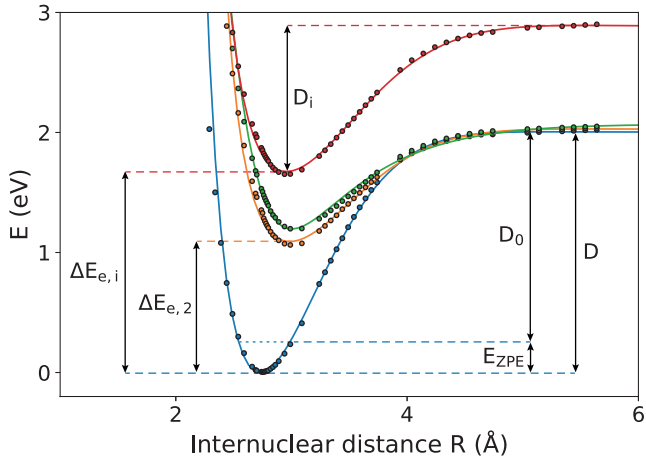

Figure 5.5: Computed data points for the ground state and first excited states of PbPo with associated fits $f(D, R_e, \omega_e, x_e, \alpha_e)$.

Table 5.2: Molecular constants for the ground and first excited states of **PbPo** (obtained by fitting Eq. A.13 to the data points).

i	$\Delta E_{e,i}$ eV	D eV	R_e Å	ω_e cm^{-1}	$\omega_e x_e$ cm^{-1}	$\omega_e y_e$ $10^{-3}cm^{-1}$	B_e $10^{-3}cm^{-1}$	D_e $10^{-6}cm^{-1}$	α_e $10^{-3}cm^{-1}$
1	0.000	2.008	2.730	166.9	0.3159	-0.6233	21.65	0.001457	0.04862
2	1.091	0.938	2.985	106.5	0.2400	-1.022	18.11	0.002093	0.05346
3	1.091	0.939	2.984	106.7	0.2436	-1.001	18.11	0.002089	0.05364
4	1.222	0.831	3.019	103.7	0.2027	-1.689	17.71	0.002065	0.05727
5	1.196	0.874	3.002	123.1	0.3970	-1.297	17.90	0.001513	0.06772
6	1.674	1.213	2.955	111.6	0.2290	-0.5426	18.47	0.002022	0.04704

5.4.2 T-dependent Gibbs free energy difference

The whole set of molecular constants determined for a specific diatomic molecule, allows to determine the energies of all coupled rotational-vibrational-electronic levels (w.r.t. the fundamental ground state) of that molecule. The latter can then be used to finally obtain the sought-after temperature-dependent stability of this molecule (i.e. the difference in Gibbs free energy of the molecular state w.r.t. the unbound state), as explained in section 4.2.4. The stability for the diatomic Po-containing molecules was calculated for 73 temperatures ranging between 1 K and 1441 K, in 20 K intervals. The result is shown in Figure 5.6 and can be accurately approximated by a 4^{th} order polynomial, which allows to recalculate the Gibbs free energy difference with a relative error below 0.3 % between 0 K and 1441 K:

$$\Delta G_{\mathrm{PoH}} = -2.158 + 6.294 \cdot 10^{-4} T + 5.090 \cdot 10^{-7} T^2 - 3.392 \cdot 10^{-10} T^3 + 8.827 \cdot 10^{-14} T^4$$

$$\Delta G_{\mathrm{LiPo}} = -1.769 + 6.730 \cdot 10^{-4} T + 3.417 \cdot 10^{-7} T^2 - 2.550 \cdot 10^{-10} T^3 + 7.059 \cdot 10^{-14} T^4$$

$$\Delta G_{\mathrm{PoO}} = -3.281 + 8.989 \cdot 10^{-4} T + 5.132 \cdot 10^{-7} T^2 - 3.797 \cdot 10^{-10} T^3 + 10.32 \cdot 10^{-14} T^4$$

$$\Delta G_{\mathrm{PbPo}} = -2.004 + 7.701 \cdot 10^{-4} T + 2.461 \cdot 10^{-7} T^2 - 1.768 \cdot 10^{-10} T^3 + 4.914 \cdot 10^{-14} T^4$$

$$\Delta G_{\mathrm{BiPo}} = -1.734 + 8.272 \cdot 10^{-4} T + 2.420 \cdot 10^{-7} T^2 - 1.716 \cdot 10^{-10} T^3 + 4.646 \cdot 10^{-14} T^4$$

$$\Delta G_{\mathrm{Po_2}} = -1.838 + 9.013 \cdot 10^{-4} T + 2.352 \cdot 10^{-7} T^2 - 1.667 \cdot 10^{-10} T^3 + 4.555 \cdot 10^{-14} T^4$$

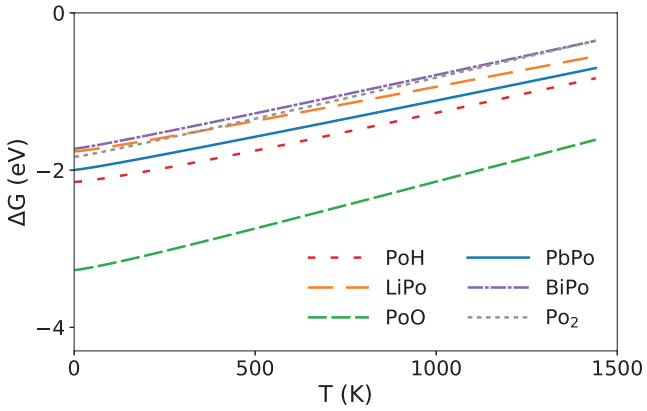

Figure 5.6: The difference in Gibbs free energy ΔG of the Po-containing molecules compared to the atomic fragments.

The temperature ranges relevant for the discussed types of reactors are fully covered. As expected, temperature destabilizes the molecules. PoO is found to be the most stable molecule over the whole temperature range, followed by PoH, PbPo, BiPo/LiPo and finally Po_2. The detailed procedure used to obtain all contributions to the presented Gibbs free energy differences is presented in the Supporting Info of paper II, specifically on pages 206–209 of this work.

5.4.3 Relative occurrence in a gas mixture

Using the obtained T-dependent stability of the different Po species, their relative occurrence in a Po-containing gas can be estimated by minimizing the total Gibbs free energy of the system $G_{\mathrm{tot}}(T)$:

$$G_{\mathrm{tot}}(T) = n \sum_{\mathrm{mol}} x_i \Delta G_i(T) + nRT \sum_{\mathrm{mol,at}} x_i \ln(x_i), \tag{5.1}$$

where the first term accounts for the formation of molecular bonds and the second for the entropy of mixing. The final molar fractions of the species x_i depend on the initial concentration of the different elements. Two realistic scenarios are described.

In the first scenario, the Ar gas atmosphere (P_{Ar} = 101300 Pa) covering the LBE coolant in the MYRRHA fast fission reactor is considered. The initial Pb and Bi concentrations in this gas are calculated using the LBE total vapor pressure recommended by Sobolev [Sob11], while the Pb and Bi fractions in the LBE vapor were determined from the paper by Ohno et al. [Ohn05]. In the equation below, P' denotes a partial vapor pressure and P a total vapor pressure. The superscripts indicate the references the values were taken from. The full derivation of the expressions is presented in in the Supporting Info on pp. 213–215. The final initial concentrations are:

$$c_{\mathrm{Pb}} = \frac{P'_{\mathrm{Pb,LBE}}}{P_{\mathrm{tot}}} \approx \frac{P^{[25]}_{\mathrm{LBE}}}{P_{\mathrm{Ar}}} \frac{P'^{[26]}_{\mathrm{Pb,LBE}}}{P^{[26]}_{\mathrm{LBE}}} = \frac{10^{9.256-9494/T}}{101300\ \mathrm{Pa}} \tag{5.2}$$

$$\begin{aligned} c_{\mathrm{Bi}} &= \frac{P'_{\mathrm{Bi,LBE}} + 2P'_{\mathrm{Bi_2,LBE}}}{P_{\mathrm{tot}}} \approx \frac{P^{[25]}_{\mathrm{LBE}}}{P_{\mathrm{Ar}}} \left(\frac{2P'^{[26]}_{\mathrm{Bi_2,LBE}} + P'^{[26]}_{\mathrm{Bi,LBE}}}{P^{[26]}_{\mathrm{LBE}}} \right) \\ &= \frac{10^{9.973-9488.4/T}}{101300\ \mathrm{Pa}} \frac{2}{1+\alpha^{[26]}} \left(1 - 10^{-0.83+300/T}\right) \end{aligned} \tag{5.3}$$

with the Bi_2–Bi dissociated fraction α:

$$\alpha^{[26]} = \left(\frac{K_P^{[27]}}{\frac{10^{10.688-9794.2/T} - 10^{9.858-9494.2/T}}{101300\ \mathrm{Pa}} + K_P^{[27]}} \right)^{1/2} \tag{5.4}$$

$$K_P^{[27]} = \exp\left(-24442.5/T + 12.5839\right). \tag{5.5}$$

The Bi_2–Bi equilibrium constant K_P was determined from the Gibbs free energy difference between Bi_2 and atomic Bi, available in the FactSage database [al.16a]. After the first irradiation campaign, 350 grams of ^{210}Po is expected to be present in the 7600 ton of LBE [Fio18], resulting in an atomic fraction of $x_{\mathrm{Po}} = 4.6 \times 10^{-8}$. The Henry constant of Po in LBE ($K_{\mathrm{Po,LBE}}$) by Prieto et al. [GP14] was used to determine the initial concentration of atomic Po in the Ar gas:

$$c_{\mathrm{Po}} = \frac{x^{[28]}_{\mathrm{Po}} K^{[29]}_{\mathrm{Po,LBE}}}{P_{\mathrm{tot}}} = \frac{4.6 \times 10^{-8} \cdot 10^{10.8\pm0.7-(8606\pm726)/T}}{101300\ \mathrm{Pa}}. \tag{5.6}$$

It is assumed that no O and H is present in the gas mixture and we allow the formation of PbPo, BiPo, Po_2, PbBi, Bi_2 and Pb_2 to minimize the Gibbs free energy (Eq. 5.1).

In the second scenario, the inert gas covering the liquid Pb-Li breeder in the DEMO fusion reactor is considered ($P_{\text{inter gas}}$ = 101300 Pa). The initial concentrations of Pb and Li in this gas were obtained using the vapor pressures reported by Kondo et al. [Kon13]:

$$c_{\text{Pb}} = \frac{P'^{[30]}_{\text{Pb,Pb-Li}}}{P_{\text{tot}}} = \frac{5.450 \times 10^9 \exp\left(-22246/T\right)}{101300\ \text{Pa}} \tag{5.7}$$

$$c_{\text{Li}} = \frac{P'^{[30]}_{\text{Li,Pb-Li}}}{P_{\text{tot}}} = \frac{8.058 \times 10^9 \exp\left(-25229/T\right)}{101300\ \text{Pa}}. \tag{5.8}$$

After the first irradiation campaign, about 0.5 grams of ^{210}Po is expected to be present in 8000 tons of Pb-Li ($x_{\text{Po}} = 5 \times 10^{-11}$). The recommended Henry constant of Po in Pb-Li $K_{\text{Po,Pb-Li}}$ [Faz15] was used to determine the initial concentration of Po in the inert gas:

$$c_{\text{Po}} = \frac{x_{\text{Po}} K'^{[31]}_{\text{Po,Pb-Li}}}{P_{\text{tot}}} = \frac{5 \times 10^{-11} \cdot 10^{7.39-6017/T}}{101300\ \text{Pa}}. \tag{5.9}$$

Again, no O and H is present in the gas mixture and now the formation of PbPo, LiPo, Po_2, Pb_2 and Li_2 is allowed to minimize the Gibbs free energy (Eq. 5.1).

Figure 5.7 shows the obtained relative occurrence of the Po species for the discussed scenarios. The green areas represent the normal operational temperature range of MYRRHA (540 K−680 K [Eng15]) and DEMO (570 K − 820 K [Boc16]) respectively. The gray band around the Po_2 line originates from the uncertainties in Eq. 5.6. The predicted relative occurrence ranges within the operational range for both reactors are given in Table 5.3.

For both scenarios, PbPo is found to be the dominant species (in agreement with the conjecture made by Feuerstein in 1992 [Feu92]), however also a non-negligible share of atomic Po is expected to be present. If a dedicated radiological accident assessment shows that the ^{210}Po inventory is too high in the cover gas, filtering techniques will have to be devised that focus on these species. It has to be noted that in case the LBE coolant/Pb-Li breeder makes contact with water (e.g. a leak of coolant accident), this assessment becomes much more complex. In this case, the PoH and

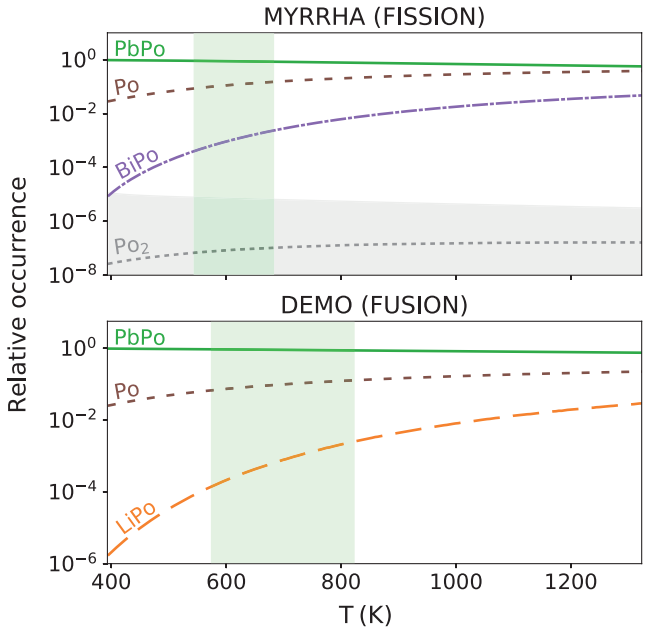

Figure 5.7: The relative occurrence of the ^{210}Po species in the cover gas of (i) the LBE coolant in the MYRRHA fission reactor and (ii) the Pb-Li breeder of the DEMO fusion reactor. Operational temperature ranges are marked in green [Eng15, Boc16].

Table 5.3: The relative occurrence of the different Po species in the cover gas of the LBE coolant in MYRRHA and the Pb-Li breeder in DEMO at the minimal and maximal operational temperature. At all other operational temperatures, the relative occurrence lies between these limiting values.

	MYRRHA		**DEMO**	
Rel. Occ. (%)	T_{min} 540 K	T_{max} 680 K	T_{min} 570 K	T_{max} 820 K
PbPo	91.6	84.7	93.3	86.9
Po	8.4	15.0	6.7	12.8
BiPo	0.037	0.23	n/a	n/a
LiPo	n/a	n/a	0.014	0.25
Po_2	7.0×10^{-8}	1.0×10^{-7}	$<10^{-10}$	$<10^{-10}$

PoO molecules have to be included as well as all other stable O and H containing molecules that could retain most of the available H and O. Also, evidence exists that some very volatile Po-containing (oxy)hydroxides could

form under these conditions [Mau14]. The primary candidates for these Po-containing (oxy)hydroxides have been determined based on chemical intuition (the preferred oxidation state of Po) and the reported existence of lighter chemical analogues. The T-dependent stability of these complex Po-containing molecules is determined in the next section and allows to assess the appearance form of gaseous Po in a broader range of realistic scenarios.

5.5 Complex Po-containing molecules

In section 5.4, the T-dependent stability of 6 diatomic Po-containing molecules of interest has been determined: PoH, LiPo, PoO, PbPo, BiPo Po_2. Recent experimental observations in transpiration and thermochromatography experiments suggest the formation of a highly volatile Po-containing hydroxide (see section 4.4). Therefore, in this section, the T-dependent stability of 3 more complex Po species containing H and/or O is determined: H_2Po, PoO_2 and H_2PoO_2. To validate the used procedure, also calculations on their lighter chemical analogues (Po→S, Se or Te) are performed. The first goal is to obtain a converged and well-founded value for the depth of the dissociation well.

5.5.1 Dissociation well depth

H_2Po and chemical analogues

For these molecules, the most appropriate active space (based on the comparison of the obtained energies with literature and the computational feasibility) was found to include:

(i) the valence p orbitals of the group VI element (S, Se, Te ,Po),
(ii) the valence 1s orbital of both H atoms, and
(iii) the 6 active electrons present in the above orbitals.

As a (manual) geometry optimization at the SO-CASSI level-of-theory is quite demanding, only the H_2Po geometry has been fully optimized. The geometry of the triatomic non-linear H_2S, H_2Se and H_2Te molecules is obtained from the literature [Hou05, NIS, Hay16]. The considered geometries for H_2S, H_2Se and H_2Te, as well as the optimized geometry for H_2Po are listed in Table 5.4.

Table 5.4: The X–H bond length and $\widehat{\text{HXH}}$ angle used in the calculations on the H_2S, H_2Se, H_2Te and H_2Po, as well as the obtained depth of the potential energy well D.

H_2X	geometry from literature			optimized
	H_2S	H_2Se	H_2Te	H_2Po
Bond length (Å)	1.336	1.460	1.690	1.776
Angle (°)	92.10	91.00	90.00	89.87
Well depth D (eV)	-7.722	-6.785	-5.737	-4.538

The geometric parameters obtained for H_2Po are found to follow the expected trends i.e. increasing bond lengths and decreasing bond angles. Also the obtained depth of the potential energy well D is in accordance with the decreasing trend observed for the chemical analogues. The obtained values of D for the lighter chemical analogues will be compared to the ones reported in literature after they have been corrected for the zero-point energy and the temperature effects at 298.15 K in the next sections.

PoO_2 and chemical analogues

The most appropriate active space (based on the comparison of the obtained energies with literature and the computational feasibility) was found to include:

(i) the valence p orbitals of the heavy group VI element (S, Se, Te ,Po),
(ii) the valence 2p orbitals of both O atoms, and
(iii) the 12 active electrons found in the above orbitals.

In this series, all molecules have been optimized at the SO-CASSI level-of-theory. The obtained geometric parameters (bond length and angle) are shown in Table 5.5 and compared to the experimental values found in literature ([Hay16] for SO_2 and SeO_2,[Zas74, Mue69] for TeO_2).

An excellent agreement is found between the calculated and experimental values, with the largest differences occurring for the Te–O bond length. It should be noted, however, that only a single experimental value was found for the Te–O bond length (1.83±0.02 Å) [Zas74] and for the bond angle (110±2°) [Mue69] and that the corresponding experiments are quite dated (values reported in 1974 and 1969 respectively). Moreover, other recently performed ab initio calculations on the TeO_2 molecule [Lee04] also seem to

Table 5.5: The optimized X–O bond length and $\widehat{\text{OXO}}$ angle at the SO-CASSI level-of-theory for the SO_2, SeO_2, TeO_2 and PoO_2 molecules, as well as the corresponding depth of the potential energy well D. The obtained geometric parameters for the lighter chemical analogues are found to be in excellent agreement with data reported in literature.

XO_2	Bond length (Å)		Angle (°)		Well depth D (eV)
	Calc.	Lit.	Calc.	Lit.	Calc.
SO_2	1.438	1.4308	118.39	119.329	-11.207
SeO_2	1.611	1.6076	113.36	113.83	-8.839
TeO_2	1.796	1.83	109.79	110	-7.990
PoO_2	1.903	-	106.03	-	-6.548

point towards a lower value for the Te–O bond length (around 1.80 Å) than the experimentally reported one, a value which is in good agreement with the one obtained in this work (note that these same calculations report a larger value for the bond angle around 112°).

The obtained values for the bond length, the bond angle and D are found to follow the expected trends i.e. increasing bond length, decreasing angle and decreasing D. The obtained values for the depth of the potential energy well D for the lighter chemical analogues will be compared to the ones reported in literature after they have been corrected for the zero-point energy and the temperature effect at 298.15 K in the next sections.

As the obtained geometric parameters for the lighter chemical analogues of PoO_2 are in excellent agreement with the values found in literature, a high accuracy is also expected for the geometrical parameters obtained for PoO_2 itself.

H_2PoO_2

The computational cost of the manual geometry optimization of the H_2PoO_2 proved to be extremely high. Because of this reason and also because of the lack of reliable data on the stability and structure of the H_2SeO_2 and H_2TeO_2 molecules, no calculations were performed on these lighter analogues. Instead, the choice of active space was based on the ones chosen for the treatment of the H_2Po and PoO_2 molecules:

(i) the valence p orbitals of the heavy group VI element (S, Se, Te ,Po),
(ii) the valence 2p orbitals of both O atoms,
(iii) the valence 1s orbital of both H atoms, and
(iv) the 14 active electrons found in the above orbitals.

In fact, the extent of the active space described above (including 14 active electrons distributed over 11 active orbitals) is close to the workable limit (the computation time increases combinatorially). As an ab initio study on H_2SO_2 isomers [Ste92] showed that the two most stable isomers are very similar in energy, both of these isomeric structures were used as starting geometries for the optimization of H_2PoO_2. The symmetry groups of the two considered structures are C_2 and C_S. The optimized structures are visualized in Figure 5.8.

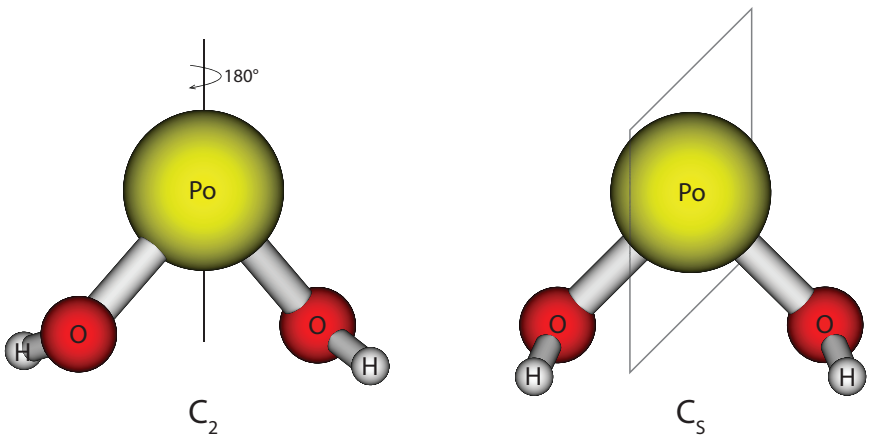

Figure 5.8: The two H_2PoO_2 being optimized at the SO-CASSI level-of-theory and their corresponding symmetry group. The C_2 variant was found to be most stable.

The geometrical parameters and depth of the dissociation well D for both optimized structures are presented in Table 5.6. The C_2 isomer is found to be more stable but only by 0.13 eV. In the performed calculations, a dissociation to (the geometrically optimized) PoO_2 molecule and 2 H atoms is considered. The potential energy difference between H_2PoO_2 and the completely dissociated state i.e. $D(\mathrm{Po{+}2O{+}2H{\rightarrow}H_2PoO_2})$, is calculated by adding the value obtained for the dissociation of PoO_2 i.e. -6.548 eV (see Table 5.5) to the value obtained for $D(\mathrm{PoO_2{+}2H{\rightarrow}H_2PoO_2})$.

Table 5.6: The geometrical parameters of the C_2 and C_S isomer of H_2PoO_2 optimized at the SO-CASSI level-of-theory. In addition, the potential energy differences of these optimized states with respect to the (PoO_2+2H) and (Po+2O+2H) situations are presented.

H_2PoO_2	symmetry state	
	C_2	C_S
Po–O (Å)	2.04	2.03
O–H (Å)	0.96	0.96
∠(OPoO) (°)	91	87
∠(PoOH) (°)	107	111
∠(OPoOH) (°)	97	88
D(PoO_2+2H→H_2PoO_2) (eV)	-7.933	-7.803
D(Po+2O+2H→H_2PoO_2) (eV)	-14.481	-14.351

5.5.2 Zero-Point Energy

The frequencies of the normal modes and the corresponding zero-point energy for the H_2Po and PoO_2 molecules are deduced directly from the obtained SO-CASSI ab initio results by performing a valence force analysis (VFA) described in section 4.4.3. This approach is also applied to the lighter chemical analogues of PoO_2, for which experimental data is available, allowing to assess the validity of the used method. A similar approach for H_2PoO_2 is computationally not manageable within a reasonable time. Instead, the MCKINLEY module of Molcas is used which allows to calculate the Hessian, frequencies and zero-point energy at a level-of-theory up to CASPT2 (which is the level chosen for our calculations). To estimate the magnitude of the introduced error by doing so, this same approach was also applied to PoO_2 and compared to the results obtained using the valence force analysis. All obtained results are presented below.

H_2Po

The calculated results obtained for the H_2Po molecule and the reported values [Hay16, Gó97] for its lighter analogues are presented in Table 5.7. Both the obtained frequencies and the corresponding zero-point energy follow the trend found for the lighter analogues. A remarkable artifact is that the symmetric stretching and asymmetric stretch frequency are found to be almost identical. Although these were expected to lie very close to each other, an actual coincidence seems unlikely. When comparing the obtained values with the experimental ones of the lighter analogues, it can be seen that the

obtained values follow the expected trend of decreasing vibration frequencies and zero-point energy.

Table 5.7: The frequencies for the symmetric stretch (ν_1), bending (ν_2) and asymmetric stretch (ν_3) normal modes, as well as the corresponding Zero-Point Energy (E_{ZPE}) for the H_2Po molecule obtained using a valence force analysis (VFA) (note that the ^{210}Po and ^{1}H isotopes were considered). The frequencies and ZPE of the lighter analogues obtained from literature [Hay16, Gó97] are also included to show that the results for H_2Po follow the expected trends. The ZPE-corrected dissociation energy at 0 K (D_0) is determined using the previously obtained depth of the potential well D (see Table 5.4).

H_2X	H_2S	H_2Se	H_2Te	H_2Po
	Lit.	Lit.	Lit.	VFA
ν_1 (cm^{-1})	2615	2345	2066	1890
ν_2 (cm^{-1})	1183	1034	861	762
ν_3 (cm^{-1})	2626	2358	2073	1890
E_{ZPE} (eV)	0.398	0.356	0.310	0.282
D_0=D+E_{ZPE}	-7.324	-6.429	-5.427	-4.256

PoO_2 and chemical analogues

The results obtained from the valance force analysis for the SO_2, SeO_2, TeO_2 and PoO_2 molecules, as well as the corresponding data available in literature [Kon98, Hay16, NIS] is presented in Table 5.8. The calculated data for the lighter analogues is found to be in relatively good agreement with the values reported in literature. However, all of the obtained values are larger than the reported one. This was expected as the used valence force analysis determines the harmonic frequencies of the system rather than the fundamental ones. Anharmonic effects are not included in this analysis and these are known to slightly decrease the final fundamental frequency. Nevertheless, the actual aim of this procedure was to obtain a good estimation of the zero-point energy, and this quantity is found never to deviate by more than 0.006 eV from the reported values. The MCKINLEY module of Molcas used at the CASPT2 level-of-theory is found to produce a slightly deviating value for the symmetric stretching frequency. The other frequency and the obtained zero-point energy are in relatively good agreement. The MCKINLEY module produces a slightly lower zero-point energy than the

VFA and this value can therefore be assumed to be further away from the actual value (given the fact that the VFA already underestimates the ZPE). This observation suggests that the zero-point energy obtained for H_2PoO_2 using the MCKINLEY module will be slightly underestimated, but only by a few hundredths of eV, which is within the accuracy level of the obtained potential energy well depths.

Table 5.8: The obtained frequencies for the symmetric stretch (ν_1), bending (ν_2) and asymmetric stretch (ν_3) normal modes, as well as the corresponding Zero-Point Energy (E_{ZPE}) for the SO_2, SeO_2, TeO_2 and PoO_2 molecules. For the lighter analogues, the results are compared to data from the literature [Kon98, Hay16, NIS]. For PoO_2, also the values obtained using the Molcas MCKINLEY module (referred to as MCK) are presented. Note that the ^{210}Po and ^{16}O isotopes were considered in this elaboration. Finally, the ZPE-corrected dissociation energy at 0 K (D_0) is determined using the previously obtained depth of the potential well D (see Table 5.5).

XO_2	SO_2		SeO_2		TeO_2		PoO_2	
	VFA	Lit.	VFA	Lit.	VFA	Lit.	VFA	MCK
ν_1 (cm^{-1})	1192	1151	946	922	859	822	766	664
ν_2 (cm^{-1})	529	518	379	373	295	279	257	244
ν_3 (cm^{-1})	1381	1362	1009	966	892	853	781	748
E_{ZPE} (eV)	0.192	0.188	0.145	0.140	0.127	0.121	0.112	0.103
D_0=D+E_{ZPE}	-11.02	-	-8.69	-	-7.86	-	-6.44	-6.45

H_2PoO_2

Table 5.9 shows the nine fundamental frequencies obtained for H_2PoO_2 using the MCKINLEY module at the CASPT2 level of theory, as well as the corresponding zero-point energy and the ZPE corrected dissociation energy at 0 K. The ZPE is found to be relatively large, as was expected given the fact that is has 3 times more normal modes than the other molecules described. In addition it contains two O–H which are known to considerable contribute to the zero-point energy. Nevertheless, based on the elaboration above on the results for PoO_2, this zero-point energy is expect to be slightly underestimated by a few hundredths of eV.

Table 5.9: The frequencies of all 9 normal modes of the H_2PoO_2 molecule, as well as the corresponding Zero-Point Energy (E_{ZPE}). The results were obtained using the Molcas MCKINLEY module applied at the CASPT2 level-of-theory (note that the ^{210}Po, ^{16}O and ^{1}H isotopes were considered). The ZPE-corrected full dissociation energy at 0 K (D_0) is determined using the previously obtained depth of the potential well D (see Table 5.6).

H_2PoO_2	MCK
ν_1 (cm^{-1})	4296.0
ν_2 (cm^{-1})	3760.8
ν_3 (cm^{-1})	1068.8
ν_4 (cm^{-1})	976.9
ν_5 (cm^{-1})	585.1
ν_6 (cm^{-1})	554.9
ν_7 (cm^{-1})	430.7
ν_8 (cm^{-1})	425.0
ν_9 (cm^{-1})	175.1
E_{ZPE} (eV)	0.761
D_0=D+E_{ZPE}	-13.72

5.5.3 T-dependent Gibbs free energy difference

In the previous section, the ZPE-corrected dissociation energy at 0 kelvin was obtained for the H_2Po, PoO_2 and H_2PoO_2 molecules. Determining the T-dependence of the stability for these molecules at the SO-CASSI level-of-theory is computationally too demanding. Some clear trends exist in the T-dependent stability of chemical analogues. Therefore, thermochemical data on the lighter chemical analogues of the Po-containing molecules of interest can be used to estimate their temperature-dependent stability, starting from the obtained dissociation energies. Such data is available in e.g. the *FactSage* Thermochemical Database System [al.16a]. In the elaboration below, the dissociation energy (i.e. Gibbs free energy difference at 0 K) is translated to a Gibbs free energy difference between the molecular and dissociated state at 298.15 K, which is the starting temperature of the data is included in the FactSage database. Next, the variation of this Gibbs free energy difference with increasing temperature is estimated for higher temperatures.

Dissociation energy to Gibbs free energy difference at 298.15 K

The variation of the Gibbs free energy difference (between the molecular and bound state) at 298.15 K ($\Delta G_{298.15\,K}$) and the dissociation energy at 0 K ($D_0 = \Delta G_{0\,K}$) can be written as:

$$\begin{aligned}\Delta G_{298.15\,K} - \Delta G_0\,K &= (\Delta H_{298.15\,K} - 298.15\,K \cdot \Delta S_{298.15\,K}) - \Delta H_{0\,K} \\ &= H^M_{298.15\,K} - \sum_A H^A_{298.15\,K} \\ &\quad - 298.15\,K \cdot \left(S^M_{298.15\,K} - \sum_A S^A_{298.15\,K} \right) \\ &\quad - H^M_{0\,K} + \sum_A H^A_{0\,K},\end{aligned} \tag{5.10}$$

where A denotes the values for the constituent atoms and M of the molecule. For H_2S, H_2Se, H_2Te, SO_2, SeO_2, TeO_2 and H_2TeO_2, as well as for all constituent atoms in the gas phase (H, O, S, Se, Te), the enthalpy and entropy at 298.15 K is readily available from the FactSage database. The missing values are the enthalpies at 0 K. These can be extrapolated from the temperature-dependence of the enthalpy at temperatures above 298.15 K, which is also reported in the FactSage database for the molecules and atoms listed above. Based on the behavior observed for the enthalpies of the studied diatomic Po-containing molecules, a cubic fit performed on the 5 lowest temperature data points reported in the FactSage database (i.e. at 298.15, 300, 400, 500 and 600 K) is expected to properly reproduce the difference of the enthalpy between 0 and 298.15 K. Only one such fit was performed for each molecule, aiming to directly determine $\Delta H_{0\,K}$ rather than performing these fits for each atom and molecule individually.

Note that the contribution of the enthalpy to the difference in Gibbs free energy between 0 and 298.15 K is considerably smaller than the one contributed by the entropy (for the diatomic Po-containing molecules, the enthalpy contribution ranges between 0.025 eV for PbPo, BiPo and Po_2 and 0.04 eV for PoH, while the entropy contributions were found to be up to an order of magnitude larger).

This procedure allows to obtain the difference in binding entropy, enthalpy and Gibbs free energy between 0 and 298.15 K for each of the lighter chemical analogues listed above. As the obtained entropy differences showed a linear decreasing trend with increasing period of the substituting atom in the molecule, the linear trend was extrapolated to obtain the

equivalent value for the corresponding Po-containing molecule. The enthalpy difference showed no clear trend and is nearly constant. Therefore the average obtained from the chemical analogues was used as value for the Po-containing molecule. Having deduced the difference in binding enthalpy and entropy, the difference in binding Gibbs free energy can be obtained using Eq. 5.10.

As for the H_2PoO_2 molecule, data on only one chemical analogue (H_2TeO_2) is available, the same binding enthalpy difference as for H_2TeO_2 was used, and the difference in binding entropy was reduced by 2.5 % (as was approximately found to be the case for both H_2Po and Po_2O with respect to H_2Te and Te_2O respectively). The results are summarized in Table 5.10. The obtained values allow to deduce the Gibbs free energy difference between molecular and dissociated state at 298.15 K for each of the studied molecules (both the Po-containing ones and the chemical analogues). For the chemical analogues, these stabilities are compared to the values listed in the FactSage database. This comparison is presented in Table 5.11.

Table 5.10: The difference in enthalpy, entropy and Gibbs free energy between 0 K and 298.15 K for their difference between the molecular and dissociated state of the listed molecules. The values for the the lighter analogue molecules were deduced from the data available in the FactSage thermochemistry database [al.16a]. The values for the Po-containing molecules were extrapolated from these results.

molecule	$\Delta H_{298K} - \Delta H_{0K}$ (eV)	$-T_{\mathrm{R}}(\Delta S_{298K} - \Delta S_{0K})$ (eV)	$\Delta G_{298K} - \Delta G_{0K}$ (eV)
SH_2	-0.104	0.593	0.489
SeH_2	-0.096	0.579	0.483
TeH_2	-0.097	0.566	0.469
PoH_2	-0.097	0.552	0.455
SO_2	-0.115	0.748	0.633
SeO_2	-0.094	0.730	0.636
TeO_2	-0.110	0.710	0.600
PoO2	-0.110	0.691	0.581
H_2TeO_2	-0.089	1.564	1.475
H_2PoO_2	-0.089	1.525	1.436

The agreement between the calculated values and the reported ones for the PoO_2 chemical analogues is exceptional, the largest deviation being

Table 5.11: A comparison of the calculated difference in Gibbs free energy between the molecular and dissociated state at 298.15 K with the ones reported in the FactSage database [al.16a]. The PoO_2 analogues are in excellent agreement. For the H_2Po analogues, the agreement is somewhat less due to the fact that their geometries have not been optimized at the SO-CASSI level-of-theory

molecule	ΔG_{0K} (eV)	$\Delta G_{298K} - \Delta G_{0K}$ (eV)	ΔG_{298K}(calc.) (eV)	ΔG_{298K}(lit.) (eV)
SH_2	-7.324	0.489	-6.835	-7.014
SeH_2	-6.429	0.483	-5.946	-6.099
TeH_2	-5.427	0.469	-4.958	-5.091
PoH_2	-4.256	0.455	-3.801	-
SO_2	-11.015	0.633	-10.382	-10.369
SeO_2	-8.694	0.636	-8.058	-8.043
TeO_2	-7.863	0.600	-7.263	-7.241
PoO2	-6.436	0.581	-5.855	-
H_2PoO_2	-13.720	1.436	-12.284	-

0.022 eV for TeO_2. For the PoH_2 analogues the agreement is somewhat less, with the results from the calculations always underestimating the overall binding energy. However, it should be noted that these molecules were not geometrically optimized at the SO-CASSI level-of-theory. Instead the geometries reported in literature were used. Performing an actual geometry optimization would further decrease the obtained values for the Gibbs free energy difference towards the reported ones. After doing so, the results are expect to show much better agreement.

T-dependent Gibbs free energy difference

The difference in Gibbs free energy between the molecular and dissociated state is found to show a linear behavior against the temperature, at least in the temperature region ranging from 298.15 K and above. This behavior was indeed also observed for the diatomic Po-containing molecules. The T-dependence of the Gibbs free energy difference for the complex Po-containing molecules can be obtained by studying this dependence for the lighter chemical analogues. A linear fit was performed to the data reported for these chemical analogues in the FactSage database. The obtained values for the slopes of these fits show a linear dependence with respect to the period number of the substituting element (slope decreases slightly as the

period of the substituting element increases). From these results, the slopes for the T-dependence of the corresponding Po-containing molecules could be determined by linear extrapolation. The final T-dependent stability of the H_2Po, PoO_2 and H_2PoO_2 molecules is found to be:

$$\Delta G_{Po+2H\rightarrow H_2Po}(\mathrm{eV}) = 2.090\cdot 10^{-3}T[\mathrm{K}] - 4.424 \tag{5.11a}$$

$$\Delta G_{Po+2O\rightarrow PoO_2}((\mathrm{eV}) = 2.436\cdot 10^{-3}T[\mathrm{K}] - 6.581 \tag{5.11b}$$

$$\Delta G_{Po+2O+2H\rightarrow H_2PoO_2}((\mathrm{eV}) = 5.188\cdot 10^{-3}T[\mathrm{K}] - 13.831 \tag{5.11c}$$

5.5.4 Dominant Po species in different atmospheres

Combining the obtained data with other data available in the *FactSage* database, the following statements can be made (where it is assumed that the Po concentration is always too small to result in non-negligible Po_2 formation and Po–Po species interaction).

1.) In an atmosphere containing only H_2, small traces of Po (and inert gas), Po will remain in its atomic form as:
   - the formation of PoH is not thermochemically favorable:

$$\Delta G_{H_2+Po\rightarrow PoH+H} = 2.335 \pm 0.002 - (1.78 \pm 0.03)10^{-4}T, \tag{5.12}$$

   - the formation of PoH_2 is not thermochemically favorable:

$$\Delta G_{H_2+Po\rightarrow PoH_2} = 0.140 \pm 0.006 + (9.53 \pm 0.08)10^{-4}T. \tag{5.13}$$

2.) In an atmosphere containing only O_2, small traces of Po (and inert gas), Po will primarily occur as PoO_2 as:
   - the formation of PoO_2 is thermochemically favorable (up to 1236 K):

$$\Delta G_{O_2+Po\rightarrow PoO_2} = -1.376 \pm 0.004 + (11.18 \pm 0.06)10^{-4}T, \tag{5.14}$$

   - the formation of PoO is thermochemically not favorable:

$$\Delta G_{O_2+Po\rightarrow PoO+O} = 1.869 \pm 0.003 - (1.26 \pm 0.03)10^{-4}T. \tag{5.15}$$

3.) In an atmosphere containing only O_2, H_2O vapor, small traces of Po (and inert gas), Po will occur primarily as PoO_2 as:

- the formation of H_2PoO_2 is not thermochemically favorable over PoO_2:

$$\Delta G_{PoO_2+H_2O\rightarrow H_2PoO_2+O} = 2.46 \pm 0.02 + (4.10 \pm 0.20)10^{-4}T. \quad (5.16)$$

4.) If PbPo evaporates in an atmosphere as described above, then:

- the only thermochemically favorable reaction that could occur is the formation of PoO:

$$\begin{aligned}\Delta G_{PbPo+O_2\rightarrow PbO+PoO} = &- 0.2402 \pm 0.0005 + (0.52 \pm 0.02)10^{-4}T \\ &- (2.17 \pm 0.12)10^{-8}T^2\end{aligned} \quad (5.17)$$

- At temperatures below 471 K (198°C), also the following reaction is favorable:

$$\Delta G_{PoO+H_2O\rightarrow H_2PoO_2} = -0.79 \pm 0.02 + (16.5 \pm 0.2)10^{-4}T \quad (5.18)$$

It has to be noted that these statements assume that no other phases than the gas phase can appear and only the following species are considered:

1.) data obtained from *FactSage*: H, O, Pb, H_2, O_2, Pb_2, H_2O, PbO, PbH;
2.) data presented in section 5.5.4 on p. 128): Po, Po_2, PoH, PoO, PbPo; and
3.) data obtained for the complex Po species (Eqs. 128): PoH_2, PoO_2, H_2PoO_2.

The made statements could therefore proof incorrect if more Po-containing hydroxides and more Pb-containing hydroxides are included and if other phases than gas (liquid, solid) are allowed. It is therefore recommended to include the new obtained data on Po-containing molecules in an extensive all-phase thermodynamic model, which can then be used to simulate the polonium evaporation and molecular manifestation for a realistic scenario and based on all thermodynamic data included in the used database. Such modeling codes and databases do exist, so the only requirement is adding the obtained data to the database it uses. This model can also be used to simulate the conditions of the performed transpiration and thermochromatography experience, helping to interpret the obtained results. Furthermore, it could be used to simulate a leak-of-LBE or leak-of-PbLi accident. Finally, these more complete models can also help to identify the knowledge gaps and missing data. In this way, the research community could be guided towards useful and dedicated experiments or computations.

5.6 Conclusions

The CASSCF/CASPT2/SO-CASSI method proves to be capable of accurately predicting dissociation energies, even for molecules containing row-6 elements, on condition that the active space is properly validated using lighter chemical analogues.

To evaluate the stability of diatomic Po-containing molecules, 5-parameter analytical potential energy functions were fitted to the SO-CASSI data points obtained at varying internuclear distance. The fitted parameters (molecular constants) allowed to determine the coupled rotational-vibrational-electronic energy levels, from which all contributions to the Gibbs free energy of the molecule at a given temperature can be extracted. Comparing the molecule's Gibbs free energy with the one of the dissociated system, the T-dependent stability of the diatomic molecules was obtained. This information was then used to estimate the relative occurrence of the different Po species in the dry and oxygen free cover gas of (i) the LBE coolant in the MYRRHA fission reactor and (ii) the Pb-Li breeder of the DEMO fusion reactor. In both cases, PbPo is found to be the dominant species (always $>84\,\%$), while almost all residual Po will appear in its atomic form (the other species combined account for less than $0.25\,\%$).

As some thermochromatography and transpiration experiments suggest the formation of very volatile (oxy)hydroxides in presence of O_2 and H_2O, some candidate molecules were selected to be studied by ab initio calculations: PoH_2, PoO_2 and $Po(OH)_2$. Given the higher complexity of these molecules, only the dissociation energy at 0 K was determined at the high CASSCF/CASPT2/SO-CASSI level-of-theory. The T-dependence of the stability was determined through extrapolation of data available on lighter chemical analogues. Combining the obtained T-dependent stability of the 6 diatomic and 3 more complex Po containing molecules with similar data available on Po-free molecules, the dominant Po species occurring in some realistic scenarios could be predicted. The presence of O_2 in a Po-containing inert gas was found to result in the formation of PoO_2. Po escaping in the form of PbPo molecules were found to transform to $Po(OH)_2$ (through consecutive interaction with O_2 and H_2O) under typical atmospheric conditions. As long as no thermochemically even more favorable Po compounds exist that have not been studied in this work, $Po(OH)_2$ is expected to be (one of) the dominant gaseous Po species occurring in the environment after escaping from a reactor.

6

Final conclusions and perspectives

6.1 Conclusions

In this work, the undesired production of highly radiotoxic ^{210}Po in the MYRRHA fast fission reactor and the European DEMO fusion reactor has been studied. The former uses Pb-Bi eutectic (44.5 wt.% Pb + 55.5. wt.% Bi) as coolant and ^{210}Po generation is triggered by unavoidable neutron captures by the implemented ^{209}Bi. In the DEMO reactor, a possible concept considered for the required tritium self-sufficiency is the installation of a blanket containing Pb-Li eutectic (15.8 at% Li + 84.2 at% Pb), completely surrounding the fusion plasma. In this case, the ^{210}Po production is initiated by a neutron capture in the used ^{208}Pb (52.4 % of natural Pb), which results in the production of ^{209}Bi. Equivalently as in MYRRHA, the produced ^{209}Bi can then capture another neutron, again resulting in ^{210}Po.

The ingestion and inhalation radiotoxicity of the undesirably produced ^{210}Po is among the highest of all known radionuclides, with a specific activity as high as 166 TBq/g and a maximum permissible body burden of $6.8 \cdot 10^{-12}$. Therefore, a considerable inventory build-up of this radionuclide within the reactor could compromise its operational safety. To assess the risk associated with the presence of ^{210}Po , two important aspects need to be studied:

(i) the expected magnitude of the ^{210}Po inventory within the reactor, and

(ii) the migration form of ^{210}Po evaporating from the liquid Pb-Bi or Pb-Li used.

Both of these topics have been considered in this work.

The production rate of ^{210}Po in the European DEMO fusion reactor has been determined by combining Monte-Carlo neutron transport calculations in MCNP with a dedicated inventory calculation code (FISPACT-II). Two breeding blanket concept are considered: the Water Cool Lithium Lead (WCLL) and the Helium Cooled Lithium Lead (HCLL) concepts. For both concepts, a detailed heterogeneous model and a simplified material-homogenized model is used.

The expected ^{210}Po inventory to be present in DEMO after the first blanket campaign is found to range between 0.02 g and 1.5 g, depending on the Pb-Li purity, the blanket model and the nuclear data library used.

The choice of nuclear data library is found to have a significant impact on the obtained ^{210}Po inventory. The final ^{210}Po inventories obtained using the ENDF/B-8.0 nuclear data library in the inventory calculations are up to 4.6 times larger than for the JEFF-3.3 library. These differences are larger than the uncertainties associated with the material homogenization of the used blanket models (up to 30 %). Therefore, until a consensus is reached on reliable ^{208}Pb and ^{209}Bi neutron captures cross sections, it will be sufficient to estimate the ^{210}Po inventory in future blanket designs by performing calculations on a homogenized model, but using multiple nuclear data libraries. Calculations on the heterogeneous detailed design will thus only be useful when the distinctions between the nuclear data libraries have been reduced to a level comparable to the material homogenization effect.

Commercially available Pb-Li typically contains a ^{209}Bi impurity content ranging between 10–33 appm. The impurity level is found to have a considerable impact on the final ^{210}Po inventory, which can be reduced by a factor 3 by using clean commercial Pb-Li (10 appm ^{209}Bi) rather than the more contaminated version (33 appm ^{209}Bi). If the Pb-Li is initially purified to 1 appm ^{209}Bi levels, the reduction of ^{210}Po could even be as high as a factor 16.

Comparable ^{210}Po inventories are expected for the HCLL and WCLL blanket concepts, with the highest difference occurring for high purity Pb-Li (1 appm ^{209}Bi) in which case the HCLL blanket produces up to 50 % more ^{210}Po .

The magnitude of of the total ^{210}Po inventory expected to be present in the DEMO reactor (up to 1.5 g) is over 200 times smaller than the ^{210}Po

inventory anticipated for the MYRRHA reactor after a single irradiation cycle of 90 days at full power (350 g). The latter reactor is foreseen to be fully operational by 2033, while DEMO will conclude its engineering design phase in 2038. Therefore, experience gained during the design phase and first operational years of MYRRHA, are believed to prove useful and applicable to the final design of DEMO.

Gaseous Po represents the greatest threat as it can escape from the reactor most easily and can be inhaled. Based on the calculated ^{210}Po inventory and evaporation data from literature, a risk analysis was performed for a leak-of-PbLi accident in DEMO. It is found that ^{210}Po will probably not pose a threat under these conditions, unless possibly when the Pb-Li makes contact with water. It should be noted that this analysis assumes PbPo as primary evaporating species, which has a vapor pressure 1000 times smaller than atomic Po, which considerably reduces the ^{210}Po release to the environment. There is however no direct evidence for this assumption and it is merely based on the fact that the vapor pressures measured above liquid Pb-Li (and LBE) approximately match the vapor pressure of PbPo. To gain more insight in the actual chemical appearance of the gaseous Po, thermodynamic data on the possibly occurring species is required.

Obtaining this data through experiments is cumbersome and expensive due to the high risk involved with the handling of ^{210}Po . Therefore, in this work, the required data is obtained through ab initio calculations. In total, 9 molecules of interest have been studied: PoH, LiPo, PoO, PbPo ,BiPo, Po_2, PoH_2, PoO_2 and H_2PoO_2. As Po, Pb and Bi are heavy element,s spin-orbit coupling effects are very prominent and should be accurately taken into account. Also a proper treatment of electron correlation is required to obtain reliable dissociation energies. The used ab inito method should therefore be capable of properly accounting for both these effects. The *SO-CASSI* method provided by the Molcas code was believed to able to do so. To verify this, a literature study was performed on the results obtained for heavy molecules using this method. In addition, extensive test calculations have been performed on the PbO and Pb_2 molecules. The outcome of both checks indeed suggested the ability of the method to provide accurate data on the dissociation profile of the heavy molecules.

The proper settings for the calculations have been identified and validated through calculations on the lighter chemical analogues of the studied molecules, for which the results can be checked against experimental

data. For the studied diatomic molecules, the T- dependence of the stability was determined based exclusively on the obtained ab initio data. For the more complex molecules, this showed to be computationally too expensive. Therefore, for these molecules, the T-dependence of the stability was extrapolated from the data available on their lighter chemical analogues and added to the ab initio obtained stability at 0 K.

The obtained data has been used to determine the relative occurrence of the different Po species in the plenum gas above the Pb-Bi coolant in MYRRHA and above the Pb-Li breeder in DEMO (in absence of H and O available for Po to bind with). For both of these closed systems, PbPo is indeed found to be the most occurring species (>84 %), while the remaining portion appears almost exclusively as atomic Po. Therefore, the assumption of PbPo as primary evaporating species seems reasonable. However, in a leak-of-PbLi accident, the Pb-Li makes contact with air and possibly water vapor. The obtained ab initio data for the molecules containing Po combined with O and/or H show that in a dry atmosphere with traces of Po, the latter would primarily occur as PoO_2, which is found to be more stable that the separated Po atom and O_2 molecule. The presence of water vapor would not change this as the formation of H_2PoO_2 under these circumstances is chemically not favorable over the PoO_2 + H_2 combination. PoO_2 is known to have a very low vapor pressure (at least an order of magnitude smaller than PbPo for the considered temperatures) [Pet06], therefore its evaporation rate is much slower than the one of PbPo. From the results obtained, it is expected that, in case Po evaporates as PbPo (or escapes from the plenum gas in this form), it would interact with O_2 to form PbO and PoO. At a temperature below 200°C, it is favorable for the latter to consecutively interact with H_2O vapor to form H_2PoO_2. The most probable final form of airborne Po is therefore expected to be the H_2PoO_2 species, which dissociates to H_2O and PoO at temperatures above 200 °C.

6.2 Perspectives

The elaboration above provides insight on the final molecular form of gaseous Po under atmospheric conditions. Note that these statements are based on the data set currently available. The inclusion of new data therefore change these conclusions. The discussion does, however, not provide information on the initial evaporating species, the evaporation rate from Pb-Li and LBE and why the evaporation rate increases in presence of $_2$O vapor.

To come to a decisive answer on the highly volatile Po species evaporating from Pb-Bi eutectic in contact with water vapor, a full thermodynamic model including not only the gas phase, but also the liquid and solid state is required. Such models do exist and the newly obtained ab inito data on the T-dependent stability of the 9 studied Po-containing molecules can now be included in the chemical database used by these models. These models will be able to show whether this new data can explain the observations made during the experiments and if not, where inhibiting knowledge gaps exist. Missing quantities could include: the Gibbs free energies of the different Po species dissolved in Pb-Bi/Pb-Li (which is very challenging to obtain through calculations at a similar accuracy as obtained in this work) and the stability of Po-containing (oxy-)hydroxides not studied in this work.

Six possibly occurring volatile Po species containing H and/or O were identified at the start of this work based on the experimental observations and chemical intuition: PoH, PoO, PoH_2, PoO_2, H_2PoO_2 and H_2PoO_3. The first five of these series have been studied in this work and data on their T-dependent stability has been provided. The most complex molecule of this series, however, H_2PoO_3 was found to be (probably) computationally too expensive to be treated at this high level-of-theory. Using some well thought-out strategies and approximations (e.g. performing the geometry optimization at a lower level-of-theory), it could still be possible to obtain limited ab initio data at the SO-CASSI level. Nevertheless, also more complex hydroxides could appear e.g. $Po(OH)_6$ which simply cannot be treated at this level. Therefore alternative methods are required to provide data on these molecules, desirably at the same accuracy. A recently developed strategy which might assist in achieving this, is based on the use of machine learning [Wel18, Che19]. In this method, a machine learning model is trained to obtain the electron correlation energy (which is computationally expensive to obtain) from the calculated Hartree energies. This could considerably reduce the required calculation time on complex large molecules, however it has to be investigated how and if such a model could also be taught to deal with spin-orbit effects.

A useful future evaporation experiment would be one using air as carrier gas rather than an inert or controlled H_2 atmosphere. This will provide more information in on the actual Po evaporation rate in case of a leak of Pb-Bi/Pb-Li in a room under atmospheric conditions. This experiment might be problematic however, as oxide layers are expected to quickly form on the Pb-Bi (Pb-Li) sample. Nevertheless, as this would also occur in the actual accident, the effect of the formation of this layer on the evaporation rate should be studied in detail.

Part III

Publications and contributions

A

Publications

Paper I

pp. 143–159

^{210}Po production in the European DEMO fusion reactor

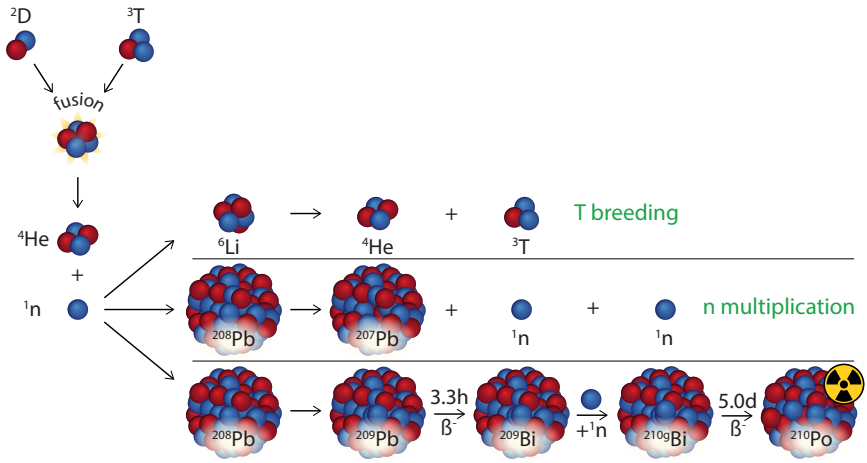

Merlijn A J Mertens, Ulrich Fischer, Pavel Pereslavtsev,
Robert Stieglitz, Jean-Marie Noterdaeme, and Stefaan Cottenier

Nuclear Fusion, **59** (10), 106029, August 2019

DOI: 10.1088/1741-4326/ab36aa

M.A.J. Mertens performed all MCNP and FISPACT-II calculations required to predict the ^{210}Po inventory expected to be present in the Pb-Li in DEMO under different conditions. In addition, the results were applied in a risk analysis considering a leak-of-PbLi accident.

^{210}Po production in the European DEMO fusion reactor

Merlijn A J Mertens[1,2,3], Ulrich Fischer[1], Pavel Pereslavtsev[1], Robert Stieglitz[1], Jean-Marie Noterdaeme[4,5] and Stefaan Cottenier[2,3]

[1] Institute for Neutron Physics and Reactor Technology, Karlsruhe Institute of Technology, Hermann-von-Helmholtz Platz 1, D-76344 Eggenstein-Leopoldshafen, Germany

[2] Center for Molecular Modeling, Ghent University, Technologiepark 903, B-9052 Zwijnaarde, Belgium

[3] Department of Electrical Energy, Metals, Mechanical Construction and Systems, Ghent University, Technologiepark 903, B-9052 Zwijnaarde, Belgium

[4] Department of Applied Physics, Ghent University, Sint-Pietersnieuwstraat 84 B4, B-9000 Ghent, Belgium

[5] Max-Planck-Institut für Plasmaphysik, Boltzmannstraße 2, D-85748 Garching, Germany

Abstract

The radionuclide inventory plays a central role in the safety of nuclear installations both during operation and their decommissioning. In nuclear fusion reactors using Pb-Li tritium breeding blankets, the undesired production of radiotoxic ^{210}Po is still an unresolved safety issue. In this work, neutron transport calculations and inventory calculations are combined to predict the ^{210}Po inventory in a DEMO fusion reactor using either a Helium Cooled Lithium Lead or a Water Cooled Lithium Lead breeding blanket. In order to guarantee that the environmental ^{210}Po release associated with an ex-vessel leak-of-PbLi accident remains below the no-evacuation limit, the ^{210}Po concentration in the Pb-Li should be kept below 1500 appt. It was found that no Pb-Li purification is required to keep the ^{210}Po concentration in DEMO below this limit. However, in case the Pb-Li makes direct contact with water, more volatile Po-containing (oxy-)hydroxides could form. If these species increase the ^{210}Po release rate by more than a factor two, safety measures will be required. Therefore, ^{210}Po generation in DEMO does not pose a hazard in case of a regular ex-vessel leak-of-PbLi accident, unless possibly in case the Pb-Li makes contact with water.

Keywords: breeding blanket, Pb-Li, Po-210, radiotoxic, DEMO, activation, inventory

Introduction

The first generation of commercial fusion reactors will generate electricity exploiting the deuterium-tritium (D-T) fusion reaction. The earth's oceans account for a virtually inexhaustible supply of deuterium as 0.0156 % of the hydrogen isotopes in ocean water is deuterium (according to the Vienna Standard Mean Ocean Water). Tritium, however, having a half-life of 12.32 years, only appears in trace amounts in nature. The very limited global inventory of tritium available today has been exclusively generated in CANDU-type fission reactors and is estimated to range between 12.2 and 27.6 kg at the start-up time of the European DEMO (DEMOnstration power station) fusion reactor, while its required start-up inventory is of the same order of magnitude [Pea18]. Therefore, in order to scale up nuclear fusion to a viable and economical source of energy, a fusion reactor will have to produce (breed) at least as much tritium as it consumes. The most realistic way to do this, is by making as many fusion neutrons as possible interact with ^{6}Li, which primarily results in the production of T and ^{4}He. As it is inevitable that some fusion neutrons will interact with other materials or will simply escape from the reactor, a neutron multiplier is indispensable. The prime candidates for this purpose are Pb and Be. They both have advantages and disadvantages and are therefore still being studied in parallel.

This work addresses the undesired production of radiotoxic ^{210}Po occurring only in the tritium breeding concepts using Pb as a neutron multiplier. In these concepts, liquid eutectic Pb-Li circulates through a blanket surrounding the fusion plasma and is frequently bypassed through a Tritium Extraction and Removal System which collects the produced T. The undesired ^{210}Po production is initiated by a radiative neutron capture by ^{208}Pb, the main component of natural Pb (52.8 %). This results in ^{209}Pb which is unstable and quickly undergoes a beta decay into ^{209}Bi ($t_{1/2} = 3.25\ \mathrm{h}$). When this isotope subsequently captures another neutron, either ground state ^{210g}Bi or metastable ^{210m}Bi is produced. The latter alpha decays into ^{206}Tl ($t_{1/2} = 3.04 \times 10^{6}\ \mathrm{y}$), while the former beta decays ($t_{1/2} = 5.01\ \mathrm{d}$) into the problematic ^{210}Po which is a strong α-emitter having a specific activity of 166 TBq/g [Hea10] (4500 times higher than ^{226}Ra) and a half-life $t_{1/2}$ of 138 days. It was found to be highly radiotoxic, with a median systemic lethal dose LD_{50} estimated in the range of only 3.773–21.56 MBq (23–130 ng) for a 70-kg male adult [Har07, Sco07]. The problematic reaction chain is visualized in Figure A.1.

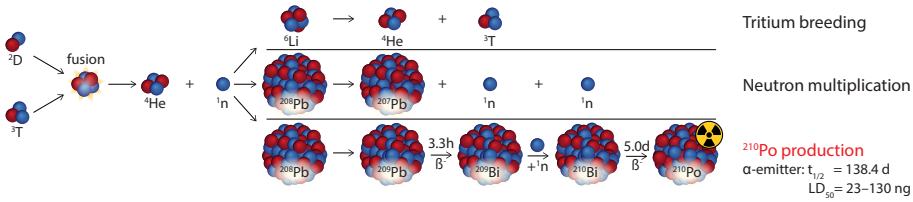

Figure A.1: A visual summary of the ^{210}Po production reaction chain. The problematic reaction chain is initiated when a (fusion) neutron is captured by ^{208}Pb instead of being multiplied (lower reaction path).

Although ^{210}Po will not pose problems during the decommissioning phase of the fusion reactor (due to its relative short half-life), its inventory needs to be monitored during operation to ensure the safety of the workers as well as to prevent a release to the environment. The aim of this study is to obtain a realistic estimation of the Po inventory in the European DEMO fusion reactor, which, if any limit value is exceeded, may stipulate complementary safety measures or a purification system.

Computational tools

Geometrical model of the European DEMO reactor

Over the years, different generic models of the European DEMO reactor have been proposed by the Power Plant Physics and Technology (PPPT) programme of the EUROfusion Consortium. These reference designs contain the foreseen implementation of the major components of the reactor (vacuum vessel, magnetic field coils, divertor, etc.) and define the residual space available for the breeding blanket. In this work, the DEMO baseline configuration 'DEMO1 2014' was used for which the most important characteristics are listed in Table A.1 [Fed14]. In order to keep the computational cost reasonable, calculations are performed in a 11.25° toroidal section of this model (making optimal use of the toroidal symmetry of the model).

Four breeding blanket concepts are currently being developed in the EU and are considered for implementation in the European DEMO [Cis18]: Helium Cooled Pebble Bed (HCPB), Helium Cooled Lithium Lead (HCLL), Water Cooled Lithium Lead (WCLL) and Dual Coolant Lithium Lead (DCLL). As the name suggest, the latter three use liquid Pb-Li as breeder/multiplier

combination. In this work, calculations on the HCLL and WCLL blanket designs have been performed. For both concepts, two implementations in the generic model were considered: (i) a homogeneous implementation in which the blanket models are filled by a concept-specific homogeneous material mixture [Ead17], and (ii) a heterogeneous implementation containing the concept-specific blanket module including e.g. cooling pipes and stiffening plates [Vil15, Pal15]. The idea behind this approach is to examine whether a homogeneous model of the design yields results comparable to the ones obtained for a detailed heterogeneous model. If this is the case, there is no need to create a heterogeneous model for all future intermediate blanket designs (which can be time-intensive), but instead the material mixture in the homogeneous model can be adapted accordingly to acquire a good (first) estimation of the ^{210}Po inventory.

Figure A.2 shows a poloidal section of the models used in the calculations. In these models, the material composition of all components has been defined. This allows us to perform realistic neutron transport calculations throughout the full model and determine the neutron flux in the components where Pb-Li is present. The total amount of Pb-Li in each model is listed in Table A.2. It is assumed that Li is enriched to a 90% ^{6}Li content to enhance the tritium breeding capability.

Number of TF coils	16
Major radius	9.0 m
Minor radius	2.25 m
Aspect ratio	3.6
Plasma elongation	1.56
Plasma triangularity	0.33
Fusion power	1572 MW
Average neutron wall loading	1.07 MW/m^2
Net electric power	500 MW
Fusion neutron source intensity	5.581×10^{20} n/s

Table A.1: Characteristics of the 'DEMO1 2014' baseline [Fed14].

Neutron transport calculations

To calculate the energy-dependent neutron flux in the Pb containing regions, neutron transport calculations were performed using the MCNP (Monte Carlo N-Particle) code [Wer17], which is currently the reference code for neutron transport calculations. It uses the Monte Carlo principle to probabilistically track the neutrons on a microscopic level from birth to

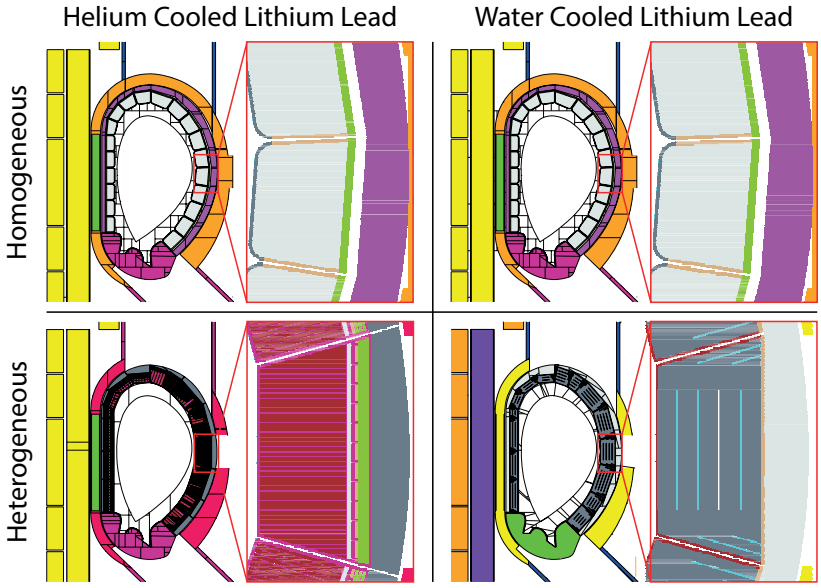

Figure A.2: A poloidal section of the 4 DEMO models used in the neutron transport calculations. For each model, the equatorial outboard module is also shown in detail.

Table A.2: The Pb-Li volumes implemented inside and outside the breeding zone (BZ) for the dfferent models.

$V_{Pb\text{-}Li}$ (m^3)	HCLL		WCLL	
	homo.	het.	homo.	het.
Inside BB	575	563	575	668
Outside BB	150	150	150	150
Total	725	713	725	818

death throughout a 3D geometry in which the material composition has been defined. Along this track, all possible physical interactions between the neutron and the material are modeled based on their probability of occurrence. A realistic fusion neutron source was used which is based on the properties of the 'DEMO1 2014' baseline (see Table A.1) and a mathematical description of a typical tokamak fusion neutron source [Fis14]. It should be noted that MCNP can not model the variation of the material composition over time resulting from transmutations. Nevertheless, the obtained initial neutron flux spectrum can be used for the whole lifetime of the reactor, as the Li burn-up and inventory build-up for a DEMO fusion reactor is quite limited, making the neutron flux spectrum approximately constant over time.

Nuclear data used in the MCNP calculations

The probability of a nuclear reaction is given by the corresponding energy-dependent cross section, which are evaluated using theoretical models (often) combined with experimentally measured cross-section data. Relying on different theoretical models, large distinctions sometimes exist between the same cross section found in different nuclear data libraries. Therefore, the choice of nuclear data library can have a significant impact on the obtained neutron flux spectrum. To allow for an unambiguous comparison of results, a common set of evaluated nuclear data for fission and fusion applications has been developed i.e. the Joint Evaluated Fission and Fusion (JEFF) nuclear library [Nuc17]. The EUROfusion project demands that all neutron transport calculations on the European DEMO are performed using this library. In this work, the JEFF-3.2 version was used.

Inventory calculation

As MCNP can not calculate the time-dependent material composition in the model, a dedicated inventory code was used for this purpose. FISPACT-II is a Fortran code developed by the United Kingdom Atomic Energy Authority allowing to perform inventory calculations [Sub17]. The required input consists of (i) the initial density of the material, (ii) the initial chemical composition and (iii) the time-dependent neutron flux in the material. The program then allows to determine the material composition at any requested time. FISPACT-II also makes use of dedicated nuclear data libraries. In this work, ten nuclear data libraries have been compared of which four were selected for detailed calculations.

The liquid Pb-Li is not static within the breeding blanket but continuously circulates through a dedicated loop of which some parts are located close to and others far away from the fusion plasma. The loop is essentially composed of the breeding blanket modules (high neutron flux), the Pb-Li manifold (lower neutron flux) and the Pb-Li storage tank, the heat exchanger, the tritium extraction system and the pumps (negligible neutron flux). In the HCLL blanket concept the Pb-Li is foreseen to complete 11 recirculations per day, while in the WCLL about 10 recirculations per day are expected [Uti19b]. This has two important consequences on the ^{210}Po inventory: (i) all activation products are continuously redistributed over the whole Pb-Li circuit rather than remaining in the area where they were produced and (ii) not all Pb-Li is continuously being exposed to a

high neutron flux, therefore areas of different neutron flux have to be distinguished.

Commercial eutectic Pb-Li available today typically contains between 10–33 appm ^{209}Bi impurities [Con14]. These impurities have an effect on the final ^{210}Po inventory as they provide a shortcut in the problematic reaction chain shown in Figure A.1. The neutrons can be captured directly by ^{209}Bi, resulting in a higher ^{210}Po production rate. This effect has to be considered to decide whether it is necessary to use a higher quality "nuclear grade" Pb-Li or even an on-site Pb-Li purification system.

DEMO is foreseen to have two breeding blanket phases. In the first phase, a so-called starter blanket will be installed limited to a maximum displacement damage to the structural material of 20 dpa. For the second phase, a new blanket generation allowing for 50 dpa structural material damage is expected, based on the progress in material irradiation studies [Cis18]. In this work, we focus on the starter blanket as this is the one currently under design. This blanket will be used during the first 5.2 years of DEMO operation and the irradiation schedule shown in Figure A.3 can be assumed for the inventory calculations. In this first blanket phase, DEMO will be operated at 30% of its full power capacity for 5.173 years, followed by 48 4-hour pulses at full power with 1-hour intervals at zero power. The total lifetime of DEMO is set at 6 full-power years (FPY). A conservative irradiation schedule would therefore be a continuous operation for 6 years at full power, which can also be considered as representative for a first generation commercial fusion reactor. Both of these irradiation schedules will be simulated and compared.

Results

Neutron flux

In the MCNP neutron transport calculations several regions containing Pb-Li were distinguished. The most important ones are the actual breeding zones. In the homogeneous models, these regions refer to the entire material mixture filling the blanket modules. In the heterogeneous models, however, they refer to the regions within the blanket module that contain pure Pb-Li. It is expected that most of the ^{210}Po will be produced within these regions as they contain the largest portion of the total Pb-Li amount and are exposed to the highest neutron flux. The obtained energy-dependent neutron flux in

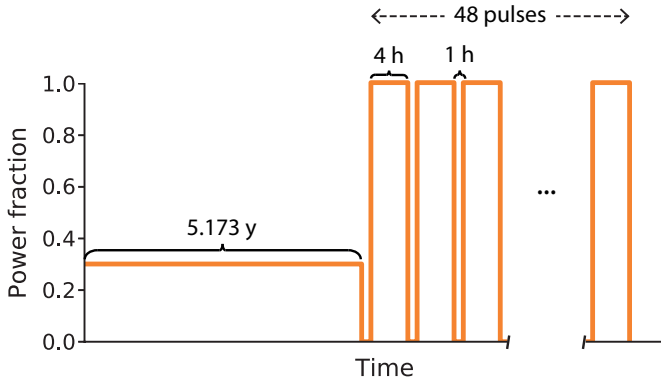

Figure A.3: DEMO first blanket irradiation schedule assumed in the activation calculations.

these regions for all four models, is shown in Figure A.4.

It can be seen that for the WCLL blanket, a softer (less-energetic) spectrum is found due to the moderation of the neutrons by water molecules . The resulting neutron spectra in the breeding regions for the homogeneous and the heterogeneous model are found to be qualitatively the same with some distinctions at lower neutron energy for which the heterogeneous models yield a lower flux. This is because of the increased absorption rate of low-energy neutrons by ^{6}Li, which is present at larger concentrations in pure Pb-Li than in the homogeneous blanket mixtures. It should be noted that in this work not only the breeding zones were considered to be contributing to the ^{210}Po production, but also all other regions containing Pb-Li with a non-negligible neutron flux such as the Pb-Li manifold and the blanket backplate.

Proof of instantaneous mixing assumption

The obtained neutron fluxes for the different regions containing Pb-Li were used to calculate the ^{210}Po inventory with FISPACT-II. In a first calculation only internal circulation of Pb-Li was allowed, meaning that activation products generated within a given region (breeding zone, manifold, backplate) always stayed within that same region. This results in an accumulation of activation products in the breeding zones where the neutron flux is higher than in the other regions. The increased ^{209}Bi concentration in the breeding zones promotes ^{210}Po production, resulting in a higher overall ^{210}Po inventory.

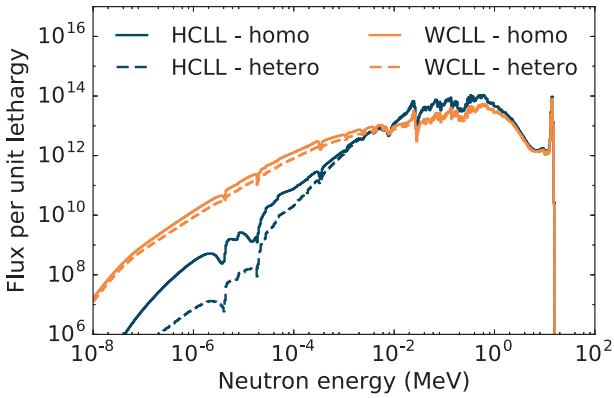

Figure A.4: Calculated neutron flux spectra in the breeding zones for the 4 considered DEMO models.

In reality however, the Pb-Li circulates through the entire Pb-Li loop at a rate specific to the breeding blanket concept. For the HCLL concept one cycle takes 2.2 hours (11 recirculations/day), while for the WCLL concept one cycle takes 2.4 hours (10 recirculations/day) [Uti19b]. A 6 FPY irradiation schedule is now considered which amounts to a total of 24107 and 21915 redistribution steps for the HCLL and WCLL designs. As simulating this large amount of redistribution steps showed to be quite demanding, at first fewer redistribution steps (and so longer redistribution intervals) are assumed. Then the number of redistribution steps is gradually increased towards the target value to study the evolution of the result. The final ^{210}Po inventory as a function of the number of redistribution steps is shown in Figure A.5 (for both the EAF-2010 and TENDL-2014 nuclear data library). It can be seen that the ^{210}Po inventory has converged to a stable value long before the actual number of redistribution steps is reached. The crosses in Figure A.5 were obtained assuming instantaneous mixing (using a single volume-averaged flux). It can be seen that the obtained results coincides with the converged result. Therefore, instantaneous mixing can be assumed which allows to volume-average the fluxes in the different regions. This way, more complex irradiation schedules can be considered using the available computational resources.

Comparing nuclear data for FISPACT-II

The final ^{210}Po inventory depends on the nuclear data library used in the FISPACT-II calculation. Two nuclear cross sections have a critical impact on the final result: the neutron capture cross section of ^{208}Pb and the neutron

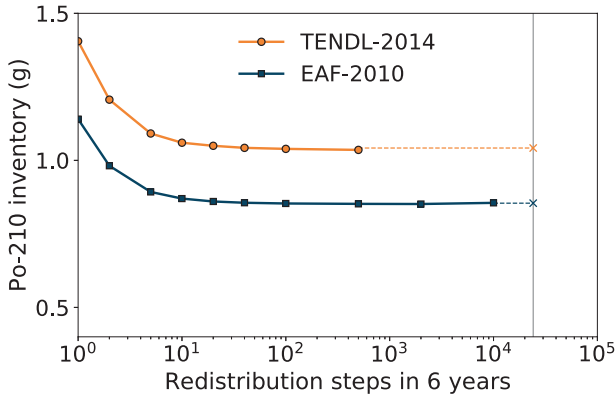

Figure A.5: The calculated ^{210}Po inventory versus the number of redistribution steps used during a 6 FPY irradiation schedule for the homogeneous HCLL model for both the EAF-2010 and TENDL-2014 libraries. The gray vertical line marks the actual number of Pb-Li cycles in 6 years. The crosses and dashed lines show the obtained value assuming instantaneous mixing.

capture cross section of ^{209}Bi resulting in ground state ^{210g}Bi. To speed up the calculations, FISPACT-II collapses the energy-dependent cross sections with the specified energy-dependent neutron flux resulting in a single effective one-group (flux spectrum weighted) cross section for every type of nuclear interaction. Figure A.6 shows these effective cross sections σ_{eff}, as well as the ^{210g}Bi/^{210}Bi$_{\text{tot}}$ branching ratios and the final ^{210}Po inventories that were all calculated for the homogeneous HCLL neutron spectrum and the DEMO first blanket irradiation schedule using 10 different nuclear data libraries. The error bars were deduced by FISPACT-II.

It can be seen that different versions of the same library tend to give similar results. The JENDL-4.0 library was found to give exactly the same result as the JEFF-3.3 library, which suggests that these libraries share nuclear data. The biggest discrepancies between the libraries were found to result from the different ^{209}Bi(n,g)^{210g}Bi cross section used. It can be seen that this cross section is roughly directly proportional to the presented branching ratios, proving that a consensus exists about the total neutron capture cross section of ^{209}Bi but not about the branching ratios. This issue has been addressed in detail by Fiorito et al. [Fio18] and in conclusion they urge the need for dedicated experiments in order to remove these discrepancies. Four well established nuclear data libraries enclosing the

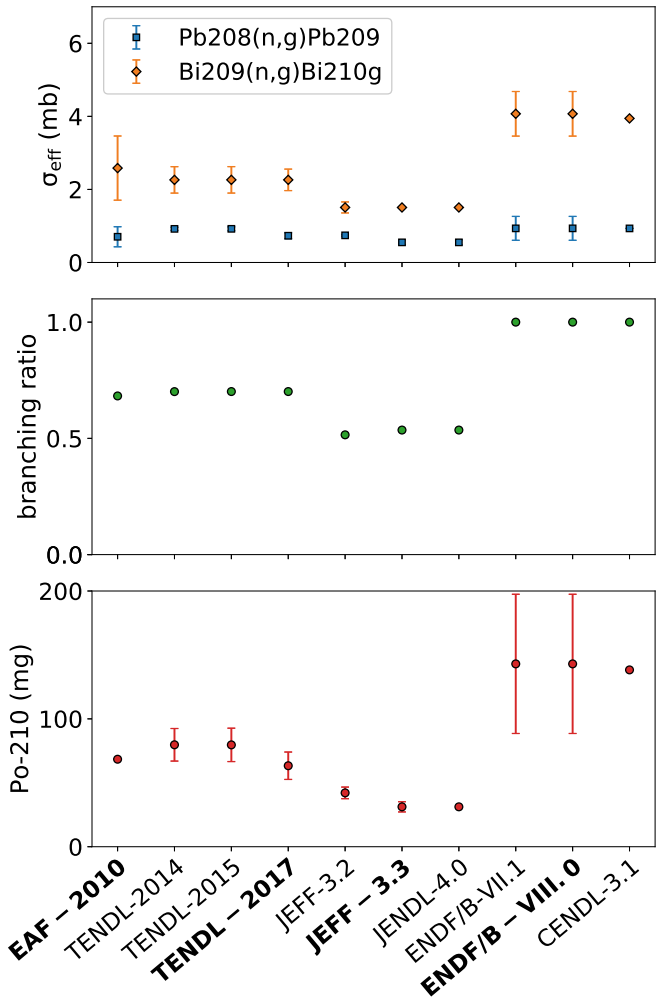

Figure A.6: The effective one-group cross sections of the important neutron captures for ^{210}Po production (top), the ^{210g}Bi/^{210}Bi$_{tot}$ branching ratios in case of a neutron capture by ^{209}Bi (center) and the final ^{210}Po inventories (bottom), all calculated for the homogeneous HCLL neutron flux spectrum and the DEMO first blanket irradiation schedule using 10 different nuclear data libraries.

entire range of results were selected for further calculations: the European Activation File 2010 (EAF-2010) [Sub10], the TALYS-based Evaluated Nuclear Data Library 2017 (TENDL-2017) [noa17a], the Joint Evaluated Fission and Fusion File 3.3 (JEFF-3.3) [Nuc17] and the U.S. Evaluated Nuclear Data File 8.0 (ENDF/B-VIII.0) [Bro18].

^{210}Po inventory: ^{209}Bi impurity level effect

Multiple ^{210}Po inventory calculations were performed using different initial ^{209}Bi impurity levels in the Pb-Li. A linear relationship was found between the final ^{210}Po inventory and the initial ^{209}Bi impurity level:

$$N_{^{210}\mathrm{Po}} = N_{^{210}\mathrm{Po}}^{\mathrm{no\,Bi}} + A N_{^{209}\mathrm{Bi,i}}. \tag{A.1}$$

In this equation, $N_{^{210}\mathrm{Po}}$ denotes the final ^{210}Po inventory for a given initial Bi impurity level $N_{^{209}\mathrm{Bi,i}}$, $N_{^{210}\mathrm{Po}}^{\mathrm{no\,Bi}}$ is the final ^{210}Po inventory for impurity-free Pb-Li and A is the determined slope. $N_{^{210}\mathrm{Po}}^{\mathrm{no\,Bi}}$ and A are presented in units of appt and appt/appm respectively in Table A.3 and A.4 for the DEMO first blanket irradiation schedule and in Table A.5 and A.6 for a 6 FPY irradiation schedule. They can also be obtained in units of mg and mg/appm by multiplying the reported values by 8.247 for the homogeneous HCLL, 8.104 for the heterogeneous HCLL, 8.242 for the homogeneous WCLL and 9.301 for the heterogeneous WCLL (these factors are obtained using the total Pb-Li volumes shown in Table A.2 and an average Pb-Li density of 9500 kg/m^3 corresponding to a Pb-Li temperature of 292°C [Sch91]).

The obtained ^{210}Po inventories are higher for the 6 FPY irradiation schedule as this is a more intensive irradiation schedule than the one foreseen for the first DEMO blankets. It can be seen that the choice of nuclear data library has a dominant impact on the resulting ^{210}Po inventory: the ENDF/B-VIII.0 library produces values up to 4.6 times (360%) higher than the ones obtained for the JEFF-3.3 library. The differences in the flux spectra obtained using the homogeneous and heterogeneous model (Figure A.4) are found to have an almost negligible effect for the HCLL blanket (maximum discrepancy in the ^{210}Po concentration is only 2%), while for the WCLL blanket the effect is somewhat larger due to the larger flux at low neutron energies (where the major discrepancies are found), resulting in a ^{210}Po concentration up to 30% higher for the homogeneous model (corresponding to a total ^{210}Po inventory higher by at most 15% given the larger Pb-Li volume in the heterogeneous model, see Table A.2). However, the effect remains small compared to the discrepancies introduced by using different nuclear data libraries. Therefore, it can be concluded that homogeneous models can be used to obtain a good first indication of the expected ^{210}Po inventory for future intermediate blanket designs. Nevertheless, it is advisable to use a detailed heterogeneous model to estimate the ^{210}Po inventory in the final blanket design.

For impurity-free Pb-Li, the HCLL concept is found to result in somewhat higher ^{210}Po concentrations than for the WCLL concept (see Table A.3 and A.5). However, the homogeneous WCLL concept is found to be more sensitive to the initial ^{209}Bi impurity level compared to the other models as can be seen from the higher slopes A (see Table A.4 and A.6). As a result, this model will result in the highest ^{210}Po concentrations whenever the initial ^{209}Bi concentration exceeds a given limit which varies between 1.4 and 36 appm depending on the nuclear data library and irradiation schedule.

Using the obtained coefficients of equation A.1, it is now possible to calculate the^{209}Bi impurity level corresponding to a 10 % increase in the final ^{210}Po inventory. The obtained values are presented in Table A.7 and A.8 for the two irradiation schedules and are a good indication for the Bi impurity level at which a noticeable impact on the final ^{210}Po inventory can be expected. All Bi impurities levels lower than the reported ones could thus be considered as having negligible impact. In case of a 6 FPY irradiation schedule, more ^{210}Po will be produced starting from ^{208}Pb compared to the first DEMO blanket irradiation schedule. This reduces the relative significance of the initial ^{209}Bi impurities present in the Pb-Li, thus resulting in higher values in Table A.8. As previously mentioned, commercial eutectic Pb-Li available today typically contains between 10–33 appm ^{209}Bi impurities [Con14]. It can be seen that all values in Table A.7 and A.8 are lower than these values, which means that the Pb-Li should be purified before operation to at least these levels if one wants to nullify the impact of the initial Bi impurities. A similar approach can be used to calculate the Bi impurity limits for e.g. a final ^{210}Po inventory of 1 appb or a total ^{210}Po inventory of 1 g in the total Pb-Li volume.

Table A.3: The final ^{210}Po inventory for a Pb-Li breeder free of ^{209}Bi impurities ($N^{\mathrm{no\,Bi}}_{^{210}\mathrm{Po}}$ in Eq. A.1) in units of appt for different blanket models and nuclear data libraries and the **DEMO first blanket irradiation schedule**.

$N^{\mathrm{no\,Bi}}_{^{210}\mathrm{Po}}$ (appt)	HCLL		WCLL	
	homo.	het.	homo.	het.
EAF-2010	8.30	8.41	5.44	4.19
TENDL-2017	7.68	7.68	6.12	4.65
JEFF-3.3	3.78	3.85	2.54	1.95
ENDF/B-VIII.0	17.3	17.7	10.7	8.18

Table A.4: Coefficient A from Eq. A.1 in units of appt ^{210}Po per appm ^{209}Bi impurities in the Pb-Li for different blanket models and nuclear data libraries and the **DEMO 1st blanket irradiation schedule**.

A (appt/appm)	HCLL		WCLL	
	homo.	het.	homo.	het.
EAF-2010	2.90	2.86	3.49	2.84
TENDL-2017	2.62	2.56	3.70	2.93
JEFF-3.3	1.69	1.68	2.04	1.64
ENDF/B-VIII.0	4.56	4.53	5.26	4.28

Table A.5: The final ^{210}Po inventory for a Pb-Li breeder free of ^{209}Bi impurities ($N_{^{210}\mathrm{Po}}^{^{\mathrm{no\,Bi}}}$ in Eq. A.1) in units of appt for different blanket models and nuclear data libraries and a **6 FPY irradiation schedule**.

$N_{^{210}\mathrm{Po}}^{^{\mathrm{no\,Bi}}}$ (appt)	HCLL		WCLL	
	homo.	het.	homo.	het.
EAF-2010	104	105	67.9	52.4
TENDL-2017	99.9	100	77.8	58.9
JEFF-3.3	47.2	48.0	31.8	24.3
ENDF/B-VIII.0	216	221	133	102

Safety analysis

In 2006, Petti et al. [Pet06] have performed a safety analysis on a conceptual 1000 MWe fusion power plant ARIES-AT. In this analysis, they estimated that in case of an ex-vessel leak-of-PbLi accident a ^{210}Po concentration of 100 appt in the eutectic Pb-Li would result in a total amount of 0.43 TBq ^{210}Po being released into the environment in the first hour after the accident before the heating-ventilation-air conditioning system of the lower

Table A.6: Coefficient A from Eq. A.1 in units of appt ^{210}Po per appm ^{209}Bi impurities in the Pb-Li for different blanket models and nuclear data libraries and a **6 FPY irradiation schedule**.

A (appt/appm)	HCLL		WCLL	
	homo.	het.	homo.	het.
EAF-2010	9.30	9.19	11.19	9.13
TENDL-2017	9.06	8.90	12.3	9.73
JEFF-3.3	5.42	5.38	6.56	5.27
ENDF/B-VIII.0	14.6	14.5	16.9	13.7

Table A.7: Maximum amount of initial ^{209}Bi impurities in ppm to keep the increase in the final ^{210}Po inventory below 10 % w.r.t. Pb-Li free of impurities for different blanket models and nuclear data libraries and the **DEMO first blanket irradiation schedule**.

$N^{10\,\%}_{^{209}\mathrm{Bi,imp}}$ (ppm)	HCLL		WCLL	
	homo.	het.	homo.	het.
EAF-2010	0.286	0.294	0.156	0.147
TENDL-2017	0.293	0.300	0.165	0.158
JEFF-3.3	0.224	0.229	0.124	0.118
ENDF/B-VIII.0	0.380	0.390	0.203	0.191

Table A.8: Maximum amount of initial ^{209}Bi impurities to keep the increase in the final ^{210}Po inventory below 10% w.r.t. Pb-Li free of impurities for different blanket models and nuclear data libraries and a **6 FPY irradiation schedule**.

$N^{10\,\%}_{^{209}\mathrm{Bi,imp}}$ (ppm)	HCLL		WCLL	
	homo.	het.	homo.	het.
EAF-2010	1.11	1.14	0.607	0.574
TENDL-2017	1.10	1.12	0.632	0.606
JEFF-3.3	0.872	0.892	0.484	0.461
ENDF/B-VIII.0	1.48	1.52	0.790	0.743

functional area (where the Pb-Li pool forms) is shut down. This quantity showed to be about half the allowable no-evacuation release limit of 0.92 TBq for a release point close to the ground, a 1 km site boundary and average weather conditions.

Consider a DEMO reactor using 'dirty' commercial Pb-Li (33 appm ^{209}Bi) and no purification system. Under these conditions, ^{210}Po inventories between 56.1 and 184 appt (depending on the nuclear data library used) are found for the DEMO first blanket irradiation schedule and between 198 and 700 appt for a 6 FPY irradiation schedule. For both cases the maximum predicted inventory is above the 100 appt limit determined for ARIES-AT. However, the ARIES-AT fusion power plant is designed to use Pb-Li both as breeder and coolant. As a result, the Pb-Li blanket outlet temperature is as high as 1125°C, which is far above the Pb-Li operation temperature foreseen for a DEMO fusion reactor using an HCLL or WCLL blanket i.e. 300°C and 328°C respectively [Uti19b, Uti19a, Uti15]. Petti et al. [Pet06] demonstrated that in case of an ex-vessel leak-of-PbLi accident at ARIES-AT, 0.64 TBq of

^{210}Po is expected to evaporate in the form of PbPo from the leaked Pb-Li pool (initially at 980°C) within the first two hours. This was found to be least 30000 times more than the amount of PbPo expected to evaporate within the first two hours in case of a leak-of-PbLi accident at DEMO, resulting in a Pb-Li pool below 300°C. This is because the PbPo mobilization rate is governed by a diffusion-limited bulk process at high temperatures, whilst being limited by a slower surface evaporation process at low temperatures.

As the surface evaporation rate is directly proportional to the ^{210}Po concentration in the Pb-Li, it could be proposed to allow ^{210}Po inventories 30000 times higher than the 100 appt limit determined for ARIES-AT. However, although PbPo is indeed expected to be the primary evaporating species in an inert atmosphere [Mer19a], recent experiments suggest that in contact with air, Po-containing (oxy-)hydroxides with a higher volatility than PbPo but lower than elementary Po will form [Mau14]. Using the known evaporation rate of elementary Po, a conservative upper limit of the^{210}Po amount evaporating within 2 hours from a DEMO-conditioned Pb-Li pool in contact with air was estimated and found to be still at least 15 times smaller than the evaporated PbPo amount at ARIES-AT. Therefore, a new ^{210}Po concentration limit of 1500 appt could be proposed for DEMO.

In the previous paragraph, it was shown that the predicted ^{210}Po inventories for DEMO using 'dirty' Pb-Li (33 appm ^{209}Bi) are at least a factor 2 below this new limit. Therefore, ^{210}Po is expected not to pose a threat in case of a leak-of-PbLi accident in which the Pb-Li is in contact with air. It should be noted however, that in case the Pb-Li makes contact with water (e.g. the coolant in the case of WCLL), Po species more volatile than elementary Po are expected to form [Mau14]. If these species increase the evaporation rate by more than a factor two, certain safety measures will be required. A dedicated study of the stability and volatility of these Po-containing (oxy-)hydroxides is required to make statements on the required ^{210}Po concentration threshold keeping the ^{210}Po release below the safe limit for this specific accident scenario. If the evaporation rate increases by not more than a factor 15, a safe ^{210}Po concentration threshold would be 100 appt which can be satisfied for the DEMO first blanket irradiation schedule by using relatively clean commercial Pb-Li ($<$ 17 appm ^{209}Bi) and for the 6 (or longer) FPY irradiation schedule by incorporating an on-site Pb-Li purification system keeping the ^{209}Bi level always below 5 appm.

Conclusions

Combining MCNP neutron transport calculations and FISPACT-II inventory calculations, the expected ^{210}Po inventories in the HCLL and WCLL breeding blankets for the DEMO fusion reactor have been determined. It was found that the discrepancies resulting from using different nuclear data libraries are often larger than the ones obtained for the different models. The inconsistency of the branching ratio between a neutron capture by ^{209}Bi resulting in either ^{210g}Bi or ^{210m}Bi is the primary cause and dedicated experiments are necessary. A safety analysis showed that in case of an ex-vessel leak-of-PbLi accident in DEMO, a ^{210}Po concentration below 1500 appt would limit the environmental ^{210}Po release to values below the no-evacuation limit. Even for the most conservative combination of Pb-Li purity, irradiation schedule and nuclear data library, the ^{210}Po concentration stays below this limit by at least a factor 2, with no need for Bi or Po removal from the Pb-Li. However, if the Pb-Li makes contact with water, very volatile Po-containing (oxy-)hydroxides could form. If these species increase the evaporation rate by more than a factor 2, certain safety measures will be required (e.g. on-site Pb-Li purification).

Acknowledgments

M.A.J.M. benefits from a PhD Fellowship of the Research Foundation - Flanders (FWO) and was awarded an additional travel grant by FWO to enable a research stay at KIT. M.A.J.M. acknowledges EUROfusion for granting the permission to use the MCNP DEMO models. S.C. acknowledges financial support from OCAS NV by an OCAS-endowed chair at Ghent University.

Paper II

pp. 163–173

Po-containing molecules in fusion and fission reactors

(Supporting Info on pages 177–215)

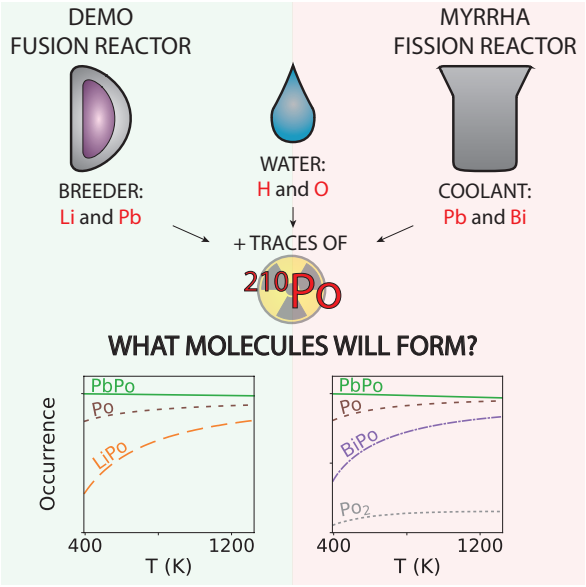

Merlijn A.J. Mertens, Alexander Aerts, Ivan Infante,
Jörg Neuhausen, and Stefaan Cottenier

Journal of Physical Chemistry Letters 2019, **10** (11), 2879–2884, June 2019

doi: 10.1021/acs.jpclett.9b00824

M.A.J. Mertens performed all required ab initio calculations and used the results to predict the relative occurrence of diatomic Po-containing molecules in fusion and fission reactors. Reprinted with permission from Merlijn A. J. Mertens, Alexander Aerts, Ivan Infante, Jörg Neuhausen, and Stefaan Cottenier, Po-containing molecules in fusion and fission reactors, *Journal of Physical Chemistry Letters* 2019, **10** (11), 2879–2884, June 2019.

Po-containing Molecules in Fusion and Fission Reactors

Merlijn A J Mertens[1,2,3], Alexander Aerts[4],Ivan Infante[5,6], Jörg Neuhausen[7], Stefaan Cottenier[1,2]

[1] Center for Molecular Modeling, Ghent University, 9052 Zwijnaarde, Belgium
[2] Department of Electrical Energy, Metals, Mechanical Construction and Systems, Ghent University, 9052 Zwijnaarde, Belgium
[3] Institute for Neutron Physics and Reactor Technology, Karlsruhe Institute of Technology, 76131 Karlsruhe, Germany
[4] Institute for Advanced Nuclear Systems, Belgian Nuclear Research Center (SCK · CEN), 2400 Mol, Belgium
[5] Nanochemistry Department, Italian Institute of Technology, 16163 Genova, Italy
[6] Department of Theoretical Chemistry, Vrije Universiteit Amsterdam, 1081 HV Amsterdam, The Netherlands
[7] Laboratory for Radiochemistry, Paul Scherrer Institute, 5232 Villigen PSI, Switzerland

Abstract

Fission and fusion reactors can only play a role in the future energy landscape if they are inherently safe by design. For some reactor concepts, a major remaining issue is the undesired production of radiotoxic ^{210}Po . To filter out the volatile Po species, information on their molecular composition is needed. An experimental characterization is very challenging due to the large required amount of radioactive Po. An alternative quantum chemistry approach was taken to predict the temperature-dependent stability of relevant diatomic Po-containing molecules. Experimental data on lighter analogue molecules was used to establish a well-founded methodology. The relative occurrence of the Po species was estimated in the cover gas of (i) the Lead-Bismuth Eutectic coolant in the accelerator-driven MYRRHA fission reactor and (ii) the Pb-Li eutectic tritium breeder in the DEMO fusion reactor. In both systems, Po is found to occur mainly as PbPo molecules and atomic Po.

Nuclear power can only play a role in the energy mix for the second half of this century if future fusion and fission reactors [Buc17, Mur15] are inherently safe by design. In this work we focus on the undesired, yet inevitable, ^{210}Po production in some of the envisioned reactor concepts. This occurs when fusion or fission neutrons are captured by ^{209}Bi, followed by a β^- decay into ^{210}Po . The ^{209}Bi isotope is present in small quantities in the liquid Pb-Li tritium breeding blanket of a fusion reactor as well as in the Pb coolant of a fast fission reactor, and in much larger quantities in fast fission reactors that use Pb-Bi eutectic (LBE) as a coolant [Zha14]. The relevant reaction chain is [Mer14]:

$$^{208}\mathrm{Pb} \xrightarrow{n,\gamma} {}^{209}\mathrm{Pb} \xrightarrow{\beta^-} {}^{209}\mathrm{Bi} \xrightarrow{n,\gamma} {}^{210}\mathrm{Bi} \xrightarrow{\beta^-} {}^{210}\mathrm{Po}.$$

^{210}Po is a powerful α-emitter with a specific activity of 166 TBq/g [Hea10] (4500 times higher than ^{226}Ra) and highly radiotoxic. Therefore it is advisable to keep the ^{210}Po concentration in the reactor below a safe threshold, either by prevention (reactor design) or by filtering. This work focuses on gaseous Po species as these can escape more easily from the reactor as compared to liquids and solids.

To devise efficient filtering techniques for the Po-containing gases, it helps to know their molecular composition. As a first step, this work targets diatomic Po-containing molecules. These contain one Po atom bound to either Pb or Li (relevant for fusion reactor Pb-Li breeding blankets), Pb or Bi (relevant for fission reactor Pb(-Bi) coolants), H or O (relevant for water contamination) or another Po atom. This results in 6 diatomic molecules of interest: PoH, LiPo, PoO, PbPo, BiPo and Po_2.

Due to the high radiotoxicity of ^{210}Po , few experiments with volatile polonium have been performed and its chemistry remains poorly known, with most chemical properties published in the 1960s [Ans12]. In fact, the only Po-containing molecule for which an experimental dissociation energy has been reported is Po_2 (1.90 eV) in 1957 by Charles et al. [Cha57]. In 1992, Feuerstein et al. [Feu92] attempted to identify the molecules formed by ^{210}Po evaporating from a Pb-Li breeding blanket. They suggested most Po evaporated as PbPo molecules, because they measured an evaporation rate 1000 times smaller than expected for pure Po, which is consistent with the vapor pressure of NaCl-type PbPo being 1000 times smaller than the one of pure Po [Wit60]. This is however only a consistency argument and not a direct proof.

An alternative approach is to calculate the dissociation profiles of the relevant molecules using quantum chemistry simulations, which provide information on their stability. This has been done by Van Yperen - De Deyne et al. [VYDD15], using density functional theory (DFT). However, their results are not always in agreement with experiment and expectation e.g. for Po_2 they reported a dissociation energy of 2.56 eV, which is rather far from the reported 1.90 eV [Cha57]. The aim of this work is to make a computational analysis using quantum chemistry methods that go beyond the accuracy of DFT.

For molecules containing heavy elements, the relativistic and electron correlation effects are very prominent. The quantum chemistry software package Molcas 8.0 [al.16b] is suitable for describing both [Roo04b]. The scalar relativistic effects are included by using the Douglas-Kroll-Hess Hamiltonian [Dou74, AH86] and the ANO-RCC basis set [Roo04c, Roo04a]. An initial guess of the orbitals is obtained from a Hartree-Fock (HF) calculation. These orbitals are then used in a series of consecutive Complete Active Space Self-Consistent Field (CASSCF) [Roo80] and Multi-State Complete Active Space Perturbation Theory of 2^{nd} order (MS-CASPT2) [And92, Fin98] calculations performed independently for each desired combination of irreducible representation (irrep) and spin state of the wave function. This is done to compute the static and dynamic electron correlation energy, which is not included in the HF calculation. In the CASSCF calculations, the orbital space is divided in three sets: the inactive space (always fully occupied), the active space (can be (partially) occupied), and the virtual space (always unoccupied). The resulting wave function is a linear combination of Slater determinants defined within the chosen active space. The configuration space of the CASPT2 calculation is generated by applying all single and double excitation operators to this CASSCF reference wave function, while defining a set of frozen orbitals that always remain fully occupied. The multi-state aspect arises from coupling CASPT2 states having the same irrep and spin state. To obtain an unambiguous set of non-interacting and orthonormal eigenstates, a Complete Active Space State Interaction (CASSI) calculation [Mal02] is performed. Spin-orbit coupling is included by determining the eigenstates of the extended Hamiltonian using the spin-free states as a basis. The final result is the energy of the ground and first excited states of the diatomic system. Repeating this for a range of internuclear distances yields the potential energy profiles of these states, which will allow us to determine the temperature-dependent stability of the molecules. Convergence tests can be found in the Supporting Info (pp. 179–182).

The choice of the active space has a significant impact on the results. Rather than choosing it based on intuition, or according to the general guidelines provided by Veryazov et al. [Ver11], exhaustive tests were performed. For every Po-containing molecule a series of analogue lighter molecules was defined by substituting one or both of the constituent atoms by lighter elements of the same group in the periodic table. As experimental dissociation energies for these lighter molecules are often known, this procedure allows to objectively decide which active space is most suited for a given type of molecule and is therefore used for the corresponding Po-containing molecule (see Supporting Info, pp. 182–184).

Figure A.7 shows the calculated profiles for PbPo. By fitting an analytic potential energy function $f(D, R_\mathrm{e}, \omega_\mathrm{e}, x_\mathrm{e}, \alpha_\mathrm{e})$ proposed by Hulburt and Hirschfelder [Hul41] to the computed data points for all electronic states i, the energies of all coupled rotational-vibrational-electronic levels (w.r.t. the fundamental ground state) can be determined. The five parameters of the function are the depth of the well D, the equilibrium bond length R_e, the fundamental vibration frequency ω_e, the first anharmonic constant $\omega_\mathrm{e}x_\mathrm{e}$ and the vibration-rotation coupling constant α_e. The energies of the rotational-vibrational-electronic levels are calculated using:

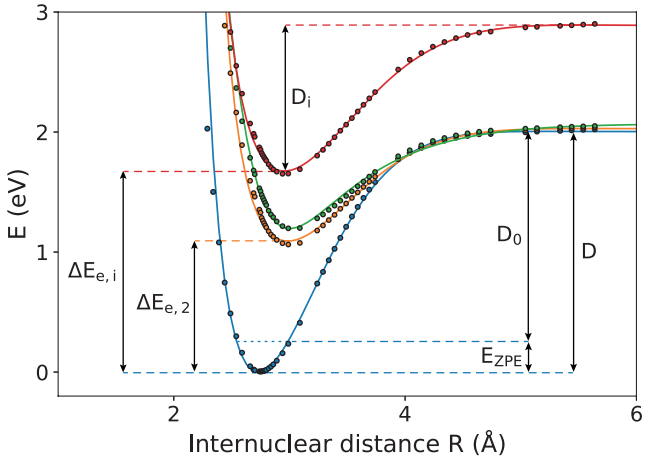

Figure A.7: Computed data points for the ground state and first excited states of PbPo with associated fits $f(D, R_\mathrm{e}, \omega_\mathrm{e}, x_\mathrm{e}, \alpha_\mathrm{e})$.

$$
\begin{aligned}
E_{i,v,J} = \Delta E_{\mathrm{e},i} - E_{\mathrm{ZPE}} \\
&+ \omega_{\mathrm{e},i}(v+\frac{1}{2}) - \omega_{\mathrm{e},i}x_{\mathrm{e},i}(v+\frac{1}{2})^2 + \omega_{\mathrm{e},i}y_{\mathrm{e},i}(v+\frac{1}{2})^3 \\
&+ B_{\mathrm{e},i}J(J+1) - D_{\mathrm{e},i}J^2(J+1)^2 \\
&- \alpha_{\mathrm{e},i}(v+\frac{1}{2})J(J+1).
\end{aligned}
\tag{A.2}
$$

Here i, v and J denote the electronic, vibrational and rotational quantum number, $\Delta E_{\mathrm{e},i}$ is the difference in energy between the minimum of the energy profile for electronic state i w.r.t. that minimum for the ground state (Figure A.7), E_{ZPE} is the zero-point energy, $\omega_{\mathrm{e},i}y_{\mathrm{e},i}$ are the second anharmonic constants, $B_{\mathrm{e},i}$ are the rotational constants and $D_{\mathrm{e},i}$ are the centrifugal distortion constants. Details on the fitting procedure and the calculation of the molecular constants discussed above are given in the Supporting Info (pp. 198–201). The obtained molecular constants for the electronic ground state of the molecules are given in Table A.9. For the other electronic states, they are presented in the Supporting Info (Tables A.15–A.20 on pp. 204–205).

Assuming a constant pressure, the temperature-dependent stability of the molecules is described by the difference in Gibbs free energy of the molecular state w.r.t. the unbound state:

$$
\begin{aligned}
\Delta G(T) = -D - (E_{\mathrm{tr}}^{\mathrm{A1}} + E_{\mathrm{el}}^{\mathrm{A1}} + E_{\mathrm{tr}}^{\mathrm{A2}} + E_{\mathrm{el}}^{\mathrm{A2}}) \\
&+ (E_{\mathrm{tr}}^{\mathrm{M}} + E_{\mathrm{ZPE}}^{\mathrm{M}} + E_{\mathrm{rovibel}}^{\mathrm{M}}) \\
&+ T(S_{\mathrm{tr}}^{\mathrm{A1}} + S_{\mathrm{el}}^{\mathrm{A1}} + S_{\mathrm{tr}}^{\mathrm{A2}} + S_{\mathrm{el}}^{\mathrm{A2}}) \\
&- T(S_{\mathrm{tr}}^{\mathrm{M}} + S_{\mathrm{rovibel}}^{\mathrm{M}}) - k_{\mathrm{B}}T,
\end{aligned}
\tag{A.3}
$$

where D is the depth of the dissociation profile, E are thermal energy corrections and S are entropic contributions. The superscripts M and A denote molecular and atomic quantities respectively, while the subscripts tr, el and rovibel designate translational, electronic and rotational-vibrational-electronic contributions. The detailed procedure used to obtain all contributions is presented in the Supporting Info (pp. 206–209).

The central result of this work i.e. the T-dependent stability of the 6 diatomic molecules of interest, is shown in Figure A.8 and given at 0, 400, 600 and 800 K in Table A.9 (a complete quantitative description is given in the Supporting Info on pp. 207–207). The temperature ranges relevant for

the discussed types of reactors are fully covered. As expected, temperature destabilizes the molecules. PoO is found to be the most stable molecule over the whole temperature range.

Table A.9: Molecular constants for the ground states of the Po-containing diatomic molecules and their stability at 0, 400, 600 and 800 K, obtained by CASSI-SO calculations.

Quantity	PoH	LiPo	PoO	PbPo	BiPo	Po_2
D(eV)	2.26	1.78	3.31	2.01	1.74	1.84
R_e(Å)	1.782	2.639	1.944	2.730	2.770	2.797
ω_e(cm^{-1})	1773	362.1	648.8	166.9	164.1	151.8
$\omega_e x_e$(cm^{-1})	34.7	2.49	2.66	0.316	0.336	0.312
$\omega_e y_e$($10^{-3}cm^{-1}$)	-425	2.6	-17	-0.62	-0.90	-0.40
B_e($10^{-2}cm^{-1}$)	533	35.7	30.0	2.16	2.10	2.05
D_e($10^{-6}cm^{-1}$)	193	1.39	0.256	0.00146	0.00137	0.00150
α_e($10^{-3}cm^{-1}$)	150	2.86	1.87	0.0486	0.0524	0.0524
ΔG_{0K}(eV)	-2.15	-1.76	-3.27	-2.00	-1.73	-1.83
ΔG_{400K}(eV)	-1.84	-1.46	-2.86	-1.66	-1.37	-1.47
ΔG_{600K}(eV)	-1.66	-1.29	-2.62	-1.48	-1.18	-1.24
ΔG_{800K}(eV)	-1.47	-1.11	-2.39	-1.30	-0.98	-1.03

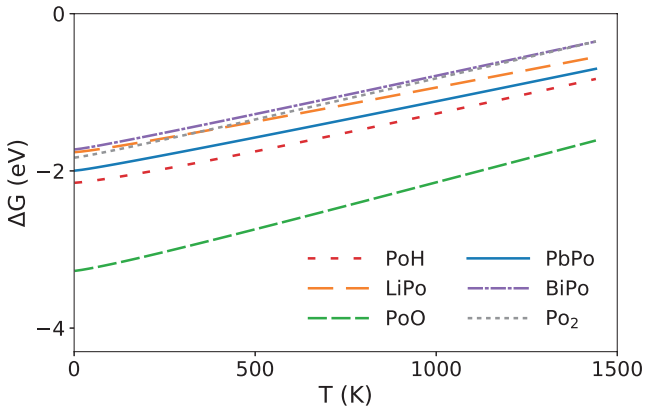

Figure A.8: The difference in Gibbs free energy ΔG of the Po-containing molecules compared to the atomic fragments.

The importance of spin-orbit coupling is illustrated by Figure A.9, in which the dissociation energies D_0 (= ΔG_{0K}) for homonuclear diatomic molecules of the Po-group are compared with the experimental values reported by Huber et al. [Hub79] and by Darwent [Dar70]. For the heavy Po_2 molecule, this effect becomes very prominent and accounts for a

decrease of the dissociation energy by 0.71 eV (for PbPo even as much as 1.68 eV), resulting in a predicted value deviating only 0.07 eV from the experimental one. The overall mean error for all 28 considered molecules with a reported experimental dissociation energy is found to be 0.08 eV (see Supporting Info on p. 185). Based on this value and the verified accuracy of the CASSCF/CASPT2/SO-CASSI approach for molecules containing period 6 main group elements (see Supporting Info on pp. 190–198), the calculated dissociation energies for the Po-containing molecules are expected to be correct within 0.1 eV. Note that the quasi-linearity in Figure A.9 cannot be used to make reliable predictions of the dissociation energy of the Po-containing molecules based on the experimental ones for molecules containing Se and Te, as for some series this extrapolation results in a value deviating more than 0.5 eV from the one obtained by direct calculation.

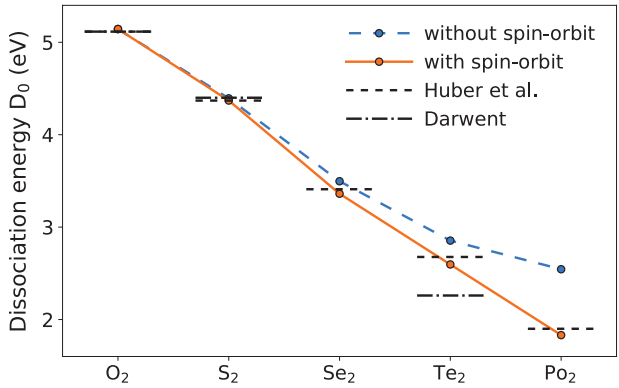

Figure A.9: Dissociation energies for homonuclear diatomic molecules of the Po-group without/with spin-orbit interaction compared to experimental values reported by Huber and Herzberg [Hub79] and Darwent [Dar70].

Using the T-dependent Gibbs free energy differences between the molecular and unbound states, the relative occurrences of the different Po species in a gas containing Po can be estimated. Given the initial atomic concentrations in the gas, the final molar fractions of the species x_i can be predicted by minimizing the total Gibbs free energy of the system $G_{\mathrm{tot}}(T)$:

$$G_{\mathrm{tot}}(T) = n \sum_{\mathrm{mol}} x_i \Delta G_i(T) + nRT \sum_{\mathrm{mol,at}} x_i \ln(x_i). \tag{A.4}$$

The first term accounts for the formation of molecular bonds and the second for the entropy of mixing. The final relative occurrences depend on the initial

concentration of the different elements. Two realistic scenarios are described.

In the MYRRHA fast fission reactor, protons will be fired at an LBE target which serves both as neutron generator and coolant. The generated neutrons maintain the fission chain reaction which is interrupted instantaneously when the proton gun is turned off, making a meltdown disaster scenario impossible by design. The Ar gas atmosphere (P_{Ar} = 101300 Pa) covering the LBE coolant in the MYRRHA reactor is now considered. The initial Pb and Bi concentrations in this gas are calculated using the LBE total vapor pressure recommended by Sobolev [Sob11], while the Pb and Bi fractions in the LBE vapor were determined from the paper by Ohno et al. [Ohn05]. In the equation below, P' denotes a partial vapor pressure and P a total vapor pressure. The superscripts indicate the references the values were taken from. The full derivation of the expressions is presented in in the Supporting Info on pp. 213–215. The final initial concentrations are:

$$c_{\mathrm{Pb}} = \frac{P'_{\mathrm{Pb,LBE}}}{P_{\mathrm{tot}}} \approx \frac{P^{[25]}_{\mathrm{LBE}}}{P_{\mathrm{Ar}}} \frac{P'^{[26]}_{\mathrm{Pb,LBE}}}{P^{[26]}_{\mathrm{LBE}}} = \frac{10^{9.256-9494/T}}{101300\ \mathrm{Pa}} \tag{A.5}$$

$$\begin{aligned} c_{\mathrm{Bi}} &= \frac{P'_{\mathrm{Bi,LBE}} + 2P'_{\mathrm{Bi_2,LBE}}}{P_{\mathrm{tot}}} \approx \frac{P^{[25]}_{\mathrm{LBE}}}{P_{\mathrm{Ar}}} \left(\frac{2P'^{[26]}_{\mathrm{Bi_2,LBE}} + P'^{[26]}_{\mathrm{Bi,LBE}}}{P^{[26]}_{\mathrm{LBE}}} \right) \\ &= \frac{10^{9.973-9488.4/T}}{101300\ \mathrm{Pa}} \frac{2}{1+\alpha^{[26]}} \left(1 - 10^{-0.83+300/T}\right) \end{aligned} \tag{A.6}$$

with the Bi_2–Bi dissociated fraction α:

$$\alpha^{[26]} = \left(\frac{K_P^{[27]}}{\frac{10^{10.688-9794.2/T} - 10^{9.858-9494.2/T}}{101300\ \mathrm{Pa}} + K_P^{[27]}} \right)^{1/2} \tag{A.7}$$

$$K_P^{[27]} = \exp\left(-24442.5/T + 12.5839\right). \tag{A.8}$$

The Bi_2–Bi equilibrium constant K_P was determined from the Gibbs free energy difference between Bi_2 and atomic Bi, available in the FactSage database [al.16a]. After the first irradiation campaign, 350 grams of ^{210}Po is expected to be present in the 7600 ton of LBE [Fio18], resulting in an atomic fraction of $x_{\mathrm{Po}} = 4.6 \times 10^{-8}$. The Henry constant of Po in LBE ($K_{\mathrm{Po,LBE}}$) by Prieto et al. [GP14] was used to determine the initial concentration of atomic Po in the Ar gas:

$$c_{\mathrm{Po}} = \frac{x^{[28]}_{\mathrm{Po}} K^{[29]}_{\mathrm{Po,LBE}}}{P_{\mathrm{tot}}} = \frac{4.6 \times 10^{-8} \cdot 10^{10.8\pm0.7-(8606\pm726)/T}}{101300\ \mathrm{Pa}}. \tag{A.9}$$

It is assumed that no O and H is present in the gas mixture and we allow the formation of PbPo, BiPo, Po_2, PbBi, Bi_2 and Pb_2 to minimize the Gibbs free energy (Eq. A.4).

In the DEMO fusion reactor, deuterium and tritium will be fused together producing helium, a neutron and energy. As tritium is scarce, it has to be produced within the reactor by making the fusion neutrons interact with a Pb-Li blanket surrounding the fusion plasma. The inert gas covering the liquid Pb-Li is now considered ($P_{\text{inter gas}}$ = 101300 Pa). The initial concentrations of Pb and Li in this gas were obtained using the vapor pressures reported by Kondo et al. [Kon13]:

$$c_{\text{Pb}} = \frac{P'^{[30]}_{\text{Pb,Pb-Li}}}{P_{\text{tot}}} = \frac{5.450 \times 10^9 \exp\left(-22246/T\right)}{101300\ \text{Pa}} \tag{A.10}$$

$$c_{\text{Li}} = \frac{P'^{[30]}_{\text{Li,Pb-Li}}}{P_{\text{tot}}} = \frac{8.058 \times 10^9 \exp\left(-25229/T\right)}{101300\ \text{Pa}}. \tag{A.11}$$

After the first irradiation campaign, about 0.5 grams of ^{210}Po is expected to be present in 8000 tons of Pb-Li ($x_{\text{Po}} = 5 \times 10^{-11}$). The recommended Henry constant of Po in Pb-Li $K_{\text{Po,Pb-Li}}$ [Faz15] was used to determine the initial concentration of Po in the inert gas:

$$c_{\text{Po}} = \frac{x_{\text{Po}} K'^{[31]}_{\text{Po,Pb-Li}}}{P_{\text{tot}}} = \frac{5 \times 10^{-11} \cdot 10^{7.39-6017/T}}{101300\ \text{Pa}}. \tag{A.12}$$

Again, no O and H is present in the gas mixture and now the formation of PbPo, LiPo, Po_2, Pb_2 and Li_2 is allowed to minimize the Gibbs free energy (Eq. A.4).

Figure A.10 shows the relative occurrence of the Po species for the discussed scenarios. In MYRRHA, the following occurrence ranges are expected during normal operation (540 K−680 K) [Eng15], in %: PbPo (91.6−84.7), Po (8.4−15.0), BiPo (0.037−0.23), Po_2 ($7.0\times10^{-8}-1.0\times10^{-7}$). The grey band around the Po_2 line originates from the uncertainties in Eq. A.9. In the DEMO fusion reactor, we have (570 K − 820 K [Boc16]), in %: PbPo (93.3 − 86.9), Po (6.7 − 12.8), LiPo (0.014 − 0.25) and negligible amounts of Po_2. For both scenarios, PbPo is found to be dominant (in agreement with the conjecture made by Feuerstein in 1992 [Feu92]), however also a non-negligible share of atomic Po is expected to be present. If a dedicated radiological accident assessment shows that the ^{210}Po inventory is too high

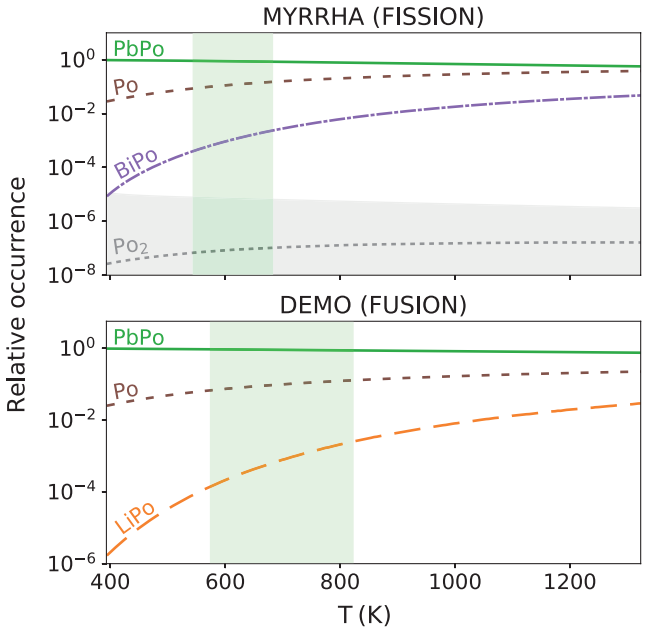

Figure A.10: The relative occurrence of the ^{210}Po species in the cover gas of (i) the LBE coolant in the MYRRHA fission reactor and (ii) the Pb-Li breeder of the DEMO fusion reactor. Operational temperature ranges are marked in green [Eng15, Boc16].

in the cover gas, filtering techniques will have to be devised that focus on these species. It has to be noted that in case the LBE coolant/Pb-Li breeder makes contact with water (e.g. a leak of coolant accident), the assessment becomes much more complex. In this case, the PoH and PoO molecules have to be included as well as all other stable O and H containing molecules that could retain most of the available H and O. Also, evidence exists that some very volatile Po-containing (oxy)hydroxides could occur [Mau14] on which currently no thermodynamic data is available.

The T-dependent stability of 6 diatomic Po-containing molecules was determined using high level ab initio calculations. A validation method based on lighter analogue molecules was used to secure the reliability of the results. The obtained data allowed to estimate the relative occurrence of the different Po species in the dry and oxygen free cover gas of (i) the LBE coolant in the MYRRHA fission reactor and (ii) the Pb-Li breeder of the DEMO fusion reactor. For both cases, PbPo is found to be the dominant species, while also a non-negligible share of atomic Po is present.

Acknowledgments

This work was supported by the project MYRTE under EURATOM Horizon2020 Grant Agreement No. 662186. The computational resources and services used in this work were provided by the VSC (Flemish Supercomputer Center), funded by the Research Foundation - Flanders and the Flemish Government – department EWI. M.A.J.M. benefits from a PhD Fellowship of the Research Foundation - Flanders (FWO). S.C. acknowledges financial support from OCAS NV by an OCAS-endowed chair at Ghent University. M.A.J.M. and S.C. acknowledge fruitful discussions with Jean-Marie Noterdaeme (UGent).

Supporting Info

The Supporting Info is reprinted on pages 177–215 and contains details on:

(i) the workflow of the calculations,
(ii) convergence tests w.r.t. the number of CI roots,
(iii) convergence tests w.r.t. the imaginary shift,
(iv) the selection procedure of the active space,
(v) the error on the dissociation energies,
(vi) the validity/accuracy of the CASSCF/CASPT2/SO-CASSI approach,
(vii) the dissociation profile fitting procedure and all molecular constants,
(viii) the T-dependent stability of the Po-molecules (+ quantitative description),
(ix) the rovibel thermal energy correction,
(x) the molar heat capacities,
(xi) the initial atomic concentrations in the gas mixtures,
(xii) the dissociation energies for all studied lighter analogue molecules and Po-containing molecules with and without spin-orbit effects (Figures A.16–A.23),
(xiii) the dissociation profiles for the important electronic states of the Po-containing molecules (Figures A.25–A.30), and
(xiv) the associated molecular constants (Tables A.15–A.20).

Paper II - Supporting Info

pp. 177–215

Po-containing molecules in fusion and fission reactors (Supporting Info)

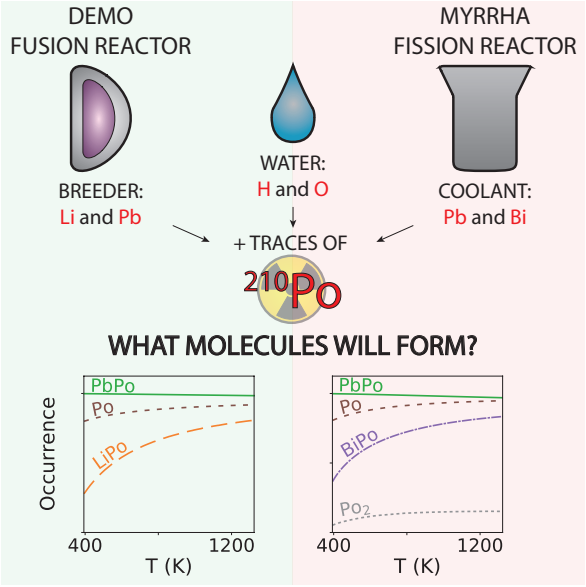

Merlijn A.J. Mertens, Alexander Aerts, Ivan Infante,
Jörg Neuhausen, and Stefaan Cottenier

Journal of Physical Chemistry Letters 2019, **10** (11), 2879–2884, June 2019

DOI: 10.1021/acs.jpclett.9b00824

M.A.J. Mertens performed all required ab initio calculations and used the results to predict the relative occurrence of diatomic Po-containing molecules in fusion and fission reactors.

Po-containing Molecules in Fusion and Fission Reactors: Supporting Info

Merlijn A J Mertens[1,2,3], Alexander Aerts[4],Ivan Infante[5,6], Jörg Neuhausen[7], Stefaan Cottenier[1,2]

[1] Center for Molecular Modeling, Ghent University, Belgium
[2] Department of Electrical Energy, Metals, Mechanical Construction and Systems, Ghent University, Belgium
[3] Institute for Neutron Physics and Reactor Technology, Karlsruhe Institute of Technology, Germany
[4] Institute for Advanced Nuclear Systems, Belgian Nuclear Research Center (SCK · CEN), Belgium
[5] Nanochemistry Department, Italian Institute of Technology, Italy
[6] Department of Theoretical Chemistry, Vrije Universiteit Amsterdam, The Netherlands
[7] Laboratory for Radiochemistry, Paul Scherrer Institute, Switzerland

Workflow of the calculations

In this section, a guideline is provided for people interested in doing similar calculations as have been performed for this work. It should be noted that all settings have to be checked for convergence and correctness by exhaustive tests and by thoroughly analyzing the output before a result may be trusted. The workflow of the performed ab initio calculations is as follows:

1. Specification of the molecular geometry, symmetry and basis set in the GATEWAY module. The internuclear distance was varied to obtain the full dissociation profile. The symmetry was always specified as a twofold rotation around the internuclear axis (point group C_2, which is specified as XY in Molcas if the z-axis is used as internuclear axis). This (low) symmetry setting makes it possible to average over degenerate components. Because of the important relativistic effects occurring in these heavy molecules, the relativistic ANO-RCC basis sets were used [Roo04c, Roo04a]. This basis has been contracted using the Douglas-Kroll-Hess Hamiltonian [Rei04]. Molcas automatically includes scalar relativistic effects when using this basis set.
2. Running the SEWARD module to generate the one- and two-electron integrals needed in the next steps.

3. A Hartree-Fock (HF) Self-Consistent Field (SCF) calculation is run using the SCF module to obtain an initial guess for the orbitals to be used in the next modules. Using the `Occupied` keyword, one can specify how much electrons should be assigned to orbitals in each of the irreducible representations (irreps) in the specified symmetry. For the C_2 point group, there are 2 irreps.
4. Performing a series of consecutive Complete Active Space Self-Consistent Field (CASSCF) [Roo80] and Multi-State Complete Active Space Perturbation Theory of 2^{nd} order (MS-CASPT2) [And92, Fin98] calculations (using the RASSCF and CASPT2 modules) for each desired combination irrep and spin state of the wave function independently. The CASSCF calculations primarily corrects for the static correlation, while the CASPT2 calculations attempts to include mainly dynamic correlation. In CASSCF, the orbital space is divided in three sets:
   (a) the orbitals that are always fully occupied i.e. the inactive space - keyword `Inactive`,
   (b) the set of orbitals that can be (partially) (un)occupied i.e. the active space - keyword `Ras2`,
   (c) the orbitals that are always unoccupied i.e. the virtual space.

   The keyword `nActEl` is used to specify the number of electrons present in the active space. The trial wave function is then a linear combination of the Slater determinants that can be created within the definition of this active space. Using the CIROOT keyword, the user can also specify the number of states to be used in the orbital optimization (see next section). The CASPT2 calculation applied consecutively gives a 2^{nd} order estimate of the difference between the CASSCF energy and the full CI energy. The configuration space is generated here by applying all single and double excitation operators on the CASSCF reference wave function (with the possibility to define a set of frozen orbitals within the inactive space that are then always left fully occupied, using the keyword `Frozen`). Finally the different CASPT2 states within each defined combination of irrep and spin state are coupled using an effective Hamiltonian computed to second order in perturbation theory, hence the multi-state (MS) aspect.
5. Finally, the RASSI module is used to perform a Complete Active Space State Interaction (CASSI) calculation [Mal02]. Here, the CASSCF individually optimized states that are still interacting and non-orthogonal are transformed into a set of unambiguous non-interacting and orthonormal eigenstates of the Hamiltonian which is dressed with the

dynamic correlation obtained from the CASPT2 calculations. Additionally, this module allows to account for spin-orbit interaction to obtain the eigenstates of the sum of the spin-free Hamiltonian and the spin-orbit operator (using the `Spin Orbit` keyword). This finally results in the energy of the ground state and first excited states (either with or without spin-orbit interaction) for the given system.

This whole routine is repeated for many different internuclear distances to obtain the full dissociation curve.

The used methodology is based on the one used by Roos and Malmqvist [Roo04b]. In order to accurately determine all electronic states of interest, the number of Configuration Interaction (CI) roots used for each symmetry type of the wave function (irrep) and each spin multiplicity in the CASSCF calculations as well as the imaginary shift used in the CASPT2 calculations had to be severely tested for convergence and correctness.

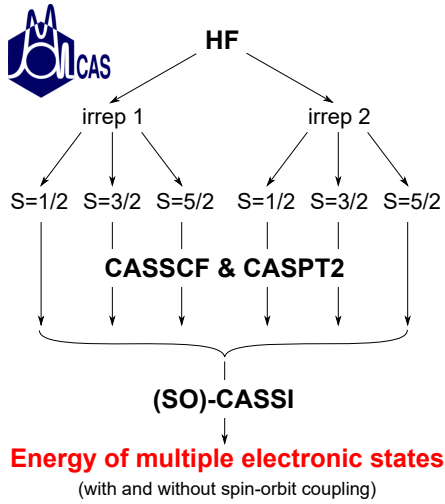

Figure A.11: The entire workflow of the calculations performed for one single spatial configuration of the nuclei.

Convergence: number of CI roots

For each irrep and spin multiplicity, the user has to specify the number of states to be used when performing the orbital optimization in the CASSCF and CASPT2 calculation. This number should be large enough to reach a converged result, however using too much states in these calculations might

lead to the emergence of so called intruder states in the CASPT2 calculation which have a negative impact on the accuracy of the dissociation energy. Intruder states are states with almost the same energy as some eigenstate of H_0 in the interacting space of the CASSCF calculation. In the CASPT2 perturbation calculations, this then leads to denominators close to zero and unphysically large contributions of these states. One can (often) avoid the occurrence of these intruder states by introducing an imaginary shift to artificially shift the energy denominators and avoid these singularities. The calculation then later corrects the resulting energy for the use of this shift. This method has however two disadvantages: it can introduce some new singularities and some of the dynamical correlation is lost. Therefore one should also investigate how the dissociation energy evolves when using different imaginary shifts (see next section). Figure A.12 shows the variation of the dissociation energy of the Po_2 molecule for a different total number of included CI roots. From a total number of 192 CI roots on, the dissociation energy is quite stable. However when going to as much as 320 states, intruder states start to develop and distort the resulting dissociation energy. In our final calculation on the Po_2 molecule, we used a total number of 224 CI roots (marked in green in Figure A.12). Table A.10 shows how many states were used for the different spin multiplicities and irreps separately (C_2 symmetry). Figure A.13 shows the complete dissociation profiles for some of the different total number of states. It can be seen how this curve converges when going to a larger number of states.

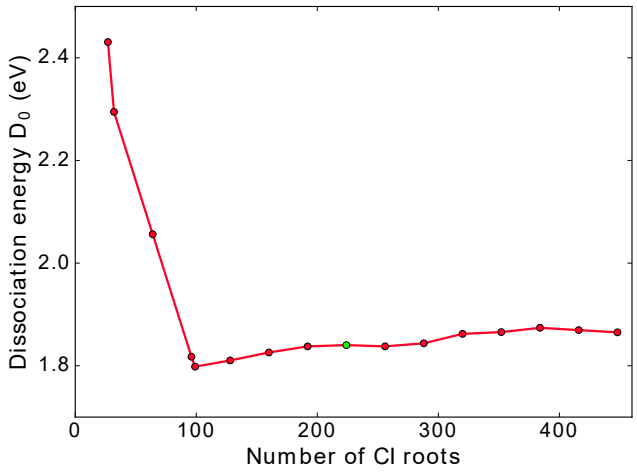

Figure A.12: Convergence of the dissociation energy with respect to the use of a different number of CI roots.

Table A.10: The number of CI roots for each spin multiplicity and irrep used to obtain Figures A.12 and A.13.

Spin=0 irrep 1	Spin=0 irrep 2	Spin=1 irrep 1	Spin=1 irrep 2	Spin=2 irrep 1	Spin=2 irrep 2	Total
5	4	5	4	5	4	27
2	2	8	8	6	6	32
4	4	16	16	12	12	64
6	6	24	24	18	18	96
5	4	21	24	25	20	99
8	8	32	32	24	24	128
10	10	40	40	30	30	160
12	12	48	48	36	36	192
14	**14**	**56**	**56**	**42**	**42**	**224**
16	16	64	64	48	48	256
18	18	72	72	54	54	288
20	20	80	80	60	60	320
22	22	88	88	66	66	352
24	24	96	96	72	72	384
26	26	104	104	78	78	416
28	28	112	112	84	84	448

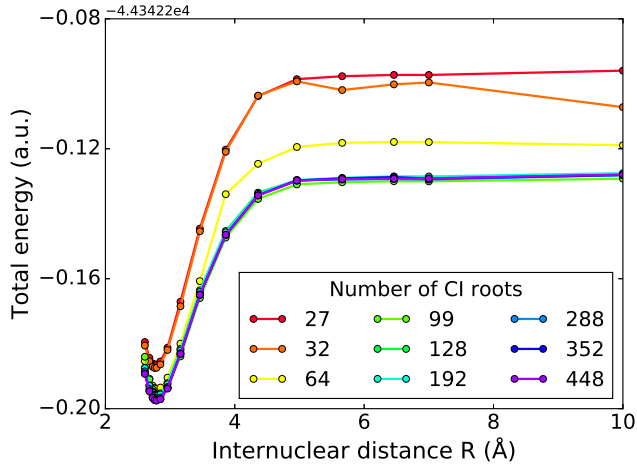

Figure A.13: Resulting dissociation curves for a different number of CI roots used.

Convergence: imaginary shift

As mentioned in the previous section, it should be investigated how the dissociation energy evolves with imaginary shift used in the CASPT2 calculation. Most of the calculations were performed with an imaginary shift of 0.25. Figure A.14 shows how the dissociation energy converges when decreasing the imaginary shift towards zero for the case of a total of 51 CI roots (for each spin state and irrep separately: 13 10 11 12 3 2, in the order as denoted in Table A.10). The difference between the dissociation energies for an imaginary shift of 0 and 0.25 is less than 0.002 eV and way smaller than the variation in this dissociation energy due to other settings (e.g. the choice of active space, the total number of CI roots). It can therefore be concluded that an imaginary shift of 0.25, which often avoids all of the intruder states, is a safe setting that does not have a major impact on the accuracy of the resulting dissociation energy by itself but rather ensures that this value can be trusted due to the absence of intruder states (which should nevertheless always be thoroughly checked for).

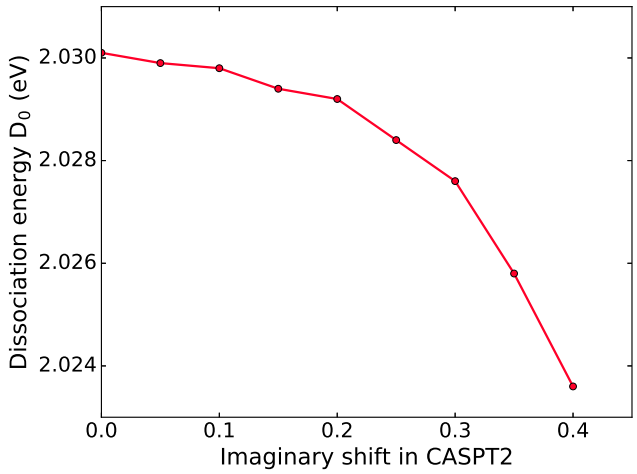

Figure A.14: Convergence of the dissociation energy for decreasing imaginary shift.

Choice of active space

Another critical setting for the CASSCF and CASPT2 calculations is the choice of the active space. It is not a straightforward choice to make and it requires a lot of experience and chemical intuition. Some general recommendations have been proposed by Veryazov et al. [Ver11]. However,

rather than blindly using these guidelines, it was chosen to extensively test many candidate active spaces in order to evaluate them quantitatively. As no experimental dissociation energies have been reported for the studied Po-containing molecules (except for Po_2), the evaluation was carried out using lighter analogue molecules. These analogue molecules were defined by substituting the Po atom (single substitution) or both atoms (double substitution) by lighter analogue atoms of the same group in the periodic system (see Figure A.15). The resulting dissociation energies of the different active spaces were compared to the experimental ones reported by Huber in 1979 [Hub79]. For each active space, all deviations for the molecules in a specific substitution series were added. The active space resulting in the lowest total deviation for a specific substitution series was then considered to be the most suited active space for the associated Po-containing molecule of that series.

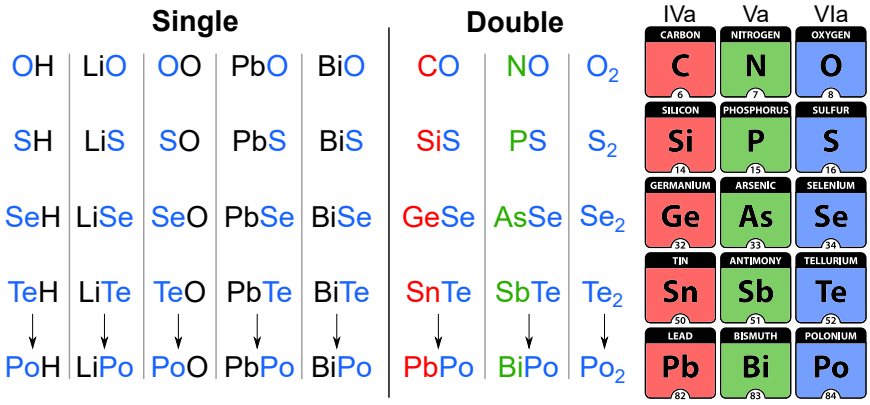

Figure A.15: Substitution series used to validate the active space.

Table A.11 summarizes all active spaces that have been evaluated and the one that turned out to be best. For each Po-containing molecule, the active space definition for the smallest tested active space (S), the largest tested active space (L) and the best active space (B) is given. The column #AS gives information on the amount of tested active spaces defined between the smallest and largest one. All of these active space choices were defined based on chemical intuition and atomic orbital definitions. The number of inactive orbitals for both irrep 1 and 2 is shown in column *inact.*, the number of active orbitals in irrep 1 and 2 in column *act* and the number of active electrons in column *act.* e^-. Finally the number of orbitals that were frozen in the CASPT2 for irrep 1 and 2 is given in the column *frozen*. For the BiPo molecule a different optimal active space was found based on the single

(s) and double (d) substitution series. However, the results for the single substitution series (s) were a lot closer to the experimental value reported by Huber. Therefore, the active space which was found to be best for the single substitution series was used for the final results of the BiPo molecule.

Table A.11: Summary of the tested active spaces for the 6 studied Po-containing diatomic molecules.

		inact. orb.		act. orb.		act. e^-	frozen orb.		#AS
irrep		1	2	1	2	/	1	2	/
PoH	B(s)	22	18	4	2	5	22	18	15
	S	22	18	2	2	5	22	18	
	L	21	18	6	4	7	21	18	
LiPo	B(s)	22	18	5	4	7	22	18	24
	S	23	18	2	2	5	23	18	
	L	21	18	6	4	9	21	18	
PoO	B(s)	23	18	5	4	10	22	18	18
	S	24	18	2	4	8	24	18	
	L	22	18	6	4	12	22	18	
PbPo	B(s,d)	43	36	5	4	8	42	36	18
	S	44	36	2	4	6	44	36	
	L	42	36	6	4	10	42	36	
BiPo	B(s)	43	36	5	4	9	42	36	18
	B(d)	44	36	4	4	7	42	36	
	S	44	36	2	4	7	44	36	
	L	42	36	6	4	11	42	36	
Po_2	B(d)	42	36	4	4	12	42	36	18
	S	44	36	2	4	8	44	36	
	L	42	36	6	4	12	42	36	

Estimated error of the dissociation energies at 0 K

Mean absolute error of the substitution series

The accuracy of the computed dissociation energies at 0 K can be estimated by comparing them to the experimental values reported by Huber, for the 28 considered molecules for which this value is available. Figures A.16–A.23 show the results for all substitution series using the matching best active space. In the captions, the mean absolute error (w.r.t. the experimental values reported by Huber) are given. An overall mean absolute error of only 0.08 eV was found. However, four outliers were identified: OH, PbO, NO and SbTe. The first three of these molecules are all lightest in one of the substitution series. The active space found to be best for the rest of the series turned out not to be ideal for these lightest analogue molecules due to a shift in the orbital energy order. These outliers are therefore not relevant for the Po-containing molecules. For the SbTe molecule, a dissociation energy of 2.54 eV was found which deviates considerably from the value reported by Huber (2.8 eV). However Darwent reported an experimental value of 2.6 eV, which casts some suspicion on Huber's value. When leaving out these four outliers, the mean absolute error on our predicted dissociation energies is reduced to only 0.05 eV.

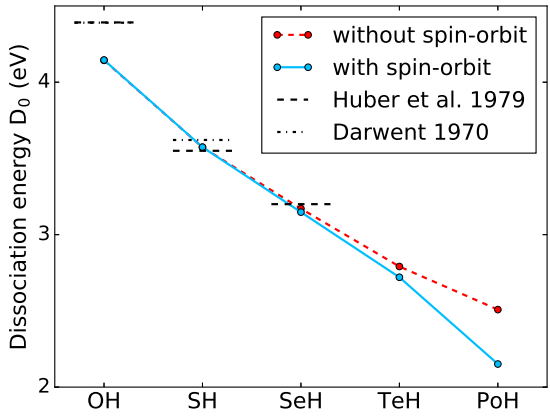

Figure A.16: Dissociation energies obtained using the best active space for the PoH single substitution series (see Table A.11). The results are compared to the experimental dissociation energies reported by Huber et al. [Hub79] and Darwent [Dar70]. The mean absolute error w.r.t. Huber was found to be 0.108 eV (from OH, SH and SeH). Without outlier OH, this reduced is to 0.038 eV.

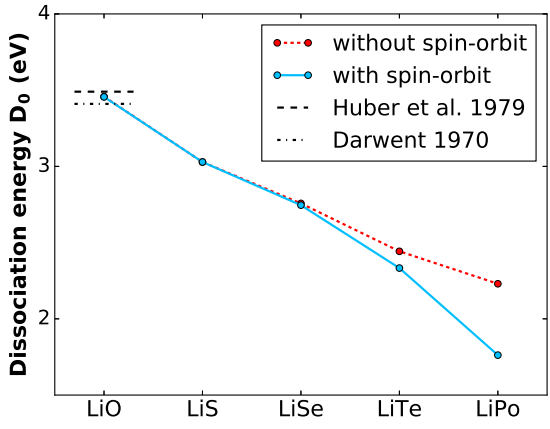

Figure A.17: Dissociation energies obtained using the best active space for the LiPo single substitution series (see Table A.11). The results are compared to experimental dissociation energies reported by Huber et al. [Hub79] and Darwent [Dar70]. The calculated result for LiO only deviates 0.034 eV from the result reported by Huber.

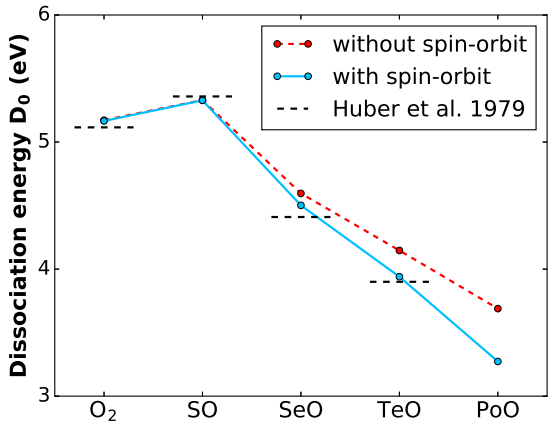

Figure A.18: Dissociation energies obtained using the best active space for the PoO single substitution series (see Table A.11). The results are compared to experimental dissociation energies reported by Huber et al. [Hub79]. The mean absolute error w.r.t. Huber was found to be 0.053 eV (from O_2, SO, SeO and TeO).

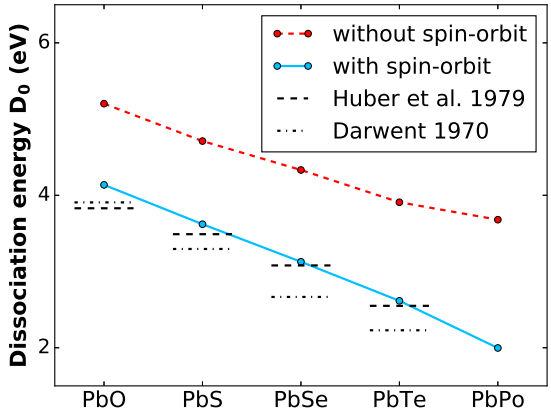

Figure A.19: Dissociation energies obtained using the best active space for the PbPo single substitution series (see Table A.11). The results are compared to experimental dissociation energies reported by Huber et al. [Hub79] and Darwent [Dar70]. The mean absolute error w.r.t. Huber was found to be 0.138 eV (from PbO, PbS, PbSe and PbTe). Without outlier PbO, this is reduced to 0.082 eV.

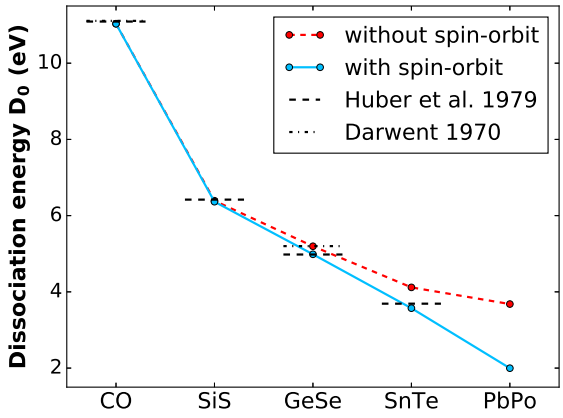

Figure A.20: Dissociation energies obtained using the best active space for the PbPo double substitution series (see Table A.11). The results are compared to experimental dissociation energies reported by Huber et al. [Hub79] and Darwent [Dar70]. The mean absolute error w.r.t. Huber was found to be 0.059 eV (from CO, SiS, GeSe and SnTe).

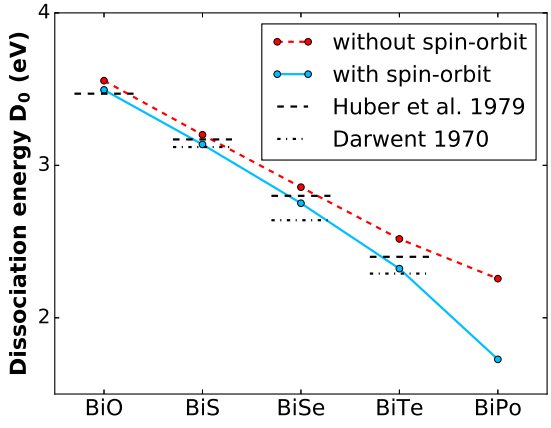

Figure A.21: Dissociation energies obtained using the best active space for the BiPo single substitution series (see Table A.11). The results are compared to experimental dissociation energies reported by Huber et al. [Hub79] and Darwent [Dar70]. The mean absolute error w.r.t. Huber was found to be 0.046 eV (from BiO, BiS, BiSe, BiTe).

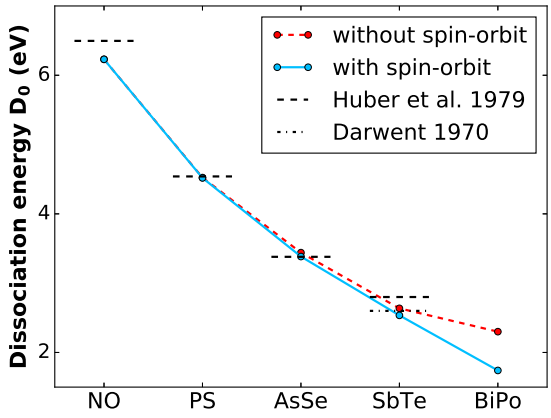

Figure A.22: Dissociation energies obtained using the best active space for the BiPo double substitution series (see Table A.11). The results are compared to experimental dissociation energies reported by Huber et al. [Hub79] and Darwent [Dar70]. The mean absolute error w.r.t. Huber was found to be 0.139 eV (from NO, PS, AsSe, SbTe). Without outliers NO and SbTe this is reduced to 0.008 eV.

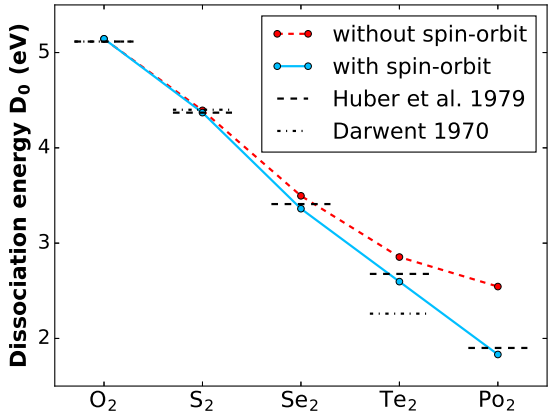

Figure A.23: Dissociation energies obtained using the optimal best active space for the Po_2 double substitution series (see Table A.11). The results are compared to experimental dissociation energies reported by Huber et al. [Hub79] and Darwent [Dar70]. The mean absolute error w.r.t. Huber was found to be 0.044 eV (from O_2, S_2, Se_2, Te_2 and Po_2).

Validity of the SO-CASSI approach for heavy molecules

Argumentation based on literature

The accuracy of the CASSCF/CASPT2/SO-CASSI method on simple molecules containing heavy main group elements has been investigated by Roos and Malmqvist for in Ref. [Roo04b] and [Roo04c].

In Ref. [Roo04b], the spin-orbit splitting of the lowest term in the sixth row main group elements (Tl, Pb, Po, At) was determined, as well as the SO stabilization of the ground state. This stabilization was found to be 0.6 eV, 1.23 eV, 1.14 eV and 0.84 eV for Tl, Pb, Po and At respectively. The error on these values was estimated to be of the order of 0.10 eV (based on the deviation between the calculated and experimentally observed SO splitting). Next, the effect of spin-orbit coupling on several molecular properties of PbO was investigated and compared to the experimental values. This molecule was primarily selected because it is one of the few molecules containing a heavy main group element for which some experimental data is available. The CASSCF/CASPT2/SO-CASSI approach was used to determine the bond length, dissociation energy, fundamental frequency, first anharmonic constant, dipole moment and polarizability of the ground state and first excited states of the PbO molecule. At the CASPT2 level of theory, a dissociation energy of 5.05 eV was found. The inclusion of spin-orbit coupling reduces this value to 4.00 eV, which is being compared to the value 3.83 ± 0.06 eV which has been experimentally determined by Drowart et al. [Dro65] using mass spectroscopy. The discrepancy of 0.17 eV could be attributed both to approximations in the used approach and errors on the experimental value by which heavy molecules are often affected (due to the limited amount of experiments performed). N.J. Friswell and D.R. Jenkins for example, have reported a PbO dissociation energy of 3.96 ± 0.08 eV based on atomic absorption spectroscopy experiments [Fri72]. This value is in close agreement with the calculated value. Also many other spectroscopic constants are found to be in correspondence with the experimental values. The authors therefore conclude that:

"This illustrative calculations shows that an approach that adds scalar relativistic effects to a non-relativistic wave function and that treats spin-orbit coupling by a configuration interaction method can be used to obtain accurate properties also for molecules containing heavy main group elements."

and

"The result obtained in present study shows that such an approach is capable of yielding molecular properties of an accuracy which is comparable with other sophisticated quantum chemistry methods."

Finally, Roos and Malmqvist determined the SO stabilization in the dissociated Pb-O system to be 1.22 eV, which can be compared to the 1.23 eV obtained for the isolated Pb atom using the same method. They therefore expect the error on the computed SO stabilization to be of the same order as the error on the atomic SO stabilization i.e. 0.1 eV.

In Ref. [Roo04c], the CASSCF/CASPT2/SO-CASSI approach is discussed in detail and used to study the spin-orbits splittings for the main group elements, the electronic spectrum of the iridium atom, the ground state of Tl_2 and Pb_2, and the electronic spectrum of PbO. The average relative error on the excitation energies to the lower excited states of the sixth row main group elements i.e. Tl, Pb, Bi, Po was determined to be 9.11 %. While this relative error is indeed higher than the relative error for the lower row elements (3.00 %, 8.28 %, 7.01 %, 7.24 % for row 2-5 respectively), the difference was found to be not that significant. As previously mentioned, the spin-orbit stabilization of the ground state was determined for the sixth rows elements in Ref. [Roo04b]. A 9.11% relative error on the values for Pb and Po, i.e. 1.23 and 1.14 respectively, results again in an estimated error of the order of 0.1 eV on these values. For the dissociation energy of the lead dimer, Roos and Malmqvist found a value of 0.917 eV which is in good agreement with the experimental value 0.86 ± 0.05 eV [Bal98]. The obtained result is also closer to the experimental value than the 0.74 eV previously obtained by Mayer et al. using two-component density functional theory with a generalized gradient exchange-correlation functional [May01]. The authors finally state:

"We conclude that the present approach is capable of describing relativistic effects on the bond formation also in systems containing sixth row main group atoms."

Argumentation based on test calculations

Literature thus suggests that the CASSCF/CASPT2/SO-CASSI approach is an appropriate way to account for spin-orbit coupling effects. However, to further demonstrate the validity of the approach, we ourselves have performed additional test calculations on the Po_2, PbO and Pb_2 molecules. The convergence tests performed on the Po_2 molecule, which were discussed above, will now be analyzed in even more detail. The active space used in the CASSCF and CASPT2 calculations include the 6s and 6p orbitals of Po. No additional orbitals were correlated (unfrozen) in the CASPT2 calculations. Calculations were performed for a varying number of CI roots included in the calculations (see Table A.10). Figure A.24 emphasizes the importance of including enough CI roots in order to obtain a converged result. It can be seen that the spin-orbit stabilization of the dissociated state is more affected by an inadequate number of CI roots than the stabilization for the molecular state. The spin-orbit stabilization for the molecule converges to 1.49 eV and for the dissociated state to 2.16 eV, i.e. 1.08 eV per Po atom. The CASPT2 dissociation energy is affected by the number of CI roots to a lesser degree and varies between 2.45 eV and 2.52 eV. For the SO-CASSI dissociation energy however, the importance of including enough CI roots is very prominent. The fact that the CASSCF/CASPT2/SO-CASSI approach may converge slowly with the number of spin-free states used to compute the spin-orbit coupling contributions has already been pointed out by Roos and Malmqvist in Ref. [Roo04b]. This is especially the case for row 6 main group elements. Therefore, the convergence of spin-orbit coupling effects with the number of CI roots included in the calculation should always be checked. It has to be noted that including too much CI roots may give rise to other problems such as intruder states in the CASPT2 calculations.

Finally, the converged values (w.r.t. number of CI roots included) of the SO stabilization and dissociation energies can be compared for different active spaces. In Table A.12 the results obtained for Po_2 using a $6p^4$ and $6s^26p^4$ active space are compared. It can be seen that the both the spin-orbit stabilization of the molecular and dissociated state give comparable values for the two active spaces (difference under 0.03 eV). Therefore, the discrepancy in the dissociation energy D_0 obtained at the SO-CASSI level of theory is found to be primarily originating from the already existing difference at the CASPT2 level of theory. This shows the importance of choosing an appropriate active space in the calculations and is the reason why so much time and effort was dedicated to this aspect in the presented work. The dissociation energy of 1.829 eV obtained using the $6s^26p^4$ active space at the SO-CASSI level of theory is in good agreement with the

experimental value 1.90 eV reported by Huber [Hub79] (note that this is the only experimental dissociation energy ever reported for a Po-containing molecule).

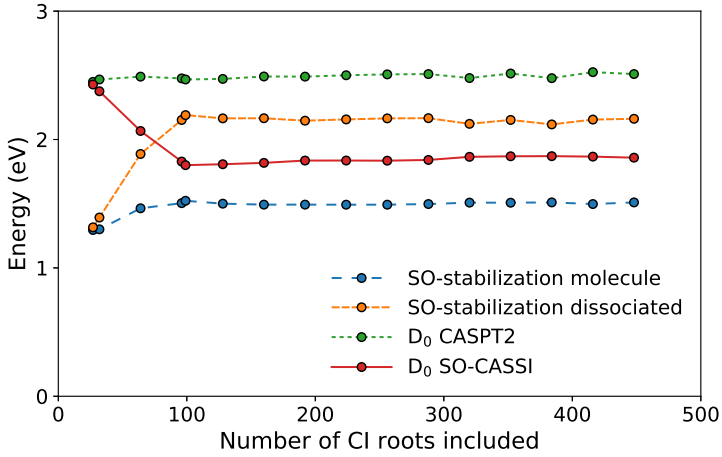

Figure A.24: The spin-orbit stabilization in Po_2 at equilibrium and in the dissociated state, as well as the dissociation energy D_0 at the CASPT2 and the SO-CASSI level of theory as a function of the number of CI roots included in the calculation (cfr. Table A.10). The active space used in the CASSCF calculations include the 6s and 6p orbitals of Po. These were also the only orbitals left unfrozen in the CASPT2 calculations.

Table A.12: The converged (w.r.t. CI roots included) spin-orbit stabilization in Po_2 at equilibrium and in the dissociated state, as well as the dissociation energy D_0 at the CASPT2 and the SO-CASSI level of theory for two different active space (A.S.) $6s^2$ and $6s^26p^4$. The final dissociation energy D_0 can be compared to the value 1.90 eV reported by Huber [Hub79]. All values are expressed in units eV.

Active space	SO-stab. molecule	SO-stab. dissociated	D_0 CASPT2	D_0 SO-CASSI
$6s^2$	1.517	2.188	2.360	1.688
$6s^26p^4$	1.495	2.161	2.495	1.829
difference	0.022	0.027	**0.135**	**0.141**

Next, some additional benchmark calculations have been performed on the PbO molecule to compare the accuracy of the CASSCF/CASPT2/SO-CASSI approach to other sophisticated ab initio methods.. An active space consisting of the 6s and 6p orbitals of Pb and the 2p orbitals of O was used. Calculations were performed first for 9 singlets, 27 triplets and 9 quintets i.e. all states that dissociate to the ($2s^2 2p^4$;^{3}P) term of O and the ($6s^2 6p^2$;^{3}P, ^{1}D,^{1}S) terms of Pb, as the latter terms are strongly coupled by spin-orbit effects. Then, the calculations were repeated once for 45 singlets, 45 triplets and 9 quintets and once for 64 singlets, 64 triplets, 64 quintets. The latter two calculations showed that the spin-orbit coupling contributions had not yet converged with respect to the CI roots included in the first calculations. For the latter two, a converged result was obtained. A dissociation energy D_0 of 3.82 eV was found. This value is in extremely good agreement with the experimental value reported by Huber et al. (3.83 eV) [Hub79]. The bond length was calculated to be 1.932 Å, which is also in fairly good agreement with the one reported by Huber et al. (1.922 Å).
The spectroscopic properties of PbO have been theoretically studied in detail by Iliaš et al. in 2005 [Ili05]. In this paper, calculations were performed on the PbO molecule using the two-component infinite-order method by Barysz, Sadlej and Snijders (BSS) [Bar02] which was interfaced with Kramers unrestricted CCSD(T) [Vis96] and the Fock space CCSD method [Vis01] was used to account for both scalar and spin-orbit relativistic effects simultaneously (the complete method is called BSS-CCSD(T)). Also calculations were performed using the Dirac-Coulomb four-component method [Vis00](DC-CCSD(T))). They compared the results to a number of values from literature originating from other ab initio methods capable of treating relativistic effects up to a certain level e.g. two-component ECP-CCSD(T), CCSD(T), ZORA and the method used in our work i.e. CASSCF/CASPT2/SO-CASSI. As the goal of our work is primarily to determine accurate dissociation energies of Po-containing molecules, the focus will be on this quantity. Table A.13 was adopted from [Ili05] and supplemented with our calculated data. The BSS-CCSD(T) method was found to give comparable results to DC-CCSD(T). The BSS-CCSD(T) in combination with the largest basis set used i.e. the decontracted ANO-RCC basis set, resulted in a potential energy well depth D of 3.91 eV and a bond length of 1.918 Å. This should be compared to the experimental values 3.87 eV and 1.922 Å and to our calculated values being respectively 3.86 eV and 1.932 Å. Both ab initio methods are found to be in good agreement with experiment and each other. The other studied methods were also found to produce reasonable results for D (except the ZORA result which is deviating somewhat more). It should be noted that the CASPT2/SO-CASSI result reported in the discussed paper varies from our results as in those

calculations the Pb 5d orbitals and the O 2s orbital were also correlated perturbatively in the CASPT2 calculations. This is something we decided not to do, based on the many calculations performed on the PbO, PbS, PbSe, PbTe and PbPo systems. Spin-orbit effects are found to reduce D significantly, ranging from 1.06-1.36 eV depending on the method used. In our calculations the destabilization was found to be 1.13 eV (resulting from a total stabilization of the atomic fragments by 1.25 eV and of the PbO molecule by 0.12 eV), which lies well within the range defined by the other methods. Therefore, we can conclude that the CASSCF/CASPT2/SO-CASSI approach is indeed an appropriate way to account for spin-orbit effects in systems containing heavy main group sixth row elements, with an accuracy comparable to the one of other sophisticated quantum chemistry methods.

Some additional test calculations were performed on the Pb dimer. The active space was defined as the 6s and 6p orbitals of Pb. Calculations were performed for 45 singlets, 45 triplets and 9 quintets. The depth of the potential energy profile D was found to be 0.85 eV and 2.05 eV at the SO-CASSI and CASPT2 level respectively. The destabilization due to spin-orbit coupling is thus estimated to be 1.20 eV (resulting from a total atomic fragment stabilization of 2.48 eV and a stabilization of the molecule by 1.28 eV). The dissociation energy of 0.85 eV is again in very good agreement with literature, as can be seen from Table A.14. In fact, the consensus on the dissociation energy of the lead dimer is remarkable compared to what can be found in literature on other diatomic molecules containing heavy elements. This makes the lead dimer an ideal system to test the validity of the used CASSCF/CASPT2/SO-CASSI approach. The fact that our calculated value is found to be in excellent agreement with the recommended experimental value (0.86 eV), suggests that our approach indeed yields reliable results. Abe et al. have also performed high level of theory ab initio calculations on the Pb dimer using the DC-CASCI/DC-CASPT2 approach (DC denotes Dirac-Coulomb) [Abe08]. This methods combines the complete active-space second order perturbation theory with the four-component Dirac Hamiltonian. Finally, a dissociation energy of 0.55 eV is reported, which is rather far from the experimental value. In this case, the CASSCF/CASPT2/SO-CASSI approach is found to perform better. It should be noted that the results of the DC-CASCI/DC-CASPT2 results were still very dependent on the basis set used, indicating that the basis set used was probably too limited to properly describe the system.

Finally, the accuracy of the substitution series containing heavy elements can be considered. In order to obtain reliable values of the dissociation

Table A.13: Bond length R_e, potential energy well depth D and spin-orbit coupling destabilization of the molecule $\Delta_{SO}D$ for different high level of theory ab initio methods capable of (partially) accounting for scalar and spin-orbit relativistic effects. This table was taken from the paper by Iliaš et al. [Ili05] and supplemented with our calculated data. *sf* denotes spin-free.

Method	R_e (Å)	D (eV)	$\Delta_{SO}D$ (eV)
NpPol basis [a]			
BSSsf-CCSD(T)[Ili05]	1.937	4.85	-1.22
BSS-CCSD(T)[Ili05]	1.934	3.63	
DCsf-CCSD(T)[Ili05]	1.936	4.8	-1.11
DC-CCSD(T)[Ili05]	1.933	3.69	
ANO-RCC basis [b]			
BSSsf-CCSD(T)[Ili05]	1.920	5.20	-1.29
BSS-CCSD(T)[Ili05]	1.918	3.91	
Other ab initio methods			
1c sf ECP-CCSD(T)[Liu01]	1.926	5.11	-1.18
2c ECP-CCSD(T)[Liu01]	1.924	3.93	
sf CCSD(T)[Han03]	1.922	5.10	-1.23
CCSD(T)[Met00]	1.923	3.87	
sf CASPT2[Roo04b]	1.923	5.10	-1.06
CASPT2/SO-CASSI[Roo04b]	1.926	4.04	
sf ZORA[Len96]	1.939	5.51	-1.36
ZORA[Len96]	1.937	4.15	
Our results			
sf CASPT2	1.927	4.99	-1.13
CASPT2/SO-CASSI	1.932	3.86	
Experiment			
Drowart et al.[Dro65]	1.9218	3.87	

[a] virtual spinors with energies higher than 700 a.u. deleted
[b] virtual spinors with energies higher than 10 a.u. deleted

energies for PbPo and BiPo, calculations have been performed on the (PbO - PbS -PbSe - PbTe) and (BiO - BiS - BiSe - BiTe) series respectively. The mean absolute error with respect to the values reported by Huber et al. [Hub79] for the (PbO - PbS -PbSe - PbTe) series was found to be 0.138 eV, which is rather large compared to overall mean absolute error of 0.08 eV obtained for all calculations. However, PbO was found to behave somewhat different from the other molecules in that series, making the best overall active space for the series not ideal for this molecule. If this molecule is left out of consideration, the mean absolute error for the (PbS -PbSe - PbTe) series is

Table A.14: Experimental data on the lead dimer dissociation energy. The boldfaced value is the recommended one. This data was obtained from the comprehensive handbook of chemical bond energies by Yu-Ran Luo [Luo07].

Method	D_0 (eV)
Mass spectroscopy[Gin76]	0.80±0.06
Review[Mie79]	0.82
Mass spectroscopy[Pit81]	**0.86±0.01**
Review[MS96]	0.83

reduced to 0.082 eV, which is still somewhat larger than the overall mean absolute error calculated leaving 4 outliers out of consideration i.e. 0.05 eV. The mean absolute error on the (BiO - BiS - BiSe - BiTe) series was found to be only 0.046, which is thus better than average. The increased error in the (PbS - PbSe - PbTe) series is not that significant and could as well be attributed to possible errors on the reported values as not many experiments have been performed on these heavy molecules. We conclude that the accuracy reached for the substitution series containing heavy main group elements of period 6 is satisfying, certainly when taking in consideration the increased uncertainty on the reported experimental value.

We can finally conclude that the CASSCF/CASPT2/SO-CASSI approach is suitable for treating molecules containing heavy main group elements of period 6 because:

- The approach results in a reasonably sized spin-orbit splitting of the lower term for these heavy elements with an mean relative error to experiment of 9.11%, which corresponds to a mean absolute error of the order of 0.1 eV. The errors on the SO stabilization of simple molecules are expected to be of the same error.

- The obtained dissociation energies for PbO, Pb_2 and Po_2 were all found to be in excellent agreement with the experimental values reported.

- Converged values are obtained for the SO (de)stabilization of the system which are equal for different active spaces. This suggests that if enough CI roots are included, the obtained spin-free eigenstates are a good basis to compute the spin-orbit interaction matrix elements to finally obtain the spin-orbit eigenstates. Furthermore, the obtained values are in good agreement with other sophisticated ab initio meth-

ods capable of treating spin-orbit interaction e.g. BB-CCSD(T) and 2c ECP CCSD(T).

- The approach performs better on the Pb_2 system than the relativistic multireference DC-CASCI/DC-CASPT2 approach.
- The mean absolute error on the dissociation energy with respect to experimental values reported by Huber et al. is found to be satisfying even for substitution series containing heavy period-6 elements e.g. for (PbS - PbSe - PbTe) it is 0.082 eV and for (BiO - BiS - BiSe - BiTe) 0.046 eV. These are satisfying results, certainly considering the increased uncertainty on dissociation energies on heavier molecules (due to the few experiments performed).

Profile fitting and molecular constants

As discussed in the main article, the five-parameter potential energy function $f(D, R_\mathrm{e}, \omega_\mathrm{e}, \omega_\mathrm{e}x_\mathrm{e}, \alpha_\mathrm{e})$ proposed in 1941 by Hulbert and Hirschfelder [Hul41] was fitted to the ab initio computed data points of the dissociation profile. It is given by:

$$V(R) = D[(1 - e^{-x})^2 + c_1 x^3 e^{-2x}(1 + c_2 x)] \tag{A.13}$$

with the dimensionless parameter x being

$$x = 2\beta\xi = \frac{\omega_\mathrm{e}}{2(B_\mathrm{e}D)^{1/2}}\left(\frac{R - R_\mathrm{e}}{R_\mathrm{e}}\right), \tag{A.14}$$

and the parameters c_1 and c_2 given by

$$c_1 = 1 + a_1\left(\frac{D}{a_0}\right)^{1/2}, \tag{A.15}$$

$$c_2 = 2 + \left[\frac{7}{12} - \frac{Da_2}{a_0}\right] \Big/ c_1, \tag{A.16}$$

where a_0, a_1 and a_2 are the Dunham coefficients [Dun32]

$$a_0 = \frac{\omega_\mathrm{e}^2}{4B_\mathrm{e}}, \tag{A.17a}$$

$$a_1 = -1 - \frac{\alpha_\mathrm{e}\omega_\mathrm{e}}{6B_\mathrm{e}^2}, \tag{A.17b}$$

$$a_2 = \frac{5}{4}a_1^2 - \frac{2}{3}\frac{\omega_\mathrm{e}x_\mathrm{e}}{B_\mathrm{e}}, \tag{A.17c}$$

and the rotational constant B_e being

$$B_\mathrm{e} = \frac{h}{8\pi^2 \mu R_\mathrm{e}^2 c}. \tag{A.18}$$

The five parameters to be fitted are: the depth of the well D, the equilibrium bond length R_e, the fundamental vibration frequency ω_e, the first anharmonic constant $\omega_\mathrm{e}x_\mathrm{e}$ and the vibration-rotation interaction constant α_e. Other physical quantities appearing are Planck's constant h, the reduced mass of the molecule μ and the speed of light in vacuum c. This five-parameter function can be reduced to a four-parameter function by assuming that:

$$\alpha_\mathrm{e} = 6B_\mathrm{e}x_\mathrm{e}\left[\left(\frac{B_\mathrm{e}}{\omega_\mathrm{e}x_\mathrm{e}}\right)^{1/2} - \frac{B_\mathrm{e}}{\omega_\mathrm{e}x_\mathrm{e}}\right], \tag{A.19}$$

as Pekeris showed to good approximation by calculating the rotational energy using perturbation theory [Pek34]. A second free parameter can be excluded by assuming that all anharmonic constants except for the first one ($\omega_\mathrm{e}x_\mathrm{e}$) are equal to zero. In that case we have:

$$\omega_\mathrm{e}x_\mathrm{e} = \frac{\omega_\mathrm{e}^2}{4D}. \tag{A.20}$$

With these 2 assumptions, the general five-parameter potential energy function is reduced to the three-parameter Morse potential [Mor29]:

$$V(R) = D[(1 - e^{-x})^2]. \tag{A.21}$$

By fitting any of the 3 discussed potential energy functions (having respectively 3, 4 or 5 free parameters) to the computed data points, values can be calculated for D, ω_e, $\omega_\mathrm{e}x_\mathrm{e}$, B_e, and α_e. As a direct fit to the five-parameter function was found to be quite sensitive to the initial guesses for the parameters, it was decided to start by performing a fit to the three-parameter Morse potential. The resulting values for D, R_e, ω_e and $\omega_\mathrm{e}x_\mathrm{e}$ were consecutively used as initial guesses for the four-parameter function fit. This way, we obtained good initial guesses for the 5 parameters appearing in Eq. A.13 so that the five-parameter fit procedure resulted in correct and meaningful values for D, R_e, ω_e, $\omega_\mathrm{e}x_\mathrm{e}$ and α_e. These values can now be used to calculate the rotational constant B_e (Eq. refeq:Be), the centrifugal distortion constant D_e (Eq. refeq:De), the second anharmonic constants $\omega_e y_e$ (Eq. refeq:wy) and the zero-point energy E_ZPE (Eq. refeq:ZPE) as explained below.

Assuming a negligible coupling between the rotation of the molecule and the spins and motions of the electrons, Pekeris [Pek34] proved the centrifugal distortion constants $D_{\mathrm{e},i}$ are given by:

$$D_{\mathrm{e},i} = \frac{4B_{\mathrm{e},i}^3}{\omega_{\mathrm{e},i}^2}. \tag{A.22}$$

The second anharmonic constants $\omega_{\mathrm{e},i}y_{\mathrm{e},i}$ were determined by imposing that the maximal reachable vibrational energy for electronic state i ($\max E_{\nu,i}$) is equal to the depth of its energy well D_i:

$$D_i = \max\left(\omega_{\mathrm{e},i}(v+\frac{1}{2}) - \omega_{\mathrm{e},i}x_{\mathrm{e},i}(v+\frac{1}{2})^2 + \omega_{\mathrm{e},i}y_{\mathrm{e},i}(v+\frac{1}{2})^3\right) \tag{A.23}$$

This equation is then solved numerically for $\omega_{\mathrm{e},i}y_{\mathrm{e},i}$.

Finally, the zero-point energy E_{ZPE} is given by:

$$E_{\mathrm{ZPE}} = \frac{1}{2}\omega_{\mathrm{e},0} - \frac{1}{4}\omega_{\mathrm{e},0}x_{\mathrm{e},0} + \frac{1}{8}\omega_{\mathrm{e},0}y_{\mathrm{e},0}. \tag{A.24}$$

Applying this procedure to the electronic ground state as well as to the stable excited states, the energies of all rotational-vibrational levels for these electronic states with respect to the fundamental ground state can be calculated:

$$\begin{aligned} E_{i,v,J} = \Delta E_{\mathrm{e},i} &- E_{\mathrm{ZPE}} \\ &+ \omega_{\mathrm{e},i}(v+\frac{1}{2}) - \omega_{\mathrm{e},i}x_{\mathrm{e},i}(v+\frac{1}{2})^2 + \omega_{\mathrm{e},i}y_{\mathrm{e},i}(v+\frac{1}{2})^3 \\ &+ B_{\mathrm{e},i}J(J+1) - D_{\mathrm{e},i}J^2(J+1)^2 \\ &- \alpha_{\mathrm{e},i}(v+\frac{1}{2})J(J+1). \end{aligned} \tag{A.25}$$

Figures A.25 – A.30 show the resulting dissociation profiles for the molecules PoH, LiPo, PoO, PbPo, BiPo and Po_2. Every stable electronic molecular state is included. All associated molecular constants are given in Tables A.15 – A.20.

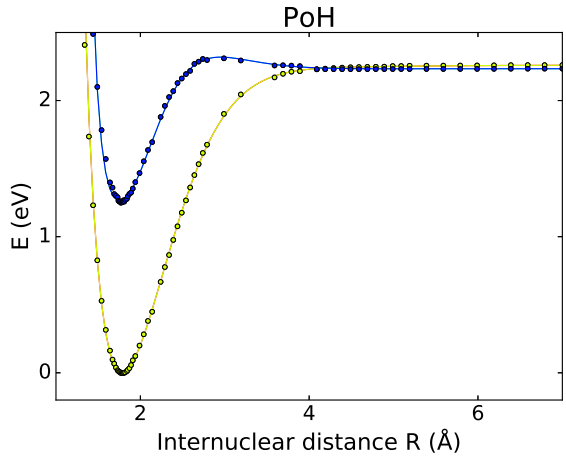

Figure A.25: Ab initio computed data points for the ground and first excited states of PoH. A five-parameter potential energy function (Eq. A.13) was fitted to each electronic state.

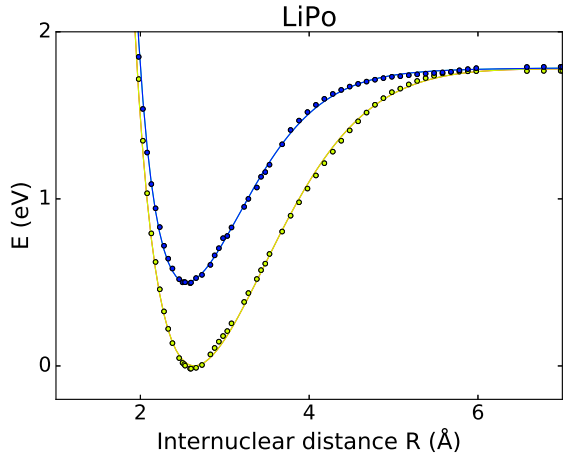

Figure A.26: Ab initio computed data points for the ground and first excited states of LiPo. A five-parameter potential energy function (Eq. A.13) was fitted to each electronic state.

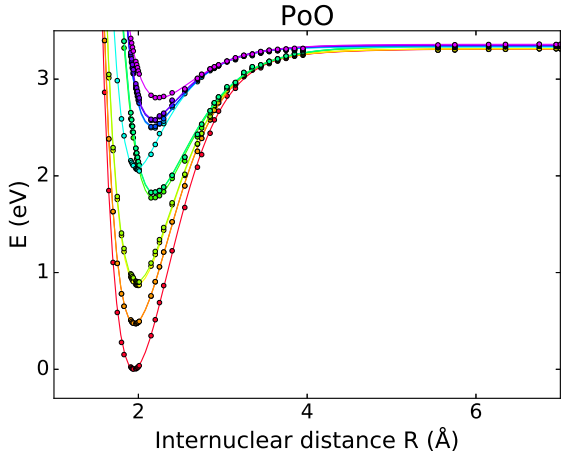

Figure A.27: Ab initio computed data points for the ground and first excited states of PoO. A five-parameter potential energy function (Eq. A.13) was fitted to each electronic state.

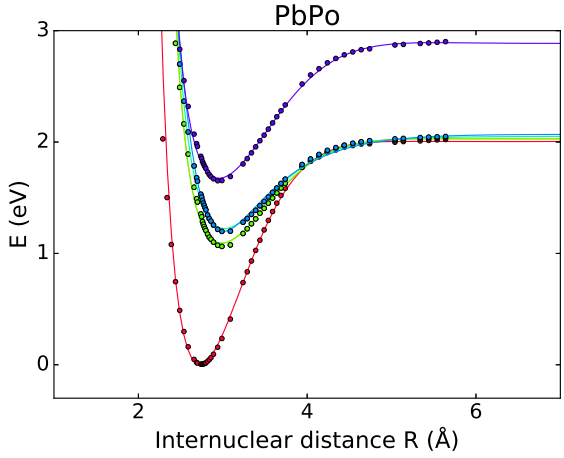

Figure A.28: Ab initio computed data points for the ground and first excited states of PbPo. A five-parameter potential energy function (Eq. A.13) was fitted to each electronic state.

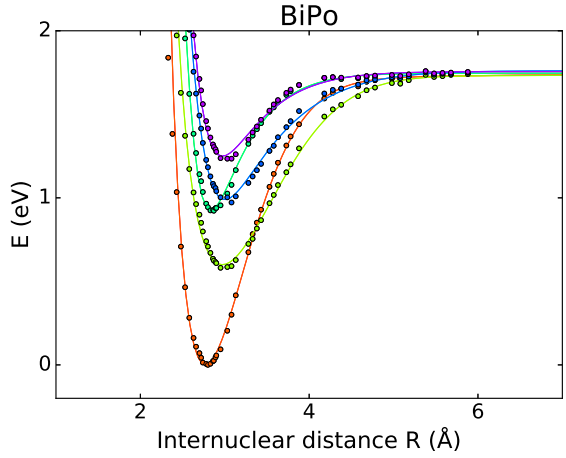

Figure A.29: Ab initio computed data points for the ground and first excited states of BiPo. A five-parameter potential energy function (Eq. A.13) was fitted to each electronic state.

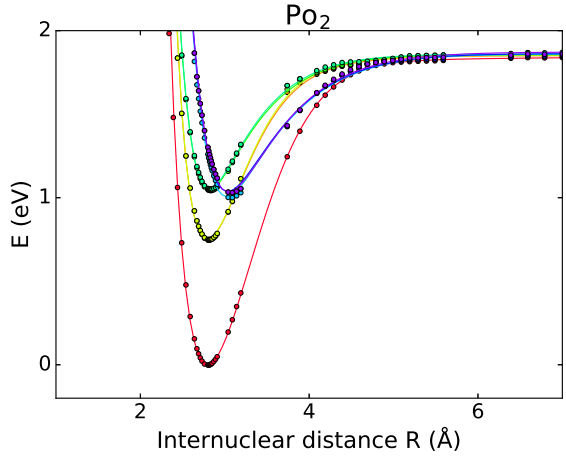

Figure A.30: Ab initio computed data points for the ground and first excited states of Po_2. A five-parameter potential energy function (Eq. A.13) was fitted to each electronic state.

Table A.15: Molecular constants for the ground and first excited states of **PoH** (obtained by fitting Eq. A.13 to the data points).

i	$\Delta E_{\mathrm{e},i}$ eV	D eV	R_e Å	ω_e cm^{-1}	$\omega_\mathrm{e}x_\mathrm{e}$ cm^{-1}	$\omega_\mathrm{e}y_\mathrm{e}$ $10^{-3}\mathrm{cm}^{-1}$	B_e $10^{-3}\mathrm{cm}^{-1}$	D_e $10^{-6}\mathrm{cm}^{-1}$	α_e $10^{-3}\mathrm{cm}^{-1}$
1	0.000	2.260	1.782	1773	34.71	-425.2	5333	193.0	150.2
2	0.000	2.260	1.782	1773	34.71	-425.2	5333	193.0	150.2
3	1.263	0.971	1.756	1656	43.20	-5121	5496	242.1	207.2
4	1.263	0.971	1.756	1656	43.20	-5121	5496	242.1	207.2

Table A.16: Molecular constants for the ground and first excited states of **LiPo** (obtained by fitting Eq. A.13 to the data points).

i	$\Delta E_{\mathrm{e},i}$ eV	D eV	R_e Å	ω_e cm^{-1}	$\omega_\mathrm{e}x_\mathrm{e}$ cm^{-1}	$\omega_\mathrm{e}y_\mathrm{e}$ $10^{-3}\mathrm{cm}^{-1}$	B_e $10^{-3}\mathrm{cm}^{-1}$	D_e $10^{-6}\mathrm{cm}^{-1}$	α_e $10^{-3}\mathrm{cm}^{-1}$
1	0.000	1.784	2.639	362.1	2.488	2.587	357.3	1.392	2.861
2	0.000	1.784	2.639	362.1	2.488	2.587	357.3	1.392	2.861
3	0.501	1.287	2.547	396.0	2.622	-23.52	383.6	1.440	4.025
4	0.501	1.287	2.547	396.0	2.622	-23.52	383.6	1.440	4.025

Table A.17: Molecular constants for the ground and first excited states of **PoO** (obtained by fitting Eq. A.13 to the data points).

i	$\Delta E_{\mathrm{e},i}$ eV	D eV	R_e Å	ω_e cm^{-1}	$\omega_\mathrm{e}x_\mathrm{e}$ cm^{-1}	$\omega_\mathrm{e}y_\mathrm{e}$ $10^{-3}\mathrm{cm}^{-1}$	B_e $10^{-3}\mathrm{cm}^{-1}$	D_e $10^{-6}\mathrm{cm}^{-1}$	α_e $10^{-3}\mathrm{cm}^{-1}$
1	0.000	3.313	1.944	648.8	2.657	-16.66	299.9	0.2564	1.872
2	0.472	2.842	1.953	623.3	3.919	- 4.399	297.4	0.2709	2.185
3	0.473	2.842	1.953	619.9	3.746	- 6.160	297.3	0.2735	2.157
4	0.875	2.441	1.988	579.8	3.573	-10.61	287.0	0.2814	2.226
5	0.909	2.428	1.988	580.2	3.726	- 8.733	286.9	0.2806	2.271
6	1.764	1.578	2.187	494.3	1.433	-74.43	237.1	0.2181	2.046
7	1.818	1.526	2.187	490.2	2.239	-58.41	237.0	0.2216	2.179
8	1.820	1.524	2.193	482.7	1.351	-75.87	235.8	0.2250	2.052
9	2.071	1.261	1.979	596.6	8.708	- 1.156	289.4	0.2724	3.877
10	2.512	0.826	2.161	452.2	5.896	-63.47	242.8	0.2801	3.495
11	2.522	0.822	2.164	448.0	5.686	-66.94	242.2	0.2833	3.466
12	2.586	0.763	2.168	421.2	7.128	- 2.673	241.4	0.3170	3.740
13	2.595	0.756	2.172	418.7	6.384	-28.57	240.3	0.3167	3.656
14	2.806	0.554	2.252	302.6	4.453	-23.14	223.5	0.4880	3.626

Table A.18: Molecular constants for the ground and first excited states of **PbPo** (obtained by fitting Eq. A.13 to the data points).

i	$\Delta E_{\mathrm{e},i}$ eV	D eV	R_e Å	ω_e cm^{-1}	$\omega_\mathrm{e}x_\mathrm{e}$ cm^{-1}	$\omega_\mathrm{e}y_\mathrm{e}$ $10^{-3}\mathrm{cm}^{-1}$	B_e $10^{-3}\mathrm{cm}^{-1}$	D_e $10^{-6}\mathrm{cm}^{-1}$	α_e $10^{-3}\mathrm{cm}^{-1}$
1	0.000	2.008	2.730	166.9	0.3159	-0.6233	21.65	0.001457	0.04862
2	1.091	0.938	2.985	106.5	0.2400	-1.022	18.11	0.002093	0.05346
3	1.091	0.939	2.984	106.7	0.2436	-1.001	18.11	0.002089	0.05364
4	1.222	0.831	3.019	103.7	0.2027	-1.689	17.71	0.002065	0.05727
5	1.196	0.874	3.002	123.1	0.3970	-1.297	17.90	0.001513	0.06772
6	1.674	1.213	2.955	111.6	0.2290	-0.5426	18.47	0.002022	0.04704

Table A.19: Molecular constants for the ground and first excited states of **BiPo** (obtained by fitting Eq. A.13 to the data points).

i	$\Delta E_{\mathrm{e},i}$ eV	D eV	R_e Å	ω_e cm^{-1}	$\omega_\mathrm{e}x_\mathrm{e}$ cm^{-1}	$\omega_\mathrm{e}y_\mathrm{e}$ $10^{-3}\mathrm{cm}^{-1}$	B_e $10^{-3}\mathrm{cm}^{-1}$	D_e $10^{-6}\mathrm{cm}^{-1}$	α_e $10^{-3}\mathrm{cm}^{-1}$
1	0.000	1.738	2.770	164.1	0.3363	-0.9008	20.97	0.001369	0.05240
2	0.000	1.738	2.770	164.1	0.3363	-0.9008	20.97	0.001369	0.05240
3	0.600	1.136	2.971	104.5	0.2135	-0.5095	18.23	0.002220	0.04887
4	0.600	1.136	2.971	104.5	0.2135	-0.5095	18.23	0.002220	0.04887
5	0.926	0.820	2.834	178.0	0.8742	-4.624	20.04	0.001016	0.08861
6	0.926	0.820	2.834	178.0	0.8742	-4.624	20.04	0.001016	0.08861
7	0.989	0.772	3.001	122.7	0.6328	0.2732	17.87	0.001514	0.07768
8	0.989	0.772	3.001	122.7	0.6328	0.2732	17.87	0.001514	0.07768
9	1.249	0.507	2.973	122.0	0.8986	-0.1755	18.21	0.001624	0.1005
10	1.249	0.507	2.973	122.0	0.8986	-0.1755	18.21	0.001624	0.1005

Table A.20: Molecular constants for the ground and first excited states of **Po_2** (obtained by fitting Eq. A.13 to the data points).

i	$\Delta E_{\mathrm{e},i}$ eV	D eV	R_e Å	ω_e cm^{-1}	$\omega_\mathrm{e}x_\mathrm{e}$ cm^{-1}	$\omega_\mathrm{e}y_\mathrm{e}$ $10^{-3}\mathrm{cm}^{-1}$	B_e $10^{-3}\mathrm{cm}^{-1}$	D_e $10^{-6}\mathrm{cm}^{-1}$	α_e $10^{-3}\mathrm{cm}^{-1}$
1	0.000	1.841	2.797	151.8	0.3124	-0.4047	20.53	0.001501	0.04894
2	0.749	1.102	2.791	150.4	0.5623	-0.6400	20.60	0.001548	0.07262
3	0.750	1.102	2.791	150.8	0.5764	-0.5493	20.62	0.001541	0.07242
4	1.045	0.811	2.814	144.9	0.7943	-0.08843	20.27	0.001586	0.09243
5	1.053	0.806	2.815	144.9	0.7158	-1.041	20.26	0.001585	0.09065
6	1.008	0.852	3.023	124.9	0.5817	0.1315	17.57	0.001392	0.07173
7	1.037	0.826	3.035	121.0	0.5474	-0.01711	17.43	0.001448	0.07110
8	1.036	0.836	3.045	118.5	0.4077	-1.037	17.32	0.001480	0.06632

Temperature-dependent stability of the molecules

Assuming a constant pressure, the temperature-dependent stability of the molecules is described by the difference in Gibbs free energy of the molecular state w.r.t. the unbound state:

$$\begin{aligned}\Delta G(T) = -D &- (E_{\mathrm{tr}}^{\mathrm{A1}} + E_{\mathrm{el}}^{\mathrm{A1}} + E_{\mathrm{tr}}^{\mathrm{A2}} + E_{\mathrm{el}}^{\mathrm{A2}}) \\ &+ (E_{\mathrm{tr}}^{\mathrm{M}} + E_{\mathrm{ZPE}}^{\mathrm{M}} + E_{\mathrm{rovibel}}^{\mathrm{M}}) \\ &+ T(S_{\mathrm{tr}}^{\mathrm{A1}} + S_{\mathrm{el}}^{\mathrm{A1}} + S_{\mathrm{tr}}^{\mathrm{A2}} + S_{\mathrm{el}}^{\mathrm{A2}}) \\ &- T(S_{\mathrm{tr}}^{\mathrm{M}} + S_{\mathrm{rovibel}}^{\mathrm{M}}) - k_{\mathrm{B}}T,\end{aligned} \tag{A.26}$$

where D is the depth of the dissociation profile, E are thermal energy corrections and S are entropic contributions. The superscripts M and A denote molecular and atomic quantities respectively, while the subscripts tr, el and rovibel designate translational, electronic and rotational-vibrational-electronic contributions.

The thermal energy correction due to translation is given by (X= A,M):

$$E_{\mathrm{tr}}^{\mathrm{X}} = \frac{3}{2}RT, \tag{A.27}$$

while the translational contribution to the entropy is:

$$S_{\mathrm{tr}}^{\mathrm{X}} = R\ln\left(\frac{(2\pi m_{\mathrm{X}}k_{\mathrm{B}}T)^{3/2}}{h^3}k_{\mathrm{B}}\frac{T}{P}\right) + \frac{5}{2}R, \tag{A.28}$$

assuming that the particles behave as an ideal gas. Other thermal corrections to the energy are calculated using:

$$E_{(\mathrm{rovib})\mathrm{el}}^{\mathrm{X}} = \frac{\sum\limits_j g_j E_j \exp\left(\frac{-E_j}{k_{\mathrm{B}}T}\right)}{\sum\limits_j g_j \exp\left(\frac{-E_j}{k_{\mathrm{B}}T}\right)} = \frac{\sum\limits_j g_j E_j \exp\left(\frac{-E_j}{k_{\mathrm{B}}T}\right)}{Q(T)}, \tag{A.29}$$

where E_j is the energy of state j with degeneracy g_j and $Q(T)$ being the partition function. For the electronic contributions of the atoms $E_{\mathrm{el}}^{\mathrm{A}}$, the energies E_j are the excitation energies that can be found in the NIST database [Kra18]. For the coupled rotational-vibrational-electronic contributions of the molecules $E_{\mathrm{rovibel}}^{\mathrm{M}}$, they are calculated using Eq. A.25. The thermal contributions to the entropy are similarly calculated:

$$S_{(\mathrm{rovib})\mathrm{el}}^{\mathrm{X}} = RT\left(\mathrm{d}\ln Q/\mathrm{d}T\right) + R\ln Q. \tag{A.30}$$

The methodology described above results in the central result of this work: the T-dependent stability of the 6 diatomic molecules of interest, which is shown in Figure A.31. Some numerical values for the Gibbs free energy difference at different temperatures are given in Table A.21. Finally, a fourth order polynomial was fitted to all calculated data points (73 temperatures ranging between 1 K and 1441 K, in 20 K intervals):

$$\Delta G(T) = \mathrm{A}T^4 + \mathrm{B}T^3 + \mathrm{C}T^2 + \mathrm{D}T + \mathrm{E}. \tag{A.31}$$

The obtained coefficients are presented in Table A.22 and allow to recalculate the Gibbs free energies differences with a relative error below 0.3 % between 0 K and 1441 K.

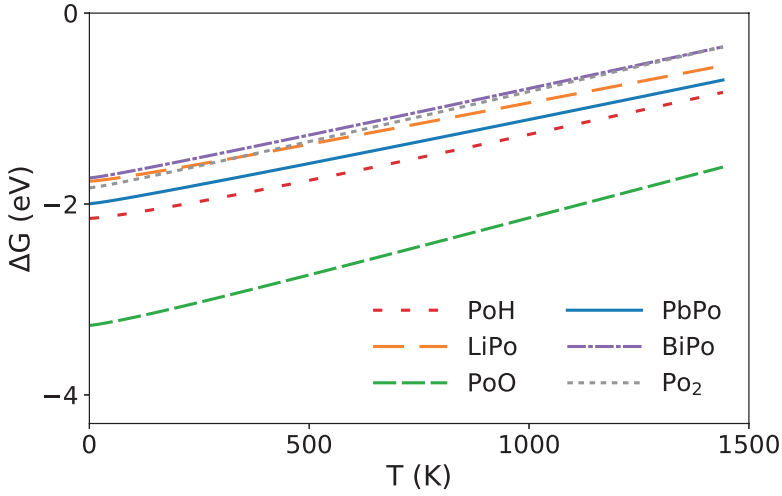

Figure A.31: The difference in Gibbs free energy ΔG of the Po-containing molecules compared to the atomic fragments.

Table A.21: Gibbs free energy difference (in eV) of the molecular state w.r.t. the unbound state.

T (K)	PoH	LiPo	PoO	PbPo	BiPo	Po2
1	-2.152	-1.762	-3.273	-1.997	-1.727	-1.831
101	-2.092	-1.701	-3.188	-1.925	-1.650	-1.746
201	-2.014	-1.623	-3.084	-1.841	-1.560	-1.649
301	-1.931	-1.542	-2.973	-1.753	-1.467	-1.549
401	-1.842	-1.458	-2.858	-1.664	-1.372	-1.447
501	-1.751	-1.373	-2.742	-1.574	-1.277	-1.344
601	-1.658	-1.287	-2.624	-1.484	-1.180	-1.241
701	-1.563	-1.201	-2.505	-1.392	-1.083	-1.137
801	-1.466	-1.114	-2.385	-1.300	-0.985	-1.032
901	-1.368	-1.026	-2.265	-1.207	-0.887	-0.927
1001	-1.270	-0.939	-2.145	-1.114	-0.789	-0.821
1101	-1.171	-0.850	-2.024	-1.021	-0.690	-0.716
1201	-1.071	-0.762	-1.903	-0.927	-0.591	-0.609
1301	-0.971	-0.674	-1.782	-0.833	-0.492	-0.503

Table A.22: The coefficients obtained by fitting the computed Gibbs free energy differences to Eq. A.31.

	$A \cdot 10^{-14}$	$B \cdot 10^{-10}$	$C \cdot 10^{-7}$	$D \cdot 10^{-4}$	E
PoH	8.827	-3.392	5.090	6.294	-2.158
LiPo	7.059	-2.550	3.417	6.730	-1.769
PoO	10.32	-3.797	5.132	8.989	-3.281
PbPo	4.914	-1.768	2.461	7.701	-2.004
BiPo	4.646	-1.716	2.420	8.272	-1.734
Po2	4.555	-1.667	2.352	9.013	-1.838

Rotational-vibrational-electronic thermal energy correction

As can be seen in Eq.A.29, a summation over the rotational-vibrational-electronic states is performed to calculate $E^{\mathrm{M}}_{\mathrm{rovibel}}$. All states contributing more than 0.000001 to the partition function and having an energy lower than the dissociation energy D_0 were included in the sum. The criteria to be included in the sum was thus:

$$(2J+1)\exp\left(\frac{E_{i,v,J}}{k_{\mathrm{B}}T}\right) > 0.000001 \qquad \text{and} \qquad E_{i,v,J} < D_0 \tag{A.32}$$

The summation is performed as follows: first the electronic and vibrational ground state is considered and the rotational quantum number J is incremented until the state does not satisfy the criteria above. Then the vibrational quantum number ν is incremented by 1 and J is scanned again. Finally, when ν becomes high enough so that state ($i = 0, \nu, J = 0$) does not longer satisfy the criteria, the next electronic state is considered. This procedure is continued until the final contributing electronic state is reached. The process of this summation is visualized in Figure A.32 (full summation) and Figure A.33 (zoom on the first vibrational states) for the Po_2 molecule at 1000 K. The upper three plots in these figure represent the electronic, vibrational and rotational quantum number of the state being considered. The fourth plot represents the corresponding energy $E_{i,\nu,J}$ of that state. The other plots show the contribution to the rotational-vibrational-electronic partition function ($Q^{\mathrm{cont}}_{\mathrm{rovibel}}$), the sum of these contributions up to the considered state ($Q^{\mathrm{sum}}_{\mathrm{rovibel}}$), the contribution to the thermal energy correction ($E^{\mathrm{cont}}_{\mathrm{rovibel}}$) and the sum of the latter quantity up to the considered state ($E^{\mathrm{sum}}_{\mathrm{rovibel}}$). A total of 117646 states were included in the sum. The used criteria were found to results in a converged value for $E^{\mathrm{cont}}_{\mathrm{rovibel}}$ deviating from the exact value by no more than 0.01%. We can thus conclude that the sums are well-converged. The total number of states included in the sum for the different molecules at the most extreme temperatures considered (1 K and 1521 K) is listed in Table A.23.

Table A.23: The number of states included in the explicit sum used to calculate the rotational-vibrational-electronic thermal energy correction for the different Po-containing molecules at 1 and 1521 K.

T (K)	PoH	LiPo	PoO	PbPo	BiPo	Po_2
1	2	12	6	24	48	25
1521	1376	29365	20676	201177	431425	313657

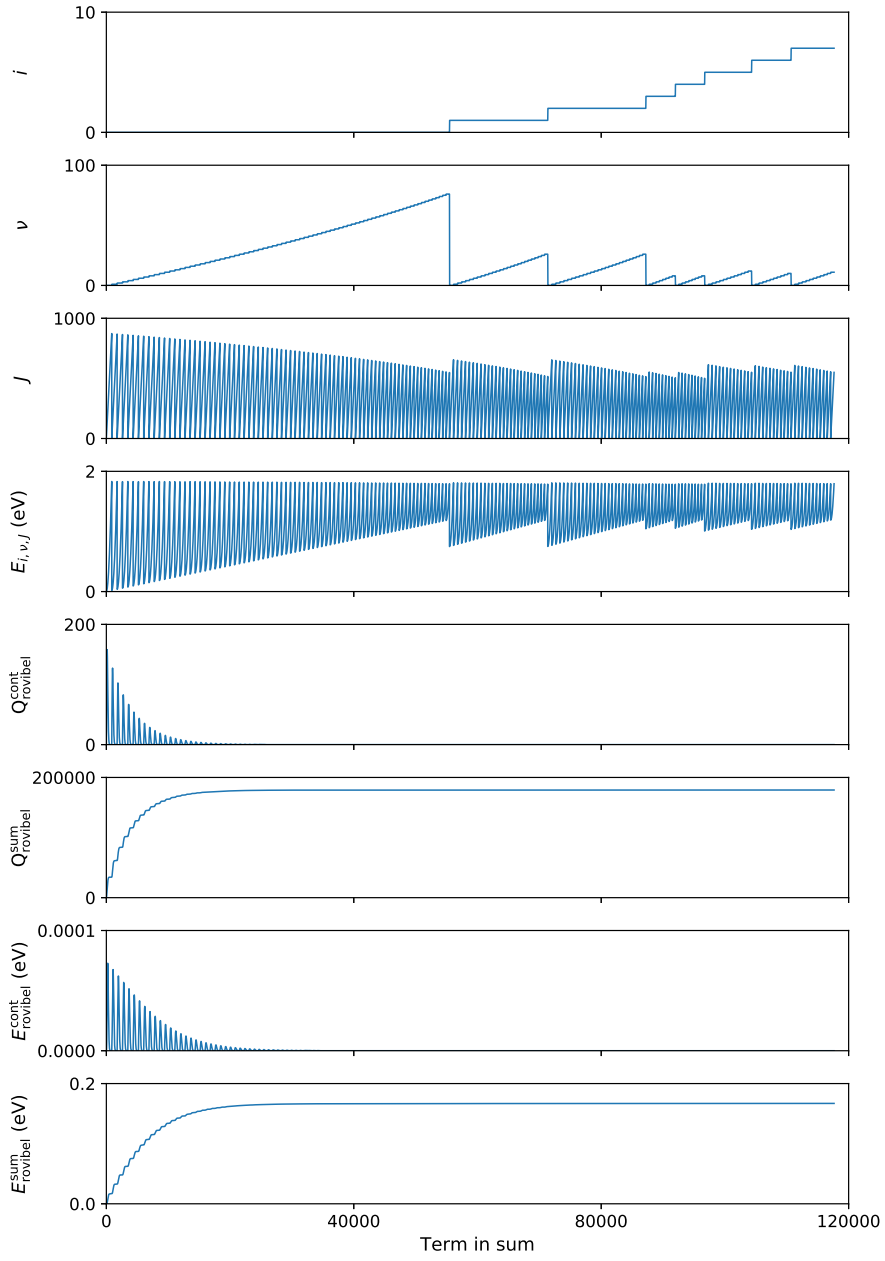

Figure A.32: The full summation progress over the rotational-vibrational-electronic states of the Po_2 molecule to calculate the corresponding partition function Q_{rovibel} and the thermal energy correction E_{rovibel}. The electronic, vibrational and rotational quantum numbers are denoted by i, ν and J respectively with $E_{i,\nu,J}$ the energy of the corresponding state.

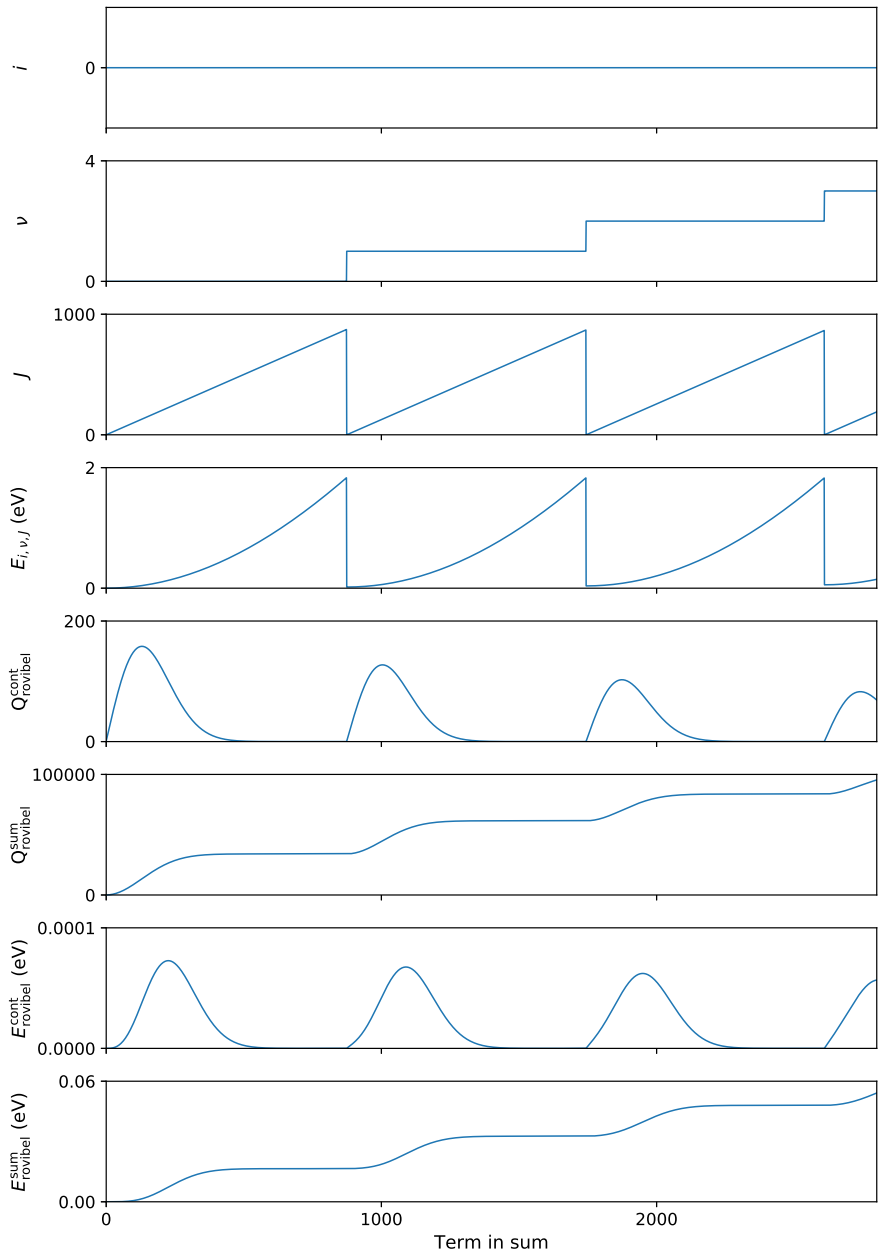

Figure A.33: A zoom on the first part of the summation progress over the rotational-vibrational-electronic states of the Po_2 molecule to calculate the corresponding partition function Q_{rovibel} and the thermal energy correction E_{rovibel}. The electronic, vibrational and rotational quantum numbers are denoted by i, ν and J respectively with $E_{i,\nu,J}$ the energy of the corresponding state.

The molar heat capacity

In addition to the temperature dependent Gibbs free energy difference between the molecular and dissociated state (see article), the molar heat capacity c_V of the molecular gases was calculated as this quantity is determined more easily in experiments. Also, it was found that it is much more sensitive to the determined molecular constants. It is given by:

$$c_V = \frac{\mathrm{d}(E_{\mathrm{tr}} + E_{\mathrm{rovibel}})}{\mathrm{dT}}. \tag{A.33}$$

The result is shown in Figure A.34. At low temperatures, the translational as well as the rotational degrees of freedom are already activated ($c_{\mathrm{V}} \approx \frac{5}{2}R$). Next, the vibrational degree of freedom is activated ($c_{\mathrm{V}} \rightarrow \frac{7}{2}R$). This happens first for the heavier molecules as these have the lowest fundamental frequency ω_0 (see Tables A.15 – A.20). Finally, the temperature is high enough to also allow electronic excitations to take place, which further increases the heat capacity. This effect is strongest for the PoO molecule as it has the lowest lying excited states of the considered molecules (see Table A.17).The figure fully covers the temperature windows that are relevant for the discussed types of reactors: the operational temperature of the Pb-Bi coolant of the fast fission reactor MYRRHA [AA12, Eng15] is foreseen to range between 540 K and 680 K, while the coolant in other Pb(-Bi) cooled reactor concepts should also not exceed 840 K [Ale14]. On the other hand, in the traditional breeding blanket concepts for fusion reactors, the temperature of the liquid Pb-Li is estimated to range between 550 K and 975 K [Smo15], although a new concept aims at an upper limit of 1275 K [Che08].

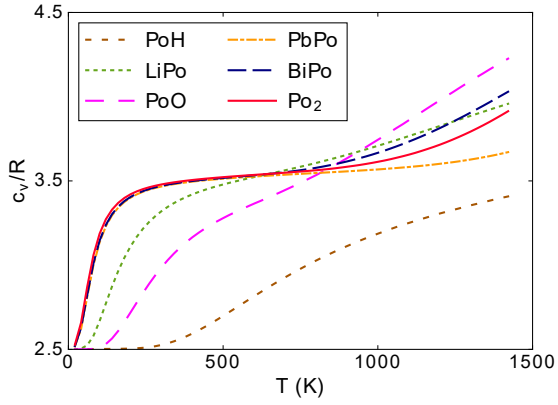

Figure A.34: The molar heat capacity c_{V} of the Po-containing diatomic molecules versus the temperature T.

Initial atomic concentrations

To calculate the molecular occurrence of the different Po-containing molecules in the gas above the liquid Pb-Li breeder in the DEMO fusion reactor or above the lead-bismuth eutectic (LBE) coolant in the MYRRHA fast fission reactor, one needs to know to initial concentration of the different elements in the gas mixture.

First, the Ar gas atmosphere above the LBE coolant in the MYRRHA reactor is considered, which is assumed to be kept at 1 standard atmosphere (P_{Ar}=101300 Pa). The total LBE vapor pressure recommended by Sobolev [Sob11] was used. The fractions of Pb and Bi in the LBE vapor were determined using the paper by Ohno et al. [Ohn05] Below, P' denotes a partial vapor pressure and P a total vapor pressure. The superscripts indicate the references the values were taken from. The obtained concentrations for Pb and Bi are:

$$\begin{aligned} c_{\mathrm{Pb}} &= \frac{P'_{\mathrm{Pb,LBE}}}{P_{\mathrm{tot}}} \\ &\approx \frac{1}{P_{\mathrm{Ar}}} P^{[41]}_{\mathrm{LBE}} \frac{P'^{[42]}_{\mathrm{Pb,LBE}}}{P^{[42]}_{\mathrm{LBE}}} \\ &= \frac{1}{P_{\mathrm{Ar}}} 1.22 \cdot 10^{10} \exp\left(-\frac{22552}{T}\right) \frac{10^{9.37-\frac{9800}{T}}}{10^{10.2-\frac{10100}{T}}} \\ &= \frac{10^{9.256-\frac{9494}{T}}}{101300\ \mathrm{Pa}} \end{aligned} \tag{A.34}$$

$$\begin{aligned} c_{\mathrm{Bi}} &= \frac{P'_{\mathrm{Bi,LBE}} + 2P'_{\mathrm{Bi_2,LBE}}}{P_{\mathrm{tot}}} \\ &\approx \frac{1}{P_{\mathrm{Ar}}} P^{[41]}_{\mathrm{LBE}} \left(\frac{2P'^{[42]}_{\mathrm{Bi_2,LBE}}}{P^{[42]}_{\mathrm{LBE}}} + \frac{P'^{[42]}_{\mathrm{Bi,LBE}}}{P^{[42]}_{\mathrm{LBE}}} \right) \\ &= \frac{1}{P_{\mathrm{Ar}}} \frac{P^{[41]}_{\mathrm{LBE}}}{P^{[42]}_{\mathrm{LBE}}} \left(\frac{2}{1+\alpha^{[42]}} P'^{[42]}_{\mathrm{Bi+Bi_2,LBE}} \right) \\ &= \frac{1}{P_{\mathrm{Ar}}} \frac{P^{[41]}_{\mathrm{LBE}}}{P^{[42]}_{\mathrm{LBE}}} \frac{2}{1+\alpha^{[42]}} P^{[41]}_{\mathrm{LBE}} \left(1 - \frac{P'^{[42]}_{\mathrm{Pb,LBE}}}{P^{[42]}_{\mathrm{LBE}}} \right) \\ &= \frac{10^{9.973-9488.4/T}}{101300\ \mathrm{Pa}} \frac{2}{1+\alpha^{[42]}} \left(1 - 10^{-0.83+\frac{300}{T}} \right) \end{aligned} \tag{A.35}$$

with the Bi_2–Bi dissociated fraction α:

$$\begin{aligned}
\alpha^{[42]} &= \left(\frac{K_P^{[43]}}{\frac{4P'^{[42]}_{\mathrm{Bi+Bi_2,LBE}}}{101300\ \mathrm{Pa}} + K_P^{[43]}} \right)^{1/2} \\
&= \left(\frac{K_P^{[43]}}{\frac{4P^{[41]}_{\mathrm{LBE}} \left(1 - \frac{P'^{[42]}_{\mathrm{Pb,LBE}}}{P^{[42]}_{\mathrm{LBE}}}\right)}{101300\ \mathrm{Pa}} + K_P^{[43]}} \right)^{1/2} \\
&= \left(\frac{K_P^{[43]}}{\frac{4.88 \cdot 10^{10} \exp\left(-\frac{22552}{T}\right)\left(1 - 10^{-0.83 + \frac{300}{T}}\right)}{101300\ \mathrm{Pa}} + K_P^{[43]}} \right)^{1/2} \\
&= \left(\frac{K_P^{[43]}}{\frac{10^{10.688 - \frac{9794.2}{T}} - 10^{9.858 - \frac{9494.2}{T}}}{101300\ \mathrm{Pa}} + K_P^{[43]}} \right)^{1/2}.
\end{aligned} \tag{A.36}$$

The Bi_2–Bi equilibrium constant K_P which was obtained from the Gibbs free energy difference between Bi_2 and atomic Bi available in the FactSage database [al.16a]. The following T-dependence was fitted:

$$\begin{aligned}
K_P^{[43]} &= \exp\left(-\frac{\Delta G^{[43]}_{\mathrm{Bi} \leftrightarrow \mathrm{Bi_2}}(T)}{RT} \right) \\
&= \exp\left(-\frac{24442.5}{T} + 12.5839 \right)
\end{aligned} \tag{A.37}$$

After the first irradiation campaign, 350 grams of ^{210}Po is expected to be present in the 7600 ton of LBE [Fio18], resulting in an atomic fraction of x_{Po}=4.6 × 10^{-8} of Po in the LBE. The Henry constant of Po in LBE by Prieto et al. [GP14] was used to determine the initial concentration of atomic Po in the gas mixture:

$$\begin{aligned}
c_{\mathrm{Po}} &= \frac{P'^{[45]}_{\mathrm{Po,LBE}}}{P_{\mathrm{tot}}} \approx \frac{x^{[44]}_{\mathrm{Po}} K^{[45]}_{\mathrm{Po,LBE}}}{P_{\mathrm{Ar}}} \\
&= \frac{4.6 \times 10^{-8} \cdot 10^{10.8 \pm 0.7 - (8606 \pm 726)/T}}{101300\ \mathrm{Pa}}.
\end{aligned} \tag{A.38}$$

Using the equations above, the initial concentrations of Pb, Bi and Po in the argon gas can be determined at any given temperature.

Next, the inert gas covering the Pb-Li breeder in the DEMO fusion reactor is considered, which is assumed to be at one standard atmosphere (P_{inertgas}=101300 Pa). The initial concentrations of Pb and Li in this gas were obtained using the vapor pressures reported by Kondo et al. [Kon13]:

$$c_{\mathrm{Pb}} = \frac{P'^{[46]}_{\mathrm{Pb,Pb\text{-}Li}}}{P_{\mathrm{tot}}} \approx \frac{\alpha'^{[46]}_{\mathrm{Pb}} P'^{[46]}_{\mathrm{Pb}}}{P_{\text{inert gas}}} = \frac{5.450 \times 10^{9} \exp\left(-22246/T\right)}{101300\ \mathrm{Pa}} \tag{A.39}$$

$$c_{\mathrm{Li}} = \frac{P'^{[46]}_{\mathrm{Li,Pb\text{-}Li}}}{P_{\mathrm{tot}}} \approx \frac{\alpha'^{[46]}_{\mathrm{Li}} P'^{[46]}_{\mathrm{Li}}}{P_{\text{inert gas}}} = \frac{8.058 \times 10^{9} \exp\left(-25229/T\right)}{101300\ \mathrm{Pa}}. \tag{A.40}$$

with α_{Pb} and α_{Li} being the chemical activity of Pb and Li in Pb-Li. After the first irradiation campaign, about 0.5 grams of ^{210}Po is expected to be present in 8000 tons of Pb-Li (x_{Po}=5 × 10^{-11}). The recommended Henry constant of Po in Pb-Li [Feu92, Faz15] was used to determine the initial concentration of Po in the gas mixture:

$$\begin{aligned} c_{\mathrm{Po}} &= \frac{P'^{[47,48]}_{\mathrm{Po,Pb-Li}}}{P_{\mathrm{tot}}} \approx \frac{x_{\mathrm{Po}} K'^{[47,48]}_{\mathrm{Po,Pb-Li}}}{P_{\text{inert gas}}} \\ &= \frac{5 \times 10^{-11} \cdot 10^{7.39-6017/T}}{101300\ \mathrm{Pa}}. \end{aligned} \tag{A.41}$$

The equations above allow to determine the initial concentration of Pb, Li and Po in the inert gas at any given temperature.

B

List of contributions

Publications in international peer–reviewed journals

Model and simulation of a vacuum sieve tray for T extraction from liquid PbLi breeding blankets
M. A. J. Mertens, D. Demange, and L. Frances,
Fusion Engineering and Design, **112**, 541–547, Nov. 2016
doi: 10.1016/j.fusengdes.2016.05.038

Po-containing molecules in fusion and fission reactors
Merlijn A. J. Mertens, Alexander Aerts, Ivan Infante, Jörg Neuhausen, and Stefaan Cottenier,
Journal of Physical Chemistry Letters, **10** (11), 2879–2884, June 2019
doi: 10.1021/acs.jpclett.9b00824
Reprinted with permission of ACS Publications on pages 163–215.

^{210}Po production in the European DEMO fusion reactor
Merlijn A. J. Mertens, Ulrich Fischer, Pavel Pereslavtsev,
Robert Stieglitz, Jean-Marie Noterdaeme, and Stefaan Cottenier,
Nuclear Fusion, **59** (10), 106029, Aug. 2019
doi: 10.1088/1741-4326/ab36aa
Reprinted with permission of IAEA on pages 143–159.

Conference contributions

Oral presentations

Po-containing molecules for fusion and fission

Merlijn A. J. Mertens

Workshop "Spin-orbit effects in molecules and solids: diversity of properties and computational precision" and Tutorial "hands-on-FPLO",

Dresden, Germany, November 13–17, 2017

Poster presentations

The production rate and molecular occurrence of ^{210}Po in Pb-Li breeding blankets

Merlijn A. J. Mertens, Ulrich Fischer, Alexander Aerts, Pavel Pereslavtsev, and Stefaan Cottenier

30th Symposium on Fusion Technology

Giardini Naxos, Sicily - Italy, September 16–21, 2018

The production rate and molecular occurrence of ^{210}Po in Pb-Li breeding blankets

Merlijn A. J. Mertens, Ulrich Fischer, Alexander Aerts, Pavel Pereslavtsev, and Stefaan Cottenier

28th Symposium on Fusion Engineering,

Ponte Vedra Beach, Florida, United States of America, June 2–6, 2019

Ph.D. events contributions

Oral presentations

The production of radiotoxic Po-210 in liquid Pb-Li breeding blankets

Merlijn A. J. Mertens

8th KIT Fusion Ph.D. Seminar

St. Martin, Germany, June 6–7, 2018

Poster presentations

The production rate and molecular occurrence of ^{210}Po in Pb-Li breeding blankets

Merlijn A. J. Mertens, Ulrich Fischer, Alexander Aerts, Pavel Pereslavtsev, and Stefaan Cottenier

6th Fusenet Ph.D. Event hosted by the ITER Organisation,

Cadarache, France, November 6–9, 2018

Master's thesis

Engineering Design of the Test Section for Tritium Extraction from PbLi using a Vacuum Sieve Tray

Merlijn A. J. Mertens

Master's thesis performed in 2015 at the Tritium Laboratory Karlsruhe (TLK), Karlsruhe Institute of Technology within the framework of Erasmus Mundus European Master of Science in Nuclear Fusion and Engineering Physics.

Thesis Promotor: Prof. Dr. ir. Jean-Marie Noterdaeme (Ghent University)
Supervisor: Dr. David Demange (Karlsruhe Institute of Technology)

Bibliography

[AA12] Aït Abderrahim H., Baeten P., De Bruyn D., and Fernandez R. MYRRHA – A multi-purpose fast spectrum research reactor. *Energy Conversion and Management*, **63**, 4–10, November 2012. ISSN 0196-8904. doi:10.1016/j.enconman.2012.02.025.

[Abd14] Abderrahim H.A. MYRRHA Spallation Target Design and Qualification R&D Programme. http://www.hep.princeton.edu/mumu/target/Abderrahim/abderrahim_140722.pdf, 2014. Transformative Hadron Beamlines Workshop, BNL, Brookhaven (NY), USA.

[Abe08] Abe M., Gopakmar G., Nakajima T., and Hirao K. Relativistic Multireference Perturbation Theory: Complete Active-Space Second-Order Perturbation Theory (CASPT2) With The Four-Component Dirac Hamiltonian. In M.K. Shukla and J. Leszczynski (editors), *Radiation Induced Molecular Phenomena in Nucleic Acids: A Comprehensive Theoretical and Experimental Analysis*, pp. 157–177. Challenges and Advances In Computational Chemistry and Physics, Springer, Dordrecht, The Netherlands, 2008. ISBN 978-1-4020-8184-2. doi:10.1007/978-1-4020-8184-2_6.

[age19] Uranium 2018: Resources, Production and Demand. *Technical Report NEA No. 7413*, Nuclear Energy Agency and International Atomic Energy Agency, OECD Publishing, Paris, France, 2019. doi:10.1787/uranium-2018-en.

[AH86] A. Hess B. Relativistic Electronic-Structure Calculations Employing a 2-Component No-Pair Formalism With External-Field Projection Operators. *Physical review. A*, **33**, 3742–3748, July 1986. doi:10.1103/PhysRevA.33.3742.

[Aie15] Aiello G. HCLL Blanket 2014 Design Description Document. *Technical Report EFDA_D_2MAW5H*, EUROfusion, January 2015.

[al.16a] Bale et al. C. FactSage thermochemical software and databases, 2010–2016. *Calphad*, **54**, 35–53, September 2016. ISSN 03645916. doi:10.1016/j.calphad.2016.05.002.

[al.16b] Aquilante et al. F. Molcas 8: New capabilities for multiconfigurational quantum chemical calculations across the periodic table. *Journal of Computational Chemistry*, **37** (5), 506–541, February 2016. ISSN 1096-987X. doi:10.1002/jcc.24221.

[Ale14] Alemberti A., Smirnov V., Smith C.F., and Takahashi M. Overview of lead-cooled fast reactor activities. *Prog. Nucl. Energy*, **77**, 300–307, November 2014. ISSN 0149-1970. doi:10.1016/j.pnucene.2013.11.011.

[And92] Andersson K., Malmqvist P.Å., and Roos B.O. Second-order perturbation theory with a complete active space self-consistent field reference function. *Journal of Chemical Physics*, **96** (2), 1218–1226, January 1992. ISSN 0021-9606. doi:10.1063/1.462209.

[Ans12] Ansoborlo E., Berard P., Den Auwer C., Leggett R., Menetrier F., Younes A., Montavon G., and Moisy P. Review of Chemical and Radiotoxicological Properties of Polonium for Internal Contamination Purposes. *Chem. Res. Toxicol.*, **25** (8), 1551–1564, August 2012. ISSN 0893-228X. doi:10.1021/tx300072w.

[Arb18] Arbeiter F., Diegele E., Fischer U., Garcia A., Ibarra A., Molla J., Mota F., Möslang A., Qiu Y., Serrano M., and Schwab F. Planned material irradiation capabilities of IFMIF-DONES. *Nuclear Materials and Energy*, **16**, 245–248, August 2018. ISSN 2352-1791. doi:10.1016/j.nme.2018.05.026.

[Aub16] Aubert J., Aiello G., Jaboulay J.C., Kiss B., and Morin A. Status on DEMO Helium Cooled Lithium Lead breeding blanket thermo-mechanical analyses. *Fusion Engineering and Design*, **109-111**, 991–995, November 2016. ISSN 0920-3796. doi:10.1016/j.fusengdes.2016.01.037.

[Bac18] Bachmann C., Ciattaglia S., Cismondi F., Eade T., Federici G., Fischer U., Franke T., Gliss C., Hernandez F., Keep J., Loughlin M., Maviglia F., Moro F., Morris J., Pereslavtsev P., Taylor N., Vizvary Z., and Wenninger R. Overview over DEMO design integration challenges and their impact on component design concepts. *Fusion Engineering and Design*, **136**, 87–95, November 2018. ISSN 0920-3796. doi:10.1016/j.fusengdes.2017.12.040.

[Bal98] Balducci G., Gigli G., and Meloni G. Dissociation energies of the Ga_2, In_2, and GaIn molecules. *Journal of Chemical Physics*, **109** (11), 4384–4388, September 1998. ISSN 0021-9606. doi:10.1063/1.477041.

[Bar02] Barysz M. and Sadlej A.J. Infinite-order two-component theory for relativistic quantum chemistry. *Journal of Chemical Physics*, **116** (7), 2696–2704, February 2002. ISSN 0021-9606. doi:10.1063/1.1436462.

[Bat10] Bateman H. Solution of a system of differential equations occurring in the theory of radioactive transformations. *Mathematical Proceedings of the Cambridge Philosophical Society*, **15**, 423–427, 1910. [online accessible: https://archive.org/details/cbarchive_122715_solutionofasystemofdifferentia1843/].

[Ber19] Bernardi D., Arbeiter F., Cappelli M., Fischer U., García A., Heidinger R., Krolas W., Martín-Fuertes F., Miccichè G., Muñoz A., Nitti F.S., Pérez M., Pinna T., Tian K., and Ibarra A. Towards the EU fusion-oriented neutron source: The preliminary engineering design of IFMIF-DONES. *Fusion Engineering and Design*, January 2019. ISSN 0920-3796. doi:10.1016/j.fusengdes.2018.12.042. [in press; published online Jan. 2019].

[Bet16] Betti R. and Hurricane O.A. Inertial-confinement fusion with lasers. *Nature Physics*, **12** (5), 435–448, May 2016. ISSN 1745-2481. doi:10.1038/nphys3736.

[Boc16] Boccaccini L.V., Aiello G., Aubert J., Bachmann C., Barrett T., Del Nevo A., Demange D., Forest L., Hernandez F., Norajitra P., Porempovic G., Rapisarda D., Sardain P., Utili M., and Vala L. Objectives and status of EUROfusion DEMO blanket studies. *Fusion Engineering and Design*, **109-111** (Part B), 1199–1206, 2016. ISSN ISSN 0920-3796. doi:10.1016/j.fusengdes.2015.12.054.

[Bog08] Bogusch E., Carré F., Knebel J.U., and Aoto K. Synergies in the design and development of fusion and generation IV fission reactors. *Fusion Engineering and Design*, **83** (7), 936–942, December 2008. ISSN 0920-3796. doi:10.1016/j.fusengdes.2008.05.019.

[Bor27] Born M. and Oppenheimer R. Zur Quantentheorie der Molekeln. *Annalen der Physik*, **389** (20), 457–484, 1927. ISSN 1521-3889. doi:10.1002/andp.19273892002. [online accessible: https://onlinelibrary.wiley.com/doi/epdf/10.1002/andp.19273892002].

[Bro55] Brooks L.S. The Vapor Pressure of Polonium. *Journal of the American Chemical Society*, **77** (12), 3211–3211, June 1955. ISSN 0002-7863. doi:10.1021/ja01617a014.

[Bro18] Brown D.A., Chadwick M.B., Capote R., Kahler A.C., Trkov A., Herman M.W., Sonzogni A.A., Danon Y., Carlson A.D., Dunn M., Smith D.L., Hale G.M., Arbanas G., Arcilla R., Bates C.R., Beck B., Becker B., Brown F., Casperson R.J., Conlin J., Cullen D.E., Descalle M.A., Firestone R., Gaines T., Guber K.H., Hawari A.I., Holmes J., Johnson T.D., Kawano T., Kiedrowski B.C., Koning A.J., Kopecky S., Leal L., Lestone J.P., Lubitz C., Márquez Damián J.I., Mattoon C.M., McCutchan E.A., Mughabghab S., Navratil P., Neudecker D., Nobre G.P.A., Noguere G., Paris M., Pigni M.T., Plompen A.J., Pritychenko B., Pronyaev V.G., Roubtsov D., Rochman D., Romano P., Schillebeeckx P., Simakov S., Sin M., Sirakov I., Sleaford B., Sobes V., Soukhovitskii E.S., Stetcu I., Talou P., Thompson I., van der Marck S., Welser-Sherrill L., Wiarda D., White M., Wormald J.L., Wright R.Q., Zerkle M., Žerovnik G., and Zhu Y. ENDF/B-VIII.0: The 8th Major Release of the Nuclear Reaction Data Library with CIELO-project Cross Sections, New Standards and Thermal Scattering Data. *Nuclear Data Sheets*, **148**, 1–142, February 2018. ISSN 0090-3752. doi:10.1016/j.nds.2018.02.001.

[Buc17] Buckthorpe D. Introduction to Generation IV nuclear reactors. In P. Yvon (editor), *Structural Materials for Generation IV Nuclear Reactors*, chapter 1, pp. 1–22. Woodhead Publishing, Cambridge, MA, USA, 1st edition, January 2017. ISBN 978-0-08-100906-2. doi:10.1016/B978-0-08-100906-2.00001-X.

[But19] Butler J. and Montzka S. The NOAA Annual Greenhouse Gas Index (AGGI). https://www.esrl.noaa.gov/gmd/aggi/aggi.html, 2019. [online; accessed 18-August-2019].

[Cet06] Cetnar J. General solution of Bateman equations for nuclear transmutations. *Annals of Nuclear Energy*, **33** (7), 640–645, May 2006. ISSN 0306-4549. doi:10.1016/j.anucene.2006.02.004.

[Cet10] Cetnar J. and Domanska G. Evaluation of circuit activation and radiotoxicity in the LBE cooled XADS experimental accelerator driven system using Monte Carlo method MCB. *Nukleonika*, **55** (1), 119–125, 2010. ISSN ISSN 0029-5922.

[Cha57] Charles G.W., Timma D.L., Hunt D.J., and Pish G. Vibrational Analysis of the Molecular Spectra of Polonium. *Journal of the*

Optical Society of America, JOSA, **47** (4), 291–296, April 1957. doi:10.1364/JOSA.47.000291.

[Che08] Chen H., Wu Y., Konishi S., and Hayward J. A high temperature blanket concept for hydrogen production. *Fusion Engineering and Design*, **83** (7), 903–911, December 2008. ISSN 0920-3796. doi:10.1016/j.fusengdes.2008.07.031.

[Che19] Cheng L., Welborn M., Christensen A.S., and Miller T.F. A universal density matrix functional from molecular orbital-based machine learning: Transferability across organic molecules. *Journal of Chemical Physics*, **150** (13), 131103, April 2019. ISSN 0021-9606. doi:10.1063/1.5088393.

[Cho08] Chontanawat J., Hunt L.C., and Pierse R. Does energy consumption cause economic growth?: Evidence from a systematic study of over 100 countries. *Journal of Policy Modeling*, **30** (2), 209–220, March 2008. ISSN 0161-8938. doi:10.1016/j.jpolmod.2006.10.003.

[Cis18] Cismondi F., Boccaccini L.V., Aiello G., Aubert J., Bachmann C., Barrett T., Barucca L., Bubelis E., Ciattaglia S., Del Nevo A., Diegele E., Gasparotto M., Di Gironimo G., Di Maio P.A., Hernandez F., Federici G., Fernández-Berceruelo I., Franke T., Froio A., Gliss C., Keep J., Loving A., Martelli E., Maviglia F., Moscato I., Mozzillo R., Poitevin Y., Rapisarda D., Savoldi L., Tarallo A., Utili M., Vala L., Veres G., and Zanino R. Progress in EU Breeding Blanket design and integration. *Fusion Engineering and Design*, **136**, 782–792, November 2018. ISSN 0920-3796. doi:10.1016/j.fusengdes.2018.04.009.

[Con14] Conde E., Barrado A.I., Pascual L., Fernández M., Salazar J.M.G.d., Barrena M.I., and Quiñones J. Behavior of the Pb–Li alloy impurities by ICP-MS. *Fusion Engineering and Design*, **89** (7), 1246–1250, October 2014. ISSN 0920-3796. doi:10.1016/j.fusengdes.2014.03.084.

[Coo84] Cooper B. and W.A. E. *The Science and Technology of Coal and Coal Utilization*. Springer US, Boston, MA, USA, 1st edition, 1984. ISBN 978-1-4684-4582-4.

[D'A17] D'Auria V., Dulla S., Ravetto P., Savoldi L., Utili M., and Zanino R. Design of a Permeator-Against-Vacuum mock-Up for the tritium extraction from PbLi at low speed. *Fusion Engineering and Design*, **121**, 198–203, October 2017. ISSN 0920-3796. doi:10.1016/j.fusengdes.2017.07.006.

[Dar70] Darwent B.d. *Bond dissociation energies in simple molecules*. NSRDS-NBS31, U.S. National Bureau of Standards; for sale by the Supt. of Docs., U.S. Govt. Print. Off., Washington, USA, 1970.

[DB15] De Bruyn D., Abderrahim H.A., Baeten P., and Leysen P. The MYRRHA ADS Project in Belgium Enters the Front End Engineering Phase. *Physics Procedia*, **66**, 75–84, January 2015. ISSN 1875-3892. doi:10.1016/j.phpro.2015.05.012.

[DN14] Del Nevo A. WCLL Blanket Design Description Document. *Technical Report EFDA_D_2MFB7B*, EUROfusion, November 2014.

[DN17] Del Nevo A., Martelli E., Agostini P., Arena P., Bongiovì G., Caruso G., Di Gironimo G., Di Maio P.A., Eboli M., Giammusso R., Giannetti F., Giovinazzi A., Mariano G., Moro F., Mozzillo R., Tassone A., Rozzia D., Tarallo A., Tarantino M., Utili M., and Villari R. WCLL breeding blanket design and integration for DEMO 2015: status and perspectives. *Fusion Engineering and Design*, **124**, 682–686, November 2017. ISSN 0920-3796. doi:10.1016/j.fusengdes.2017.03.020.

[Dou74] Douglas M. and Kroll N.M. Quantum electrodynamical corrections to the fine structure of helium. *Annals of Physics*, **82** (1), 89–155, January 1974. ISSN 0003-4916. doi:10.1016/0003-4916(74)90333-9.

[Dro65] Drowart J., Colin R., and Exsteen G. Mass-Spectrometric Study of the Vaporization of Lead Monoxide. Dissociation Energy of PbO. *Transactions of the Faraday Society*, **61**, 1376–1383, January 1965. doi:10.1039/TF9656101376.

[Dun32] Dunham J.L. The Energy Levels of a Rotating Vibrator. *Physical Review*, **41** (6), 721–731, September 1932. doi:10.1103/PhysRev.41.721.

[Ead17] Eade T., Garcia M., Garcia R., Ogando F., Pereslavtsev P., Sanz J., Stankunas G., and Travleev A. Activation and decay heat analysis of the European DEMO blanket concepts. *Fusion Engineering and Design*, **124**, 1241–1245, November 2017. ISSN 0920-3796. doi:10.1016/j.fusengdes.2017.02.100.

[Eck13] Eckerman K., Harrison J., Menzel H.G., and Clement C.H. ICRP Publication 119: Compendium of Dose Coefficients based on ICRP Publication 60. *Annals of the ICRP*, **42** (4), e1–e130, August 2013. ISSN 0146-6453. doi:10.1016/j.icrp.2013.05.003.

[EG09] El-Guebaly L.A. and Malang S. Toward the ultimate goal of tritium self-sufficiency: Technical issues and requirements imposed on ARIES advanced power plants. *Fusion Engineering and*

Design, **84** (12), 2072–2083, December 2009. ISSN 0920-3796. doi:10.1016/j.fusengdes.2008.12.098.

[Ein05] Einstein A. Ist die Trägheit eines Körpers von seinem Energieinhalt abhängig? *Annalen der Physik*, **323** (13), 639–641, 1905. ISSN 1521-3889. doi:10.1002/andp.19053231314.

[Ell17] Ellis R. Demo Plant Requirements Document (PRD). *Technical Report EFDA_D_2MG7RD v2.2*, EUROfusion, January 2017.

[Eng15] Engelen J., Aït Abderrahim H., Baeten P., De Bruyn D., and Leysen P. MYRRHA: Preliminary front-end engineering design. *International Journal of Hydrogen Energy*, **40** (44), 15137–15147, November 2015. ISSN 0360-3199. doi:10.1016/j.ijhydene.2015.03.096.

[Eri19] Ericsson G. Advanced Neutron Spectroscopy in Fusion Research. *Journal of Fusion Energy*, (3–4), February 2019. ISSN 1572-9591. doi:10.1007/s10894-019-00213-9.

[EUR18] EUROfusion. European Research Roadmap to the Realisation of Fusion Energy. https://www.euro-fusion.org/eurofusion/roadmap/, 2018. [online; accessed 31-July-2019].

[Eyn15] Eynde G.V.d., Malambu E., Stankovskiy A., Fernandez R., and Baeten P. An updated core design for the multi-purpose irradiation facility MYRRHA. *Journal of Nuclear Science and Technology*, **52** (7-8), 1053–1057, August 2015. ISSN 0022-3131. doi:10.1080/00223131.2015.1026860.

[Fa10] Fa W. and Jin Y. Global inventory of Helium-3 in lunar regoliths estimated by a multi-channel microwave radiometer on the Chang-E 1 lunar satellite. *Chinese Science Bulletin*, **55** (35), 4005–4009, December 2010. ISSN 1861-9541. doi:10.1007/s11434-010-4198-9.

[Faz15] Fazio C., Sobolev V.P., Aerts A., Gavrilov S., Lambrinou K., Schuurmans P., Gessi A., Agostini P., Ciampichetti A., Martinelli L., Gosse S., Balbaud-Celerier F., Courouau J.L., Terlain A., Li N., Glasbrenner H., Neuhausen J., Heinitz S., Zanini L., Dai Y., Jolkkonen M., Kurata Y., Obara T., Thiolliere N., Martin-Munoz F.J., Heinzel A., Weisenburger A., Mueller G., Schumacher G., Jianu A., Pacio J., Marocco L., Stieglitz R., Wetzel T., Daubner M., Litfin K., Vogt J.B., Proriol-Serre I., Gorse D., Eckert S., Stefani F., Buchenau D., Wondrak T., and Hwang I.S. Handbook on Lead-bismuth Eutectic Alloy and Lead Properties, Materials Compatibility, Thermal-hydraulics and Technologies - 2015 Edition. *Technical Report NEA–7268*, Nuclear

Energy Agency of the Organisation for Economic Co-Operation and Development (NEA), 2015. (INIS Volume 46, Issue 48).

[Fed14] Federici G., Kemp R., Ward D., Bachmann C., Franke T., Gonzalez S., Lowry C., Gadomska M., Harman J., Meszaros B., Morlock C., Romanelli F., and Wenninger R. Overview of EU DEMO design and R&D activities. *Fusion Engineering and Design*, **89** (7), 882–889, October 2014. ISSN 0920-3796. doi:10.1016/j.fusengdes.2014.01.070.

[Fed17] Federici G., Biel W., Gilbert M.R., Kemp R., Taylor N., and Wenninger R. European DEMO design strategy and consequences for materials. *Nuclear Fusion*, **57** (9), 092002, June 2017. ISSN 0029-5515. doi:10.1088/1741-4326/57/9/092002.

[Fed19] Federici G., Boccaccini L., Cismondi F., Gasparotto M., Poitevin Y., and Ricapito I. An overview of the EU breeding blanket design strategy as an integral part of the DEMO design effort. *Fusion Engineering and Design*, **141**, 30–42, April 2019. ISSN 0920-3796. doi:10.1016/j.fusengdes.2019.01.141.

[Feu91] Feuerstein H., Gräbner H., and Horn S. Extraction of Tritium from Molten Pb-17li by use of solid getters. *Fusion Technology 1990*, pp. 646–649, January 1991. doi:10.1016/B978-0-444-88508-1.50113-4.

[Feu92] Feuerstein H., Oschinski J., and Horn S. Behavior of Po-210 in molten Pb-17li. *Journal of Nuclear Materials*, **191**, 288–291, September 1992. ISSN 0022-3115. doi:10.1016/S0022-3115(09)80052-4.

[Feu95] Feuerstein H., Graebner H., Oschinski J., Beyer J., Horn S., Hoerner L., and Santo K. Compatibility of 31 metals, alloys and coatings with static Pb-17li eutectic mixture. *Technical Report FZKA–5596*, Forschungszentrum Karlsruhe GmbH Technik und Umwelt (Germany). Hauptabteilung Ingenieurtechnik, 1995.

[FG96] F. Gromov B., I. Efimov E., P. Leonchuk M., A. Veremeev A., V. Chekunov V., I. Orlov Y., V. Pankratov D., S. Stepanov V., and T. Gorshkov V. Liquid-metal lead-bismuth target for high-energy protons as an intensive neutron source in accelerator-controlled systems. *Atomic Energy*, **80**, 378–384, May 1996. doi:10.1007/BF02418720.

[Fin93] Finkel E. Quantum chemistry, Fourth Edition (Levine, Ira N.). *Journal of Chemical Education*, **70** (5), A145, May 1993. ISSN 0021-9584. doi:10.1021/ed070pA145.

[Fin98] Finley J., Malmqvist P.Å., Roos B.O., and Serrano-Andrés L. The multi-state CASPT2 method. *Chemical Physics Letters*, **288**, 299–306, May 1998. ISSN 0009-2614. doi:10.1016/S0009-2614(98)00252-8.

[Fio18] Fiorito L., Stankovskiy A., Hernandez-Solis A., Eynde G.V.d., and Zerovnik G. Nuclear data uncertainty analysis for the Po-210 production in MYRRHA. *EPJ Nuclear Sciences & Technologies*, **4**, 48, 2018. ISSN 2491-9292. doi:10.1051/epjn/2018044.

[Fis12] Fischer U. Mcnp model for WP12-DTM04 tasks. *Internal IDM document EFDA_D_2LC5VA*, EUROfusion, 2012.

[Fis14] Fischer U. Guidelines for PPPT neutronic analyses. *Internal IDM document EFDA_D_2L8TR9 v1.7*, EUROfusion, 2014.

[Fis15] Fischer U., Bachmann C., Palermo I., Pereslavtsev P., and Villari R. Neutronics requirements for a DEMO fusion power plant. *Fusion Engineering and Design*, **98-99**, 2134–2137, October 2015. ISSN 0920-3796. doi:10.1016/j.fusengdes.2015.02.029.

[Fis19] Fischer U., Bienkowska B., Drozdowicz K., Frisoni M., Mota F., Ogando F., Qiu Y., Stankunas G., and Tracz G. Neutronics of the IFMIF-DONES irradiation facility. *Fusion Engineering and Design*, February 2019. ISSN 0920-3796. doi:10.1016/j.fusengdes.2019.02.057. [in press; published online Feb. 2019].

[For97] Forsberg N. and Malmqvist P.k. Multiconfiguration perturbation theory with imaginary level shift. *Chemical Physics Letters*, **274** (1), 196–204, August 1997. ISSN 0009-2614. doi:10.1016/S0009-2614(97)00669-6.

[Fra17] Franza F. and Spagnuolo A. Collection of Key Parameters for DEMO Breeding Blankets Tritium Studies. *Technical Report EFDA_D_2L5SS4 v1.4*, EUROfusion, January 2017.

[Fri72] Friswell N.J. and Jenkins D.R. Identification of lead compounds in flames and determination of the PbO bond energy. *Combustion and Flame*, **19** (2), 197–201, October 1972. ISSN 0010-2180. doi:10.1016/S0010-2180(72)80210-4.

[Fro17] Froio A., Casella F., Cismondi F., Del Nevo A., Savoldi L., and Zanino R. Dynamic thermal-hydraulic modelling of the EU DEMO WCLL breeding blanket cooling loops. *Fusion Engineering and Design*, **124**, 887–891, November 2017. ISSN 0920-3796. doi:10.1016/j.fusengdes.2017.01.062.

[Gó97] Gómez P.C. and Jensen P. A Potential Energy Surface for the Electronic Ground State of H2te Derived from Experiment. *Journal of Molecular Spectroscopy*, **185** (2), 282–289, October 1997. ISSN 0022-2852. doi:10.1006/jmsp.1997.7386.

[Gar17] Garcinuño B., Rapisarda D., Fernández I., Moreno C., Palermo I., and Ibarra n. Design of a permeator against vacuum for tritium extraction from eutectic lithium-lead in a DCLL DEMO. *Fusion Engineering and Design*, **117**, 226–231, April 2017. ISSN 0920-3796. doi:10.1016/j.fusengdes.2016.06.036.

[Gat81] Gat J.R. and Gonfiantini R. Stable isotope hydrology. Deuterium and oxygen-18 in the water cycle. *Technical Report series 210 - no. 337*, International Atomic Energy Agency, Vienna, Austria, 1981.

[Gil15] Gilbert M. and Eade T. DEMO MCNP models used for the 2015 PMI-3.3-T006-D001 in-vessel component activation calculations task. *Internal IDM document EFDA_D_2LJD5D*, EUROfusion, 2015.

[Gin76] Gingerich K.A., Cocke D.L., and Miller F. Thermodynamic investigation of the lead molecules Pb_2, Pb_3, and Pb_4 by mass spectrometry. *Journal of Chemical Physics*, **64**, 4027–4033, May 1976. ISSN 0301-0104. doi:10.1063/1.432036.

[Gol11] Goldberg S.M. and Rosner R. *Nuclear Reactors: Generation to Generation*. American Academy of Arts and Sciences, Cambridge, MA, USA, 1st edition, May 2011. ISBN 0-87724-090-6.

[GP14] Gonzalez Prieto B., Marino A., Lim J., Rosseel K., Martens J., Rizzi M., Neuhausen J., Van den Bosch J., and Aerts A. Use of the transpiration method to study polonium evaporation from liquid lead-bismuth eutectic at high temperature. *Radiochimica Acta*, **102** (12), 1083–1091, August 2014. doi:10.1515/ract-2014-2263.

[Gre16] Gregory J.M. and Andrews T. Variation in climate sensitivity and feedback parameters during the historical period. *Geophysical Research Letters*, **43** (8), 3911–3920, 2016. ISSN 1944-8007. doi:10.1002/2016GL068406.

[Gyo16] Gyorgy H. and Czifrus S. The utilization of thorium in Generation IV reactors. *Progress in Nuclear Energy*, **93**, 306–317, November 2016. ISSN 0149-1970. doi:10.1016/j.pnucene.2016.09.007.

[Han03] Han Y.K. Comment on 'Theoretical study on PbS, PbO and their anions' [Chem. Phys. Lett. 370 (2003) 39]. *Chemical Physics*

Letters, **381** (1), 248–250, November 2003. ISSN 0009-2614. doi:10.1016/j.cplett.2003.08.098.

[Har35] Hartree D.R. and Hartree W. Self-consistent field, with exchange, for beryllium. *Proceedings of the Royal Society of London. Series A - Mathematical and Physical Sciences*, **150** (869), 9–33, May 1935. doi:10.1098/rspa.1935.0085.

[Har07] Harrison J., Leggett R., Lloyd D., Phipps A., and Scott B. Polonium-210 as a poison. *Journal of Radiological Protection*, **27** (1), 17–40, March 2007. ISSN 0952-4746. doi:10.1088/0952-4746/27/1/001.

[Hay16] Haynes W.M. (editor). *CRC Handbook of Chemistry and Physics, 97th Edition*. CRC Press, Boca Raton, FL, USA, 97th edition, June 2016. ISBN 978-1-4987-5428-6.

[Hea10] Health Physics Society. Polonium-210: Contamination Information and Updates - fact sheet. http://hps.org/newsandevents/polonium210.html, May 2010. [online; accessed 31-July-2019].

[Hei11] Heinitz S., Neuhausen J., and Schumann D. Alkaline extraction of polonium from liquid lead bismuth eutectic. *Journal of Nuclear Materials*, **414** (2), 221–225, July 2011. ISSN 0022-3115. doi:10.1016/j.jnucmat.2011.03.043.

[Her56] Herzberg G. *Molecular spectra and molecular structure. II. Infrared and Raman spectra of polyatomic molecules*. Van Nostrand, Princeton, NJ, USA, 7th edition, 1956.

[Her03] Herczeg J.W. The advanced fuel cycle initiative: the future path for advanced spent fuel treatment and transmutation research in the United States. In *Actinide and fission product partitioning and transmutation*, pp. 43–44. OECD Publishing, Paris, France, 2003. ISBN 92-64-02125-6. EUR 20618 EN.

[Her18] Hernández F.A. and Pereslavtsev P. First principles review of options for tritium breeder and neutron multiplier materials for breeding blankets in fusion reactors. *Fusion Engineering and Design*, **137**, 243–256, December 2018. ISSN 0920-3796. doi:10.1016/j.fusengdes.2018.09.014.

[Her19] Hernández F.A., Pereslavtsev P., Zhou G., Neuberger H., Rey J., Kang Q., Boccaccini L.V., Bubelis E., Moscato I., and Dongiovanni D. An enhanced, near-term HCPB design as driver blanket for the EU DEMO. *Fusion Engineering and Design*, February 2019. ISSN

0920-3796. doi:10.1016/j.fusengdes.2019.02.037. [in press; published online Feb. 2019].

[Hou05] Housecroft C.E. and Constable E.C. *Chemistry: An Introduction to Organic, Inorganic & Physical Chemistry*. Prentice Hall, Harlow, England ; New York, 3rd edition, October 2005. ISBN 978-0-13-127567-6.

[Hub79] Huber, K. P. and Herzberg, G. *Molecular Spectra And Molecular Structure, IV. Constants Of Diatomic Molecules*. Van Nostrand Reinhold Company, New York, USA, 1979.

[Hub06] Huba J.D. NRL Plasma Formulary. *Technical Report OBM No. 0704-0188*, NAVAL RESEARCH LAB WASHINGTON DC PLASMA PHYSICS DIV, Washington, DC, USA, January 2006.

[Hul41] Hulburt H.M. and Hirschfelder J.O. Potential Energy Functions for Diatomic Molecules. *Journal of Chemical Physics*, **9** (1), 61–69, January 1941. ISSN 0021-9606. doi:10.1063/1.1750827.

[Hur14] Hurricane O.A., Callahan D.A., Casey D.T., Celliers P.M., Cerjan C., Dewald E.L., Dittrich T.R., Döppner T., Hinkel D.E., Hopkins L.F.B., Kline J.L., Le Pape S., Ma T., MacPhee A.G., Milovich J.L., Pak A., Park H.S., Patel P.K., Remington B.A., Salmonson J.D., Springer P.T., and Tommasini R. Fuel gain exceeding unity in an inertially confined fusion implosion. *Nature*, **506** (7488), 343–348, February 2014. ISSN 1476-4687. doi:10.1038/nature13008.

[Ili05] Iliaš M., Aa. Jensen H.J., Kellö V., Roos B.O., and Urban M. Theoretical study of PbO and the PbO anion. *Chemical Physics Letters*, **408** (4), 210–215, June 2005. ISSN 0009-2614. doi:10.1016/j.cplett.2005.04.027.

[Int18a] International Atomic Energy Agency (editor). *Non-baseload Operation in Nuclear Power Plants: Load Following and Frequency Control Modes of Flexible Operation*. International Atomic Energy Agency, Vienna, Austria, June 2018. ISBN 978-92-0-110816-6.

[Int18b] International Energy Agency. *World Energy Outlook 2018*. IEA Publications, Paris, France, 2018. ISBN 978-92-64-30677-6. doi:10.1787/weo-2018-en.

[Int19] International Atomic Energy Agency. *Nuclear Power Reactors in the World 2019*. IAEA-RDS-2/39, IAEA, Vienna, Austria, 2019. ISBN 978-92-0-102719-1.

[Jab16] Jaboulay J.C., Aiello G., Aubert J., Villari R., and Fischer U. Comparison over the nuclear analysis of the HCLL blanket for the European DEMO. *Fusion Engineering and Design*, **109-111**, 365–370, November 2016. ISSN 0920-3796. doi:10.1016/j.fusengdes.2016.02.097.

[Jab17] Jaboulay J.C., Aiello G., Aubert J., Morin A., and Troisne M. Nuclear analysis of the HCLL blanket for the European DEMO. *Fusion Engineering and Design*, **124**, 896–900, November 2017. ISSN 0920-3796. doi:10.1016/j.fusengdes.2017.01.050.

[JAE17] Collaboration between SCK · CEN and JAEA for Partitioning and Transmutation through Accelerator-Driven System. *Technical Report JAEA-Review 2017-003 & SCK·CEN/20862373*, Japan Atomic Energy Agency, March 2017. doi:10.11484/jaea-review-2017-003.

[Kik12] Kikuchi M., Lackner K., and Tran M. (editors). *Fusion Physics*. International Atomic Energy Agency, Vienna, Austria, December 2012. ISBN 978-92-0-130410-0.

[Kon98] Konings R.J.M., Booij A.S., and Kovács A. The infrared spectra of SeO2 and TeO2 in the gas phase. *Chemical Physics Letters*, **292** (4), 447–453, August 1998. ISSN 0009-2614. doi:10.1016/S0009-2614(98)00689-7.

[Kon13] Kondo M. Boiling points of liquid breeders for fusion blankets. *Fusion Engineering and Design*, **Volume 88**, Pages 2556–2559, October 2013. doi:10.1016/j.fusengdes.2013.05.049.

[Kon14] Koning A., Rochman D., van der Marck S., Kopecky J., Sublet J.C., Pomp S., Sjostrand H., Forrest R., Bauge E., Henriksson H., Cabellos O., S. G., Leppanen J., Leeb H., Plompen A., and Mills R. TENDL-2014: TALYS-based evaluated nuclear data library. www.talys.eu/tendl-2014.html, 2014. [online; accessed 31-July-2019].

[Kov17] Kovari M., Coleman M., Cristescu I., and Smith R. Tritium resources available for fusion reactors. *Nuclear Fusion*, **58** (2), 026010, December 2017. ISSN 0029-5515. doi:10.1088/1741-4326/aa9d25.

[Kra18] Kramida A., Yu. Ralchenko, Reader J., and NIST ASD Team. Nist atomic spectra database (ver. 5.5.6). https://physics.nist.gov/asd, 2018. [online; accessed 31-July-2019].

[Lee04] Lee E.P.F., Mok D.K.W., Chau F.t., and Dyke J.M. Ab initio calculations on low-lying electronic states of TeO_2 and Franck-Condon simulation of the $(1)^1B_2 \leftarrow X^1A_1$ TeO_2 absorption spectrum including

anharmonicity. *Journal of Chemical Physics*, **121** (7), 2962–2974, July 2004. ISSN 0021-9606. doi:10.1063/1.1768164.

[Len96] van Lenthe E., Snijders J.G., and Baerends E.J. The zero-order regular approximation for relativistic effects: The effect of spin–orbit coupling in closed shell molecules. *Journal of Chemical Physics*, **105** (15), 6505–6516, October 1996. ISSN 0021-9606. doi:10.1063/1.472460.

[Liu01] Liu W., van Wüllen C., Han Y.K., Choi Y.J., and Lee Y.S. Spectroscopic constants of Pb and Eka-lead compounds: comparison of different approaches. In *Advances in Quantum Chemistry*, volume 39 of *New Perspectives in Quantum Systems in Chemistry and Physics, Part 1*, pp. 325–355. Academic Press, January 2001. ISBN 9780080916149. doi:10.1016/S0065-3276(05)39019-8.

[Lov17] Loveland W.D., Morrissey D.J., and Seaborg G.T. Fission. In *Modern Nuclear Chemistry*, chapter 11, pp. 305–338. John Wiley & Sons, Ltd, Hoboken, NJ, USA, 2nd edition, 2017. ISBN 978-1-119-34845-0. doi:10.1002/9781119348450.ch11.

[Luo07] Luo Y.R. *Comprehensive Handbook of Chemical Bond Energies*. CRC Press, Boca Raton, FL, USA, 1st edition, March 2007. ISBN 978-1-4200-0728-2. Google-Books-ID: kM3mwD4y_TAC.

[Mal02] Malmqvist P.Å., Roos B.O., and Schimmelpfennig B. The restricted active space (RAS) state interaction approach with spin–orbit coupling. *Chemical Physics Letters*, **357** (3), 230–240, May 2002. ISSN 0009-2614. doi:10.1016/S0009-2614(02)00498-0.

[Mar10] Marques J.G. Evolution of nuclear fission reactors: Third generation and beyond. *Energy Conversion and Management*, **51** (9), 1774–1780, September 2010. ISSN 0196-8904. doi:10.1016/j.enconman.2009.12.043.

[Mau14] Maugeri E.A., Neuhausen J., Eichler R., Piguet D., Mendonça T.M., Stora T., and Schumann D. Thermochromatography study of volatile polonium species in various gas atmospheres. *Journal of Nuclear Materials*, **450** (1), 292–298, July 2014. ISSN 0022-3115. doi:10.1016/j.jnucmat.2013.11.024.

[May83] Mayer I. and Révész M. Bond orders and valences in some simple sulphur compounds. *Inorganica Chimica Acta*, **77**, L205–L206, January 1983. ISSN 0020-1693. doi:10.1016/S0020-1693(00)82616-X.

[May01] Mayer M., Krüger S., and Rösch N. A two-component variant of the Douglas–Kroll relativistic linear combination of Gaussian-type orbitals density-functional method: Spin–orbit effects in atoms and diatomics. *Journal of Chemical Physics*, **115** (10), 4411–4423, August 2001. ISSN 0021-9606. doi:10.1063/1.1390509.

[Mer14] Merrill B.J., Wong C.P.C., Cadwallader L.C., Abdou M., and Morley N.B. Normal operation and maintenance safety lessons from the ITER US PbLi test blanket module program for a US FNSF and DEMO. *Fusion Engineering and Design*, **89** (9), 1989–1994, October 2014. ISSN 0920-3796. doi:10.1016/j.fusengdes.2014.04.076.

[Mer16] Mertens M.A.J., Demange D., and Frances L. Model and simulation of a vacuum sieve tray for T extraction from liquid PbLi breeding blankets. *Fusion Engineering and Design*, pp. 541–547, June 2016. doi:10.1016/j.fusengdes.2016.05.038.

[Mer19a] Mertens M.A.J., Aerts A., Infante I., Neuhausen J., and Cottenier S. Po-Containing Molecules in Fusion and Fission Reactors. *Journal of Physical Chemistry Letters*, **10** (11), 2879–2884, June 2019. ISSN 1948-7185. doi:10.1021/acs.jpclett.9b00824.

[Mer19b] Mertens M.A.J., Fischer U., Pereslavtsev P., Stieglitz R., Noterdaeme J.M., and Cottenier S. ^{210}Po production in the European DEMO fusion reactor. *Nuclear Fusion*, **59** (10), 106029, aug 2019. ISSN 0029-5515. doi:10.1088/1741-4326/ab36aa.

[Met00] Metz B., Stoll H., and Dolg M. Small-core multiconfiguration-Dirac–Hartree–Fock-adjusted pseudopotentials for post-d main group elements: Application to PbH and PbO. *Journal of Chemical Physics*, **113** (7), 2563–2569, August 2000. ISSN 0021-9606. doi:10.1063/1.1305880.

[Mie79] Miedema A.R. and Gingerich K.A. On the formation enthalpy of metallic dimers. *Journal of Physics B Atomic Molecular Physics*, **12** (13), 2081–2095, July 1979. ISSN 0953-4075. doi:10.1088/0022-3700/12/13/005.

[Mon03] Moniz E.J. *The future of nuclear power - An interdisciplinary MIT study*. Massachusetts Institute of Technology, Cambridge, MA, USA, 2003. ISBN 0-615-12420-8.

[Mor29] Morse P.M. Diatomic Molecules According to the Wave Mechanics. II. Vibrational Levels. *Physical Review*, **34** (1), 57–64, July 1929. doi:10.1103/PhysRev.34.57.

[Mor18] Moro F., Del Nevo A., Flammini D., Martelli E., Mozzillo R., Noce S., and Villari R. Neutronic analyses in support of the WCLL DEMO design development. *Fusion Engineering and Design*, **136**, 1260–1264, November 2018. ISSN 0920-3796. doi:10.1016/j.fusengdes.2018.04.113.

[MS96] M Smirnov B. and Yatsenko A. Properties of dimers. *Physics-uspekhi*, **39** (3), 211–230, March 1996. doi:10.1070/PU1996v039n03ABEH000135.

[Mue69] Muenow D.W., Hastle J.W., Hauge R., Bautista R., and Margrave J.L. Vaporization, thermodynamics and structures of species in the tellurium + oxygen system. *Transactions of the Faraday Society*, **65** (0), 3210–3220, January 1969. ISSN 0014-7672. doi:10.1039/TF9696503210.

[Mur15] Murray R.L. and Holbert K.E. *Nuclear Energy: An Introduction to the Concepts, Systems, and Applications of Nuclear Processes*. Butterworth Heinemann - Elsevier, Waltham, MA, USA, 7th edition, January 2015. ISBN 978-0-12-416654-7. Google-Books-ID: v607AgAAQBAJ.

[Nap08] Napolion B., Huang M.J., and Watts J.D. Coupled-Cluster Study of Isomers of H2so2. *Journal of Physical Chemistry A*, **112** (17), 4158–4164, May 2008. ISSN 1089-5639. doi:10.1021/jp8009047.

[Nat] National Oceanic and Atmospheric Administration - US Department of Commerce. ESRL Global Monitoring Division - Global Greenhouse Gas Reference Network. https://www.esrl.noaa.gov/gmd/ccgg/trends/. [online; accessed 18-August-2019].

[NIS] Nist computational chemistry comparison and benchmark database, nist standard reference database number 101, ed. russell d. johnson iii. http://cccbdb.nist.gov/. Release 19, April 2018.

[noa04] The United Nations on World Population in 2300. *Population and Development Review*, **30** (1), 181–187, 2004. ISSN 1728-4457. doi:10.1111/j.1728-4457.2004.00009.x.

[noa17a] TENDL-2017 nuclear data library. https://tendl.web.psi.ch/tendl_2017/tendl2017.html, 2017. [online; accessed 31-July-2019].

[noa17b] World Population Prospects: The 2017 Revision, Volume I: Comprehensive Tables. *Technical Report ST/ESA/SER.A/399*, United Nations Department of Economic and Social Affairs - Population Division, 2017.

[noa18] *Climate Change and Nuclear Power 2018*. Non-serial Publications, International Atomic Energy Agency, Vienna, Austria, 2018.

[noa19] World Development Indicators (WDI) | Data Catalog. https://datacatalog.worldbank.org/dataset/world-development-indicators, 2019. [online; accessed 16-May-2019].

[Noc19] Noce S., Moro F., Romanelli F., and Villari R. Nuclear analysis of the Single Module Segment WCLL DEMO. *Fusion Engineering and Design*, **147**, 111207, October 2019. ISSN 0920-3796. doi:10.1016/j.fusengdes.2019.05.026.

[Nuc17] Nuclear Energy Agency. JEFF Nuclear Data Library. https://www.oecd-nea.org/dbdata/jeff/, 2017. [online, accessed 31-July-2019].

[OA09] Ortiz Amaya L. and Braet J. Purification of Lead-Bismuth Eutectic Used in Accelerator Driven Systems. In *2009 Waste Management Symposium Proceedings*, volume 1. Phoenix, AZ, United States, March 2009.

[Ohn05] Ohno S., Miyahara S., and Kurata Y. Experimental Investigation of Lead-Bismuth Evaporation Behavior. *Journal of Nanoscience and Technology*, **42** (7), 593–599, July 2005. ISSN 0022-3131. doi:10.1080/18811248.2004.9726426.

[Oki12] Okino F., Noborio K., Yamamoto Y., and Konishi S. Vacuum sieve tray for tritium extraction from liquid Pb–17li. *Fusion Engineering and Design*, **87** (7), 1014–1018, August 2012. ISSN 0920-3796. doi:10.1016/j.fusengdes.2012.02.071.

[Oki15] Okino F., Calderoni P., Kasada R., and Konishi S. Feasibility analysis of vacuum sieve tray for tritium extraction in the HCLL test blanket system. *Fusion Engineering and Design*, **109**, October 2015. doi:10.1016/j.fusengdes.2015.10.004.

[Pal15] Palermo I., Fernadez I., Rosa E., Moro F., and Fischer U. 2014 DEMO HCLL MCNP model. *Internal IDM document EFDA_D_2M82V3*, EUROfusion, 2015.

[Pau25] Pauli W. Über den Zusammenhang des Abschlusses der Elektronengruppen im Atom mit der Komplexstruktur der Spektren. *Zeitschrift für Physik*, **31** (1), 765–783, February 1925. ISSN 0044-3328. doi:10.1007/BF02980631.

[Pea18] Pearson R.J., Antoniazzi A.B., and Nuttall W.J. Tritium supply and use: a key issue for the development of nuclear fusion energy. *Fusion Engineering and Design*, **136**, 1140–1148, November 2018. ISSN 0920-3796. doi:10.1016/j.fusengdes.2018.04.090.

[Pek34] Pekeris C.L. The Rotation-Vibration Coupling in Diatomic Molecules. *Physical Review*, **45** (2), 98–103, January 1934. doi:10.1103/PhysRev.45.98.

[Per16] Pereslavtsev P., Bachmann C., and Fischer U. Neutronic analyses of design issues affecting the tritium breeding performance in different DEMO blanket concepts. *Fusion Engineering and Design*, **109-111** (Part B), 1207–1211, November 2016. ISSN 0920-3796. doi:10.1016/j.fusengdes.2015.12.053.

[Pet06] Petti D.A., Merrill B.J., Moore R.L., Longhurst G.R., El-Guebaly L., Mogahed E., Henderson D., Wilson P., and Abdou A. ARIES-AT safety design and analysis. *Fusion Engineering and Design*, **80** (1), 111–137, January 2006. ISSN 0920-3796. doi:10.1016/j.fusengdes.2005.06.351.

[Pio16] Pioro I. (editor). *Handbook of Generation IV Nuclear Reactors*. Woodhead Publishing Series in Energy: Number 103, Woodhead Publishing, Waltham, MA, USA, 1st edition, July 2016. ISBN 978-0-08-100149-3.

[Pit81] Pitzer K.S. Dissociation energies of molecules with very heavy atoms from mass spectrometry. *Journal of Chemical Physics*, **74**, 3078–3079, March 1981. ISSN 0301-0104. doi:10.1063/1.441398.

[Ram01] Ramaswamy V., Boucher O., Haigh J., Hauglustaine D., Haywood J., Myhre G., Nakajima T., Y Shi G., and Solomon S. Radiative Forcing of Climate Change. pp. 349–416. Cambridge University Press, Cambridge, MA, USA, January 2001.

[Rap15] Rapisarda D. Design Description Document 2015 for DCLL (update of DDD 2014). *Technical Report EFDA_D_2MT44J*, EUROfusion, 2015.

[Rei04] Reiher M. and Wolf A. Exact decoupling of the Dirac Hamiltonian. I. General theory. *Journal of Chemical Physics*, **121** (5), 2037–2047, July 2004. ISSN 0021-9606. doi:10.1063/1.1768160.

[Rit19] Ritchie H. and Roser M. Energy Production & Changing Energy Sources. https://datacatalog.worldbank.org/dataset/

world-development-indicators, March 2019. [online; accessed 18-August-2019].

[Riz14] Rizzi M., Neuhausen J., Eichler R., Türler A., Mendonça T.M., Stora T., Gonzalez Prieto B., Aerts A., and Schumann D. Polonium evaporation from dilute liquid metal solutions. *Journal of Nuclear Materials*, **450** (1), 304–313, July 2014. ISSN 0022-3115. doi:10.1016/j.jnucmat.2014.01.047.

[Roo80] Roos B.O., Taylor P.R., and Siegbahn P.E.M. A complete active space SCF method (CASSCF) using a density matrix formulated super-CI approach. *Journal of Physical Chemistry*, **48** (2), 157–173, May 1980. ISSN 0301-0104. doi:10.1016/0301-0104(80)80045-0.

[Roo04a] Roos B.O., Lindh R., Malmqvist P.Å., Veryazov V., and Widmark P.O. Main Group Atoms and Dimers Studied with a New Relativistic ANO Basis Set. *Journal of Physical Chemistry A*, **108** (15), 2851–2858, April 2004. ISSN 1089-5639. doi:10.1021/jp031064+.

[Roo04b] Roos B.O. and Malmqvist P.Å. On the Effects of Spin-Orbit Coupling on Molecular Properties. *Advances in Quantum Chemistry*, **47**, 37–49, 2004. doi:10.1016/S0065-3276(04)47003-8.

[Roo04c] Roos B.O. and Malmqvist P.k. Relativistic quantum chemistry: the multiconfigurational approach. *Physical Chemistry Chemical Physic*, **6** (11), 2919–2927, May 2004. ISSN 1463-9084. doi:10.1039/B401472N.

[Roo04d] Roos B.O., Veryazov V., and Widmark P.O. Relativistic atomic natural orbital type basis sets for the alkaline and alkaline-earth atoms applied to the ground-state potentials for the corresponding dimers. *Theoretical Chemistry Accounts*, **111** (2-6), 345–351, March 2004. ISSN 1432-881X, 1432-2234. doi:10.1007/s00214-003-0537-0.

[Rut04] Rutherford E. and Segrè E. *Radio-activity*. Cambridge, University Press, 1904. [online accessible: https://archive.org/details/radioactivity00ruthrich/].

[Sah18] Sahin S. and Wu Y. Fission Energy Production. In I. Dincer (editor), *Comprehensive Energy Systems*, chapter 3.14, pp. 590–637. Elsevier, February 2018. ISBN 978-0-12-814925-6. doi:10.1016/B978-0-12-809597-3.00331-X.

[Saw06] Sawan M.E. and Abdou M.A. Physics and technology conditions for attaining tritium self-sufficiency for the DT fuel cycle. *Fusion*

Engineering and Design, **81** (8), 1131–1144, February 2006. ISSN 0920-3796. doi:10.1016/j.fusengdes.2005.07.035.

[Sch91] Schulz B. Thermophysical properties of the Li(17)Pb(83)alloy. *Fusion Engineering and Design*, **14** (3–4), 199–205, April 1991. ISSN 0920-3796. doi:10.1016/0920-3796(91)90002-8.

[SCK16] SCK · CEN. MYRRHA technical brochure. https://www.sckcen.be/en/Technology_future/MYRRHA, November 2016. [online; accessed 16-May-2019].

[Sco07] Scott B.R. Health Risk Evaluations for Ingestion Exposure of Humans to Polonium-210. *Dose Response*, **5** (2), 94–122, April 2007. ISSN 1559-3258. doi:10.2203/dose-response.06-013.Scott.

[Sii14] Siirola J.J. Speculations on global energy demand and supply going forward. *Current Opinion in Chemical Engineering*, **5**, 96–100, August 2014. ISSN 2211-3398. doi:10.1016/j.coche.2014.07.002.

[Sla29] Slater J.C. The Theory of Complex Spectra. *Physical Review*, **34** (10), 1293–1322, November 1929. doi:10.1103/PhysRev.34.1293.

[Smo15] Smolentsev S., Morley N.B., Abdou M.A., and Malang S. Dual-coolant lead–lithium (DCLL) blanket status and R&D needs. *Fusion Engineering and Design*, **100**, 44–54, November 2015. ISSN 0920-3796. doi:10.1016/j.fusengdes.2014.12.031.

[Sob11] Sobolev V. Database of thermophysical properties of liquid metal coolants for GEN-IV (rev. dec. 2011). *Technical Report SCKCEN-BLG-1069*, Belgian Nuclear Research Centre SCKCEN, Mol, Belgium, December 2011. Scientific Report.

[Ste92] Steiger T. and Steudel R. Sulphur compounds: Part 149. Structures, relative stabilities and vibrational spectra of several isomeric forms of sulphoxylic acid (H2so2) and its anion (HSO_2^-): an ab initio study11148 see ref. 1. *Journal of Molecular Structure: THEOCHEM*, **257** (3), 313–323, May 1992. ISSN 0166-1280. doi:10.1016/0166-1280(92)85048-P.

[Str04] Straumann N. The Role of the Exclusion Principle for Atoms to Stars: A Historical Account. *eprint arXiv:quant-ph/0403199*, pp. arXiv:quant–ph/0403199, March 2004.

[Sub10] Sublet J.C., Packer L.W., Kopecky J., Forrest R.A., Koning A.J., and Rochman D.A. The european activation file: Eaf-2010 neutron-

induced cross section library. *Technical Report CCFE-R (10) 05*, Culham, UK, 2010.

[Sub17] Sublet J.C., Eastwood J.W., Morgan J.G., Gilbert M.R., Fleming M., and Arter W. FISPACT-II: An Advanced Simulation System for Activation, Transmutation and Material Modelling. *Nuclear Data Sheets*, **139**, 77–137, January 2017. ISSN 0090-3752. doi:10.1016/j.nds.2017.01.002.

[Tho01] Thomas P.A., Fisenne I., Chorney D., Baweja A.S., and Tracy B.L. Human absorption and retention of polonium-210 from caribou meat. *Radiation Protection Dosimetry*, **97** (3), 241–250, 2001. ISSN 0144-8420. doi:10.1093/oxfordjournals.rpd.a006669.

[Uti15] Utili M. Preliminary model T transport in bu for hcll and wcll - intermediate report. *Technical Report EFDA_D_2M89QE*, EUROfusion, October 2015.

[Uti19a] Utili M., Bassini S., Boccaccini L., Bühler L., Cismondi F., Del Nevo A., Eboli M., DiFonzo F., Hernandez T., Wulf S., Kordač M., Martelli D., De les Valls E.M., Melichar T., Mistrangelo C., Tarantino M., Tincani A., and Vála L. Status of Pb-16li technologies for European DEMO fusion reactor. *Fusion Engineering and Design*, May 2019. ISSN 0920-3796. [in press; published online May. 2019].

[Uti19b] Utili M., Tincani A., Candido L., Savoldi L., Zanino R., Zucchetti M., Martelli D., and Venturini A. Tritium Extraction from HCLL/W-CLL/DCLL PbLi BBs of DEMO and HCLL TBS of ITER. *IEEE Transactions on Plasma Science*, **47** (2), 1464–1471, February 2019. doi:10.1109/TPS.2018.2886409.

[Val08] Mas de les Valls E., Sedano L.A., Batet L., Ricapito I., Aiello A., Gastaldi O., and Gabriel F. Lead–lithium eutectic material database for nuclear fusion technology. *Journal of Nuclear Materials*, **376** (3), 353–357, June 2008. ISSN 0022-3115. doi:10.1016/j.jnucmat.2008.02.016.

[Ver11] Veryazov V., Malmqvist P.Å., and Roos B.O. How to select active space for multiconfigurational quantum chemistry? *International Journal of Quantum Chemistry*, **111** (13), 3329–3338, November 2011. ISSN 1097-461X. doi:10.1002/qua.23068.

[Vil15] Villari R., Jaboulay J., Aiello G., Palermo I., and Fischer U. 2014 DEMO HCLL MCNP model. *Internal IDM document EFDA_D_2M6MQZ*, EUROfusion, 2015.

[Vir17] Vira J. Geological repository for high-level nuclear waste becoming reality in Finland. In M.J. Apted and J. Ahn (editors), *Geological Repository Systems for Safe Disposal of Spent Nuclear Fuels and Radioactive Waste (Second Edition)*, chapter 23, pp. 645–666. Woodhead Publishing Series in Energy, Woodhead Publishing, Cambridge, MA, USA, January 2017. ISBN 978-0-08-100642-9. doi:10.1016/B978-0-08-100642-9.00023-2.

[Vis96] Visscher L., Lee T.J., and Dyall K.G. Formulation and implementation of a relativistic unrestricted coupled-cluster method including noniterative connected triples. *Journal of Chemical Physics*, **105** (19), 8769–8776, November 1996. ISSN 0021-9606. doi:10.1063/1.472655.

[Vis00] Visscher L. and Saue T. Approximate relativistic electronic structure methods based on the quaternion modified Dirac equation. *Journal of Chemical Physics*, **113** (10), 3996–4002, August 2000. ISSN 0021-9606. doi:10.1063/1.1288371.

[Vis01] Visscher L., Eliav E., and Kaldor U. Formulation and implementation of the relativistic Fock-space coupled cluster method for molecules. *Journal of Chemical Physics*, **115** (21), 9720–9726, November 2001. ISSN 0021-9606. doi:10.1063/1.1415746.

[VYDD15] Van Yperen-De Deyne A., Rijpstra K., Waroquier M., Van Speybroeck V., and Cottenier S. Binary and ternary Po-containing molecules relevant for LBE cooled reactors at operating temperature. *Journal of Nuclear Materials*, **458**, 288–295, March 2015. ISSN 0022-3115. doi:10.1016/j.jnucmat.2014.11.064.

[Wei35] Weizsäcker C.F.v. Zur Theorie der Kernmassen. *Zeitschrift für Physik*, **96** (7), 431–458, July 1935. ISSN 0044-3328. doi:10.1007/BF01337700.

[Wel18] Welborn M., Cheng L., and Miller T.F. Transferability in Machine Learning for Electronic Structure via the Molecular Orbital Basis. *Journal of Chemical Theory and Computation*, **14** (9), 4772–4779, September 2018. ISSN 1549-9618. doi:10.1021/acs.jctc.8b00636.

[Wer17] Werner C. (editor). *MCNP Users Manual - Code Version 6.2*. Los Alamos National Security, LCC, 2017. ISBN LA-UR-17-29981.

[Wig83] Wigley T.M.L. The pre-industrial carbon dioxide level. *Climatic Change*, **5** (4), 315–320, December 1983. ISSN 1573-1480. doi:10.1007/BF02423528.

[wik19a] wikipedia. MYRRHA. https://en.wikipedia.org/wiki/MYRRHA, April 2019. [online; accessed 13-June-2019].

[wik19b] wikipedia. Nuclear fusion. https://en.wikipedia.org/wiki/Nuclear_fusion, May 2019. [online; accessed 31-July-2019].

[Wit60] Witteman W.G., Giorgi A.L., and Vier D.T. The Preparation and Identification of some Intermetallic Compounds of Polonium. *Journal of Physical Chemistry*, **64** (4), 434–440, April 1960. ISSN 0022-3654. doi:10.1021/j100833a014.

[Wu15] Wu Y., Song J., Zheng H., Sun G., Hao L., Long P., and Hu L. CAD-based Monte Carlo program for integrated simulation of nuclear system SuperMC. *Annals of Nuclear Energy*, **82**, 161–168, August 2015. ISSN 0306-4549. doi:10.1016/j.anucene.2014.08.058.

[Zas74] Zasorin E.Z., Zharskii I.M., Pinaev G.F., Kupreev V.N., and Spiridonov V.P. Electron-diffraction investigation of the selenium and tellurium dioxide molecules. *Journal of Structural Chemistry*, **15** (4), 588–590, July 1974. ISSN 1573-8779. doi:10.1007/BF00747201.

[Zha14] Zhang J. Lead–Bismuth Eutectic (LBE): A Coolant Candidate for Gen. IV Advanced Nuclear Reactor Concepts. *Adv. Eng. Mater.*, **16** (4), 349–356, 2014. ISSN 1527-2648. doi:10.1002/adem.201300296.

[Zhe16] Zheng S., King D.B., Garzotti L., Surrey E., and Todd T.N. Fusion reactor start-up without an external tritium source. *Fusion Engineering and Design*, **103**, 13–20, February 2016. ISSN 0920-3796. doi:10.1016/j.fusengdes.2015.11.034.

[Zin13] Zinkle S.J. and Möslang A. Evaluation of irradiation facility options for fusion materials research and development. *Fusion Engineering and Design*, **88** (6), 472–482, October 2013. ISSN 0920-3796. doi:10.1016/j.fusengdes.2013.02.081.

During this work, Merlijn A.J. Mertens benefited financial support from a PhD fellowship of the Research Foundation - Flanders (FWO). This international joint Ph.D. of the Ghent University and the Karlsruhe Institute of Technology, was realized within the framework of the Erasmus Mundus Fusion-DC. This work was supported by the MYRTE project under EURATOM Hoizon 2020 Grant Agreement No. 662186. Merlijn A.J. Mertens was awarded an additional travel grant by FWO to enable a research stay at the Karlsruhe Institute of Technology for the duration of 6 months. Finally, we acknowledge EUROfusion for granting the permission to use the MCNP DEMO models.

The computational resources (Stevin Supercomputer Infrastructure) and services used in this work were provided by the VSC (Flemish Supercomputer Center), funded by Ghent University, FWO, and the Flemish Government – department EWI.